

# Sheffield Hallam University

*Development of corrosion resistant niobium-based PVD coatings.*

PARITONG, Hilke.

Available from the Sheffield Hallam University Research Archive (SHURA) at:

<http://shura.shu.ac.uk/20185/>

## A Sheffield Hallam University thesis

This thesis is protected by copyright which belongs to the author.

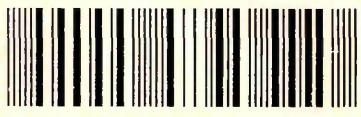
The content must not be changed in any way or sold commercially in any format or medium without the formal permission of the author.

When referring to this work, full bibliographic details including the author, title, awarding institution and date of the thesis must be given.

Please visit <http://shura.shu.ac.uk/20185/> and <http://shura.shu.ac.uk/information.html> for further details about copyright and re-use permissions.

CITY CAMPUS, POND STREET,  
SHEFFIELD, S1 1WS.

101 568 279 0



**Fines are charged at 50p per hour**

13 FEB 2002

3.58 pm

13.2.

7.56 pm

29 MAR 2006 *CPM*

12 JUN 2008 *JF*

**Key Text**  
**REFERENCE**

ProQuest Number: 10700830

All rights reserved

INFORMATION TO ALL USERS

The quality of this reproduction is dependent upon the quality of the copy submitted.

In the unlikely event that the author did not send a complete manuscript and there are missing pages, these will be noted. Also, if material had to be removed, a note will indicate the deletion.



ProQuest 10700830

Published by ProQuest LLC (2017). Copyright of the Dissertation is held by the Author.

All rights reserved.

This work is protected against unauthorized copying under Title 17, United States Code  
Microform Edition © ProQuest LLC.

ProQuest LLC.  
789 East Eisenhower Parkway  
P.O. Box 1346  
Ann Arbor, MI 48106 – 1346

**DEVELOPMENT OF CORROSION RESISTANT  
NIOBIUM-BASED PVD COATINGS**

**Hilke Paritong**

**A thesis submitted in partial fulfilment of the requirements of  
Sheffield Hallam University for the degree of Doctor of  
Philosophy**

**February 2000**



LEVEL 1

## Abstract

Niobium is well known for its excellent corrosion resistance based on the formation of a stable passive oxide layer, which protects the metal against corrosion in most aqueous media and makes it an interesting candidate for corrosion resistant coating applications. However, deposition of Nb films is restricted to few technologies and difficulties arise from the toxic nature of the electrolytes employed in electrodeposition of Nb, the high reactivity of the metal with residual gases in vacuum plasma spraying and its high melting point ( $T_M = 2500^\circ\text{C}$ ) in PVD deposition.

The present thesis describes the development of corrosion resistant Nb coatings on stainless steel and brass substrates by the combined steered arc/ unbalanced magnetron sputtering technique. Evaluation of the corrosion behaviour is performed by potentiodynamic polarisation measurements in 3% NaCl. It is shown that corrosion resistant Nb coatings, with passivation characteristics similar to that of bulk Nb, can be produced on stainless steel substrates by unbalanced magnetron sputtering at a low deposition temperature ( $T = 250^\circ\text{C}$ ) under reduced ion bombardment. However, the ion etching pre-treatment of the substrate prior to deposition has a significant influence on the corrosion resistance of the coating/ substrate system. The employed polarisation measurements reveal that a fully passive and protective behaviour could only be achieved if Nb ions from the cathodic arc source are chosen as the etching species. In contrast, coatings deposited after Cr ion etching from the arc source and inert Ar ion etching, utilising a glow discharge, exhibit localised breakdown and pitting of the substrate. Cross sectional TEM imaging and STEM-EDX analyses reveal that bombardment of the stainless steel substrate by the multiply charged Nb ions generates a compositionally intermixed, very fine crystalline or "amorphised" interface layer, with a thickness of ~3-8nm, depending on the Nb ion energy. It is proposed that this layer acts as an additional barrier against corrosion due to (i) the structural homogeneity achieved by amorphisation and (ii) chemical stabilisation due to the introduction of Nb in the near surface region. The energy of the bombarding Nb ions, i.e. the substrate bias voltage during the etching stage, was found to further influence the corrosion resistance. Best results are achieved with "medium" bias voltages in the range of -600V to -800V, which is believed to be due to an optimum combination of structural and chemical protection mechanisms.

The fully passive corrosion behaviour could not be observed in the case of brass substrates. However, the PVD coating systems on brass and on stainless steel are superior, in the employed polarisation measurements, to commercially produced, electroplated Cr, Ni and Ni/Cr coatings on the same substrate materials.

Other coating properties investigated in the present study include microstructure, hardness, crystallographic orientation and residual film stresses.

## Acknowledgements

I would like to thank the following people for their help and support:

- My Director of Studies Professor Wolf-Dieter Münz for his advice, help, commitment and inspiration throughout this study
- My Supervisors Dr. D. Brian Lewis and Dr. Stuart B. Lyon for their advice and support
- All members of the Surface Engineering Group especially Russ Day, Gary Robinson, the “German Gang” Cornelia Schönjahn, Mirrka Lembke and Arutjun Ehasarian
- Dr. Lee Donohue and Dr. Paul Walke
- Special thanks to my parents, Dagmar and Rolf Paritong for their limitless support throughout my education

## Advanced Studies

The following conferences were attended during the studies for this thesis:

- (I) Third Sheffield ABS Days, July 1997, Sheffield, UK
- (II) Annual Congress of the Institute of Physics, March 1997, Leeds, UK
- (III) Fourth Sheffield ABS Days, July 1998, Sheffield, UK
- (IV) 14<sup>th</sup> International Vacuum Congress, August/ September 1998, Birmingham, UK
- (V) 6<sup>th</sup> International Conference on Plasma Surface Engineering, September 1998, Garmisch Partenkirchen, Germany
- (VI) Workshop Surface Engineering & Design, September 1998, Schwäbisch Gmünd, Germany
- (VII) Fifth Sheffield ABS Days, July 1999, Sheffield, UK
- (VIII) Euromat 99, International Congress on Advanced Materials and Processes, September 1999, Munich, Germany

## Publications & Patents

- (I) *Corrosion Resistant Nb Coatings Grown by Combined Arc/ Unbalanced Magnetron Deposition*, H.Paritong, I.Wadsworth, L.A.Donohue, W.-D.Münz, Trans IMF, 76 (4), (1998), 144
- (II) *Influence of Ion Bombardment on Structure and Properties of Unbalanced Magnetron Grown CrN Coatings*, T.Hurkmans, D.B.Lewis, H.Paritong, J.S.Brooks, W.-D. Münz, Surf.Coat.Technol., 114, (1999), 52
- (III) *Characterisation of Co-Sputtered Nb:Cr Coatings grown by the Combined Arc/ Unbalanced Magnetron Sputtering Technique*, H.Paritong, M.Lembke, D.B.Lewis, W.-D. Münz, Surf.Coat.Technol., 116-119, (1999), 1145  
Presented at PSE '98, September 1998, Garmisch Partenkirchen, Germany
- (IV) *Improvement of Corrosion Resistance of Unbalanced Magnetron Deposited Nb Coatings by High Energy Metal Ion Pretreatment*, H.Paritong, Surf.Eng., 15 (2), (1999), 144  
First prize in the 1998 Bodycote International Paper Prize Competition, presented at the Bodycote AGM, December 1998, Manchester UK
- (V) *PVD Interface Design by Cathodic Arc Generated High Energy Ion Bombardment*, H.Paritong, C.Schoenjahn, L.A.Donohue, W.-D. Münz, to be published in: Interface Controlled Materials, Proc. Euromat '99, September 1999, Munich, Germany  
Presented at Euromat '99, September 1999, Munich, Germany
- (VI) *Influence of Cr<sup>+</sup> and Nb<sup>+</sup> Substrate Sputter Cleaning on the Formation of Ti<sub>1-x</sub>Al<sub>x</sub>N/ Steel Interfaces Generated in a Combined Cathodic Arc/ Unbalanced Magnetron Deposition System*, C.Schönjahn, H.Paritong, L.A.Donohue, W.-D.Münz, R D.Twesten, I.Petrov, in Electron Microscopy and Analysis 1999, Proc. I.o.P. EMAG, August 1999, Sheffield, UK, 75
- (VII) *Source combinee, arc cathodique et magnetron desequilibre pour le depot de couche minees (Arc Bond Sputtering : ABS)*, W.-D.Münz, C.Schönjahn, H.Paritong, I.J.Smith,
- (VII) *Einfluss der Teilchenenergie von Nb-Ionen beim Ätzen von Substraten auf das Korrosionsverhalten nach der Beschichtung*, H.Paritong, C.Schoenjahn, W.-D. Münz, Pending Patent, DPA 19933930.9

# Contents

<b>1. Introduction.....</b>	<b>1</b>
<b>2. Literature Review.....</b>	<b>7</b>
<b>2.1. Niobium and its Properties</b>	<b>7</b>
2.1.1. Physical and Mechanical Properties	7
2.1.2. Chemical Properties and Corrosion Resistance	8
2.1.2.1. Reaction with Gases	8
2.1.2.2. Reaction with Liquid Metals	9
2.1.2.3. Aqueous Corrosion	9
<b>2.2. Metallic Coatings for Corrosion Protection</b>	<b>14</b>
<b>2.3. Nb Coatings</b>	<b>16</b>
2.3.1. Electrodeposition	16
2.3.2. Vacuum Plasma Spraying	16
2.3.3. Physical Vapour Deposition	17
2.3.3.1. Thermal Evaporation	17
2.3.3.2. Sputtering	18
<b>2.4. Coating Technology</b>	<b>20</b>
2.4.1. Cathodic Arc Evaporation	20
2.4.1.1. Random Arc/ Steered Arc	22
2.4.2. Sputtering	24
2.4.2.1. Glow Discharge Sputtering	24
2.4.2.2. Magnetron Sputtering	27
2.4.2.3. Unbalanced Magnetron Sputtering	28
2.4.2.4. Closed Field - Unbalanced Magnetron Sputtering	29
2.4.3. The Arc Bond Sputter (ABS) Technique	29
<b>2.5. Structure Zone Models</b>	<b>30</b>
<b>3. Experimental .....</b>	<b>37</b>
<b>3.1. Coating System</b>	<b>37</b>
<b>3.2. Deposition Procedure</b>	<b>39</b>
3.2.1. Substrates and Substrate Preparation	39
3.2.2. Deposition Parameters	40

<b>3.3. Evaluation Techniques</b>	46
3.3.1. Hardness	46
3.3.2. Roughness	46
3.3.3. Transmission Electron Microscopy (TEM)	47
3.3.4. Scanning Eletrcon Microscopy	48
3.3.5. X-ray Diffraction	48
3.3.5.1.Texture	50
3.3.5.2. Residual Stresses	51
3.3.6. Corrosion Measurements	54
<b>4. Results.....</b>	<b>57</b>
<b>4.1. Nb Coatings on Steel Substrates</b>	<b>57</b>
<b>4.1.1. Comparison of Nb coatings deposited by UBM and SCAE</b>	<b>57</b>
4.1.1.1. Physical Properties	57
4.1.1.2. Microstructure	57
4.1.1.3. Texture and Residual Stress	59
4.1.1.4. Corrosion Resistance	62
<b>4.1.2. Influence of Temperature and Ion Bombardment on UBM Nb coatings</b>	<b>65</b>
4.1.2.1. Physical Properties	65
4.1.2.2. Microstructure	65
4.1.2.3. Texture and Residual Stress	66
4.1.2.4. Corrosion Resistance	68
<b>4.1.3. Influence of the Ion Etching Pre-Treatment prior to UBM Deposition</b>	<b>70</b>
4.1.3.1. Physical Properties	70
4.1.3.2. Microstructure	70
4.1.3.3. Texture and Residual Stress	72
4.1.3.4. Corrosion Resistance	75
<b>4.1.4. Nb-Ion Etching Prior to Coating Deposition : Influence of Working Gas Pressure and Substrate Bias Voltage during Etching</b>	<b>77</b>
4.1.4.1. Microstructure	77
4.1.4.2. Texture	83
4.1.4.3. Corrosion Resistance	85
<b>4.1.5. Intermediate Nb-Ion Etching</b>	<b>89</b>
4.1.5.1. Physical Properties	89
4.1.5.2. Microstructure	89

4.1.5.3. Crystallographic Structure	90
4.1.5.4. Corrosion Resistance	92
<b>4.1.6. Etching Rate</b>	<b>93</b>
<b>4.2. Niobium Coatings on Brass Substrates</b>	<b>95</b>
4.2.1. Substrate Ion Etch	95
4.2.2. Zn-Diffusion Barrier	97
4.2.3. Intermediate Nb Ion Etching	100
<b>4.3. Industrial Applications</b>	<b>101</b>
4.3.1. Niobium Coatings on Stainless Steel Substrates	101
4.3.2. Niobium Coatings on Brass Substrates	102
<b>5. Discussion.....</b>	<b>103</b>
<b>5.1. Nb Coatings on Steel Substrates</b>	<b>103</b>
5.1.1. Corrosion Resistance/ Microstructure	103
5.1.1.1. UBM Coatings/ Interface Region	103
5.1.1.2. SCAE/ UBM	112
5.1.1.3. General Remarks on Corrosion	113
5.1.2. Other Properties and Resume	114
5.1.2.1. Comparison of Nb Coatings deposited by UBM and SCAE	114
5.1.2.2. Influence of Temperature and Ion Bombardment on UBM Nb coatings	116
5.1.2.3. Influence of the Ion Etching Pre-Treatment prior to UBM Deposition	118
5.1.2.4. Nb-Ion Etching Prior to Coating Deposition: Influence of Working Gas Pressure and Substrate Bias Voltage during Etching	119
5.1.2.5. Intermediate Nb-Ion Etching	120
<b>5.2. Niobium Coatings on Brass Substrates</b>	<b>121</b>
<b>5.3. Summary and Future Work</b>	<b>122</b>
<b>6. Conclusions.....</b>	<b>126</b>
<b>7. Appendix.....</b>	<b>127</b>
Appendix I Deposition Parameters	128
Appendix II Publications	137

## 1. Introduction

The present thesis describes the development of corrosion resistant niobium-based coating systems deposited in an industrial sized PVD coating equipment.

Niobium is well known for its excellent corrosion resistance, which is based on the spontaneous formation of a passive oxide film, which protects the metal against corrosion in most aqueous environments. Only some hot concentrated mineral and halide acids attack the metal, as do strong alkaline solutions. The tendency of Nb to form stable oxide compounds is related to its negative standard potential, e.g.  $-0.64$  V (SHE) [1] for the Nb/ Nb<sub>2</sub>O<sub>5</sub> equilibrium, which lies well below the H<sub>2</sub>O/ H<sub>2</sub> and O<sub>2</sub>/ H<sub>2</sub>O equilibria potentials [2]. The closely related tantalum exhibits even better corrosion resistance, however, Nb was chosen in the present work due to its lower melting point, lower density and greater availability and therefore its lower cost.

The most common application of the metal is as alloying additions to steels and superalloys. Applications as a coating material include corrosion protection, superconducting devices and recently as a material for orthopaedic implants due to its biocompatibility and chemical resistance to physiological fluids. However, there are not many published papers on the use of Nb as a coating material, which might be related to the difficulties involved with the deposition of Nb. The deposition technologies used to produce Nb coatings include electrodeposition in molten alkali halides or organic solvents, vacuum plasma spraying, thermal evaporation and sputtering. Disadvantages arise from the toxic nature of the electrolytes and the high temperatures involved in electrodeposition, the high reactivity of Nb with residual gases in the case of plasma spraying and the high melting point of the metal ( $T_M=2500^\circ\text{C}$ ) in the case of thermal evaporation processes.

The present work investigates the properties of PVD Nb thin films with main emphasis on the corrosion resistance. The coating equipment used for film deposition is a Hauzer ABS (Arc Bond Sputter) coating unit, which combines the two PVD techniques of steered cathodic arc evaporation and unbalanced magnetron sputtering. The industrial scale of the equipment would allow direct transfer from research to potential commercial applications. The major part of the work (chapter 4.1.) is focused on the corrosion behaviour of the coatings on austenitic stainless steel substrates. Stainless steel as well is characterised by a comparatively high corrosion resistance due to the formation of a passive oxide layer. However, the stability of the protective layer is

restricted, as stainless steel is susceptible to pitting and crevice corrosion, especially in the presence of chloride anions and in physiological fluids. A thin Nb film could act as a protective barrier against pitting and corrosive attack of the steel substrate. The corrosion behaviour is monitored using potentiodynamic polarisation measurements in a 3%NaCl solution. Additionally, other coating properties are investigated including microstructure, hardness, crystallographic orientation and residual stresses.

In the second part of the thesis (chapter 4.2.) first results are obtained from deposition of Nb coatings on brass substrates. PVD coated brass is mainly used for decorative applications such as bath fittings, writing tools, door handles, watches etc. The PVD coatings used are for example ZrN, TiN, TiCN or TiAlN. However, these top-coatings are normally thin and a corrosion resistant interlayer is often necessary to prevent corrosive failure. At present, these interlayers are mainly electroplated coatings such as Ni/ Cr. It would be desirable to replace the electrodeposit by a corrosion resistant PVD interlayer such as Nb for two reasons. Firstly, PVD is a “cleaner“ i.e. environmentally more acceptable technology and secondly, the whole coating system could be deposited in one single process step. A problem arising from direct film deposition on brass substrates in vacuum technology is the high vapour pressure of zinc. Outgassing of Zn from the alloy during the initial stages of film deposition and diffusion through barrier- and top-coating restrict the maximum deposition temperature to 250°C at a typical operational gas pressure of  $2.5 \cdot 10^{-3}$  mbar in PVD [3]. Hence, a main incentive throughout the research work was to investigate whether Nb could successfully be deposited under process conditions allowing low operating temperatures of around 250°C.

Section 4.1.1. compares deposition of Nb coatings by the two different techniques i.e. steered cathodic arc evaporation (SCAE) and unbalanced magnetron sputtering (UBM). In principle, the high melting point of Nb is regarded as a disadvantage in PVD deposition, as it becomes increasingly difficult to produce dense film morphologies with increasing melting point of the coating material, as described by the structure zone models shown in section 2.5. In terms of corrosion protection, a largely underdense or voidal coating morphology naturally would be detrimental. An advantage of SCAC over UBM is the high degree of ion flux and ion energies towards the growing film i.e. the presence of multiply charged metal ions. This can influence the coating morphology by decreasing the minimum homologous temperature necessary to produce dense films.

However, disadvantages of the arc technique can arise from the instability of the arc discharge on Nb and a low deposition rate, both factors again originating from the high melting point of the metal and from its low vapour pressure. Furthermore, the generation of macroparticles and higher coating temperatures due the increased ion bombardment during arc evaporation might have to be taken into consideration. It will be shown that UBM is the favourable deposition technique to produce Nb coatings compared with SCAE. The subsequent research work was therefore focused on UBM deposition.

The work presented in section 4.1.2. was carried out to investigate whether it is possible to successfully sputter deposit Nb coatings at low deposition temperatures and under reduced ion bombardment. The ABS coating unit allows control of the ion flux reaching the substrate by adjusting the unbalancing effect of the magnetrons via electromagnetic coils. The deposition temperature is influenced, regardless of additional heating elements, by (i) the ion flux i.e. the unbalancing coil current, (ii) the ion energy i.e. the substrate bias voltage and (iii) the cathode power. As it was not desirable to change the two latter parameters [4], adjustment of the unbalancing coil current was used to reduce the coating temperature from 420°C to 250°C. It will be shown that under the employed process conditions, a deposition temperature of 250°C and an unbalancing coil current of 3A are sufficient to produce corrosion resistant Nb coatings on stainless steel substrates.

In section 4.1.3. the influence of the ion etching pre-treatment of the substrate on the properties of subsequently sputter-deposited, low temperature Nb coatings is investigated. Substrate sputter cleaning with Nb ions from the cathodic arc source, as used in the previous coating processes, is compared to cathodic arc Cr ion etching and inert Ar ion etching utilising an ion-enhanced glow discharge. The incentive behind Cr ion etching was its proven qualities to promote excellent adhesion in hard coating systems and its characteristics to form the smallest sized droplets, in relatively low concentration, of refractory metals [5], [6]. Furthermore, the lower melting point and higher vapour pressure of Cr leads to an increase in stability of the arc discharge compared with Nb. Inert Ar ion etching was chosen due the absence of droplet or macroparticle generation, possibly resulting in a reduction of growth defects and hence improved corrosion resistance. Additionally, the relatively low ion bombardment

generated during glow discharge sputter cleaning compared with cathodic arc metal ion etching, results in greater controllability of the substrate temperature. However, it will be shown that Nb ion etching is superior to the two other etching modes in terms of the corrosion resistance of the stainless steel/ Nb coating system. This will be related to the differences in the nature of the interface regions.

As bombardment of the stainless steel substrate with Nb ions from the cathodic arc source had proved to have a beneficial influence on the corrosion properties of the substrate/ coating system, the interface region was further investigated. In section 4.1.4. the effect of substrate bias voltage and working gas pressure, during the substrate cleaning stage, on the nature of the interface region and corrosion properties is investigated. A possible reduction in the substrate bias voltage from the previously used, standard value of  $-1200\text{V}$  to lower values would allow greater controllability of the substrate temperature as it results in a reduction of the ion energy and substrate bias current and hence energy dissipation on the substrate. Lowering of the working gas pressure was performed to investigate whether enhanced substrate ion bombardment, stemming from a decrease in charge exchange events between the Nb ions and the working gas Ar, might possibly further influence the corrosion resistance. However, a higher working gas pressure was always desirable due to a greater stability of the arc discharge and, again, easier control of the process temperature. To clarify the influence of the interface region further, the coating thickness of the subsequently sputter deposited Nb coatings was reduced from over  $1\mu\text{m}$  to  $300\text{nm}$ . Additionally, the corrosion resistance of “as etched” substrates with no additional coating is discussed, again as a function of the substrate bias voltage. It will be shown that the influence of the interface region on the corrosion resistance is significant and that the nature or “architecture” of this region can be controlled via the substrate bias voltage to optimise the corrosion properties.

Due to the beneficial effect of Nb ion bombardment found in the substrate ion etching step, it was assumed that interruption of the coating growth in UBM deposition by short term Nb ion etching from the cathodic arc source might have similar effects. Chapter 4.1.5. lists results obtained from Nb coatings subjected to two “intermediate” etching steps during sputter deposition under variation of the substrate bias voltage.

The last paragraph in chapter 4.2. investigates the etching or removal rate of substrate material by Nb ion bombardment from the cathodic arc source. This was done by etching a NiCr coating, as an imitation of stainless steel substrate material, and comparing the thicknesses of etched and non-etched coating areas. The latter was achieved by masking a part of the coating during the etching trial.

In the second part of chapter 4 results are presented from UBM deposition of Nb based coatings on brass substrates. It will be shown in section 4.2.1. that the beneficial effects of substrate bombardment with Nb ions prior to deposition could not be transferred to brass. Therefore Ar ion etching was chosen as the etching mode prior to coating deposition due to easier control of the substrate temperature as compared with metal ion etching and the high sputter yields of Cu and Zn.

One way to avoid outdiffusion of Zn in the PVD chamber, is to deposit a Cu- based diffusion barrier prior to deposition of Nb [3]. Three different interlayers were compared, i.e. Cu, CuAlFe, and CuAlFe/ NiCr, as shown in section 4.2.2. The incentive behind CuAlFe bronze is its well known corrosion resistance as bulk material. The NiCr layer was added due to its proven ability to act as an electrodeposited “buffer” layer between brass and PVD coatings [7]. Section 4.2.3. investigates whether Nb ion etching of the Cu based interlayer rather than the brass substrate can result in any improvement of the corrosion resistance.

Finally, in chapter 4.3. the corrosion performance of the Nb- based PVD coatings on stainless steel and brass is compared to commercially used electroplated coatings, deposited on the same substrate materials.

## References to Chapter 1

- [1] Anorganische Chemie, E.Riedel, Walter de Gruyter & Co., 1989, Berlin, Germany, 694
- [2] J.van Mulder, M.Pourbaix, Techn.Rep.No. 53, Centre Belge d'Etude de la Corrosion, (1957), Brussels, Belgium
- [3] B.Langer, M.Phil. Thesis, Sheffield Hallam University, 1995, Sheffield, UK
- [4] E.E.Salagean, D.B.Lewis, J.S.Brooks, W.-D.Münz, I.Petrov, J.E.Greene, Surf.Coat.Technol., 82, (1996), 57
- [5] S.Creasey, D.B.Lewis, I.J.Smith, W.-D.Münz, Surf.Coat.Technol., 97, (1997), 163
- [6] W.-D.Münz, I.J.Smith, D.B.Lewis, S.Creasey, Vacuum., 48, (1997), 473
- [7] H.Erhart, S.Bastian, H.Petersen, in Plasma Surface Engineering, E.Boszeit, W.-D.Münz, H.Oechsner, K.-T.Rie, G.K.Wolf (Ed.), Vol.2, DGN Informations Gesellschaft Verlag, 1989, Oberursel, Germany, 603

## **2. Literature Review**

### **2.1. Niobium and its Properties**

Niobium, formerly known as columbium, was discovered in 1801 by Hattchet and first prepared in 1864 by Blomstrand by reduction of niobium chloride [1]. Its properties are very similar to those of tantalum, caused by lanthanide contraction, which lead to controversy about the identity of the two metals in the years of their discovery. The element is found in niobite, niobite-tantalite, pyrochlore and euxenite [2]. Niobium belongs to the family of the refractory metals, which constitute the fifth and sixth group of the transition elements. It is a shiny, silvery- grey metal.

The most common application for niobium is as an alloying addition to steels and superalloys for elevated temperature service, particular in aerospace applications. Due to its excellent chemical stability it is often used in areas where protection is needed from corrosive environments i.e. from aqueous corrosion, hot gas corrosion or liquid metal corrosion. Although Ta exhibits even better corrosion behaviour, Nb is preferred for many applications due to its lower melting point, lower density and greater availability and therefore its lower cost. Further applications of Nb as a metal or as an alloying addition can be found in cathodic protection systems, heat exchangers, electronic components, superconductors, nuclear industry and more [3], [4]. There is also growing awareness of Nb for use as a biomaterial because of its chemical resistance and considerable biocompatibilty [5], [6], [7].

#### **2.1.1. Physical and Mechanical Properties**

Niobium has a density close to that of copper, but only about half the density of tantalum and tungsten. As a member of the group of the refractory metals, it is characterised by a high melting point ( $T_M=2500^{\circ}\text{C}$ ). The metal exhibits good thermal conductivity.

Niobium is a tough, ductile metal, which undergoes ductile to brittle transition below  $147^{\circ}\text{K}$ . It has moderate strength and can be work hardened to a certain degree. It can be rolled, drawn and extruded. Nb has a body centred cubic crystal structure. The physical and mechanical properties are summarised in table 1.

Atomic Weight	92.0946
Density	8.66 g/cm <sup>3</sup>
Melting Point	2468°C
Boiling Point	4297°C
Coefficient of Thermal Expansion	7.1 10 <sup>-6</sup> /°C
Electrical Resistivity	15.22 μΩ/cm (T=0°C), 19.18 μΩ/cm (T=100°C)
Thermal Conductivity	52.3 W/(m*K) (T=0°C), 54.4 W/(m*K) (T=100°C)
Crystal Structure	bcc A2, a = 3.294 Å
Atomic Diameter	0.294 nm
Hardness	60 HV (annealed), 150 HV (cold worked)
Elastic Modulus	103 GPa
Poisson's Ratio	0.38
Ductile Brittle Transition Temp.	<147 °K

Table 2.1. Physical and mechanical properties of Nb [1], [3], [4]

## 2.1.2. Chemical Properties and Corrosion Resistance

As an element of the fifth group of the transition elements, Nb has five valence electrons. The electron configuration of Nb is [Kr]4d<sup>3</sup>5s<sup>2</sup> or [Kr]4d<sup>4</sup>5s<sup>1</sup>, where one of the s electrons had been demoted in an attempt to help the d-subshell approach the more stable half-filled condition [8]. Its maximum and most important oxidation number is +5. In this oxidation state niobium forms practically no cations but does form some anion complexes, a behaviour very similar to non-metals [9]. Other oxidation states are +2, +3 and +4.

### 2.1.2.1. Reaction with Gases

The oxidation resistance of Nb at elevated temperatures is poor. Below 300- 400°C the first stages of oxidation are determined by chemisorption and diffusion of oxygen in the Nb lattice and the formation of sub-oxides [10], [11]. The onset of accelerated or “breakaway” oxidation [11] at higher temperatures is associated with the formation of a porous, non-protective scale of Nb<sub>2</sub>O<sub>5</sub>, which offers little protection against further

oxidation. The formation of this scale is often regarded as a result of cracking of an initially adherent and protective scale. This is associated with the high oxide to metal volume ratio ( $\text{Nb}_2\text{O}_5 / \text{Nb}$ : 2.69 [12]), inducing high compressive biaxial stresses, which lead to breakdown of the protective scale [8], [12], [13].

Niobium absorbs hydrogen and nitrogen at temperatures above 300°C [3], [14]. Even a small amount of absorbed hydrogen markedly reduces the ductility of the metal. The crystallinity of the formed hydrides depends on the hydrogen amount; above a certain concentration the one phase solid solution ( $\alpha$ -phase) segregates into two brittle phases ( $\alpha$ -phase and  $\beta$ -phase), characterised by different hydrogen amounts. The  $\alpha$ -phase possesses the bcc lattice of the pure metal, being expanded to accommodate the hydrogen atoms. The  $\beta$ -phase phase has a slightly distorted cubic symmetry with orthorhombic symmetry characteristics [10]. At higher hydrogen concentrations, approaching  $\text{NbH}_{1.0}$ , the system becomes homogenous again [8], [10]. The reaction of Nb with nitrogen also leads to embrittlement of the metal with phase separation at the approximate concentration of  $\text{Nb}_2\text{N}$  into two phases,  $\alpha$ -phase and  $\beta$ -phase. The  $\alpha$ -phase again being the interstitial bcc solid solution, while the  $\beta$ -phase possesses a hexagonal structure [10]. Further increase in the nitrogen content leads to the formation of a series of different phases. However, the amount of both, hydrogen and nitrogen, necessary to embrittle Nb is below their limit of solubility [8]. The low oxidation resistance of niobium and the high susceptibility to embrittlement makes it necessary to place the metal in protective atmosphere or vacuum when processed even at moderate temperatures [2].

#### 2.1.2.2. Reaction with Liquid Metals

Niobium is resistant to attack in most liquid metals:  $\text{Li} < 1000^\circ\text{C}$ ,  $\text{Na}$ ,  $\text{K} < 1000^\circ\text{C}$ ,  $\text{Mg} < 850^\circ\text{C}$ ,  $\text{U} < 1400^\circ\text{C}$ ,  $\text{Zn} < 450^\circ\text{C}$ ,  $\text{Pb} < 850^\circ\text{C}$ ,  $\text{Bi} < 500^\circ\text{C}$  and  $\text{Hg} < 600^\circ\text{C}$ , which makes it a good candidate in applications in liquid metal cooled nuclear reactors [3].

#### 2.1.2.3. Aqueous Corrosion

Niobium is characterised by its excellent corrosion resistance in most aqueous media. This corrosion resistance is not based on the nobility of Nb, i.e. a wide range of

chemical immunity or a noble standard dissolution potential, but rather on its strong tendency to passivate in most environments. Pourbaix [15] classifies the range of nobility effectively as the combination of the regions of immunity and passivation. Only the latter justifies classing Nb as a noble metal, as shown by the Pourbaix diagram in fig.2.1. The range of immunity is not very large with a calculated equilibrium potential of immunity of  $-1.14$  V vs. SHE (Standard Hydrogen Electrode) at pH7 [16]. However, there is no area of active corrosion but passivation of the metal in all areas of the Pourbaix diagram, i.e. at all pH values. Due to this extended range of passivity, Nb is ranked as the second most noble metal as shown in fig.2.2. The figure gives a classification of metals in order of their nobility based on immunity only (column a) and based on immunity and passivation column (b).

The passivity of Nb is based on the formation of a protective oxide film as can be seen from fig.2.1. The tendency of Nb to form stable oxide compounds is related to its negative standard potential, e.g.  $-0.64$  V (SHE) [9] for the Nb/  $\text{Nb}_2\text{O}_5$  equilibrium, which lies well below the  $\text{H}_2\text{O}/ \text{H}_2$  and  $\text{O}_2/ \text{H}_2\text{O}$  equilibria potentials [17]. At all pH values, the metal tends to form an oxide layer, which is extremely stable to complexing specimen.

The known oxides of the metal are niobium pentoxide ( $\text{Nb}_2\text{O}_5$ ), niobium dioxide ( $\text{NbO}_2$ ), a homologous series of  $\text{Nb}_{3n+1}\text{O}_{8n-2}$  (with  $n=5,6,7,8$ ) and niobium monoxide ( $\text{NbO}$ ) [9], [10], [16].  $\text{NbO}$  has a sodium chloride-type cubic structure, which may be described as having eight niobium vacancies at the corners and one oxygen vacancy at the centre.  $\text{NbO}_2$  has a distorted rutile structure. The most stable oxide,  $\text{Nb}_2\text{O}_5$ , presents an extended polymorphism giving rise to a homologous series of structurally related phases of the general formula  $\text{Nb}_{3n+1}\text{O}_{8n-2}$  ( $n=5-8$ ) [17]. Below  $500^\circ\text{C}$   $\text{Nb}_2\text{O}_5$  is amorphous [18]. It is an oxygen-deficient oxide with n-type semiconductor properties. The lower oxides,  $\text{NbO}$  and  $\text{NbO}_2$  are thermodynamically unstable in the presence of water, acids and alkalis at all pH values as can be seen from the Pourbaix diagram. The diagonals ① and ② in fig.2.1. represent the following reactions:



$\text{NbO}_2$  is oxidised to  $\text{Nb}_2\text{O}_5$  at potentials and pH values defined by diagonal ③;



$\text{Nb}_2\text{O}_5$  is stable in the presence of water and most acids and alkalis at all pH values. Depending on the “quality” of the oxide layer, i.e. homogeneity, density and

thermodynamic stability in the given environment, Nb will behave as a noble (non-corrodable) or non-noble (corrodable) metal [16].

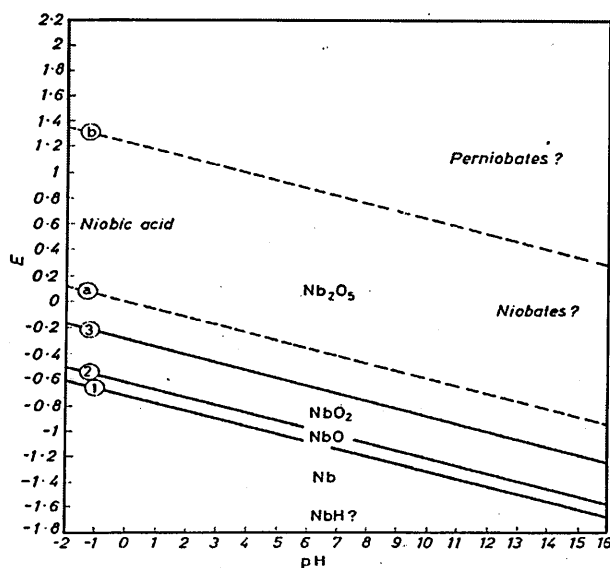


Fig. 2.1. Voltage/ pH diagram of the Nb/ water system at 25°C [16]

Column A		Column B	
(Immunity)		(Immunity and Passivation)	
<u>Noble Metals</u>			
1	Gold	Rhodium	1
..	..	<b>Niobium</b>	2
3	Platinum	Tantalum	3
4	Rhodium	Gold	4
...	...	...	...
7	Mercury	Platinum	6
...	...	Titanium	7
10	Selenium	Mercury	10
...	...	Aluminium	19
19	Lead	Indium	20
20	Rhenium	Chromium	21
21	Nickel	Selenium	22
...	...	Nickel	29
29	Germanium	...	...
...	...	Lead	32
33	<b>Niobium</b>	Rhenium	35
34	Tantalum	...	...
35	Chromium	Germanium	39
...	...	...	...
39	Aluminium	Magnesium	41
...	...	...	...
41	Titanium	...	...
42	Magnesium	...	...
<u>Non-noble Metals</u>			

Fig.2.2. Classification of metals in order of thermodynamic nobility (after [15])

Anodic polarisation of Nb can be used to produce dense, homogenous films of Nb<sub>2</sub>O<sub>5</sub> with controllable thickness [19]. The metal is polarised as the anode in an electrolytic cell and the applied current sets up an electrostatic field, which enhances the ionic movement through the oxide, hence causing continuous growth of the oxide layer. The thickness of the oxide film can be expressed, at a first approximation, as thickness/electrode potential, which is 2.25 nmV<sup>-1</sup> for Nb [17]. Anodic oxide films of Nb show bright interference colours, which are a function of the oxide thickness and can hence be accurately controlled via the applied current or potential.

The corrosion resistance of Nb is excellent at room temperature but deteriorates above 100°C. The metal is not attacked by most inorganic acids at low temperatures, irrespective of the acid concentration. Nb is however attacked by some hot concentrated mineral acids such as sulphuric acid and its anhydrides which lead to embrittlement of the metal and partial dissolution [1], [20]. Corrosion in these concentrated solutions is probably due to reduction of the water activity, which leads to a stabilisation of Nb(V) complexes by reduced hydrolysis action and hence increased corrosion [17].

Hydrofluoric acid and solutions of its salts as well as a mixture of hydrofluoric acid and nitric acid are detrimental and dissolve the metal, especially when hot [1]. Again, this is related to the formation of a stable, non-hydrolysable fluor-complex. Similarly, other halide acids attack Nb but only when very concentrated, probably due to a similar mechanism. Halide acids in low concentrations, except HF, form much less stable complexes, which undergo hydrolysis and hence do not attack the metal [17].

Niobium resists attack of most organic acids, including acetic, oxalic, tartaric and lactic acid. The metal is readily attacked by strong alkaline solutions e.g. solutions of sodium hydroxide and potassium hydroxide which cause severe embrittlement of the metal [1], [21]. The corrosive attack at high pH values is related to the formation of niobates (e.g. NaNbO<sub>3</sub>) and polyniobates [17]. The phase responsible for the embrittlement was identified as β-niobium hydride with the formula NbH<sub>0.7</sub> [1]. Table 2.2 summarises the corrosion behaviour of Nb in acids and alkaline solutions.

Hydrogen embrittlement also takes place when Nb is subjected to water steam over a longer time period. Similar to corrosion by alkaline solutions NbH<sub>0.7</sub> was identified in the metal.

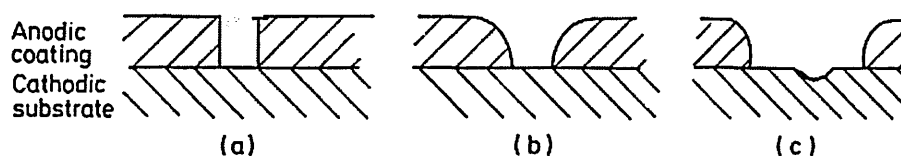
Corrosive Medium	Temperature [°C]	Weight Loss [g * m <sup>-2</sup> * 24h <sup>-1</sup> ]	Condition after test
HCl 20%	21	25*10 <sup>-8</sup>	No change
HCl conc.	21	6*10 <sup>-8</sup>	Slightly etched
HCl conc.	100	2.3*10 <sup>-6</sup>	Brittle
HNO <sub>3</sub> conc.	100	nil	No change
Aqua regia	22	nil	No change
H <sub>2</sub> SO <sub>4</sub> 25% <sub>vol.</sub>	21	nil	No change
H <sub>2</sub> SO <sub>4</sub> conc.	21	5.6*10 <sup>-8</sup>	Partial Embrittlement
H <sub>2</sub> SO <sub>4</sub> conc.	100	1.1*10 <sup>-5</sup>	brittle
H <sub>2</sub> SO <sub>4</sub> conc.	175	1.2*10 <sup>-4</sup>	Compl. dissolved
H <sub>3</sub> PO <sub>4</sub> 85%	21	0.7*10 <sup>-8</sup>	No change
H <sub>3</sub> PO <sub>4</sub> 85%	100	1.9*10 <sup>-6</sup>	Brittle
NaOH 5%	21	6.6*10 <sup>-7</sup>	Brittle
NaOH 5%	100	1.3*10 <sup>-3</sup>	Brittle
KOH 5%	21	4.4*10 <sup>-6</sup>	Brittle
KOH 5%	100	2.7*10 <sup>-5</sup>	Brittle

Table 2.2. Corrosion of Nb in aqueous media ([1] after [22])

## 2.2. Metallic Coatings for Corrosion Protection

Metallic coatings for corrosion control usually serve two functions. Firstly, the coating has a more active corrosion potential than the base material. In this case the coating is *anodic* to the substrate and will corrode sacrificially. Secondly, the metallic coating has a less active i.e. nobler corrosion potential than the base material. In this case, the coating is *cathodic* to the substrate and will act as a corrosion resistant barrier to the environment [23]-[27]. In both cases, cracks or pores in the coating lead to galvanic coupling between the coating and the substrate material with the following well-known effects:

### i) Anodic coating:



### ii) Cathodic coating:

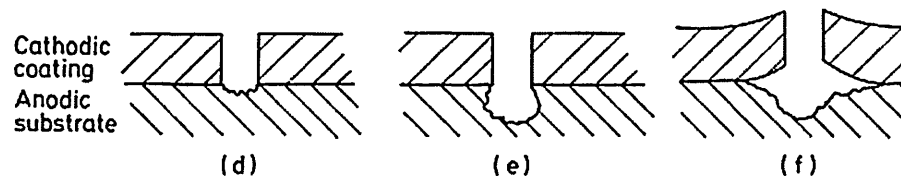


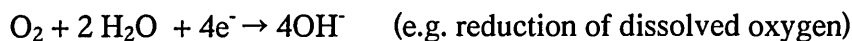
Fig. 2.3. Galvanic effects on coating/ substrate systems [23]

Simplified, the anodic and cathodic reactions involved can be expressed as follows:

#### i) Anodic reaction:



#### ii) Cathodic reaction:



In the case of an anodic coating, the coating corrodes and cathodically protects the substrate at breaks in the coating (fig.2.3. (a), (b)). Cathodic reactions take place at the substrate surface such as hydrogen evolution or oxygen reduction. The anodic current

density is low as the surface area ratio between anode and cathode is large and the anodic current  $i_a$  equals the cathodic current  $i_c$  as defined by the mixed potential theory [24]. If the process progresses too far the coating will lose its cathodic protection (fig.2.3. (c)). In the case of a cathodic coating, exposure of the substrate to the corrosive environment can be detrimental (fig.2.3. (d), (e)). The anodic substrate can corrode severely as a result of the high anodic current density i.e. small anode to cathode surface area ratio, finally leading to blistering or uplifting of the protective coating (fig.2.3. (f)). However, the above mechanisms are rather general and simplified and other aspects have to be considered in “real life” corrosion. These include the formation of non- or slowly soluble corrosion products, which can accumulate in the breaches of the film and add another barrier to attack of the substrate or the formation of passive oxide films. If for example a fresh Nb surface is coupled with a fresh stainless steel surface, Nb will behave anodically with respect to the steel; it will however not “corrode freely” as stated above but the anodic reaction will result in the formation of a protective oxide layer.

A variety of processes exist to produce corrosion protective metallic coatings, which cover a wide range of techniques and film properties. A broad classification is given below [23]

- (i) Mechanical applications (e.g. cladding, extruding)
- (ii) Molten applications (e.g. hot dipped zinc, aluminium)
- (iii) Electrodeposition (e.g. electroplated chromium, nickel, copper, zinc)
- (iv) Chemical deposition (e.g. electroless nickel, copper)
- (v) Diffusion coatings (e.g. chromium diffusion coating)
- (vi) Spray applications (e.g. plasma spraying, arc spraying)
- (vii) Vapour deposition (chemical vapour deposition, physical vapour deposition)

The following criteria are important for the choice of coating technique as well as coating material:

- (I) Economic and environmental aspects
- (II) Performance of the coating/ substrate system, determined by
  - (i) galvanic action between coating and substrate in a given environment
  - (ii) formation of suitable corrosion products
  - (iii) adhesion of the coating
  - (iv) coating thickness
  - (v) microstructure of the coating

## **2.3. Niobium Coatings**

The properties of niobium, such as its high melting point, reduce the number the possible deposition techniques to produce Nb coatings. The only three deposition techniques commonly used are electrodeposition, vacuum plasma spraying and physical vapour deposition.

### **2.3.1. Electrodeposition**

Successful electrodeposition of Nb is regarded as difficult owing to the earlier mentioned properties of the metal, which are [28]:

- (i) its rather negative reduction potential, which leads to interference by hydrogen evolution in aqueous media
- (ii) the tendency to react with oxygen to form electrically inactive compounds, even in certain non-aqueous media
- (iii) the tendency of Nb to form stable cluster-compounds at low valence states [9]

The initial work on Nb plating was carried out in the 1960's by [29]. Electrodeposition of Nb is based on the reduction of Nb(V) from Nb salts e.g.  $K_2NbF_7$  in appropriate electrolytes, typically molten alkali fluorides (KF, LiF) (e.g. [29-33]), alkali chlorides [34],[35] or organic solvents [28]. However, high operating temperatures (typically above 700°C) and the toxic nature of the employed electrolytes, make electrodeposition a rather impractical technique to produce Nb coatings.

### **2.3.2. Vacuum Plasma Spraying**

Nb coatings with a thickness of 250µm were deposited on steel substrates for corrosion protection using low-pressure vacuum plasma spraying [36]. Polarisation measurements in hydrochloric acid indicate that the coatings are resistant to general and localised corrosion with no significant substrate effect. However, the anodic current densities were higher for the coated samples compared to bulk Nb. Similar results were obtained by Lugscheider et al. who also produced 250µm thick Nb coatings by low-pressure vacuum plasma spraying [37].

### 2.3.3. Physical Vapour Deposition

#### 2.3.3.1. Thermal Evaporation

Deposition of niobium by evaporation techniques such as arc evaporation yields in general low deposition rates owing to its high evaporation enthalpy and low vapour pressure. Mainly thin films of Nb for superconductive devices were produced by arc evaporation (e.g. [38],[39]).

Nb coatings with a thickness of  $0.2\mu\text{m}$  were deposited on silicon substrates by electron-beam-evaporation with an additional ion source (IBAD) [40]. The authors investigated the influence of the deposition temperature and low-energy ion bombardment on the stress behaviour in the coatings and found that the stress state of Nb films can be substantially modified, i.e. tensile to compressive, using  $100\text{eV}$  Ar ion bombardment. The obtained stress values range from approximately  $+0.8\text{ GPa}$  to  $-0.3\text{ GPa}$ .

Hsieh et al. deposited Nb coatings at room temperature with a thickness of  $\sim 3\mu\text{m}$  on stainless steel substrates also by ion-beam assisted deposition (IBAD) using electron-beam evaporation [41]. It is reported that bombardment of the growing film with  $250\text{eV}$  Ar ions and an  $\text{Ar}^+/\text{Nb}$  ratio of  $0.68-0.80$  produces coatings with a dense microstructure (investigated by SEM), which behave in a similar manner to bulk Nb when tested in potentiodynamic polarisation measurements in  $3\%$  NaCl. No current densities are reported. The authors extended their studies to co-deposited Nb/ Cr coatings using IBAD and investigated the corrosion behaviour as a function of the Nb/ Cr ratio [42].

Ji et al. investigated the texture, surface morphology and microstructure of thin Nb coatings ( $<1\mu\text{m}$ ) deposited by IBAD as a function of the ion bombardment [43]. The authors found that ion channelling in easy channel directions in a grain causes differential sputtering and hence influences texture development, microstructure and surface morphology by preferential growth and shadowing effects.

However, sputtering appears to be the preferred PVD technique to produce Nb coatings, as it is a non-thermal vaporisation technique, in which the deposition- i.e. sputter rate is foremost a function of the surface binding energy of the cathode material and independent of its thermal properties. The following section gives an overview of recent literature describing deposition of Nb and Nb/ metal alloys by sputtering.

### 2.3.3.2. Sputtering

#### (i) Pure Nb coatings

Only a few studies have been published on the corrosion resistance of sputtered pure Nb coatings. Datta et al. first reported about the potential of Nb coatings on stainless steel substrates, deposited by magnetron sputtering/ ion plating, for biomedical implants in 1988 [5]. The authors investigated the corrosion performance by polarisation measurements and the microstructure (SEM) of 3-9 $\mu\text{m}$  thick magnetron sputtered coatings on stainless steel substrates as a function of the substrate bias voltage, the Ar gas pressure and the coating thickness [5], [7], [44], [45]. The best corrosion resistance is reported for Nb coatings deposited at substrate bias voltages of  $-1000\text{V}$  and  $-2000\text{V}$ , which is related in the studies to the dense, pore-free nature of the coatings. However, the corrosion performance of all the coated substrates is poor compared with bulk Nb and the substrates corrode actively. The corrosion currents measured at a potential of  $+1000\text{mV}$  are  $2 \times 10^{-3} \text{ Acm}^{-2}$  for the coated samples compared with  $1 \times 10^{-4} \text{ Acm}^{-2}$  for bulk Nb. The fact that the coatings deposited at low bias voltages with an open columnar structure still exhibit better corrosion resistance than uncoated stainless steel is related by the authors to the formation of a thin, extremely dense amorphous layer during the initial stages of film growth [5]. However, no further explanation about the origin of this layer is given. With regard to the Ar pressure and coating thickness, an increase in corrosion performance was found with decreasing Ar gas pressure and increasing coating thickness. The morphologies of the sputtered films are characterised as zone 1 structures at low bias voltages ( $-200\text{V}$  to  $-400\text{V}$ ), zone T structures at  $0\text{V}$  bias voltage and zone 2 and 3 structures at  $-1000\text{V}$  and  $-2000\text{V}$ .

The deposition of  $1\mu\text{m}$  thick Nb films on stainless steel by the combined steered cathodic arc evaporation/ unbalanced magnetron sputtering technique is reported [46]. The corrosion resistance or rather macroporosity of the films, investigated by the ferroxyl test, was determined as a function of the substrate bias voltage and an optimum performance was found at a bias voltage of  $-75\text{V}$ . The interfacial region and the coating morphology were investigated with regards to the mode of sputter cleaning pre-treatment of the substrate. It was found that etching with Nb ions from the cathodic arc source generates a sharp interface with a Nb-rich interlayer, approximately  $5\text{nm}$  thick. The coatings deposited after Nb ion etching showed a strong preferred  $\{110\}$  orientation while a nearly random distribution of crystallographic planes was found for

the film deposited after Ar ion etching. The texture was independent of the substrate bias voltage, whereas a minimum lattice strain is reported for a substrate bias voltage of  $-75\text{V}$ .

Wu conducted a systematic study on the effect of the substrate bias voltage and the Ar gas pressure on the morphology (SEM) and residual stresses in magnetron sputtered Nb coatings, with a thickness of  $0.3\mu\text{m}$  [47]. An increase in substrate bias voltage ( $-100\text{V}$  to  $-300\text{V}$ ) lead to a decrease in column size and smoother coating surfaces, while increasing the Ar content and compressive stresses in the film. Low Ar gas pressures also lead to an increase in Ar content, refined coating morphologies and a shift from a tensile to a compressive stress state. The reported stress values range from approximately  $+0.4\text{ GPa}$  to  $-1.5\text{ GPa}$ .

The stress behaviour in r.f.sputter deposited,  $0.1\mu\text{m}$  thick Nb coatings, which were under compressive stresses, was investigated as a function of post-deposition high-energy ion bombardment ( $300\text{keV}$  and  $600\text{keV}$  Xe-ions) [48]. Bombardment with  $300\text{keV}$  merely expanded the distorted as-deposited Nb unit cell, while bombardment with  $600\text{keV}$  ions lead to a stress relaxation in the film. The results were obtained by means of lattice parameter measurements; no absolute stress values are presented.

The effect of off-normal, low-energy ion bombardment on the crystallographic orientation of ion-beam sputtered Nb coatings with a thickness of several hundreds of nanometers on amorphous silica substrates was investigated [49]. It was shown that glancing angle ion bombardment can have a pronounced effect on the texture due to ion channelling and preferential re-sputtering i.e. preferential growth of grains oriented in easier channelling directions.

The microstructure, hardness and the scratch test adhesion of  $6$  to  $8\mu\text{m}$  thick magnetron sputtered coatings was investigated as a function of the Ar gas pressure during deposition [50]. The morphology of the coatings is described as zone 1 structures with average column diameters at the surface of  $0.15\mu\text{m}$  to  $0.6\mu\text{m}$ . An increase in critical load values from  $0.2\text{N}$  to  $0.4\text{N}$  was observed with decreasing Ar gas pressure, while the hardness of the coatings was not influenced by the change in pressure with an average value of  $\text{HV}_{0.05} = 400$ . The crystallographic orientation of  $6$  to  $8\mu\text{m}$  thick magnetron sputtered Nb coatings was evaluated as a function of various process parameters [51]. Predominantly  $\{111\}$ ,  $\{211\}$  and  $\{100\}$  preferred orientations were found in the films. The thermodynamically favoured  $\{110\}$  orientation was never dominant. A study on the wear and fatigue behaviour of the same coatings on stainless steel substrates for

biomedical implant applications was conducted [7]. The results obtained by pin on disc tests with a polyethylene counterpart indicate improved wear behaviour of the coated specimen compared to stainless steel by a factor of  $\approx 2$  in terms of % weight loss. There was no improvement in the fatigue behaviour compared to uncoated stainless steel.

In a recent study the influence of the deposition temperature on 1.5 $\mu\text{m}$  thick Nb coatings deposited by magnetron sputtering on Cu substrates for superconducting technologies is investigated [52]. The films exhibit the preferred {110} orientation, independent of the deposition temperature. Increasing the substrate temperature resulted in a decrease in the Ar content together with a decrease in the compressive film stresses. No concrete stress values are presented but rather lattice strain values.

#### (ii) Co-sputtered Nb/ Metal coatings

The microstructure of Nb/ Cr alloys deposited by magnetron sputtering on steel substrates was investigated by scanning electron microscopy [53], [54] However, no comparison was made to pure Nb coatings. A number of authors report about the corrosion behaviour of co-sputtered Nb/ Metal coatings, where metal = Cr [55], [56], Zr [57], Mo [58], Cu [59] and Fe-Cr-Ni [60]. The coatings exhibit corrosion behaviour similar to or better than that of the alloy constituents in terms of anodic current densities and the stability of the passive layer. However, in most cases inert substrates such as glass were used, such that an evaluation of the “real-life” corrosion performance of these coatings is not possible.

## 2.4. Coating Technology

### 2.4.1. Cathodic Arc Evaporation

The cathodic arc is a state of a discharge at low pressures with high current/ low voltage characteristics, which produces high velocity jets of mostly ionised atomistic material. The arc is struck on the surface to be evaporated (the cathode), while the chamber wall, which is usually operated at ground potential, acts as the anode. Arcing is initiated by the application of a high voltage pulse to an electrode placed near the cathode. Electron emission, resulting from thermoionic and field emission mechanisms, is concentrated in a small area of the cathode. The concentrated electron flow generates a very high temperature locally, resulting in explosive evaporation of a minute liquid pool of molten

cathode material. This local region of electron emission and metal vaporisation is the cathode spot. The cathode spot is characterised by a small spot size ( $10^{-4}$  to  $10^{-8}$  m), extremely high current densities ( $10^6$  to  $10^{12}$  Am<sup>-2</sup>) [61] and temperatures ( $4 \times 10^3$  to  $10^4$  K [65]). Simultaneously to evaporation, the spot migrates to another location to repeat the process. With a velocity in the order of  $10^2$  ms<sup>-1</sup> the cathode spot and hence the arc move rapidly across the surface of the cathode [61].

A dense, hot local plasma is generated above the cathode spot by collision of the emitted electrons with the evaporating metal atoms, resulting in ionisation of the latter (Fig.2.4.). The electrons are accelerated away leaving behind a space charge, which is positive to the surrounding area. Due to the space charge a potential hump is formed, which, in a dynamic equilibrium, retards the electrons and accelerates the positive ions away from the cathode; a high velocity plasma jet is formed with ion energies in the range of 50 to 150eV [62], [63]. Some of the positive ions are also accelerated back towards the cathode thus assisting in the local heating of the cathode. The high local temperature of the cathode spot and the field generated by the metal vapour plasma support thermoionic and field emission of the electrons, sustaining high electron current flows [63].

Once initiated, the arc is self-sustaining owing to the generated metal vapour plasma, which, in the absence of a gas background, serves as the sole conducting medium for the vacuum arc. However, sometimes an inert gas is used to help sustain the arc. The discharge characteristics of the vacuum arc are in the range of 10-50V for the cathode potential and 50- 400A for the discharge current.

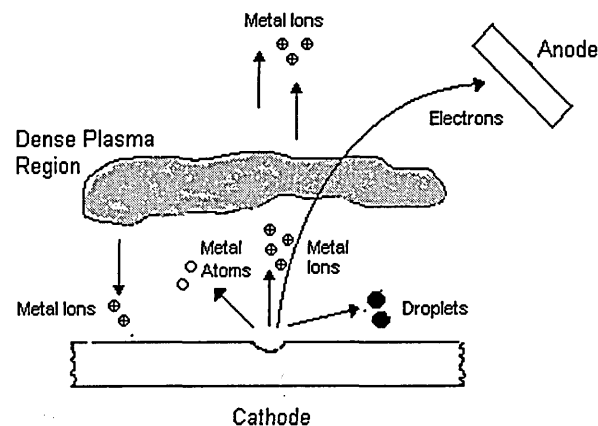


Fig.2.4. Cathode spot region (stationary model) (after [65])

The flux emitted from an arc source consists of ions, neutrals and macroparticles [62], [64] (fig.2.4.). A major characteristic of the cathodic arc is the high degree of ionisation

of the emitted material up to approaching 100%, depending on the distance to the source [61], [65]. Furthermore, the ions exist in multiple charge states. The average charge state for e.g. Nb is 2.79 [66] or 3.00 [67] and for Cr is 1.99 [66] or 2.09 [67] respectively. The ion energy can be increased by applying a negative bias voltage to the substrate, accelerating the generated ions. The events on the substrate surface are influenced by the energy of the arriving ions, i.e. by the charge state of the ion and the applied potential difference, and range from condensation at low ion energies to re-sputtering of surface atoms and ion implantation at higher ion energies. Hence, the highly energetic ion flux from a cathodic arc source can be used to produce dense coatings as well as to sputter clean and penetrate the substrate prior to coating deposition, resulting in superior film adhesion [68], [69].

However, a disadvantage of the cathodic arc is the generation of liquid droplets or macroparticles. The mechanism of droplet formation can be described as follows [70]: (i) formation of a comparatively large molten pool of material, (ii) transport of liquid metal to the periphery of the molten pool by impinging ions and plasma pressure resulting in macroparticle emission and (iii) droplet extraction by a strong local electrical field. The size of the droplets can be in the sub-micron range up to several tens of micrometers, their size and number depending on the melting point of the cathode material, the discharge current and the cathode temperature [71]-[75]. Droplets are undesirable in coating deposition as they can affect the coating quality by generating growth defects.

#### 2.4.1.1. Random Arc/ Steered Arc

In the absence of any constraining magnetic field, the cathode spot migrates randomly on the surface of the cathode (Random Arc) and shows a tendency to dwell in certain areas, producing relatively large molten pools [72], [76]. Rapid motion of the cathode spot will in principle force the spot to burn in a “virgin” area, resulting initially in a relatively low local surface temperature and hence a reduced volume of molten material in the vicinity of the active spot. This leads to a reduction in macroparticle erosion compared to a stationary cathode spot [72], [77]. A magnetic field can be used to confine or steer the arc (Steered Arc), allowing control of the arc velocity and the arc path, preventing local overheating. The steered arc method was invented by Ramalingham in 1987 by placing a permanent magnet array directly behind the target of

the arc cathode [78]. This magnet array was subjected to a special movement adjusted to the geometry of the target. The magnetic field lines penetrate the cathode and exert a Hall force on the arc as a current carrying conductor. However, the Hall force is also exerted on the positive ions from the plasma cloud, which are attracted back to the cathode, resulting in a circular deflection of the ions in the vicinity of the arc spot (Fig.2.5.). This new impact point is heated locally, emits electrons and prepares a new location for the cathodic arc spot [77]. Furthermore, the arc spots sits preferentially at the point where the vertical component of the magnetic field is zero [79], resulting in an arc track as shown in fig.2.5. Due to the Hall effect, the arc will travel along this track at high velocity. The spot velocity increases with increasing magnetic field and saturates at a certain field ( $V = 10-100\text{ms}^{-1}$ ) [70]. The direction of the arc motion is known as “retrograde”, as it is opposite to the Ampere rule. This arises from the fact that the current is mainly carried by the positive ions, hence reversing the direction of the Hall effect.

It has been shown, that steering the arc with magnetic fields results in the following effects compared to the random arc [77]:

- (i) smaller average size of the erosion craters
- (ii) the craters are positioned directly one behind the other, resulting in:
- (iii) reduced overlapping of the craters and
- (iv) reduced presence of large molten areas

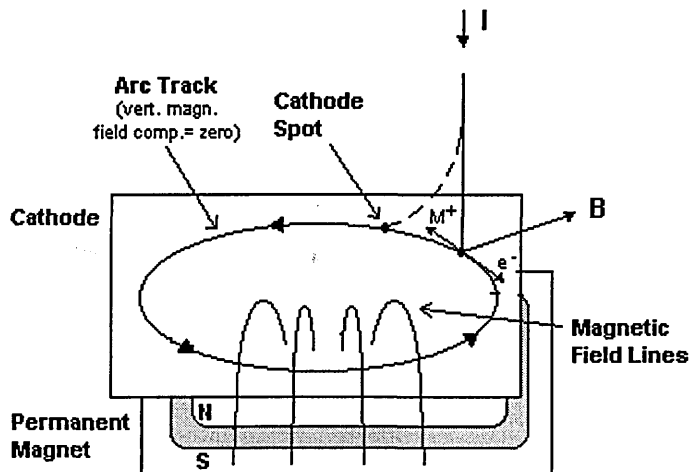


Fig.2.5. Arc spot motion in a steered cathodic arc

## 2.4.2. Sputtering

Sputtering is a non-thermal vaporisation process in which surface atoms are physically ejected from a surface by momentum transfer from an energetic bombarding species of atomic/ molecular size [80]. Main uses of sputtering are (i) Coating deposition, in which the sputtered atoms are re-deposited onto a substrate and (ii) Sputter etching, in which the removal of surface atoms is used as a cleaning pre-treatment of the substrate prior to coating deposition. The simplest arrangement of sputtering is dc glow discharge sputtering.

### 2.4.2.1. Glow Discharge Sputtering

In glow discharge sputtering, a plasma is generated by introducing an inert gas and applying a high potential between two electrodes, where the target material to be sputtered normally constitutes the cathode and the chamber wall, operated at ground potential, acts as the anode. Initially, at a low potential, a small current will be observed which stems from movement of the naturally occurring charge carries. With increasing voltage, ionisation in the gas begins and the current rises. With even higher voltages, the current becomes large enough to establish a glow discharge, which is accompanied by a considerable drop in voltage and rise in current. Positive ions are accelerated towards the cathode and their impingement on the cathode surface causes a variety of effects, which are discussed in more detail below, including the liberation of secondary electrons. It is these secondary electrons that are primarily responsible for sustaining the glow discharge.

The architecture of the glow discharge is composed of several regions as shown schematically in figure 2.6 [80]-[82]:

Directly in front of the cathode is the cathode glow region, which is luminous due to recombination events at the cathode surface. Next to the cathode glow region is the cathode dark space, across which most of the voltage is dropped. Electrons emitted from the cathode surface are accelerated by the electric field and cause ionisation of gas atoms and creation of further electrons by multiple collision events. The large number of positive ions produced creates a positive space charge across the dark space, which causes the large voltage gradient and provides the accelerating force for the positive

ions towards the target surface. The energies of most electrons in the dark space lie far beyond the maximum of the excitation functions, hence little visible light is emitted from this region. At the end of the cathode dark space, the current is nearly all carried by the electrons, whose number is then so great, that they considerably reduce the positive net space charge. The negative glow region begins. With little acceleration forces, the energy of the electrons is mainly adsorbed by intense excitation and ionisation events, resulting in the brightness of the negative glow. When the negative space charge reaches its maximum, the energy for excitation and ionisation is exhausted, resulting in the Faraday dark space. After the Faraday dark space the positive column begins. In the positive column, the concentration of electrons and ions is equal and the net charge space is zero. The voltage gradient is very low, merely to maintain sufficient ionisation to compensate for losses by recombination. The energy of the electrons is sufficient for excitation and ionisation events and the positive column is hence luminous. With decreasing pressure and cathode to anode distance, the positive column and the Faraday dark space can be “consumed”, i.e. the substrate becomes immersed in the negative glow region [81], [82].

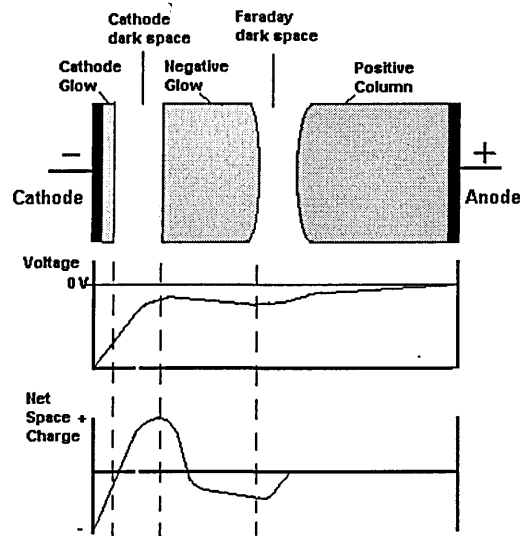


Fig.2.6. Glow Discharge characteristics

The type of discharge used in sputtering is the “abnormal glow discharge”. At low applied voltages and low resulting currents the discharge is characterised by constant voltage and constant current density (“normal glow region”). Increasing the power increases the current carrying area (current increases, while voltage and current density

remain constant) until the whole cathode surface is utilised by the discharge. The glow is now “abnormal” and any increase in power results in an increase in current, current density and voltage [82]. The cathode potential in glow discharge sputtering, without application of any external magnetic fields, is in the order of 1-5 kV. It is that large potential drop that accelerates the ions towards the cathode, causing sputtering of target material and other events as described below.

A variety of interactions can occur when the target surface is bombarded by ions. These interactions include [80],[82]:

- (i) Reflection of the incident ion as an ion or neutral
- (ii) Liberation of secondary electrons
- (iii) Ion implantation
- (iv) Radiation damage (creation of vacancies, interstitials or gross lattice defects)
- (v) Local heating
- (vi) Ejection of an atom or ion (Sputtering)

Which of these events occur and to what extent is a function of various parameters such as the ion energy, target characteristics, angle of incidence etc. Sputtering is the result of a collision cascade within the target, independent on the thermal properties of the target material. The incident ion knocks, in a primary collision event, target atoms from their equilibrium position. The atoms then move through the material and undergo further collisions and so forth, resulting in a collision cascade, which either heads off to the interior of the target or leads to sputter ejection of a surface atom. The sputter ejection is rather ineffective with only 1% of the incident energy being transferred to the sputtered atoms. The probability of the sputter event happening can be described by the sputter yield  $S$ , which is defined as the number of target atoms (or molecules) ejected per incident ion. The sputter yield can be obtained from [82]:

$$S = \frac{3\alpha}{4\pi^2} \frac{4m_i m_t}{(m_i + m_t)^2} \frac{E}{U_0} \dots\dots\dots\text{equation 2.1.}$$

where  $m_i$  and  $m_t$  are the incident ion and target atom mass,  $E$  is the energy of the incident ion,  $U_0$  is the surface binding energy of the target material and  $\alpha$  is a function of  $m_t/m_i$ , which increases with increasing values [82]. The expression  $4m_i m_t/(m_i+m_t)^2$

describes the energy transfer in a binary collision. In contrast to arc evaporation, more than 90% of the sputtered material are neutrals with low kinetic energies (5 to 20eV).

#### 2.4.2.2. Magnetron Sputtering

Magnetron sputtering is a special sputtering technique in which magnetic fields are used to make more efficient use of the electrons by minimising their loss due to recombination at the anode, i.e. the chamber walls. Most of the plasma is confined to the near target region by magnets behind the cathode, hence, ionisation and sputter rates are increased by a factor of up to ten, leading to a typical discharge voltage of  $-500\text{V}$ . An electron leaving the target surface at an angle to the magnetic field lines will be subjected to the Lorentz force. As a result, the electron will describe a circular motion around the magnetic field line and return to the surface, hence being trapped in the near cathode region (fig.2.7.). The addition of an electric field, as is the case in magnetron sputtering, changes the orbit of the electron from circular to cycloidal [82]. For the magnetic fields used in sputtering, mainly the electrons will be affected, while the ions are too heavy ( $m_{Ar}/m_e \approx 10^5$ ).

Rhode [80] summarised the advantages of magnetron sputtering over conventional sputtering as (i) increased sputter i.e. deposition rates, (ii) reduced sputtering from the substrate and the chamber walls, (iii) reduced substrate heating from electron and ion bombardment and (iii) reduced working gas pressure requirements

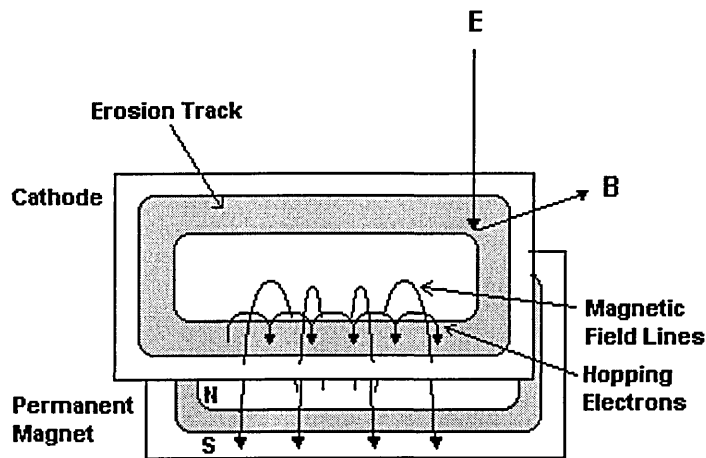


Fig.2.7. (Planar) Magnetron sputtering configuration

### 2.4.2.3. Unbalanced Magnetron Sputtering

However, the use of conventional magnetrons is restricted by the sharp decrease in ionisation with increasing distance from the target to the substrate and shadowing effects, which make coating of large three-dimensional parts difficult and can lead to inferior coating quality by the reduced ion bombardment during deposition [80], [83].

An improvement was achieved with the invention of the unbalanced magnetron in 1986 [84]. In a narrow sense, an unbalanced magnetron is understood to be a magnetron with strengthened outer poles [84]. Strengthening the outer poles, which can be achieved with additional or larger magnets or electromagnetic coils, leads to the outer magnetic field lines to be merged deeper into the space of the chamber. A considerable portion of the secondary electrons and hence the positive ions will follow the magnetic field lines. Therefore, the plasma glow is no longer confined to the front of the cathode but expands outwards resulting in increased ion bombardment of the substrate (fig.2.8.). Beneficial effects of this arrangement are [80],[83],[84] (i) increased “throwing distance” of the depositing species, (ii) high ion to neutral ratios (up to 6– 10), characteristic of a typical ion-plating technique [83], (iii) increase in the substrate bias current density by approximately two orders of magnitude compared to a conventional balanced magnetron, (iv) high bias current densities even at larger target to substrate distances, (v) controllability of ion energy and ion flux almost independently of each other, (vi) less dependence of the coating properties on deposition parameters and (vii) all of the above resulting in superior and easier controllable coating properties.

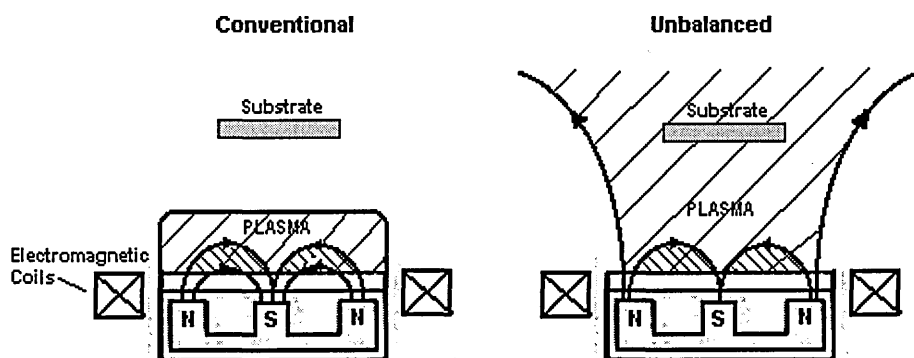


Fig. 2.8. Unbalanced Magnetron (after [83])

#### 2.4.2.4. Closed Field – Unbalanced Magnetron Sputtering

The extended target-to-substrate distances achieved by unbalanced magnetron sputtering make it possible to produce coatings in large multi-cathode systems. Linking the field lines between the north and the south pole of two adjacent cathodes in a multi-cathode system results in a closed field arrangement (Fig.2.9.). The closed field configuration reduces the loss of secondary electrons to the anode and distributes them and the plasma evenly around the multi cathode system i.e. the substrate region, hence enhancing deposition conditions.

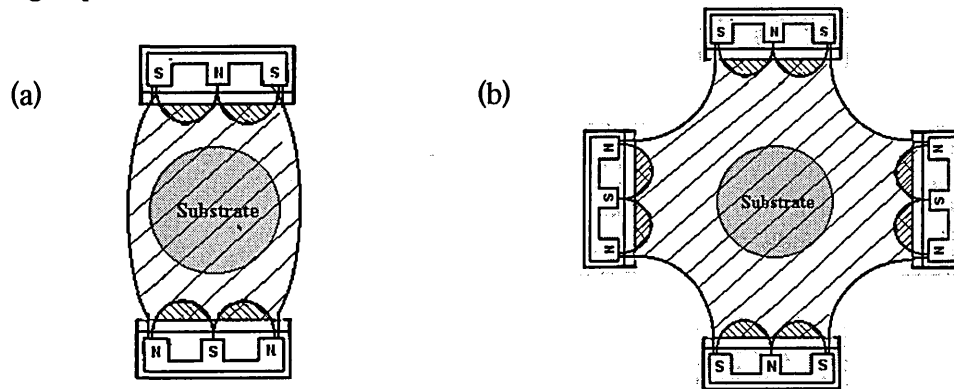


Fig.2.9. Closed-Field configuration: Two opposing cathodes (a), Quadruple arrangement (b)

#### 2.4.3. Arc Bond Sputter (ABS) Technique

The Arc Bond Sputter technique, employed in the present study, combines the two PVD techniques of Steered Cathodic Arc Evaporation (SCAE) and Closed Field- Unbalanced Magnetron Sputtering (UBM) [85]. The idea behind this arrangement is the combination of the advantages of each technology into one system [85], [86]. The main advantages can be summarised as follows:

(i) Steered Cathodic Arc Evaporation :

- Superior film adhesion obtained by bombardment of the substrate with multiply charged metal ions from the steered cathodic arc source prior to coating deposition due to high etching rates and less influence of residual gases [68], [69]

(ii) Unbalanced Magnetron Sputtering :

- Versatility of materials selection
- Droplet-free coating deposition
- High and controllable degree of ion bombardment of the growing film

As a result of these characteristics a “typical” ABS process employs the arc source for the substrate sputter cleaning step prior to coating deposition, while the film deposition is carried out using unbalanced magnetron sputtering. The ABS coating technology is described in more detail in chapter 3.

## 2.5. Structure Zone Models

The microstructure of sputter deposited coatings is influenced by a number of deposition and process parameters including substrate temperature, gas pressure, ion-to-neutral ratio, the substrate bias current density and the ion energy i.e. substrate bias voltage [83-84],[87],[90-91]. All of these factors influence the energy delivered to the growing film and influence the coating morphology by controlling the adatom surface mobility and the reactivity of the condensation process. The first structure zone model was developed by Movchan and Demchishin (Fig. 2.10.) [88]. The MD model applies to vacuum-evaporated coatings and describes the influence of the substrate temperature (i.e. the ratio of substrate temperature  $T_S$  to the melting point of the material  $T_M$ ) on the film morphology in absence of any ion bombardment during film growth. The model distinguishes between three discrete zones. Zone 1 at low temperatures is characterised by an open columnar or “porous” structure arising from insufficient atom surface mobility and dominant shadowing effects. An increase in temperature in zone 2 leads to an increase in adatom surface diffusion and densification of the still columnar structure. High temperature deposition in zone 3, i.e. temperature close to the melting of the material, allows bulk diffusion and recrystallisation resulting in fully dense, equiaxed grain structures.

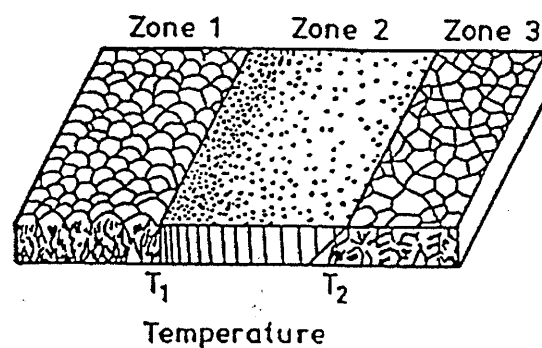


Fig.2.10. Structure Zone Model after Movchan and Demchishin [88]

The structure zone model was further developed by Thornton [89] and Messier [90] for sputtered coatings to include the effect of gas pressure and ion bombardment on the coating microstructure (Fig. 2.11). The effect of the working gas pressure is added in the Thornton model, accounting for gas phase scattering, as well a fourth zone, the transition zone T. Zone T consists of densely packed fibrous grains, grown under bombardment of high-energetic neutrals reflected from the sputtering target at low pressures. Messier replaced the pressure axis with a substrate bias voltage axis to include the influence of the ion energy during film growth. An increase in energy of the bombarding ions enhances adatom surface mobility and suppresses the formation of zone 1. Similar results were reported earlier by Mattox and Kominiak [91] who found considerable densification of dc sputtered Ta coatings with increasing negative substrate bias voltage. Freller et.al. investigated the influence of bias current density rather than bias voltage on the coating morphology and found that a minimum threshold current density (i.e.  $2\text{mA}/\text{cm}^2$ ) is necessary to sputter deposit dense TiN coatings on geometrical complex substrates [92].

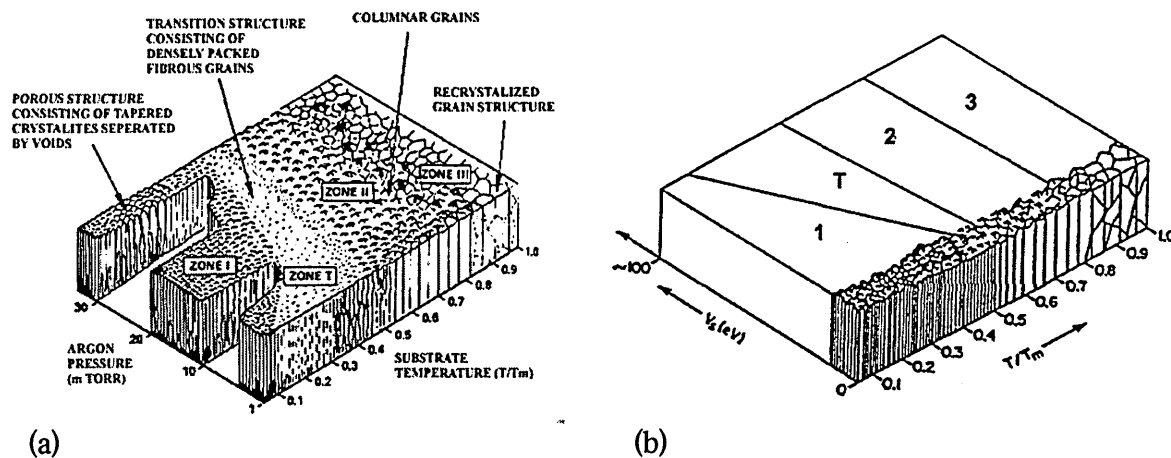


Fig.2.11. Structure Zone Model after Thornton (a) [89] and Messier (b) [90]

Recently, Kelly and Arnell developed a new structure zone model for the special case of closed field unbalanced magnetron sputter deposition (Fig.2.12.) [87]. The model describes the coating morphology as a function of the temperature, the ion flux (i.e. ion-to-neutral ratio) and the ion energy (i.e. substrate bias voltage). The formation of zone 1 is completely suppressed and the minimum temperature necessary for the formation of zone 2 and 3 is shifted towards lower values compared to the earlier SZMs These

findings were related to the high ion-to-neutral ratios obtainable by the closed field unbalanced magnetron deposition process.

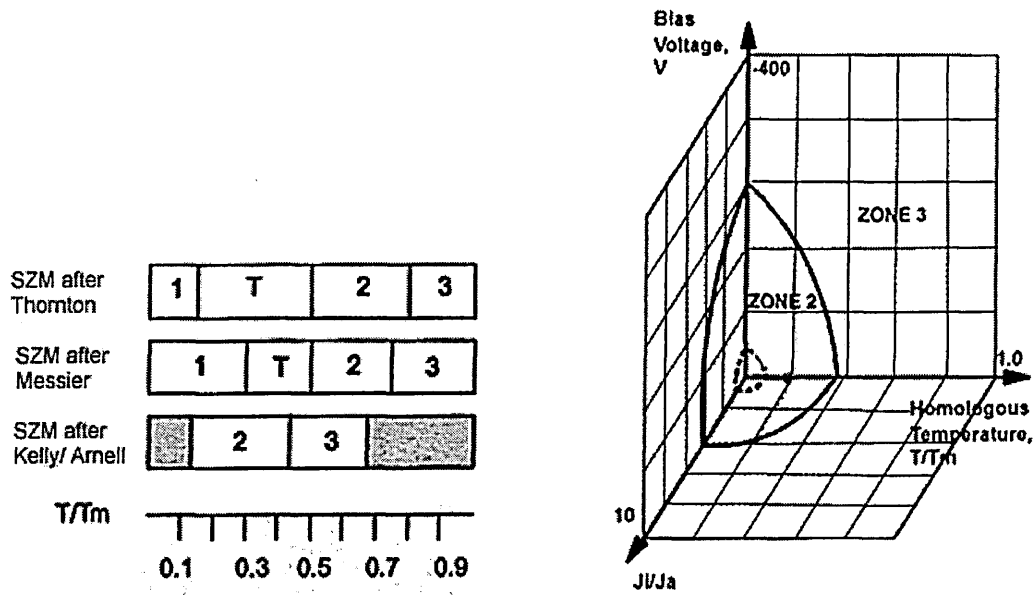


Fig.2.12. Structure Zone Model after Kelly/ Arnell [87]

## References to Chapter 2

- [1] Tantalum and Niobium, G.L.Miller, Butterworth Scientific Publications, 1995, London, UK
- [2] CRC Handbook of Chemistry and Physics, 74<sup>th</sup> Edition, D.R.Lide (Ed.), CRC Press, 1993-1994, Boca Raton, USA
- [3] R.W.Balliett, M.Coscia, F.J.Hunkeler, J. of Metals, 38 (9), (1986), 25
- [4] Metals Handbook, 9<sup>th</sup> Edition, Vol.2, ASM International, 1979, Ohio, USA, 1144
- [5] P.K.Datta, K.N.Strafford, L.P.Ward, Proc. 28<sup>th</sup> Conf. Australasian Corr. Assoc., (1988), 7-10.1
- [6] J.Gluszek, J.Masalaski, Brit.Corr.J., 27 (2), (1992), 135
- [7] L.P.Ward, K.N.Strafford, T.P.Wilks, C.Subramanian, J.Mater.Proc.Technol., 56, (1996), 364
- [8] Properties of Refractory Metals, W.D.Wilkinson, AMS, Gordon and Breach Science Publishers Inc., 1969, New York, USA
- [9] Anorganische Chemie, 2<sup>nd</sup> Edition, E.Riedel, Walter de Gruyter & Co., 1989, Berlin, Germany
- [10] The Chemistry of Niobium and Tantalum, F.Fairbrother, Elsevier Publishing Company, 1967, Amsterdam, The Netherlands
- [11] High Temperature Oxidation of Metals, P. Kofstad, John Wiley & Sons, 1966, New York, USA
- [12] W.D. Klopp, C.T.Sims, R.J.Jaffee, Proc. 2<sup>nd</sup> U.N. Int. Confer. on the Peaceful Use of Atomic Energy, Geneva, (1958), 502
- [13] Oxidation of Metals and Alloys, O.Kubaschewski, B.E.Hopkins, Butterworths, 1962, London, UK
- [14] CD-Roempp Chemie Lexikon, J.Falbe, M.Regitz (Ed.), Georg Thieme Verlag, 1995, Stuttgart, Germany
- [15] Lectures on Electrochemical Corrosion, M.Pourbaix, Plenum Press, 1973, New York, USA
- [16] J.van Mulder, M.Pourbaix, Techn.Rep.No. 53 (1957) Centre Belge d'Etude de la Corrosion, Brussels, Belgium
- [17] C.V.D'Alkaine, L.M.M. deSouza, F.C.Nart, Corr.Sci., 34 (1), (1992), 109
- [18] F.Holtzberg, A.Reisman, M.Berry, M.Berkenbilit, J.Am.Chem.Soc., 79, (1957), 2039

- [19] Anodic Oxide Films, L.Young, Academic Press Inc., 1961, London, UK
- [20] A.Robin, M.E. de Almeida, C.A.Nunes, Corrosion, 47 (6), (1991), 443
- [21] A.G.Gad Allah, J.Appl.Electrochem., 21, (1991), 346
- [22] Columbium, Fansteel Metallurgical Cooperation, 1946, 433
- [23] Metallic Coatings for Corrosion Control, V.E.Carter, Butterworth & Co. (Publishers) Ltd., 1977, London, UK
- [24] Principles and Prevention of Corrosion, D.A.Jones, Macmillan Publishing Company, 1992, New York, USA
- [25] Corrosion Testing, H.A.Jehn, A.Zielonka in ASM Handbook Vol.5, ASM International, 1994, Ohio, USA, 635
- [26] W.B.Nowak, Surf.Coat.Technol., 49, (1991), 71
- [27] H.A.Jehn, M.E.Baumgaertner, Surf.Coat.Technol., 54/ 55, (1992), 108
- [28] N.S.Chong, J.L.Anderson, M.L.Norton, J.Electrochem.Soc., 136 (4), (1989), 1245
- [29] G.W.Mellors, S.Senderoff, J.Electrochem.Soc., 112, (1965), 266
- [30] P.Taxil, J.Mahenc, Corr.Sci., 21, (1971), 31
- [31] U.Cohen, J.Electrochem.Soc., 128 (4), (1981), 731
- [32] E.Christensen et al., J.Electrochem.Soc., 141 (5), (1994), 1212
- [33] P.Chamelot, B.Lafage, P.Taxil, Electrochimica Acta, 43 (5-6), (1997), 607
- [34] A.Girginov, T.Z.Tvetkoff, M.Bojinov, J.Appl.Electrochem., 25, (1995), 993
- [35] B.Gillesberg et al., J.Appl.Electrochem., 29, (1999), 939
- [36] J.D.Reardon, F.N.Longo, C.R.Clayton, K.G.K.Doss, Thin solid films, 108, (1983), 459
- [37] E.Lugscheider, H.Eschnauer, B.Haeuser, D.Jaeger, J.Vac.Sci.Technol., A3 (6), (1985), 2469
- [38] M.S.P.Lucas, C.R.Vail, W.C.Stewart, H.A.Owen, Proc.2<sup>nd</sup> Int'l. Con. Sci. and Technol., (1962), 988
- [39] Y.Igarashi, M.Kanayama, J.Appl.Phys.57 (3), (1985), 849
- [40] J.J.Cuomo et al., J.Vac.Sci.Technol, 20 (3), (1982), 349
- [41] H.J.Hsieh et al., Surf.Coat.Technol., 49, (1991), 83
- [42] H.J.Hsieh, W.Wu, R.A.Erck, G.R.Fenske, Y.Y.Su, M.Marek, Surf.Coat.Technol., 51, (1992), 212
- [43] H.Ji, G.S.Was, J.W.Jones, N.R.Moody, J.Appl.Phys., 81 (10), (1997), 6754
- [44] L.P.Ward, Proc. AMPT, (1995), Dublin, Ireland, 79
- [45] L.P.Ward, P.K.Datta, Proc. AMPT, (1995), Dublin, Ireland, 1240

- [46] E.E.Salagean, D.B.Lewis, J.S.Brooks, W.-D.Münz, I.Petrov, J.E.Greene, Surf.Coat.Technol., 82, (1996), 57
- [47] C.T.Wu, Thin Solid Films, 64, (1979), 103
- [48] D.M.Pease et al., Thin Solid Films, 120, (1984), 239
- [49] L.S.Yu, J.M.E Harper, J.J.Cuomo, D.A.Smith, J.Vac.Sci.Technol., A4 (3), (1986), 443
- [50] L.P.Ward, P.K.Datta, Thin solid films, 271, (1995), 101
- [51] L.P.Ward, P.K.Datta, Thin solid films, 272, (1996), 52
- [52] R.Russo, S.Sgobba, Particle Accelerators, 60, (1998), 135
- [53] M.Turley, Surf.Coat.Technol., 39/ 40, (1989), 135
- [54] K.J.A.Mawella, J.A.Sheward, Thin solid films, 193/ 194, (1990), 27
- [55] J.H.Kim et al., Corr.Sci., 36 (3), (1994), 511
- [56] X.-Y.Li et al., Corr.Sci., 40 (4/ 5), (1998), 821
- [57] L.Fedrizzi, Y.Massiani, J.P.Croussier, M.Dapor, P.L.Bonora, Corrosion, 46 (6), (1990), 499
- [58] P.Y.Park et al., Corr. Sci., 38 (10), (1996), 1731
- [59] E.Hirota et al., Corr. Sci., 32, (1991), 1213
- [60] X.-Y.Li, E.Akiyama, H.Habazaki, A.Kawashima, K.Asami, K.Hashimoto, Corr.Sci., 41, (1999), 1095
- [61] The Cathodic Arc Plasma Deposition of Thin Films, P.C.Johnson, Physics of Thin Films, Vol.14
- [62] R.L.Boxman, S.Goldsmith, Surf.Coat.Technol., 33, (1987), 153
- [63] R.L.Boxman in Handbook of Vacuum Science and Technology, R.L.Boxman, P.J.Martin, D.M.Sanders (Ed.), Noyes Publications, 1995, New Jersey, USA, 3
- [64] J.E.Daalder, J.Phys.D: Appl.Phys., 8, (1975), 130
- [65] H.Randhawa, P.C.Johnson, Surf.Coat.Technol, 31, (1987), 303
- [66] I.G.Brown, B.Feinberg, J.E.Galvin, J.Appl.Phys., 63 (10), (1988), 4889
- [67] A.Anders, Phys.Rev.,E55, (1997), 969
- [68] W.-D.Münz, J.Schroeder, H.Pechstein, G.Håkansson, L.Hultman, J-E.Sundgren, Proc. SURTEC Berlin, A.Czichos, L.G.Vollrath (Ed.), Hanser, 1989, Muenchen, Germany, 61
- [69] G.Håkansson, L.Hultman, J-E.Sundgren, J.E.Greene, W.-D.Münz, Surf.Coat.Technol., 48, (1991), 51
- [70] J.Vysocil, J.Musil, J.Vac.Sci.Technol., A 10 (4), (1992), 1740

- [71] J.D.Daalder, J.Phys.D: Appl.Phys., 9, (1976), 2379
- [72] R.L.Boxman, S.Goldsmith, Surf.Coat.Technol., 52, (1992) 39-50
- [73] P.J.Martin in Handbook of Vacuum Science and Technology, R.L.Boxman, P.J.Martin, D.M.Sanders (Ed.), Noyes Publications, 1995, New Jersey, USA, 367
- [74] S.Creasey, D.B.Lewis, I.J.Smith, W.-D.Münz, Surf.Coat.Technol., 97, (1997), 163
- [75] W.-D.Münz, I.J.Smith, D.B.Lewis, S.Creasey, Vacuum., 48, (1997), 473
- [76] M.Ives, Ph.D. Thesis, 1994, Sheffield Hallam University, Sheffield, UK
- [77] E.Ertürk, H.-J.Heuvel, H.-G.Dederichs, Surf.Coat.Technol., 39/40, (1989), 455
- [78] S.Ramalingham, USP 4673477/ 1987
- [79] P.D.Swift, D.R.McKenzie, I.S.Falconer, J.Phys.D.: Appl.Phys., 66, (1989), 505
- [80] Sputter Deposition, S.L.Rohde, in ASM Handbook Vol.5, ASM International, 1994, Ohio, USA
- [81] M.Howatson, An Introduction to Glow Discharge Processes, Pergamon Press Ltd., 1976, Oxford, UK
- [82] B.Chapman, Glow Discharge Processes, John Wiley & Sons, 1980, New York, USA
- [83] W.-D.Münz, Surf. Coat. Technol., 48, (1991), 81
- [84] B.Windows, N.Savvides, J.Vac.Sci. Technol., A4 (2), 453
- [85] W.-D.Münz, F.J.M.Hauzer, D.Schulze, B.Buil, Surf.Coat.Technol., 49, (1991), 161
- [86] W.-D.Münz, D.Schulze, F.J.M.Hauzer, Surf.Coat.Technol., 50 (1992), 169
- [87] P.J.Kelly, R.D.Arnell, J.Vac.Sci.Technol., A16 (5), (1998), 2858
- [88] B.A.Movchan, A.V.Demchishin, Phys.Met.Metallogr., 28, (1969), 83
- [89] A.Thornton, J.Vac.Sci.Technol., 11, (1974), 666
- [90] R.Messier, A.P.Giri, R.A.Roy, J.Vac.Sci.Technol., A 2, (1984), 500
- [91] D.M.Mattox, G.J.Kominiak, J.Vac.Sci.Technol, 9 (1), (1972), 528
- [92] H.Freller, H.P.Lorenz, J.Vac.Sci.Technol., A4 (6), (1986), 2691

### 3. Experimental

#### 3.1. Coating System

All samples considered in this study were produced in an industrial sized Hauzer Techno Coating (HTC) 1000-4 Arc Bond Sputter (ABS) PVD unit [1], [2].

The unit is a four-cathode system with an octagonal cross-section as shown in fig. 3.1. The vacuum chamber consists of stainless steel and has a volume of approximately  $1\text{m}^3$ . The substrate table is located in the centre of the chamber. Samples are mounted on satellite assemblies, which are designed to allow one-, two-, or three-fold planetary rotation of the substrates, depending on their geometry and size. Two doors on either side give access to the inside of the vacuum chamber. Radiant heating is accomplished by one heater on each door and one heater under the substrate table. The walls of the chamber are water cooled during operation. The pumping system consists of two Balzers TPH 2200 turbomolecular pumps with a nominal pumping speed of  $4400\text{ L s}^{-1}$  in combination with a roots pump and a rotary vane pump. The turbomolecular pumps are connected to the vacuum chamber with two gate valves and can hence be kept at full speed when the system is open to air.

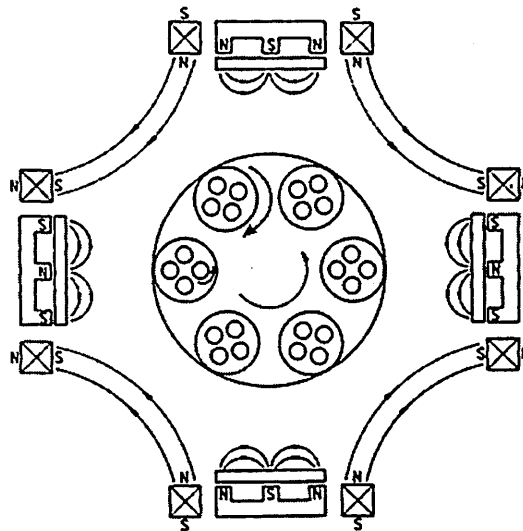


Fig. 3.1. Cross-section of ABS coating chamber [2]

The cathodes are designed to integrate the functions of both, the cathodic arc evaporator and the unbalanced magnetron, into one single unit. The magnetron discharge is achieved by positioning a set of permanent magnets directly behind the target.

Unbalancing of the magnetron is accomplished by electromagnetic coils, which are concentrically mounted to the cathodes as shown in fig.3.2., generating a magnetic field of up to 10000 ampere turns [2]. The unbalancing effect and hence the ion bombardment or substrate bias current density can be precisely adjusted by the magnetic field generated by the electromagnetic coils. This allows control of coating properties or the deposition temperature independently of e.g. the cathode power or the substrate bias voltage. Fig.3.3. shows the ion flux, as determined by Langmuir probe measurements in the ABS coating machine, as a function of the unbalancing coil current [3].

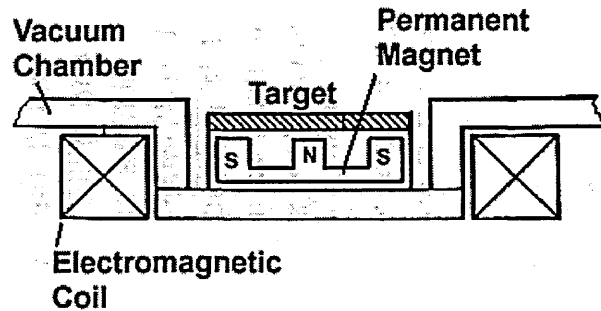


Fig. 3.2. UBM cathode with permanent magnets and electromagnets [2]

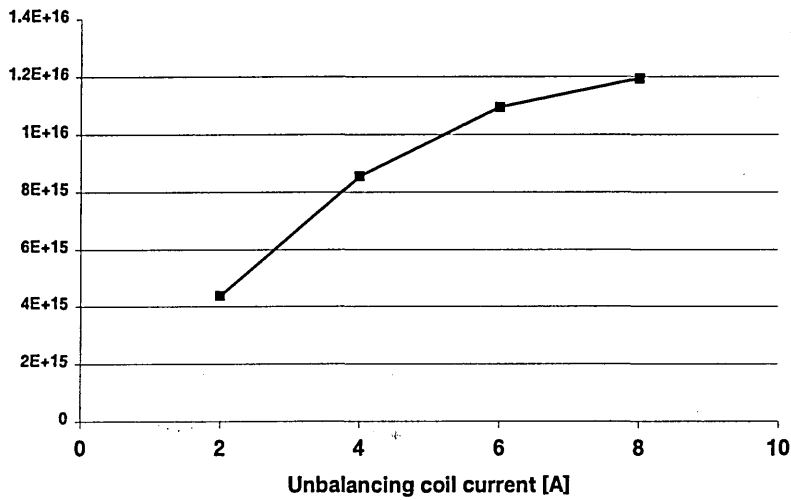


Fig.3.3. Substrate ion flux vs. unbalancing coil current (Langmuir probe measurement, 3 kW Cr UBM discharge) [3]

The closed field configuration is accomplished by linking the field lines between the north and the south pole of two adjacent cathodes (fig. 3.1.). In the unbalanced magnetron sputtering mode, average values of  $4 \text{ mAcm}^{-2}$  for the bias current density and

2-3 for the ion to neutral ratio can be reached with this system. Both parameters were measured at a target/ substrate distance of 50 cm [2].

The UBM cathode is converted to an arc cathode by moving the permanent magnet array away from the cathode, which weakens the magnetic fields at the surface of the target (Fig. 3.4.). The steered arc moves along a racetrack defined by the zero of the normal component of the magnetic fields. Sweeping of the arc across the target surface for higher target utilisation can be accomplished by moving the zero of the normal field component, which is done by periodically changing the current in the electromagnetic coils. The power supply of the cathodes provides values of up to 40A/ 750V in the magnetron mode (low current/ high voltage) and values of up to 100A/ 80V in the arc mode (high current/ low voltage). The maximum power for each cathode is 20kW.

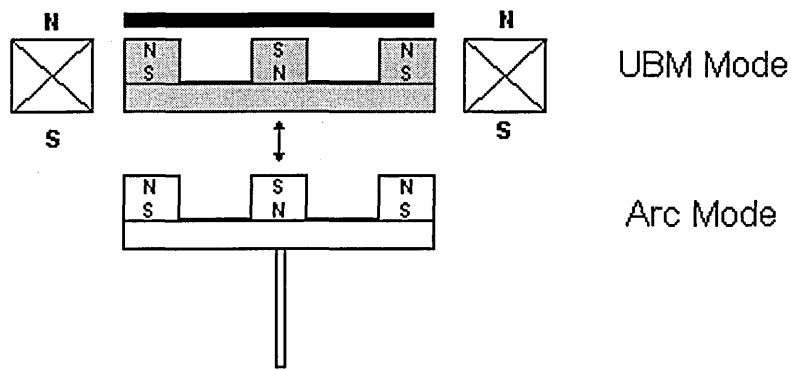


Fig. 3.4. Arrangements of magnets for alternative UBM and Arc mode

### **3.2. Deposition Procedure**

#### **3.2.1. Substrates and Substrate Preparation**

Table 3.1. summarises the substrate materials used and the condition, respectively the pre-treatment, of the substrates prior to the coating process. A consistent surface finish was important for the stainless steel coupons used for evaluation of the corrosion resistance, as the surface roughness can have a marked effect on the microstructure of thin films. The polished substrates, high speed steel, stainless steel and brass, were cleaned in an ultrasonically agitated acetone bath for 10min, rinsed with methanol and dried under hot air before coating. The bright-annealed stainless steel substrates used for XRD and TEM were cleaned in an industrial sized cleaning line. This consisted of a series of cleaning tanks namely two alkaline baths with ultrasonic agitation, a city water

rinsing bath and de-ionised water with and without ultrasonic agitation. Finally, the substrates were dried in hot air before they were mounted in the coating chamber.

Substrate Material	Condition prior to coating	Analytical Use
M2 High speed steel (Ø30mm x 8mm discs)	Ground and polished to 1µm diamond paste mirror finish	Hardness Roughness
304 L austenitic stainless steel (25mm x 25mm x 0.8mm )	Ground and polished to 1µm diamond paste mirror finish	Corrosion
304 L austenitic stainless steel (25mm x 25mm x 0.8mm )	Bright annealed	X-ray Diffraction TEM
Brass 90/ 10 (Ø30mm x 3mm)	Ground and polished to 1µm diamond paste mirror finish	Corrosion

Table 3.1. Substrate preparation and analytical use

### 3.2.2. Deposition Parameters

A typical coating process consists of the following steps:

- (i) Heating and pump down
- (ii) Target sputter cleaning
- (iii) Substrate sputter cleaning
- (iv) Coating deposition
- (v) Cool down and vent

- (i) Heating and pump down

Prior to coating deposition the vacuum chamber is evacuated and heated until the required base pressure and temperature are reached. The chamber is evacuated in two stages. Firstly, the pressure is reduced to  $1 \times 10^{-1}$  mbar via the rotary vane pump and the roots pump. At this point, the fine pumping system is opened, consisting of the two turbomolecular pumps, and the pressure is further reduced to the required base pressure, typically  $< 8 \times 10^{-5}$  mbar. The required temperature, typically 250°C, is reached via radiant heating during the fine pumping stage.

(ii) Target sputter cleaning

The targets are sputter cleaned in a glow discharge to remove surface contamination such as oxides. During this stage shutters are moved in front of the targets to avoid pre-coating of the substrates. In the case of severe target contamination, the targets were cleaned in a separate process.

(iii) Substrate sputter cleaning

The substrates are sputter cleaned to remove surface contaminants prior to coating deposition. A high negative substrate bias voltage, typically  $-1200\text{V}$ , is applied and the substrates are sputter cleaned by ion bombardment. The ions can be either singly charged, inert  $\text{Ar}^+$  ions from the glow discharge or multiply charged, highly energetic metal ions such as  $\text{Nb}^{3+}$  from the steered cathodic arc source. Steered cathodic arc evaporation is normally used as the ion source in the ABS system for reasons of superior adhesion as described in section 2.4. If not otherwise stated in the following, all substrate ion etching steps were carried out using a bias voltage of  $-1200\text{V}$  and a gas pressure of  $2 \times 10^{-3}$  mbar.

(iv) Coating deposition

Coating deposition is carried out from one Nb target using unbalanced magnetron sputtering or steered cathodic arc evaporation in a non-reactive Ar atmosphere. Additional radiant heating can be used during coating deposition to maintain the desired operational temperature. UBM deposition was carried out at  $420^\circ\text{C}$  with an unbalancing coil current of 6A and at  $250^\circ\text{C}$  with an unbalancing coil current of 3A. The first will be denoted “high temperature” and the latter “low temperature” deposition process in the following. If not otherwise stated, all process steps were carried out using a substrate three-fold rotational mode.

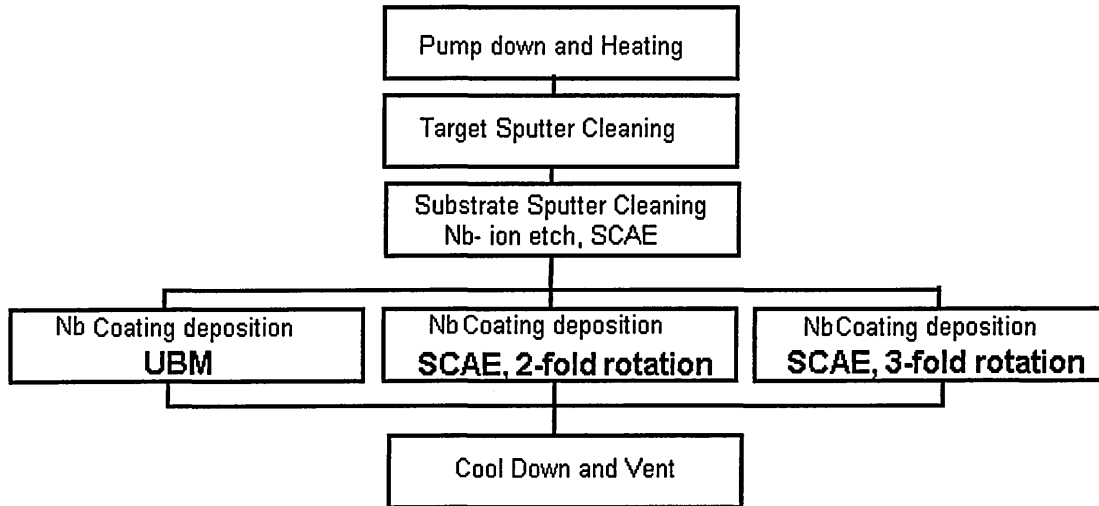
(v) Cool down and vent

After each process the vacuum chamber is allowed to cool down below  $170^\circ\text{C}$ .

The different processes are shown schematically below. The detailed process parameters are listed in the Appendix I.

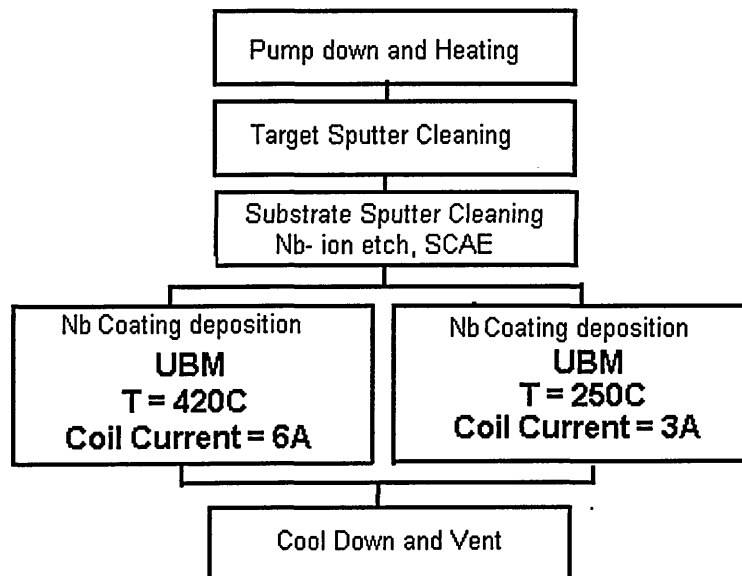
### I) Comparison of Nb Coatings deposited by UBM and SCAE

Nb coatings were deposited by the two different techniques of unbalanced magnetron sputtering and steered cathodic arc evaporation, both in high temperature processes. During SCAE, the substrates were additionally rotated in a 2-fold rotation mode to allow an increase in coating thickness.



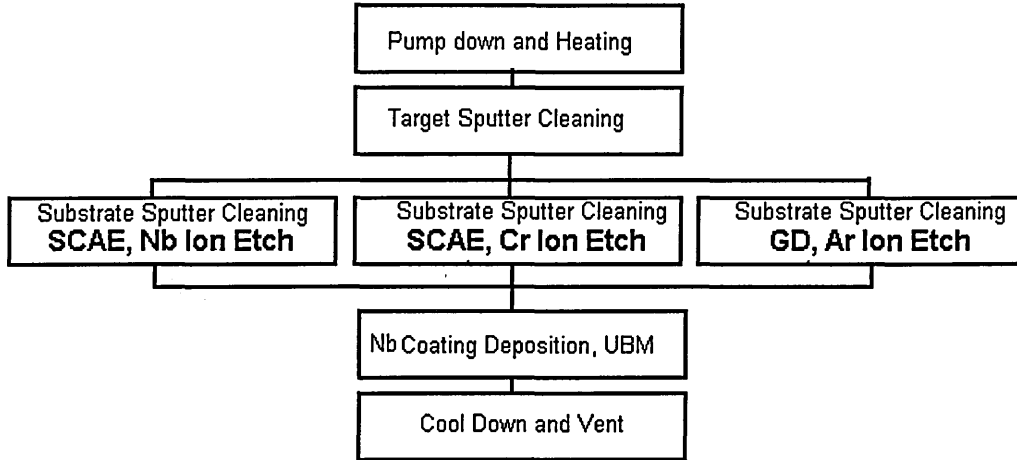
### II) Influence of Temperature and Ion Bombardment on UBM Nb Coatings

Two Nb coatings were deposited under variation of the coating temperature and the ion bombardment, i.e. unbalancing coil current, during UBM deposition (low and high temperature deposition).



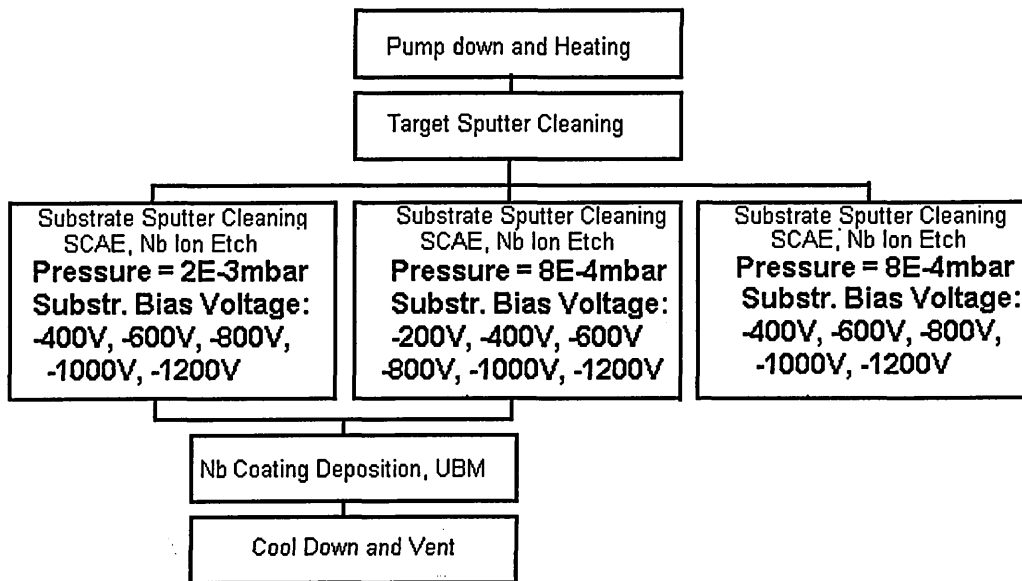
### III) Influence of the Ion Etching Pre-Treatment prior to UBM Deposition

The substrates ion etching pre-treatment prior to Nb UBM deposition was varied. The different ion species were Nb and Cr ions from the steered cathodic arc source and inert Ar ions from a glow discharge. All three coatings were produced in low temperature deposition processes.



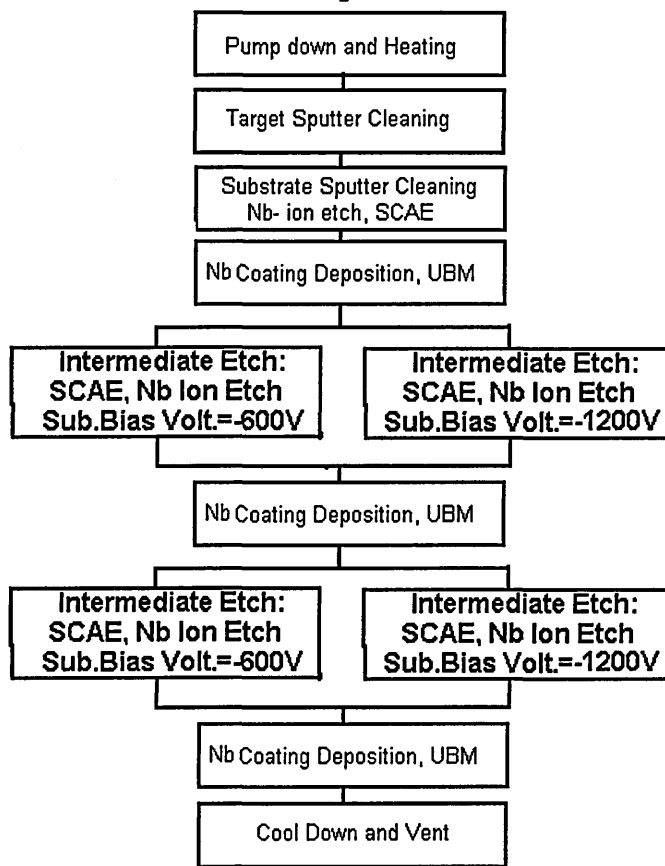
### IV) Nb-Ion Etching prior to Sputter Deposition : Influence of Working Gas Pressure and Substrate Bias Voltage

Two sets of samples were Nb ion etched using different working gas pressures and substrate bias voltages in the range of  $-200\text{V}$  to  $-1200\text{V}$ . The samples were then sputter coated with a 300nm thick Nb coating in high temperature deposition processes. Another set of samples was Nb ion etched under variation of the substrate bias voltage with no additional Nb coating.



### (V) Intermediate Nb Ion Etching

Sputter deposition of high temperature Nb coatings was interrupted twice by intermediate etches from the Nb arc, using two different bias voltages.



### (VI) Etching Rate

Steel substrate was coated with a Ni/Cr coating in UBM mode. This coating was used to “imitate” stainless steel substrate material of a defined thickness. One half of the coating was subsequently masked with a single-edge razor blade as shown below. The sample, masked and unmasked area, was then subjected to a 12min SCAE Nb ion etch, using a substrate bias voltage of  $-1200V$  and three-fold substrate rotation. Comparison of the coating thickness of the masked, i.e. etched and the unmasked, i.e. non-etched, coating area will yield the etching rate, i.e. the rate of removal of coating material.

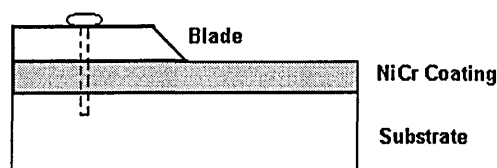
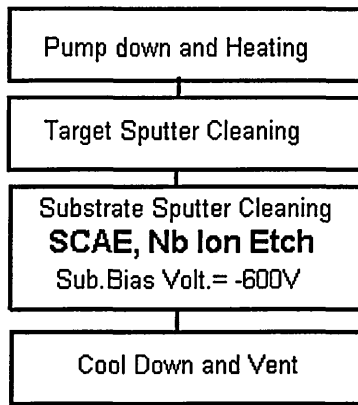


Fig.3.5. Determination of etching rate

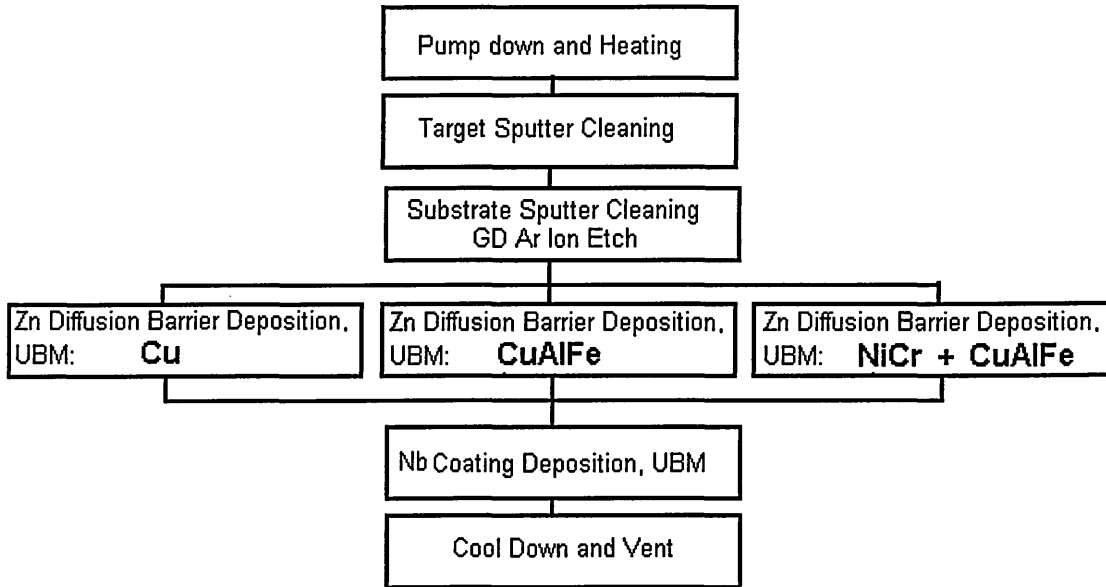
### (VII) Niobium Coatings on Brass Substrates: Substrate Ion Etch

The brass substrate was subjected to a Nb ion etch using a bias voltage of  $-600\text{V}$  with no additional coating.



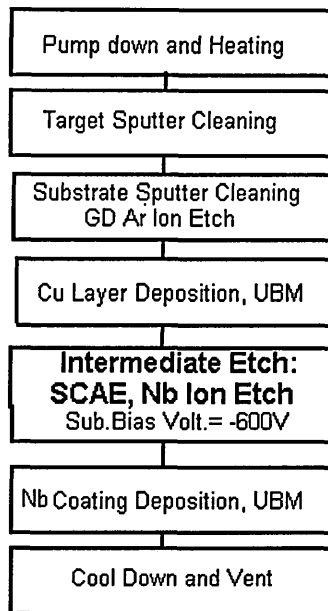
### (VIII) Niobium Coatings on Brass Substrates : Zn-Diffusion Barrier

Brass substrates were coated with different Cu-based diffusion barriers prior to sputter deposition of Nb, i.e. Cu, CuAlFe (target composition: 8%Al, 3%Fe), and NiCr (target composition: 80%Ni) plus CuAlFe. All deposition steps were carried out in low temperature processes.



### (IX) Intermediate Nb Ion Etching of Cu Baselayer

The Cu baselayer was subjected to a Nb ion etch using a substrate bias voltage of  $-600\text{V}$  prior to deposition of the Nb top coating



### **3.3. Evaluation Techniques**

#### **3.3.1. Hardness**

Hardness measurements are based on the resistance of a material to penetration by another body under load [4]. In the present study, the hardness of the PVD coatings was determined using a Knoop indenter, which consists of diamond ground to a rhombic-base pyramid with a ratio between the long and short diagonals of about 7:1 [5]. By applying a defined load the hardness of the coating can be calculated from the dimensions of the pyramid-shaped indentation by the following equation.

$$HK = C * P / d^2 \quad \text{.....equation 3.1.}$$

where C is a constant, P is the applied load in Kg and d is the length of the longest diagonal in mm. All measurements were taken on a Mitutoyo MVK-G1 tester using a load of 3g.

#### **3.3.2. Roughness**

The surface roughness of the coatings was determined by means of the  $R_a$  value, which is the arithmetic mean of the departures of the roughness profile from the mean line.

The instrument employed was a UBM Laser Profilometer. Here, an infrared beam is focused on the sample and the reflected beam is detected by varying the position of the objective lens in the instrument. The surface roughness is then calculated by the displacement of the objective lens necessary to focus the reflected beam.

### 3.3.3. Transmission Electron Microscopy

The microstructure of the sputtered coatings was investigated by cross-sectional transmission electron microscopy (X-TEM). In principle, a TEM consists of an electron gun and an assembly of lenses, all enclosed in a vacuum column. A schematic presentation is given in fig. 3.6. [6]. The condenser lens system collimates the electron-beam onto the thin specimen. The transmitted and scattered electrons will then be recombined by the objective lens system to form a first focused image in the intermediate image plane and a diffraction pattern in the back focal plane of the objective lens. The intermediate projector lens system magnifies the image, formed in the intermediate image plane, or the diffraction pattern, formed in the back focal plane, onto a fluorescent screen or photographic plates. Image formation in TEM is based on the intensity distribution of the electrons leaving the bottom of the thin specimen. Images can be generated either by the primary transmitted electron beam, or zero order spot, (bright field imaging) or by one the diffracted beams (dark field imaging) by suitable placement of the objective aperture. In bright field imaging, dark areas indicate that diffraction has occurred. The diffraction pattern, formed in the back focal plane by focusing rays that were deflected at the same angle into single spots, gives crystallographic information such as lattice spacing or crystallographic orientation.

The TEM used in these studies was a Philips CM20 STEM microscope with a LaB<sub>6</sub> filament using an acceleration voltage of 200KV.

TEM studies require electron-transparent specimen with a thickness of approximately 200nm. The coated samples were cut with a cutting wheel into cross-sections (3mm x 1mm x 0.8mm). They were subsequently mounted onto glass slides and mechanically ground and polished on both sides to a 1 $\mu$ m diamond finish and a thickness of not more than 20 to 30 $\mu$ m. Finally, the samples were placed in an ion beam thinner (Gatan PIPS 691) and thinned from the back side with argon ions (5keV) until the first occurrence of perforation in the coating area was observed. The angle of incidence of the ion beam on

the sample was kept between  $3^\circ$  and  $5^\circ$  to maximise the amount of electron-transparent area and to minimise the damage induced by the ion bombardment.

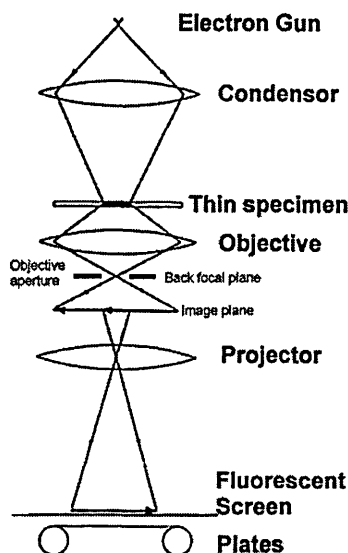


Fig.3.6. Transmission electron microscope

### 3.3.4. Scanning Electron Microscopy (SEM)

In a typical SEM an electron beam is focused by two electromagnetic lenses to a fine spot on the sample. At the same time, the beam is scanned in x- and y-direction on the sample. A series of signals and detectors can be used for SEM imaging. Secondary electrons leaving the sample are used to visualise topographic images. The backscattering coefficient is element specific, therefore back scattered electron images show atomic number contrast. Energy dispersive X-ray spectroscopy (EDX) coupled with a SEM can give information about the elemental composition and the elemental distribution on the sample.

The SEM used in these studies was a Philips XL40 instrument.

### 3.3.5. X-Ray Diffraction

X-ray diffraction (XRD) can be used to investigate a series of structural characteristics of thin films. Some major uses of XRD are: Determination of lattice parameter, crystal structure, texture, lattice strains, identification of phases and estimation of superlattice wavelengths. X-ray diffraction is based on the phase relationship of two or more rays from an incident X-ray that have been scattered by periodically repeating planes of

atoms. Interaction of the rays results in constructive or destructive interference. In order for two rays, ray 1 and ray 2, scattered from two parallel planes of atoms with the interplanar spacing  $d$ , to interact constructively, they must be in phase, i.e. their path difference must be equal to a whole number  $n$  of the wavelength  $\lambda$  (Fig. 3.7.) [7].

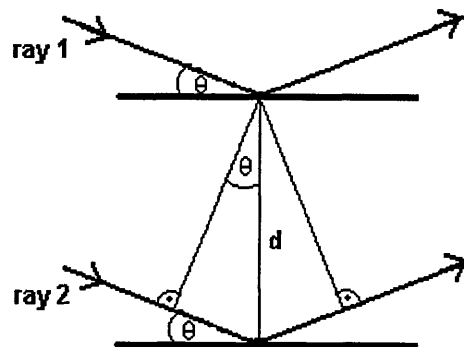


Fig.3.7. Diffraction of X-rays by a crystal

This is described by Bragg’s law :

$$n\lambda = 2d \sin \theta \quad \dots\dots\dots\text{equation 3.2.}$$

where  $\theta$  is the Bragg angle and  $n$  is the order of reflection, normally taken as one. In a diffractometer a monochromatic source of X-rays of the wavelength  $\lambda$  is incident on the surface of the specimen under examination. In Bragg-Brentano geometry, the rotating specimen is maintained at an angle  $\theta$  while the detector is kept at an angle of  $2\theta$  relative to the incident beam to maintain the Bragg conditions (fig.3.8.). Thus, the only planes to diffract are those parallel with the surface [8]. The intensity of the diffracted beams is recorded as a function of the diffraction angle  $2\theta$ .

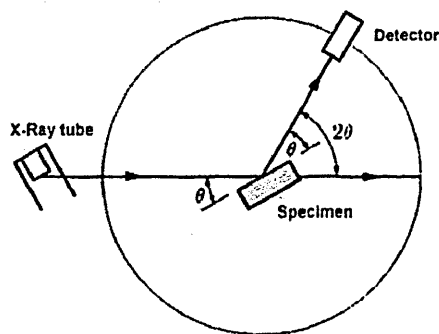


Fig. 3.8. X-ray diffractometer in Bragg-Brentano geometry

### 3.3.5.1.Texture

The texture or preferred orientation in a thin film, i.e. the non-random distribution of crystal orientations, can be determined by the Inverse Pole Figure technique [9], [10]. In Bragg-Brentano geometry, the technique is used to determine the crystallographic orientation of the planes *parallel* to the substrate/ coating interface. The texture value P represents the proportion of grains with a specific orientation relative to a randomly orientated powder material:

$$P = \frac{\frac{I_{hkl}}{R_{hkl}}}{\frac{1}{n} \sum_0^n \frac{I_{hkl}}{R_{hkl}}} \quad \text{.....equation 3.3.}$$

where  $I_{hkl}$  are the intensities from the hkl reflections in the specimen and  $R_{hkl}$  are the intensities of the hkl reflections from a random powder. Thus a P value of one signifies a random orientation whilst a P value greater than one signifies a preferred orientation. The  $I_{hkl}$  values were determined from the peak integral of each reflection. The  $R_{hkl}$  values can be taken from a random powder as stated above, where the thickness of the specimen is infinite relative to the depth of penetration of the X-rays. However, the reflected intensity is a function of the penetration depth, due to absorption of the X-rays, and becomes a function of the coating thickness and of  $\theta$  in the case of thin films, as the thickness of the specimen, i.e. the coating thickness, is finite relative to the penetration depth. Hence, in the present study, the  $R_{hkl}$  values were calculated according to equation 3.4. [9].

The reflected intensity  $I_d$  from a coating of the thickness t is given by :

$$I_d = \frac{I_0 \sin\theta}{2\mu} \left( 1 - e^{-\frac{2\mu t}{\sin\theta}} \right) \quad \text{.....equation 3.4.}$$

where  $I_0$  is the intensity of the incident beam ( $I_0 = 1$ ) and  $\mu$  is the absorption coefficient ( $\mu = 148.8 \text{ cm}^{-1}$  for Nb).  $R_{hkl} \approx I_d$ , but beside absorption the following factors influence  $R_{hkl}$ :

$$R_{hkl} = I_d * \frac{1}{V^2} * X * F^2 * LP * M * e^{-2m} \quad \dots\dots\dots\text{equation 3.5.}$$

where :

V = Volume of unit cell (V = 24.005 Å for Nb)

X = Irradiated volume (X = S \* (sinθ)<sup>-1</sup> and S = irradiated area = 1)

F = Structure Factor

The structure factor F takes into account that the scattering intensity is a function of the scattering angle. In the case of a simple cubic cell (e.g. Nb bcc), the scattering intensity is equivalent to the sum of the atomic scattering factors f :  
 $F_{hkl} = 2f$  (for h+k+l = even), (f values for Nb were taken from [7])

LP = Lorentz Polarisation Factor

The Lorentz polarisation factor, LP, takes into account the deviation of the reflection angle from Bragg's law as well as polarisation of the beam by the specimen and the monochromator.

$$LP = \frac{1 + \cos^2 2\alpha * \cos^2 2\theta}{\sin^2 \theta * \cos \theta} \quad \dots\dots\dots\text{equation 3.6.}$$

where α is the incidence angle of the beam to the monochromating crystal

M = Multiplicity Factor

The multiplicity factor takes into account that several sets of the same plane can contribute to the reflected intensity (M{hkl}=48, M{hkk}=24, M{hk0}=24, M{hh0}=12, M{hhh}=8, M{h00}=6)

e<sup>-2m</sup> = Temperature Factor (e<sup>-2m</sup> was assumed =1 for lack of available data)

### 3.3.5.2. Residual Stresses

Stress measurements using X-ray diffraction are based on the change in interplanar spacing or strain in the specimen [11]. An unstressed isotropic body can be considered a sphere with the coordinates x, y and z. Stresses in thin films are considered to be biaxial, i.e. the stresses perpendicular to the surface are zero. The sphere becomes an ellipsoid under the action of a equi-biaxial compressive stress with contraction in the x and y direction with expansion along the z-direction. Without rotation, the stress system

is two-dimensional in XRD and can be considered a cross-section through the ellipsoid. The diffracting planes are parallel (in z-direction), perpendicular (in x-direction) or at an angle  $\psi$  (in  $\psi$ -direction) with respect to the coating surface (fig.3.9.) [8].

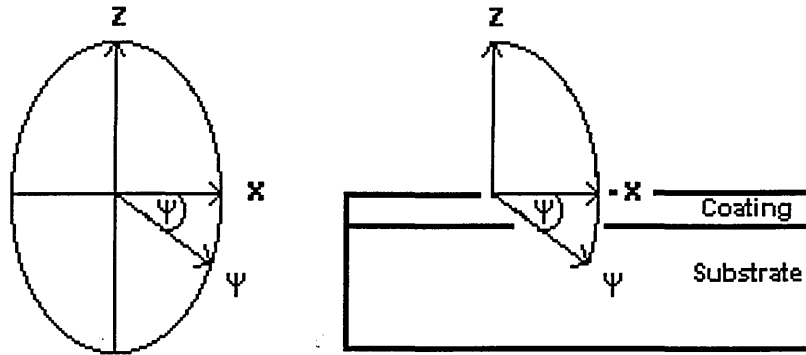


Fig. 3.9. Planar section through an ellipsoid

Residual film stresses were calculated with the  $\sin^2\psi$  method in these studies [11],[12]. For this technique the diffractometer is set in the “theta offset” position as shown in fig. 3.10. The offset angle  $\psi$  is fixed and the sample and the diffractometer rotate by  $\theta$  and  $2\theta$  respectively to maintain Bragg-Brentano conditions. In this arrangement the diffracting planes are at an angle  $\psi$  to the coating surface [8]. Thus, the lattice deformation can be observed as a function of  $\psi$  i.e. a strain distribution can be obtained.

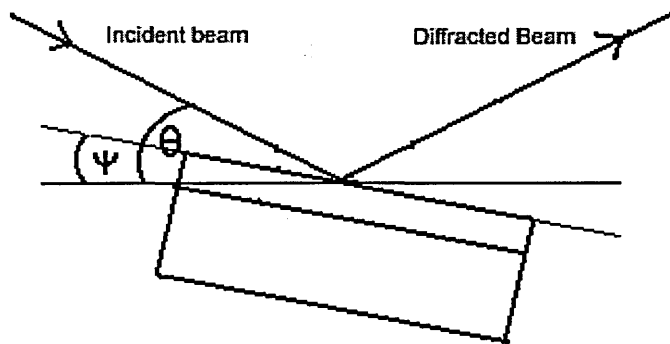


Fig. 3.10. “Theta Offset” configuration for stress measurements

The measurement is based on the following relation :

$$d_{\psi}^{hkl} = \left[ \sigma * d_0^{hkl} * \frac{1+\nu}{E} \right] * \sin^2 \psi + d_{(\psi=0)}^{hkl} \quad \text{.....equation 3.7}$$

where :

$d_{\psi}^{hkl}$  is the lattice parameter at angles  $\psi$ ,  $d_0^{hkl}$  is the stress - free lattice parameter and  $d_{(\psi=0)}^{hkl}$  is the lattice parameter at  $\psi$  equals zero, i.e. in the planes parallel to the coating surface.

E is Young's modulus (E=103 GPa for bulk Nb) and  $\nu$  is Poisson's ratio ( $\nu=0.38$  for bulk Nb). The stress free lattice parameter was taken from the value of bulk Nb i.e.  $d_{(220)} = 1.165\text{\AA}$ . All stress measurements were taken from the {220} reflection with the offset angle  $\psi$  varying from  $5^\circ$  to  $30^\circ$  in  $5^\circ$  increments. The lattice parameter d was substituted by the lattice constant a in all measurements. The  $a_{\psi}$  values were plotted against  $\sin^2\psi$  according to equation 3.6. and the residual stress values were calculated from the gradient of the linear function.

Residual stresses  $\sigma_r$  in thin films combine intrinsic stresses  $\sigma_i$ , i.e. growth induced stresses, and thermal stresses  $\sigma_{th}$  :  $\sigma_r = \sigma_i + \sigma_{th}$ . [11]. The thermal stress component arises from differences in the expansion coefficients between the coating and the substrate material.  $\sigma_{th}$  was calculated according to equation 3.8. for the two different deposition temperatures used in the present study. The intrinsic stresses were calculated from the difference in the measured residual stresses and the calculated thermal stresses.

$$\sigma_{th} = (\alpha_c - \alpha_s) * (T_2 - T_1) * \frac{E_c}{(1 - \nu_c)} \quad \dots\dots\dots\text{equation 3.8.}$$

where :

$\alpha_c$  = Thermal expansion coefficient of the coating ( $\alpha \approx 7.24 \mu\text{m} * \text{m}^{-1} * ^\circ\text{C}^{-1}$  for Nb)

$\alpha_s$  = Thermal expansion coefficient of the substrate ( $\alpha \approx 17.55 \mu\text{m} * \text{m}^{-1} * ^\circ\text{C}^{-1}$  for 304 stainless steel)

$T_2$  = Coating temperature

$T_1$  = Room temperature

$E_c$  = Young's modulus of the coating

$\nu_c$  = Poisson's ratio of the coating

The X-ray diffractometer used in the present studies was a Philips powder diffractometer with Cu  $K\alpha$  radiation.

### 3.3.6. Corrosion Measurements

Evaluation of the corrosion resistance of the coated substrates was carried out by potentiodynamic polarisation measurements in a 3% NaCl solution open to air. In these measurements, the coated sample is polarised as the working electrode (WE). The current  $I$  is supplied to the working electrode via two auxiliary carbon electrodes in parallel (AE) placed on each side of the WE. The potential  $E$  of the working electrode is measured with respect to the reference electrode (RE) and adjusted via the current to the nominal potential value  $E_N$ . A saturated Calomel electrode (SCE) was used in the experiments as the RE, which was placed within 1mm distance to the WE via a Luggin probe. The potential is increased continuously and the current i.e. current density is recorded as the dependent variable. Schematic drawings of the experimental set up are shown in fig.3.11. Below the free corrosion potential  $E_{\text{corr}}$ , defined by the mixed potential theory, the sample is polarised cathodically i.e. an excess of electrons causes the electrode potential to shift from  $E_{\text{corr}}$  to  $E$ . The negative potential shift increases the rate of cathodic reaction and suppresses the rate of anodic reaction until it is insignificant. The difference between the anodic and the cathodic current is the applied current. Polarisation in the anodic direction is analogous. Electrons are drawn out of the WE and the current flows in opposite direction from the cathodic currents. The deficiency of electrons cause a potential shift to a more positive value with respect to  $E_{\text{corr}}$ , and the anodic oxidation rate is increased while the cathodic reduction rate is suppressed [13].

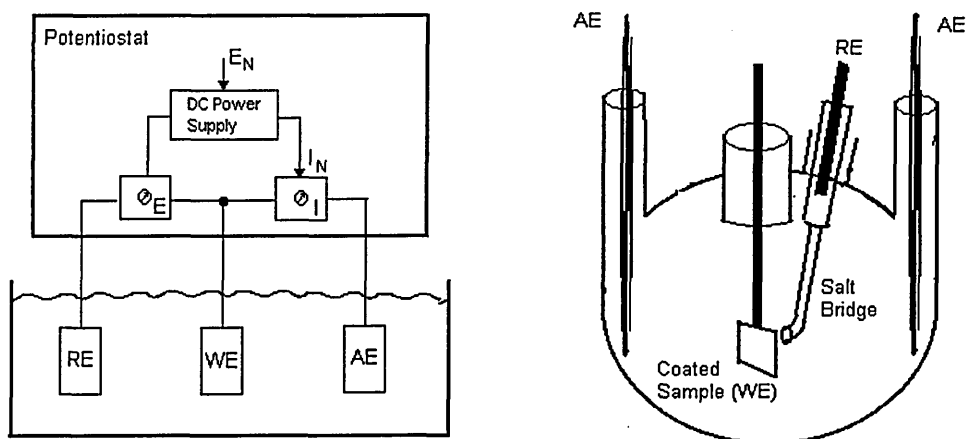


Fig.3.11. Schematic of experimental setup

The exposed surface area of the samples was  $0.78 \text{ cm}^2$ , defined by masking the whole coated sample with a beeswax/ resin mixture except a circular area of 1 cm diameter. The advantage of the beeswax/ resin mixture is that it does not lead to crevice corrosion as is the case for other masking media such as lacquer. Before each polarisation measurement, the solution was aerated and the samples were cathodically cleaned at a potential of typically  $-1500\text{mV}$  (all potentials versus SCE) followed by a 40 min period to allow stabilisation of the free corrosion potential. The samples were then polarised from typically  $-800\text{mV}$  to  $+900\text{mV}/ +1000\text{mV}$  or until a maximum recordable current density of  $0.1 \text{ Acm}^{-2}$  was reached. The scan rate was  $0.5 \text{ mVs}^{-1}$ . All experiments were carried out in a non-agitated, naturally aerated 3% NaCl solution at room temperature. Metals that exhibit passivation, such as niobium or stainless steel, are characterised by very distinctive polarisation curves in the anodic region as shown schematically in fig.3.12. At low potentials, the anodic current density increases with increasing applied potential. Above a certain potential, the passive potential  $E_p$ , the passive film becomes stable and the current density drops to low values or stabilises around a constant value due to the limited ionic mobility in passive films. The metal is now in the passive state and the corrosion rate is extremely low. Above the pitting potential  $E_{pit}$ , the passive film can break down and the corrosion rate increases in the transpassive region as indicated by the increasing anodic current density. The corrosion resistance of the Nb coated stainless steel substrates were judged by (a) the range of passivity i.e. the pitting potential and (b) by the anodic current density at a certain potential, typically  $+700\text{mV}$ . The potentiostat used in these studies was an EG&G Potentiostat/ Galvanostat 263A.

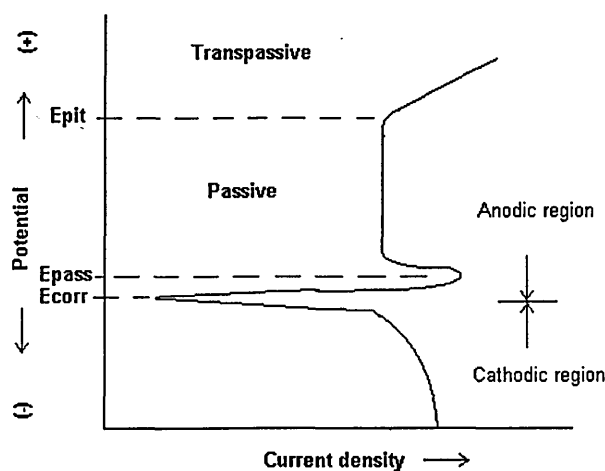


Fig.3.12. Schematic of polarisation curve

### References to Chapter 3

- [1] W.-D.Münz, F.J.M.Hauzer, D.Schulze, B.Buil, Surf. Coat. Technol., 49, (1991), 161
- [2] W.-D.Münz, D.Schulze, F.J.M.Hauzer, Surf. Coat. Technol., 50 (1992), 169
- [3] A.Ehiasarian, M.Phil. Transfer Report, Sheffield Hallam University, 1999, Sheffield, UK
- [4] Hardness Testing, H.E.Boyer, ASM International, 1987, Ohio, USA
- [5] M.Ives, Ph.D. Thesis, Sheffield Hallam University, 1994, Sheffield, UK
- [6] Electron Microscopy and Analysis, P.J.Goodhew, F.J.Humphreys, Taylor and Francis, 1988, London, UK
- [7] Elements of X-Ray Diffraction, B.D.Cullity, Addison-Wesley Publishing Company Inc., 1978, Reading, USA
- [8] D.B.Lewis, Lecture notes, Sheffield Hallam University, 1995, Sheffield, UK
- [9] Physical Metallurgy Vol.1, K.W.Andrews, George Allen & Unwin Ltd., 1973, London, UK
- [10] G.B.Harris, Phil.Mag., 43, (1952), 113
- [11] Stress Determination for Coatings, J.A.Sue, G.S.Schajer, in ASM Handbook, Vol.5, ASM International, 1994, Ohio, USA
- [12] D.S.Rickerby, A.M.Jones, B.A.Bellamy, Surf.Coat.Technol., 37, (1989), 111
- [13] Principles and Prevention of Corrosion, D.A.Jones, Macmillan Publishing Company, 1992, New York, USA

## 4. Results

### 4.1. Niobium Coatings on Steel Substrates

#### 4.1.1. Comparison of Nb Coatings deposited by UBM and SCAE

The following section describes the results obtained from Nb coatings deposited by unbalanced magnetron sputtering and steered cathodic arc evaporation at 420°C as described in 3.2.2. (I).

##### 4.1.1.1. Physical Properties

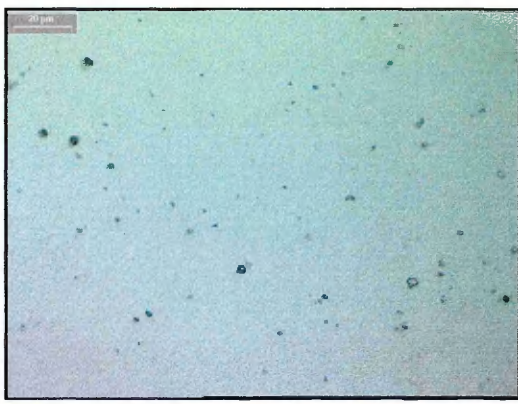
The thickness of the films is approximately 1.3µm for the UBM coating, 0.6µm for the SCAE coating (3-fold rotation) and 1µm for the SCAE coating deposited in 2-fold rotation. The deposition rates are 0.74 µm·h<sup>-1</sup> for UBM deposition and 0.15 µm·h<sup>-1</sup> (3-fold rotation) and 0.25 µm·h<sup>-1</sup> (2-fold rotation) for arc evaporation of Nb.

The microhardness values of the coatings are HK<sub>0.003</sub>= 600 for the UBM coating and HK<sub>0.003</sub>= 560 for the SCAE coating with a thickness of 1µm.

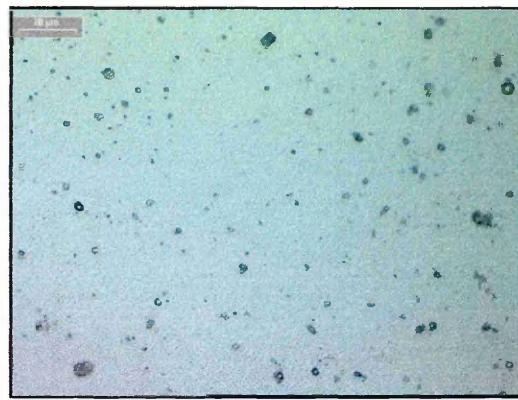
The roughness values of the coatings on polished HSS are R<sub>a</sub>= 0.065µm (UBM), R<sub>a</sub>= 0.108µm (SCAE 0.6µm) and R<sub>a</sub>= 0.132µm (SCAE 1.0µm).

##### 4.1.1.2. Microstructure

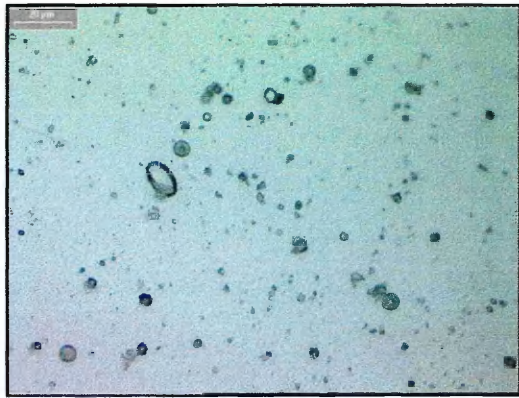
Figure 4.1. shows optical micrographs of the surface morphology of the different Nb films. It is apparent that the number and size of macroparticles or 'droplets' is higher in the case of arc evaporated films compared with the sputtered coating where droplet generation only occurs during the substrate ion etching stage in the cathodic arc mode. When comparing the two SCAE coatings, it is evident that using two-fold rotation as opposed to three-fold rotation further increases the droplet size and density, as a result of the longer effective deposition time. When droplets become detached during or after coating deposition they can cause defects in the film as shown in the SEM micrograph of the arc evaporated coating in fig.4.1.(d).



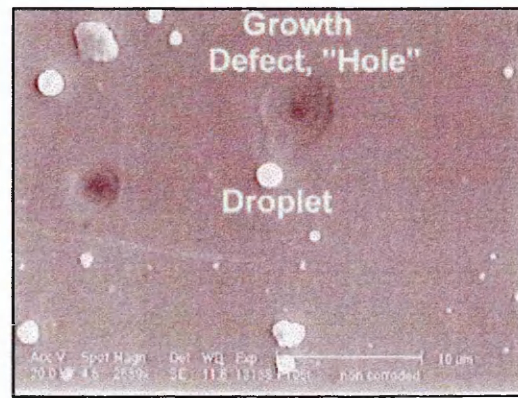
(a) UBM



(b) SCAE 0.6 $\mu\text{m}$



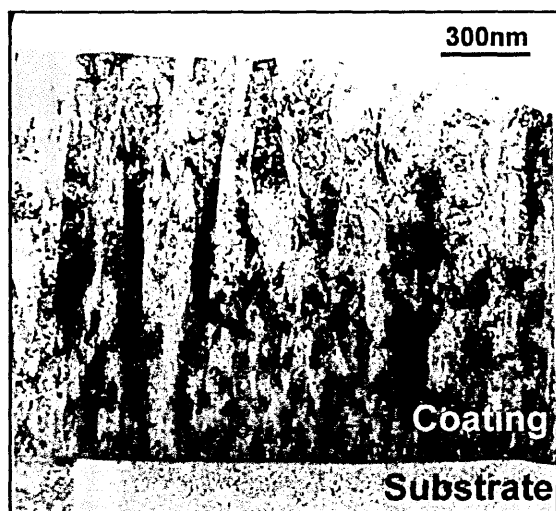
(c) SCAE 1.0 $\mu\text{m}$



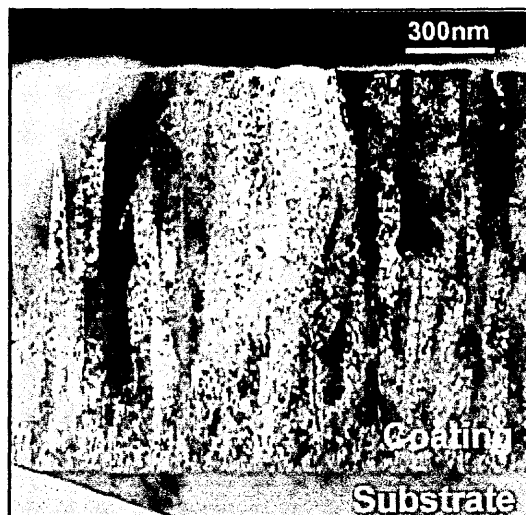
(d) Growth defect

Fig. 4.1. Surface topography (Scalebar for fig. (a), (b) and (c): 40 $\mu\text{m}$  )

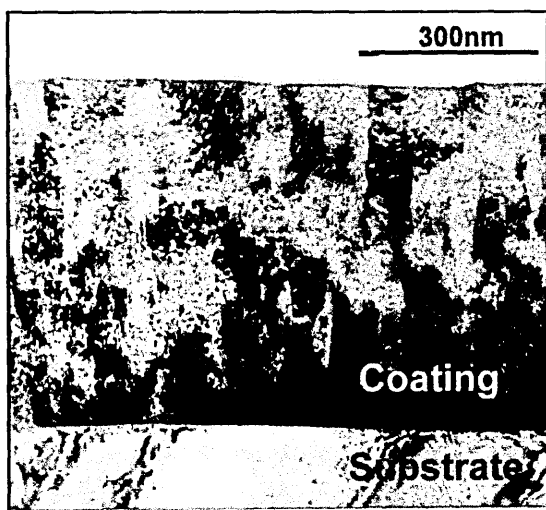
Cross-sectional TEM micrographs in fig. 4.2. compare the microstructure of sputtered and arc evaporated Nb coatings. Both films exhibit a clear columnar structure with no apparent inter- or intracolumnar porosity. The sputtered coating is characterised by a region of competitive growth near the interface, followed by evolution of the columnar morphology with an average column diameter of 65nm, measured at 0.5 $\mu\text{m}$  from the coating/ substrate interface. The average column diameter of the arc evaporated coating, measured at a similar position, is smaller with a value of approximately 50nm. Furthermore, the region of competitive growth in the early stages of film evolution is less pronounced. The dark field images were taken from the (110) diffraction spot, parallel to the growth direction, from a diffraction pattern with a  $\langle 111 \rangle$  zone axis.



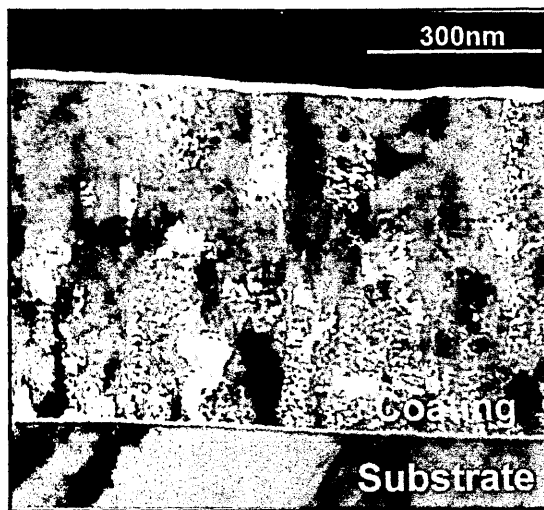
(a) UBM: BF image



(b) UBM: DF image



(c) SCAE: BF image



(d) SCAE: DF image

Fig.4.2. Cross-sectional TEM images

#### 4.1.1.3. Texture and Residual Stress

High angle XRD traces of the different coatings are shown in figure 4.3. The corresponding texture values, determined by the inverse pole figure technique (section 3.3.5.1.), are compared in figure 4.4. The sputtered coating shows a strong preferred  $\{110\}$  orientation with a texture value  $P$  approaching six, i.e. the highest possible value as six reflections are considered. The  $\{110\}$  texture is less pronounced for the SCAE coatings, whose crystallographic orientation is defined by mixed texture components with a major  $\{110\}$  component with  $P$ -values of 4.1 (SCAE  $0.6\mu\text{m}$ ) and 3.7 (SCAE

1.0 $\mu\text{m}$ ) and a minor  $\{111\}$  component with P values of 1.7 (SCAE 0.6 $\mu\text{m}$ ) and 1.65 (SCAE 1.0 $\mu\text{m}$ ) respectively.

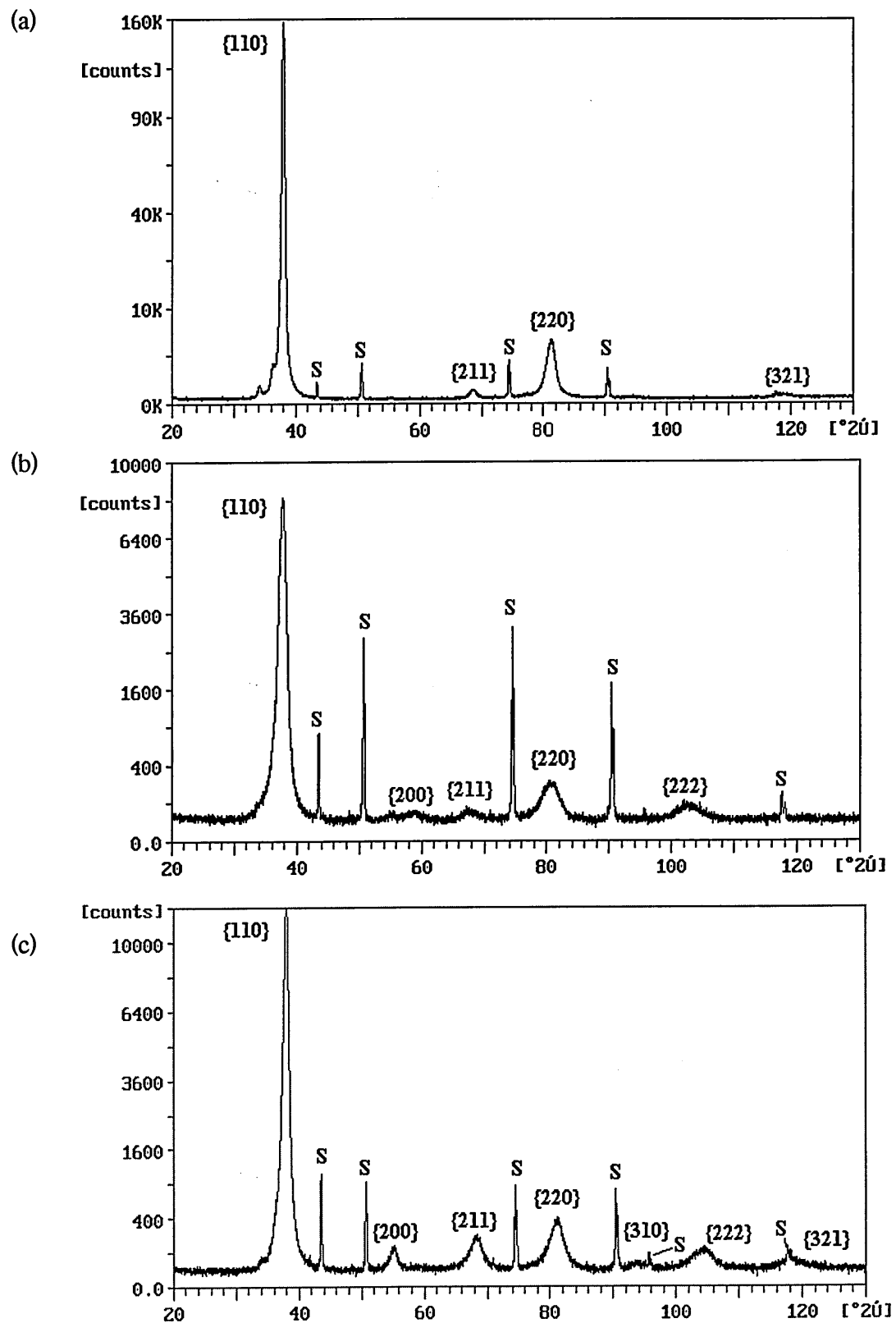


Fig.4.3. High angle XRD traces: UBM (a), SCAE 0.6 $\mu\text{m}$  (b) and SCAE 1 $\mu\text{m}$  (c)

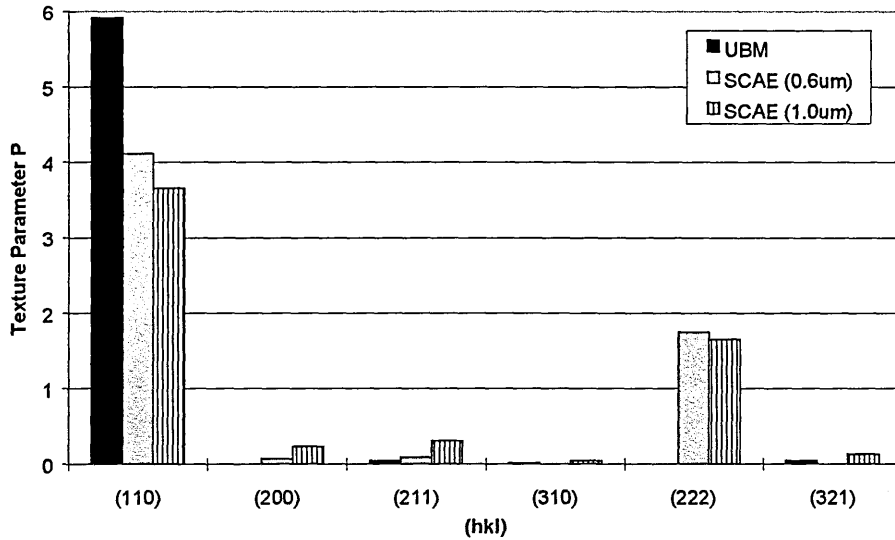


Fig.4.4. Texture values

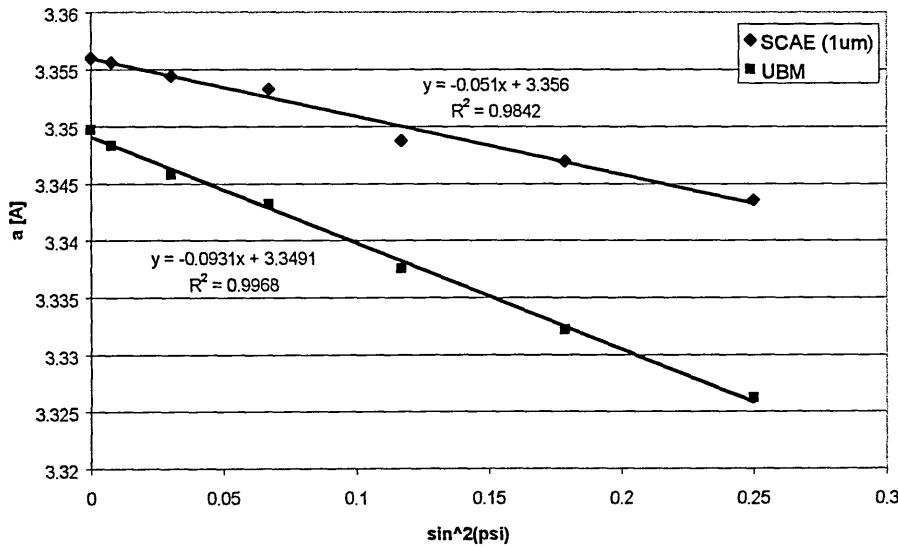


Fig.4.5.  $\sin^2\psi$  plots

Residual stresses, calculated by the  $\sin^2\psi$  method (section 3.3.5.2.), were determined only for the coatings with comparable coating thicknesses. The corresponding  $\sin^2\psi$  plots are shown in figure 4.5. The intrinsic and thermal stress components, calculated according to equation 3.8., are both of compressive nature (table 4.1.). The intrinsic stress in the UBM deposited Nb coating is approximately three times higher than that in the arc evaporated film. It is interesting to note, that although the stress is higher, the lattice parameter is smaller in the UBM film with a value of  $a = 3.349\text{\AA}$  compared to  $a = 3.355\text{\AA}$  for the SCAE film.

	UBM	SCAE (1 $\mu$ m)
Residual Stress [GPa]	-2.10	-1.15
Thermal Stress Component [GPa]	-0.68	-0.68
Intrinsic Stress Component [GPa]	-1.42	-0.47

Table 4.1. Residual Stresses

#### 4.1.1.4. Corrosion Resistance

The corrosion resistance of the different films on stainless steel as well as of bulk niobium and uncoated stainless steel substrate, evaluated by potentiodynamic polarisation measurements, is compared in figure 4.6. The corrosion potential  $E_{\text{corr}}$  of bulk Nb is  $-400\text{mV}$ , while that of stainless steel is nobler with a value of  $-220\text{mV}$ . Bulk Nb exhibits the typical behaviour of a passivating metal. The polarisation curve is characterised by a low and constant current density (around  $10^{-6} \text{ Acm}^{-2}$ ) in the anodic region indicating passivation, i.e. the formation of a stable oxide layer of  $\text{Nb}_2\text{O}_5$ . The oxide film protects the metal against any corrosive attack, i.e. pitting and anodic dissolution, throughout the whole range of the scan. Passivation is also evident in the case of stainless steel between  $-200$  and  $+200\text{mV}$ , which is related to the formation of an chromium-rich oxide film. The passive current density is similar to that of bulk Nb. However, the stability of the passive layer on stainless steel is restricted by the presence of chloride anions, which eventually leads to film breakdown. This breakdown occurs at about  $+200\text{mV}$  and leads to nucleation of pits (pit initiation), pit growth (pit propagation) and finally severe corrosion of the steel substrate as indicated by the steep increase in current density up to the maximum recordable value of  $10^{-1} \text{ Acm}^{-2}$ .

The corrosion behaviour of the sputtered Nb coating on stainless steel is shown in figure 4.6.(b). The polarisation curve in the passive region as well as the passive current density (around  $10^{-6} \text{ Acm}^{-2}$ ) are very similar to that of bulk Nb. The coating passivates over the whole range of the scan and fully protects the stainless steel substrate against pitting or any form of corrosive attack. No pits were observed on the surface of the coated sample after the corrosion test as shown in figure 4.7.(b).

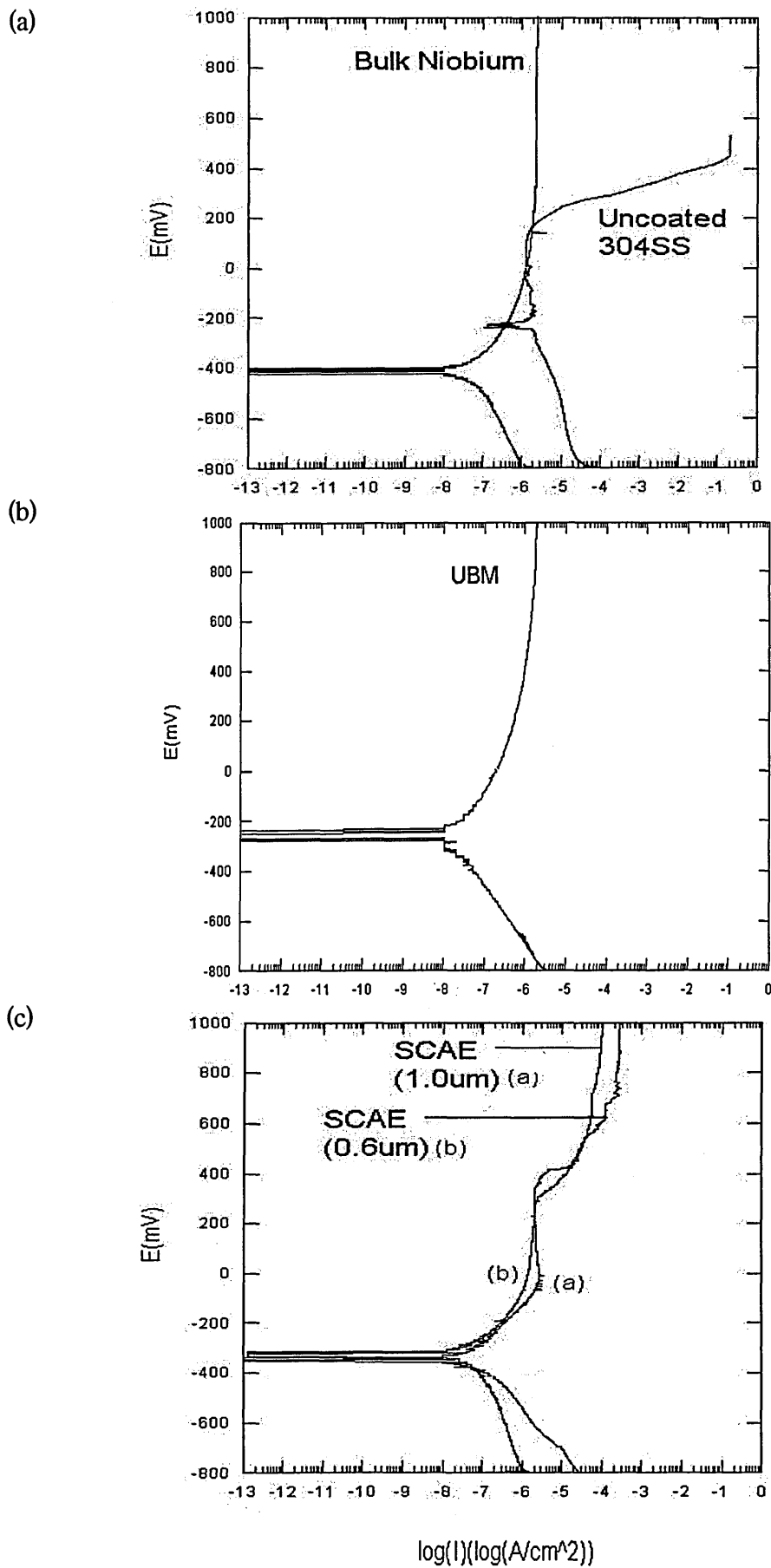
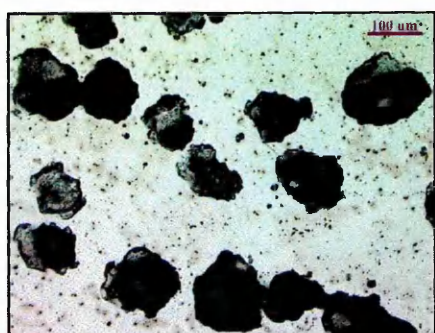


Fig.4.6. Potentiodynamic polarisation curves in 3% NaCl solution

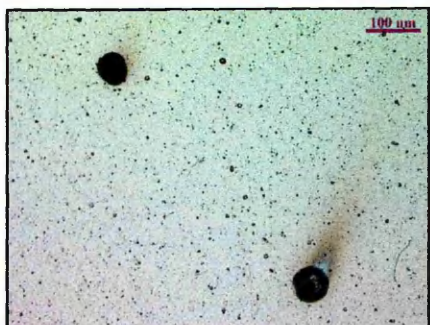
A different corrosion behaviour can be observed for the two arc evaporated coatings. Both Nb films exhibit passivation up to a potential of +300mV (SCAE 1.0 $\mu$ m) and +400mV (SCAE 0.6 $\mu$ m) respectively. However, at these potentials, the increase in current density is indicative for localised breakdown of the protective coating followed by corrosive (pitting) attack of the steel substrate. The current densities increase initially and then tend to a limit, at around +700mV, of  $1 \cdot 10^{-4}$  A/cm<sup>2</sup> for the 1.0 $\mu$ m thick coating and of  $3 \cdot 10^{-4}$  A/cm<sup>2</sup> for the coating with a thickness of 0.6 $\mu$ m. Figure 4.7. shows the surfaces of the samples after the corrosion test. Heavy pitting and localised dissolution of the metal characterises the surface of the uncoated stainless steel substrate. There is no evidence of any corrosive attack on the sputter-coated sample. The Nb film fully protects the steel substrate as already suggested by the polarisation curve shown above. The arc-evaporated sample exhibits some local corrosive attack of the steel substrate, which initiates through defects in the coating and propagates under the Nb coating. This results in the typical “blistering” of the film as can be seen from the magnified SEM image in figure 4.7.(d). These defects, acting as pathways for the corrosive medium to the substrate, can be e.g. growth defects generated by droplets or macroparticles in the film.



(a) Uncoated 304 SS



(b) UBM



(c) SCAE



(d) Typical pit formation

Fig.4.7. Surface of corroded area

## 4.1.2 Influence of Temperature and Ion Bombardment on UBM Nb Coatings

This section reports about two different Nb coatings deposited by UBM with variation of the coating temperature ( $T=250^{\circ}\text{C}$  and  $T=420^{\circ}\text{C}$ ) and the ion bombardment i.e. unbalancing coil current ( $I_{\text{coil}} = 3\text{A}$  and  $I_{\text{coil}} = 6\text{A}$ ) during deposition, as described in 3.2.2. (II). The increase in unbalancing coil current from 3A to 6A resulted in an increase in the substrate bias current density, i.e. ion flux, by a factor of approximately two (section 3.1., fig.3.3.).

### 4.1.2.1. Physical Properties

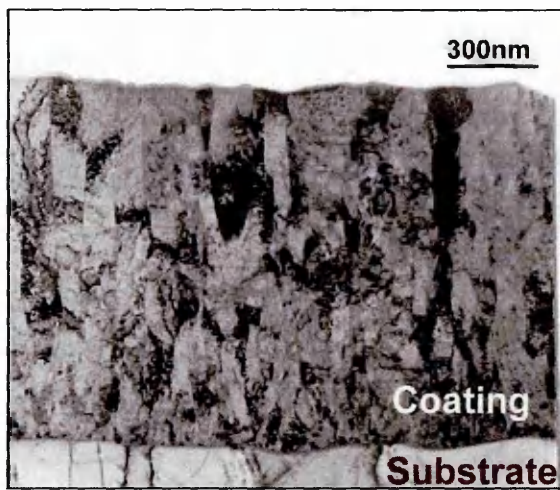
The thickness of both coatings is approximately  $1.3\mu\text{m}$ . The microhardness values are  $\text{HK}_{0.003} = 520$  for the film deposited at  $250^{\circ}\text{C}$  with a coil current of 3A and  $\text{HK}_{0.003} = 600$  for the coating deposited at  $420^{\circ}\text{C}$  with a coil current of 6A.

The roughness values on polished HSS are  $R_a = 0.092$  ( $250^{\circ}\text{C}$ , 3A) and  $R_a = 0.065$  ( $420^{\circ}\text{C}$ , 6A)

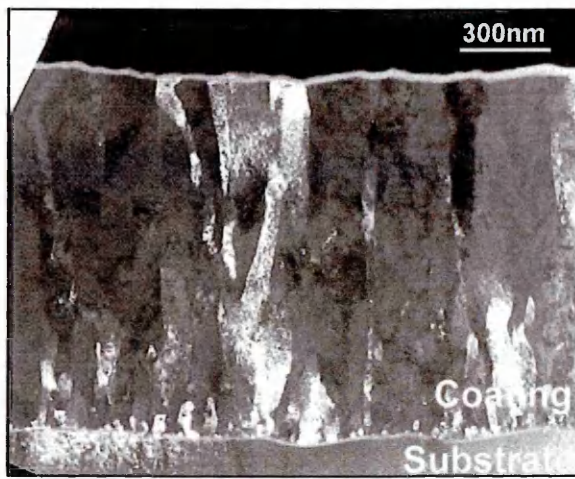
### 4.1.2.2. Microstructure

TEM cross-sections of the two coatings on stainless steel are shown in figure 4.8. Both coatings show a clear columnar coating morphology with no apparent porosity. The low temperature film grown under reduced ion bombardment (fig.4.8.(a),(b)) is characterised by pronounced competitive growth, a coarse, irregular columnar morphology and rounded column tops. The average column diameter is 90nm measured at  $0.5\mu\text{m}$  from the substrate/ coating interface

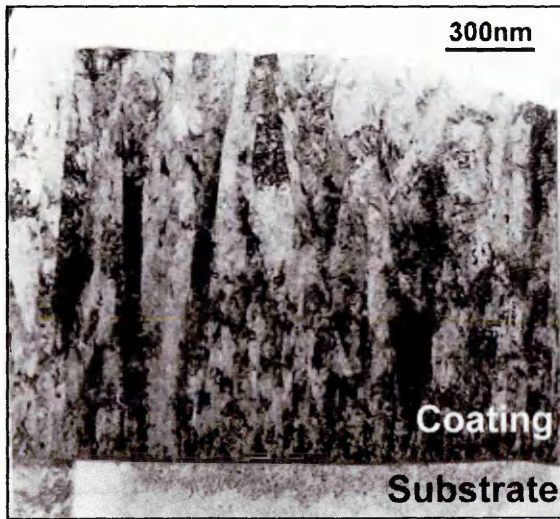
The Nb coating deposited at  $420^{\circ}\text{C}$  under higher ion bombardment ( $I_{\text{coil}} = 6\text{A}$ ) (fig.4.8.(c),(d)) also exhibits some competitive growth, however, less pronounced than the low temperature film. The columnar coating structure is more regular and refined with smaller column diameters (average diameter = 65nm at 500nm from the interface). The dark field images were taken from the  $\{110\}$  diffraction spot, parallel to the growth direction, from diffraction patterns with a  $\langle 111 \rangle$  (high temperature coating) and a  $\langle 311 \rangle$  (low temperature coating) zone axis respectively.



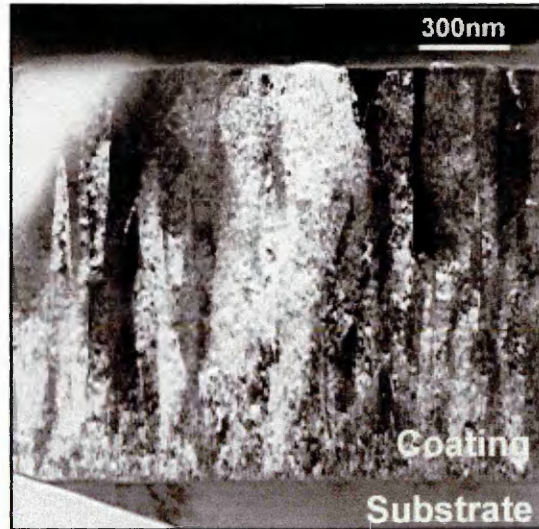
(a)  $T = 250^{\circ}\text{C}$ ;  $I_{\text{coil}} = 3\text{A}$ : BF image



(b)  $T = 250^{\circ}\text{C}$ ;  $I_{\text{coil}} = 3\text{A}$ : DF image



(c)  $T = 420^{\circ}\text{C}$ ;  $I_{\text{coil}} = 6\text{A}$ : BF image



(d)  $T = 420^{\circ}\text{C}$ ;  $I_{\text{coil}} = 6\text{A}$ : DF image

Fig.4.8. Cross-sectional TEM images

#### 4.1.2.3. Texture and Residual Stress

- High angle XRD traces of the coatings are given in figure 4.9. Texture values are shown in figure 4.10. There is no significant influence of coating temperature or ion bombardment on the texture evolution. Both films show a strong preferred  $\{110\}$  orientation with texture values approaching six.  $\text{Sin}^2\psi$  plots and the corresponding stress values are given below (figure 4.11., table 4.2.). The difference in thermal stresses obviously arises from the different deposition temperatures. The intrinsic i.e. growth induced stress values are compressive and increase from 0.76 GPa to 1.42 GPa with an increase in unbalancing coil current from 3A to 6A. The difference in the residual compressive stresses is reflected in the lattice parameter, which is considerably higher for the coating deposited at  $420^{\circ}\text{C}$  under enhanced ion bombardment with a value of a =

3.349Å compared with  $a = 3.331\text{Å}$  for the low temperature/ reduced ion bombardment film.

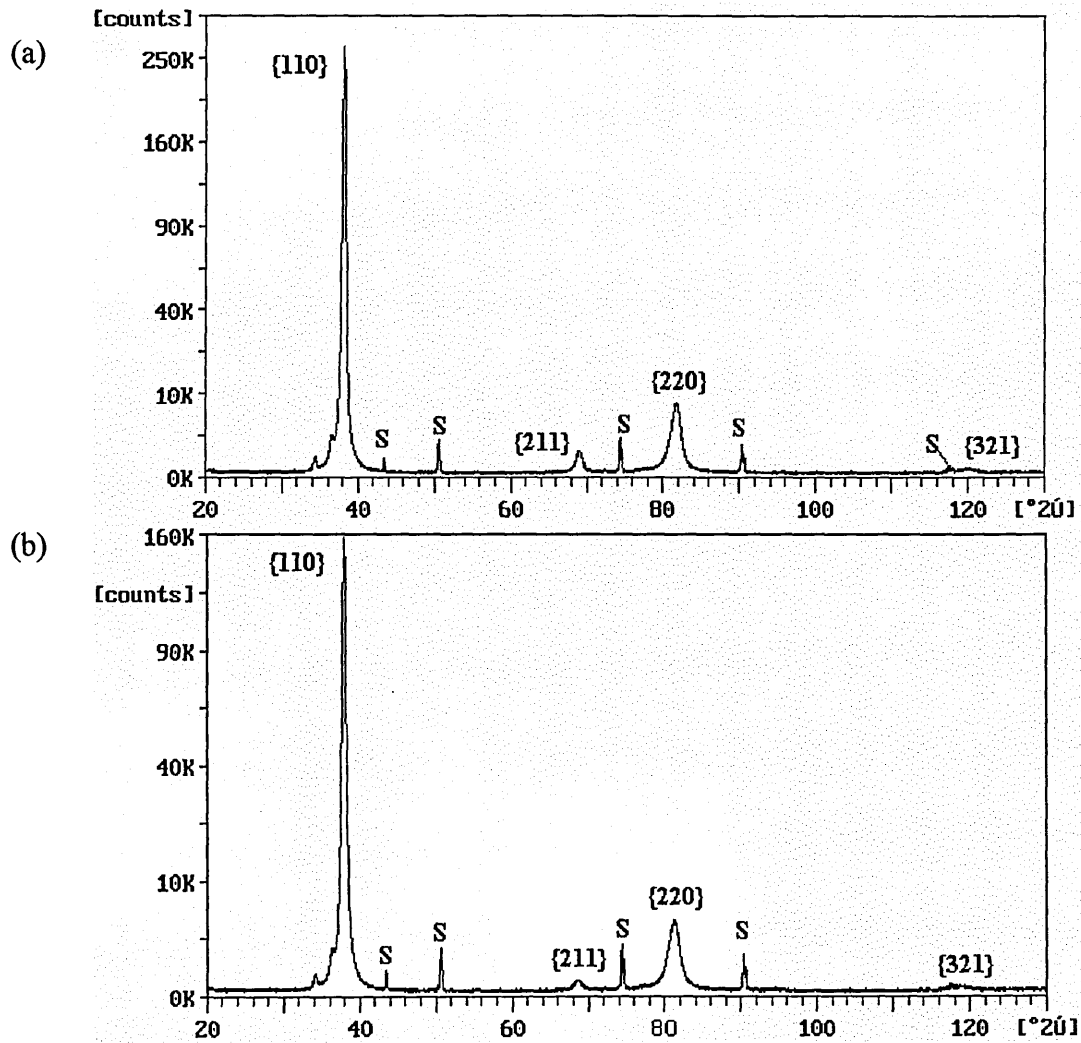


Fig. 4.9. High angle XRD traces:  $T = 250^\circ\text{C}$ ,  $I_{\text{coil}} = 3\text{A}$  (a);  $T = 420^\circ\text{C}$ ,  $I_{\text{coil}} = 6\text{A}$  (b)

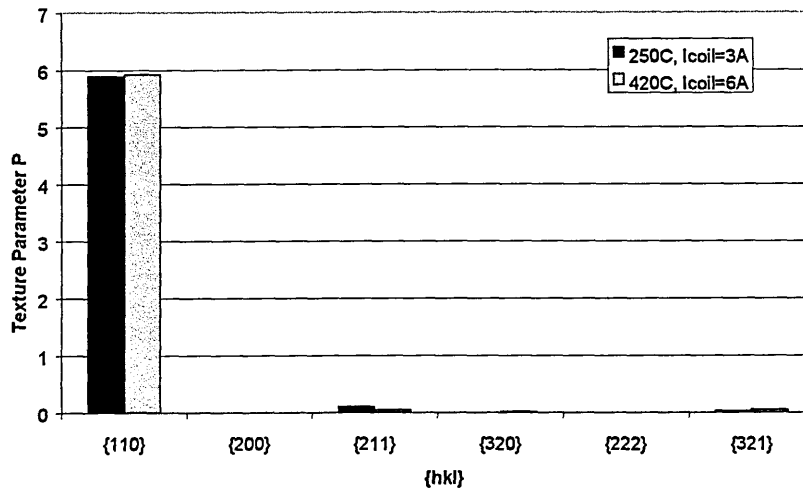


Fig. 4.10. Texture values

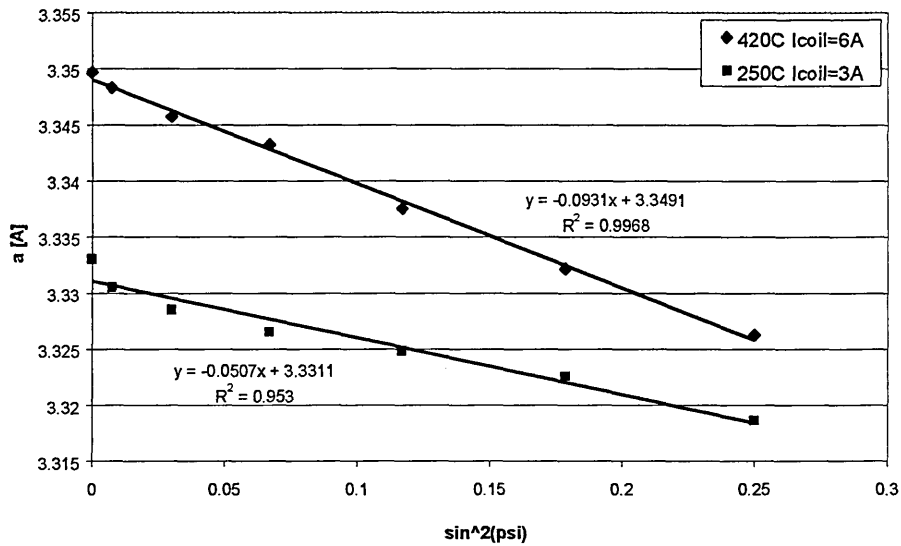


Fig. 4.11. Sin<sup>2</sup>ψ plots

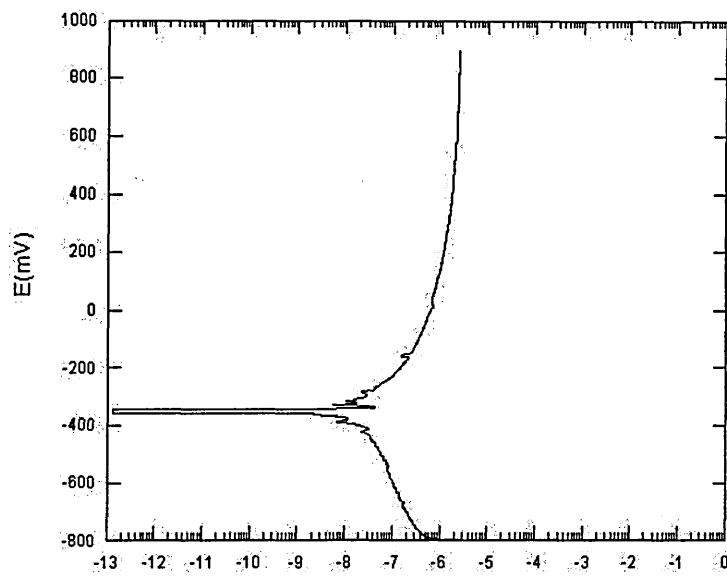
	T = 250°C; I <sub>coil</sub> = 3A	T = 420°C; I <sub>coil</sub> = 6A
Residual Stress [GPa]	-1.15	-2.1
Thermal Stress Component [GPa]	-0.39	-0.68
Intrinsic Stress Component [GPa]	-0.76	-1.42

Table 4.2. Residual Stresses

#### 4.1.2.4. Corrosion Resistance

Potentiodynamic polarisation plots of the two coatings on stainless steel are shown in figure 4.12. The corrosion behaviour of the two coated samples in the anodic region is very similar and apparently not influenced by the deposition temperature and ion bombardment during film growth. Both coatings passivate and fully protect the stainless steel substrate throughout the range of the scan. No corrosive attack of the steel substrate could be observed after the polarisation scan. The passive current densities are in the range of  $10^{-6} \text{ Acm}^{-2}$ , similar to that of bulk Nb.

(a)



(b)

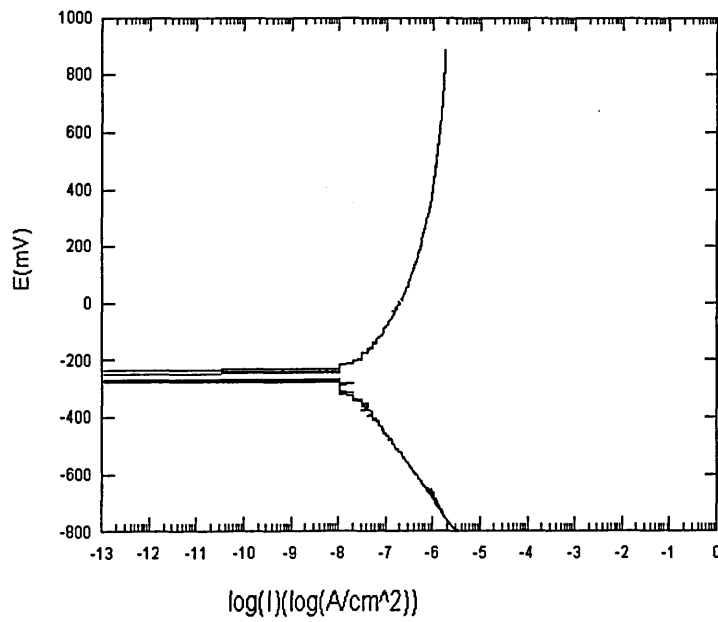


Fig. 4.12. Potentiodynamic polarisation curves in 3% NaCl solution :  $T=250^{\circ}\text{C}$ ,  $I_{\text{coil}}=3\text{A}$  (a);  $T=420^{\circ}\text{C}$ ,  $I_{\text{coil}}=6\text{A}$  (b)

### 4.1.3. Influence of the Ion Etching Pre-Treatment prior to UBM Deposition

The influence of the mode of substrate ion etching prior to deposition on the properties of sputter deposited Nb coatings is outlined in the following paragraph. The substrates were treated using metal ions from the cathodic arc source i.e. multiply charged Nb- and Cr- ions as well as inert, singly charged Ar ions from a glow discharge as described in 3.2.2.(III).

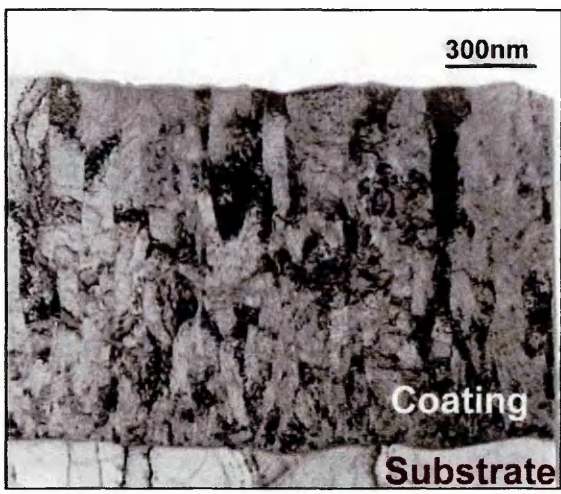
#### 4.1.3.1. Physical Properties

The coating thickness is  $1.3\mu\text{m}$  for all three films. Hardness values were measured as  $\text{HK}_{0.003} = 520$  for the coating deposited after a Nb ion etch,  $\text{HK}_{0.003} = 560$  for the coating deposited after a Cr ion etch and  $\text{HK}_{0.003} = 650$  for the Ar ion etch sample.

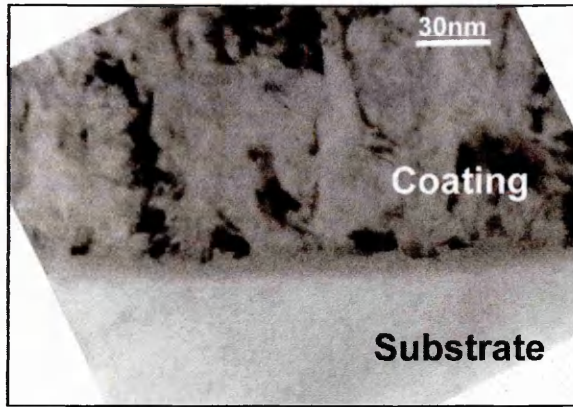
The surface roughness values of the Nb coatings are  $R_a = 0.092\mu\text{m}$  (Nb-etch),  $R_a = 0.099\mu\text{m}$  (Cr-etch) and  $R_a = 0.042\mu\text{m}$  (Ar-etch).

#### 4.1.3.2. Microstructure

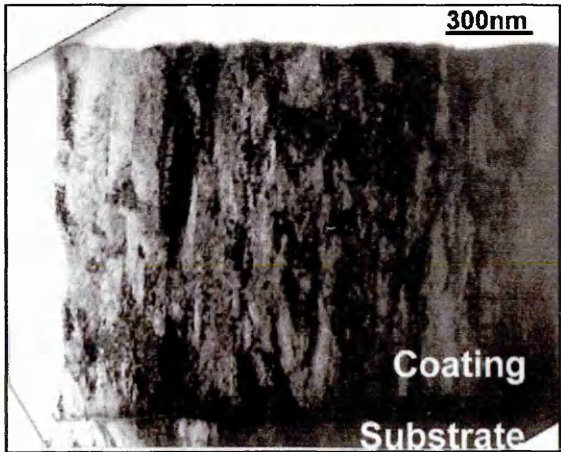
Cross-sectional TEM micrographs of the films and of the interface regions are shown in figure 4.13. In general, the morphology of the three coatings is similar with a broad columnar structure, pronounced competitive growth and no apparent inter- or intra-columnar porosity in the films. The average column diameter is approximately 90nm in all three coatings, measured at  $0.5\mu\text{m}$  from the interface. However, the column size seems to differ in the early stages of film growth i.e. it appears to be smaller for the coating deposited after the Ar ion etch and possibly also after the Cr ion etch compared with that of the Nb ion etch coating. Significantly different features can be found in the interface regions arising from the different mode of substrate treatment prior to deposition. The sample produced using Nb ions from the steered cathodic arc discharge as the etching species is characterised by an approximately 8nm thick, sharp ribbon (fig. 4.13.(b)). This ribbon is a very fine crystalline, Nb-rich layer grown under the impact of the heavy high energetic Nb ions ( $E_{\text{ion}} = 3.6 \text{ keV}$ , assuming an average charge state of +3 as described in section 2.4.1.). The nature of this interface layer will be discussed in



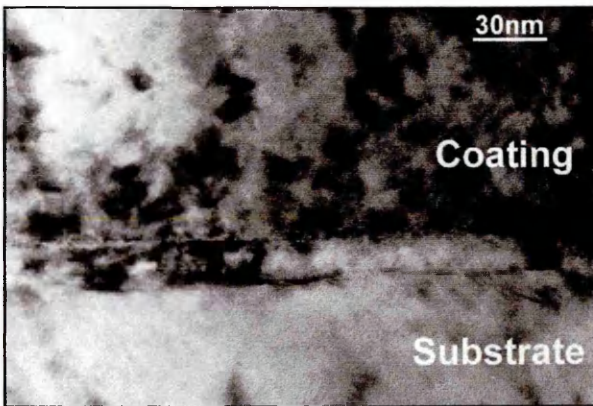
(a) Nb-etch : BF of whole coating



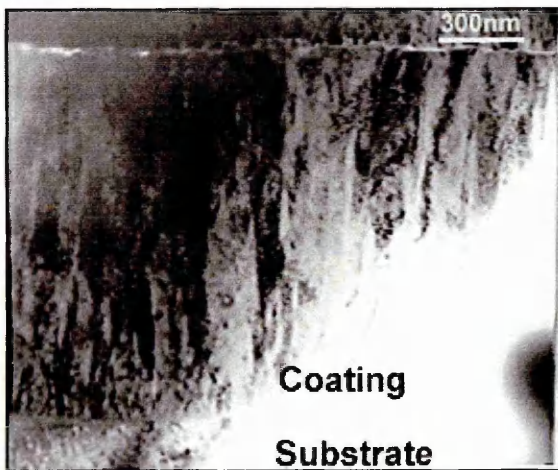
(b) Nb-etch : Interfacial region



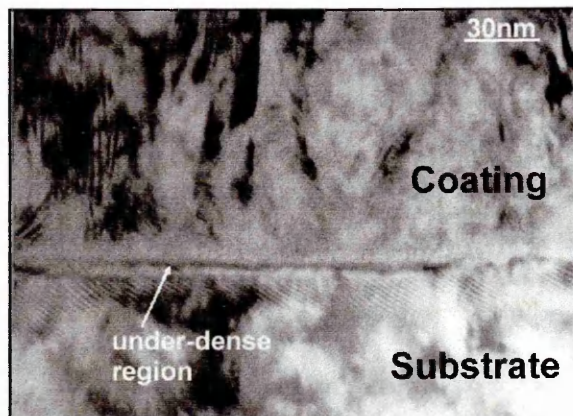
(c) Cr-etch : BF of whole coating



(d) Cr-etch : Interfacial region



(e) Ar-etch : BF of whole coating



(f) Ar-etch : Interfacial region

Fig. 4.13. Cross-sectional TEM images

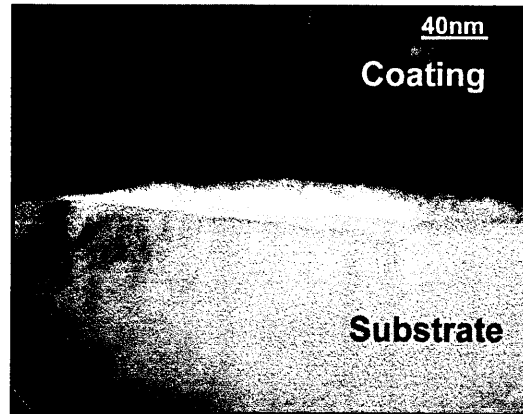


Fig. 4.14. Void formation at the interface (Ar-etch)

more detail in paragraph 4.1.4. A very different interface is generated during bombardment with Cr ions from the arc discharge as can be seen from fig. 4.13.(d). The impact of Cr ions with average ion energies of 2.4keV (assuming an average charge state of +2, section 2.4.1.) on the stainless steel substrate generates an abrupt interface with a structurally altered, approximately 20nm thick, region below the substrate/ film interface. There is no evidence of the very fine crystalline region that was observed in the case of Nb ions as the etching species. Substrate sputter cleaning in the glow discharge mode using inert, singly ionised Ar ions ( $E_{ion, max.} = 1.2keV$ ) generates a diffuse substrate/ film interface with clear evidence of underdense regions and local voids at the interface as can be seen from figures 4.13.(f) and 4.14.

#### 4.1.3.3. Texture and Residual Stress

High angle X-ray diffraction traces and the corresponding texture values are given below (fig.4.15, fig.4.16.). All coatings show a preferred {110} orientation. However, the degree of preferred orientation differs. The Nb-etch coating is strongly textured with a texture value P of 5.9 for the {110} reflection. The coating deposited after a Cr-etch shows a less pronounced {110} orientation (P = 5.4) with minor {211} (P = 0.3) and {321} (P = 0.15) texture components. The Ar-etch film exhibits a shift towards a more mixed distribution of crystallographic orientations, with preferred {110} (P = 3.25), {211} (P = 1.3) and {321} (P = 1.0) texture components. Intrinsic stresses, determined by the  $\sin^2\psi$  method (fig.4.17) are of compressive nature in all three films (table 4.3.).

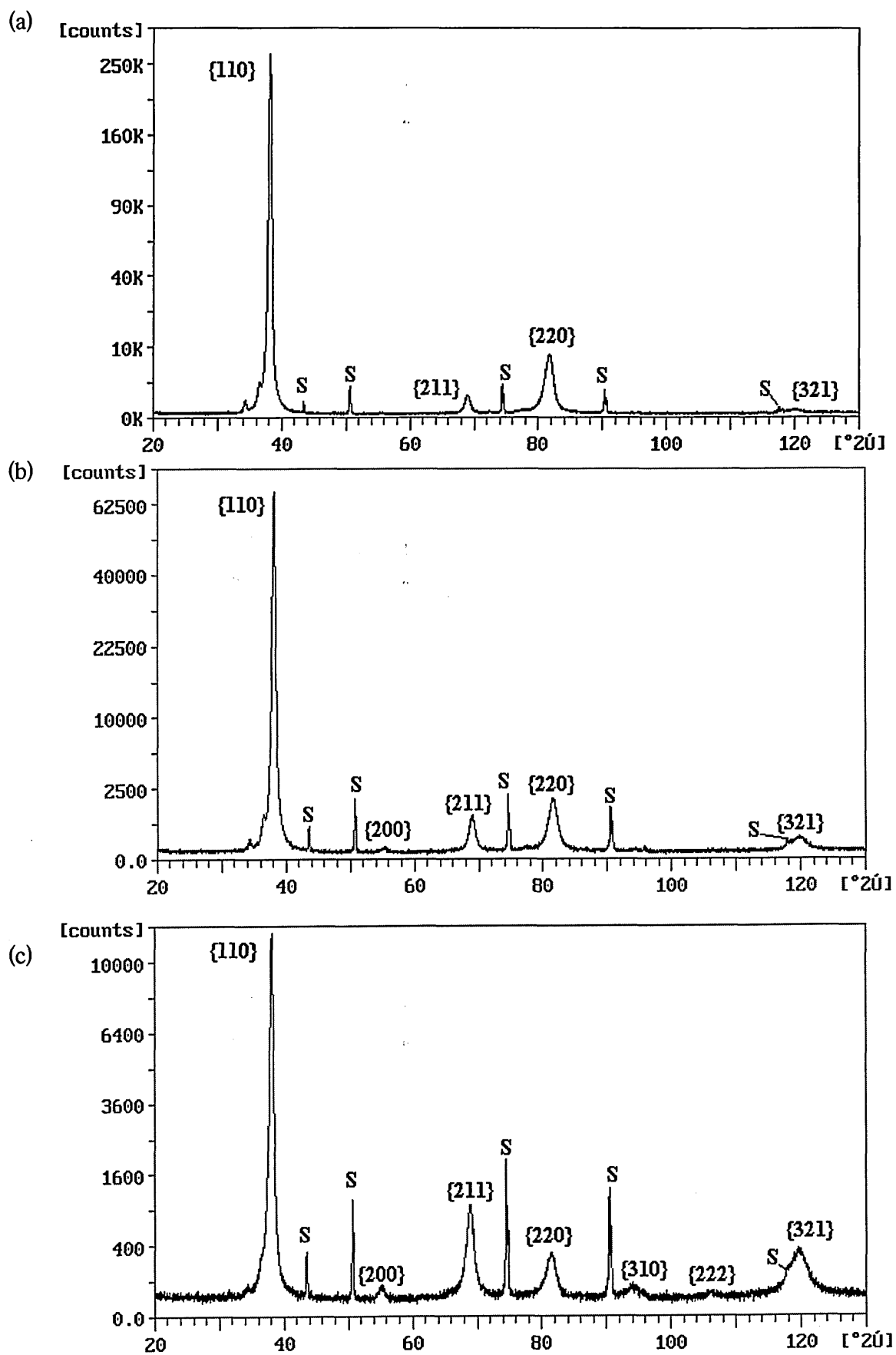


Fig. 4.15. High angle XRD traces : Nb-etch (a), Cr-etch (b), Ar-etch (c)

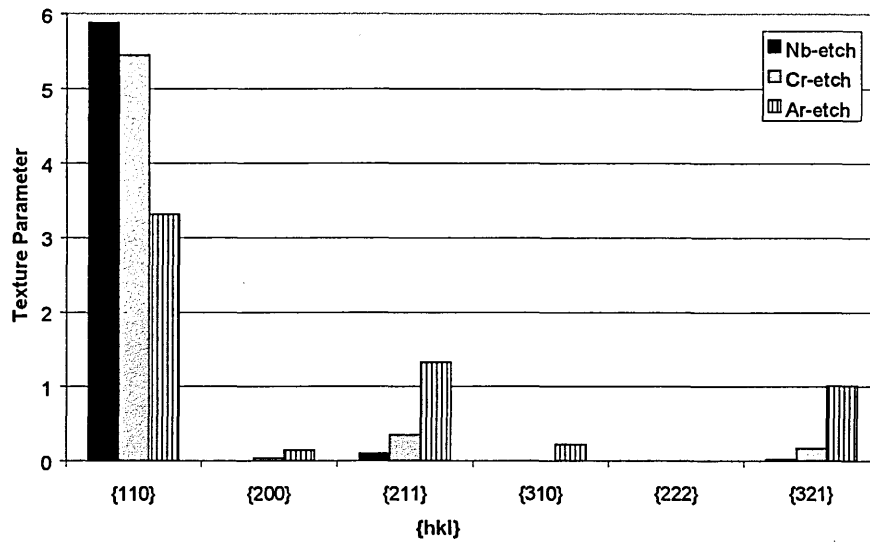


Fig. 4.16. Texture values

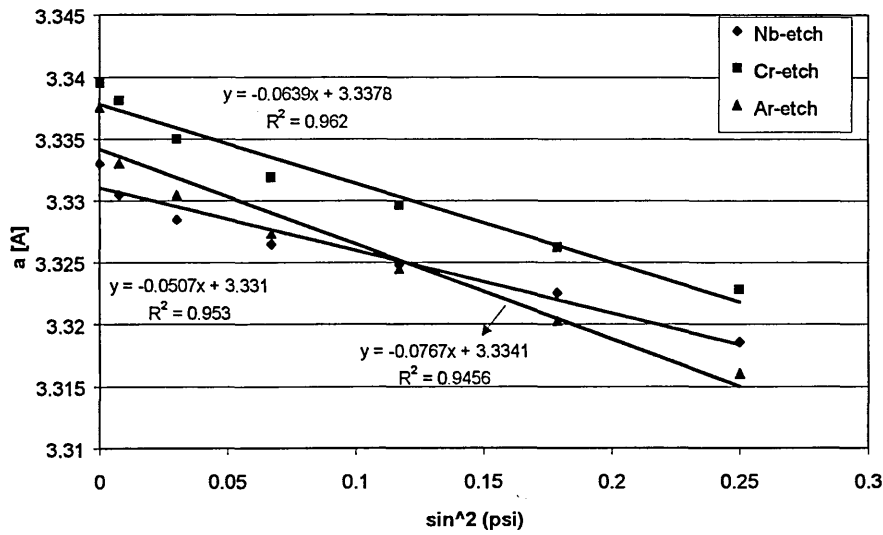


Fig. 4.17. Sin²ψ plots

	Nb-etch	Cr-etch	Ar-etch
Residual Stress [GPa]	-1.15	-1.45	-1.74
Thermal Stress Component [GPa]	-0.39	-0.39	-0.39
Intrinsic Stress Component [GPa]	-0.76	-1.06	-1.35

Table 4.3. Stress values

The stresses are highest for the Ar-etch coating, followed by the Cr-etch film and the lowest compressive stresses occur in the coating deposited after a Nb-etch, which also is reflected in the smallest lattice parameter with a value of  $a = 3.331 \text{ \AA}$ . Despite the lower stress value in the Cr-etch coating compared with the Ar-etch film, the measured lattice parameter is larger (Cr-etch:  $a = 3.338 \text{ \AA}$ , Ar-etch:  $a = 3.334 \text{ \AA}$ ).

#### 4.1.3.4. Corrosion Resistance

The corrosion resistance of the Nb coatings is compared in figure 4.18. The Nb-etch/ Nb coating exhibits passivation throughout the whole range of the scan with an anodic current density in the range of  $10^{-6} \text{ Acm}^{-2}$ . The coating fully protects the stainless steel substrate against corrosive attack during the polarisation measurement as described in 4.1.2.4. The films deposited after etching with Cr and Ar ions respectively show very different corrosion behaviour. The films do not remain passive; between +200 and +300mV the onset of pitting can be observed for both the coated specimens as indicated by the increase in anodic current density. The degree of exposure i.e. of active corrosion of the stainless steel substrate through defects in the coating or pits, represented by the anodic current density, is higher in the case of the Ar-etch specimen ( $2 \cdot 10^{-2} \text{ Acm}^{-2}$  @+700mV) than in the case of the Cr-etch coating ( $5 \cdot 10^{-4} \text{ Acm}^{-2}$  @+700mV).

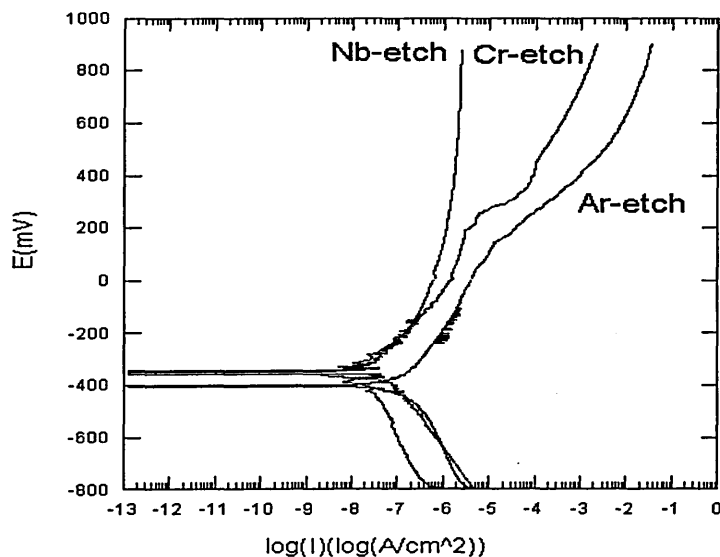


Fig. 4.18. Potentiodynamic polarisation curves in 3% NaCl solution

Plan view SEM pictures in fig. 4.19. show the condition of the coatings after the polarisation measurement. There is no evidence of corrosive attack on the Nb-etch coating, confirming the results obtained from the polarisation measurement. The surface of the Cr-etch specimen after the corrosion measurement is characterised by small, localised pits while that of the Ar-etch sample shows large areas of spallation of the Nb coating indicating some additional adhesive failure.

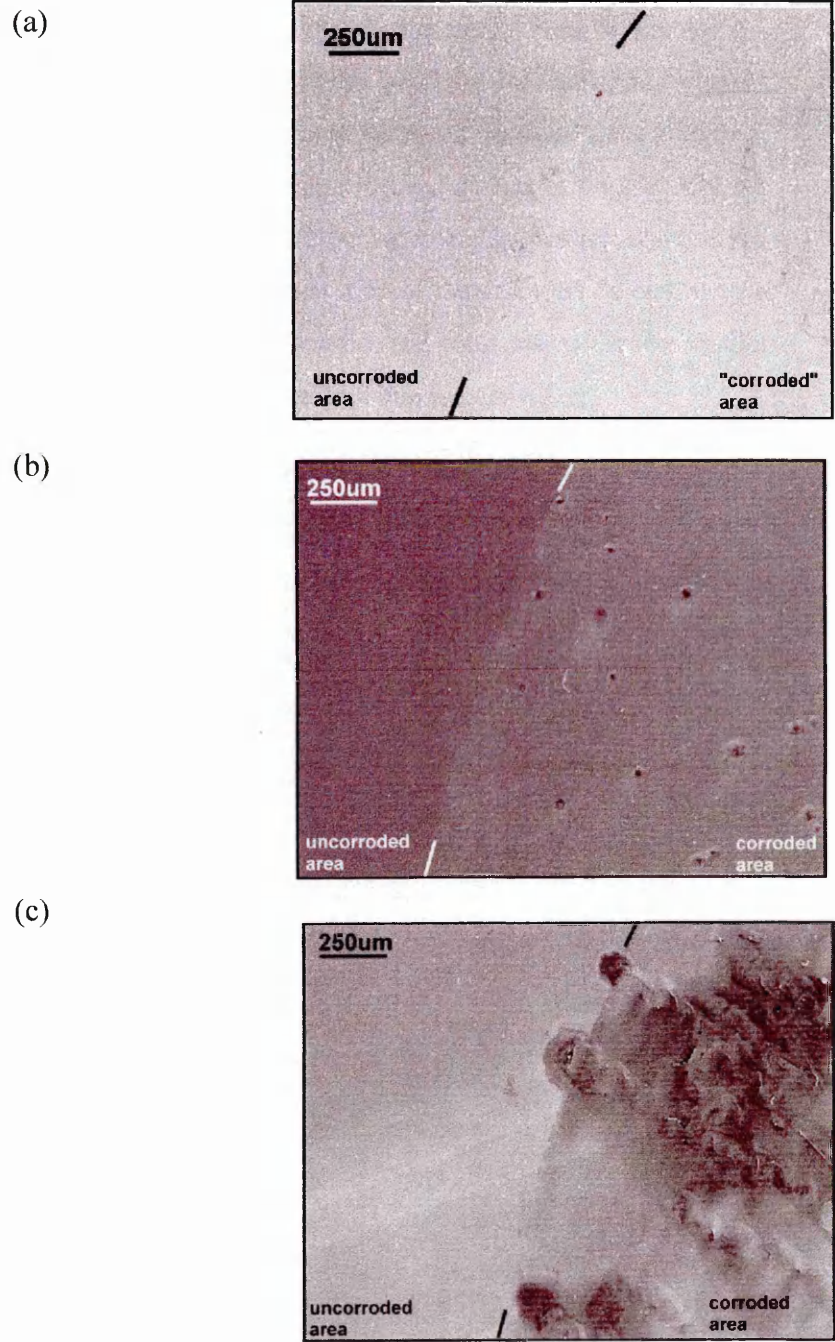


Fig.4.19 Surfaces of Nb coatings after polarisation measurement: Nb-etch (a), Cr-etch (b), Ar-etch (c)

#### 4.1.4 Nb Ion Etching prior to Coating Deposition: Influence of Working Gas Pressure and Substrate Bias Voltage during Etching

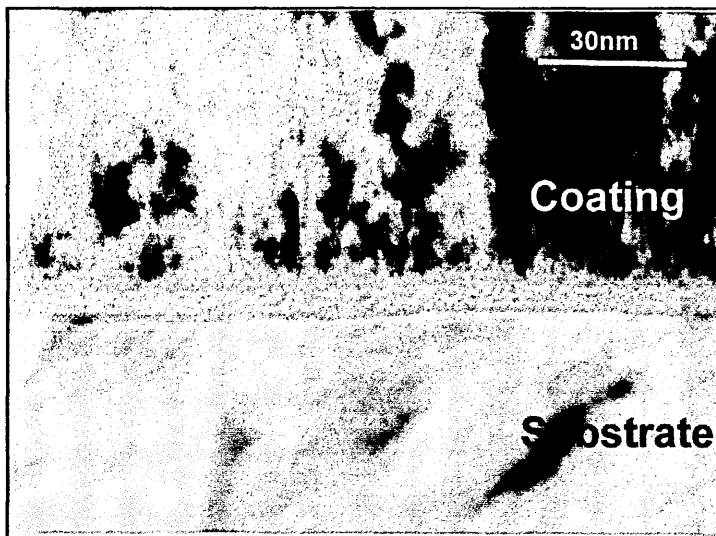
The following paragraph outlines the influence of the working gas pressure and the substrate bias voltage, i.e. the ion energy, during SCAE Nb ion etching on:

- (i) the interface region
- (ii) the properties of subsequently deposited thin Nb sputter coatings
- (iii) the substrate

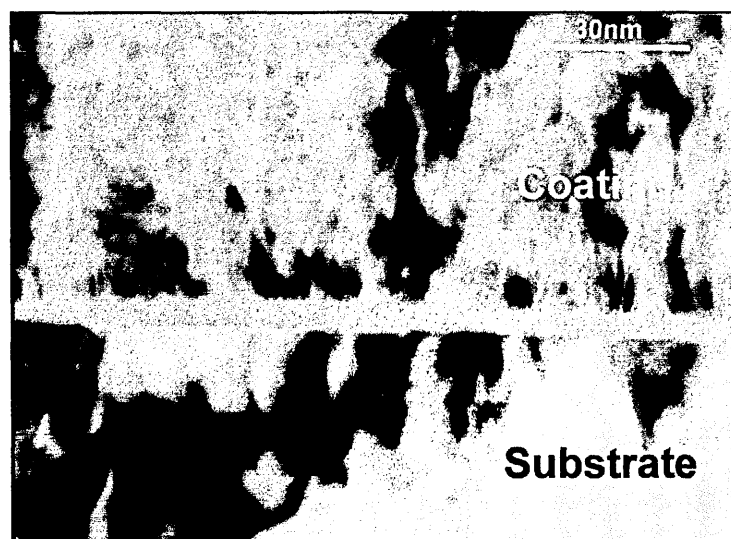
The results are presented with main emphasis on the microstructure and corrosion resistance. The stainless steel substrates were etched applying substrate bias voltages in the range of -200V to -1200V at two different pressure conditions, namely  $8.3 \times 10^{-4}$  mbar and  $2.3 \times 10^{-3}$  mbar, and subsequently coated with a 300nm thick Nb film as described in section 3.2.2.(IV). Additionally, stainless steel substrates were etched under variation of the bias voltage (-400V to -1200V) with no additional coating.

##### 4.1.4.1. Microstructure

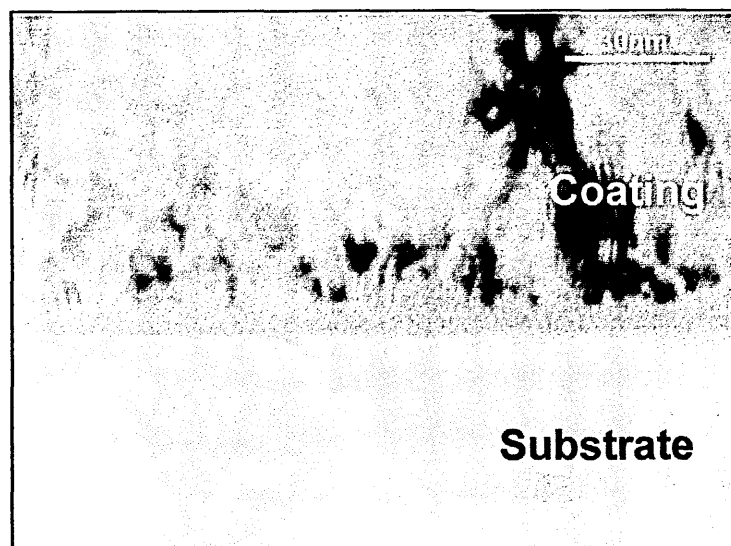
Cross-sectional TEM images (BF) of the interface and initial growth region are shown in fig.4.20. ( $P = 2.3 \times 10^{-3}$  mbar) and fig.4.21. ( $8.3 \times 10^{-4}$ ). No significant differences in the overall UBM grown coatings' morphologies were observed with regard to the etching pressure and ion energy. All coatings show the typical columnar morphology, characterised by competitive growth and no apparent inter-or intracolumnar porosity. However, significant differences were found in the interface regions generated under bombardment with Nb ions from the cathodic arc source. The samples etched using substrate bias voltages in the range of -600V to -1200V (i.e. average ion energies of 1.8keV to 3.6keV) are all characterised by a sharp interface with a clear interfacial layer (fig. 4.20.a-d., fig. 4.21.a-d). Convergent-beam/ selected area diffraction patterns shown in figure 4.22. were taken from the interface region of one sample ( $U_{\text{bias}}=-800\text{V}$ ,  $P=8.3 \times 10^{-4}$  mbar) covering an area in the range of a few nm. The patterns were taken from a thicker (fig.4.22.(a)) and a thinner sample area (fig.4.22.(b)) The diffraction patterns reveal that the layer is of an extremely fine crystalline nature, i.e. "micro-crystalline" which will be denoted as *amorphised* in the following.



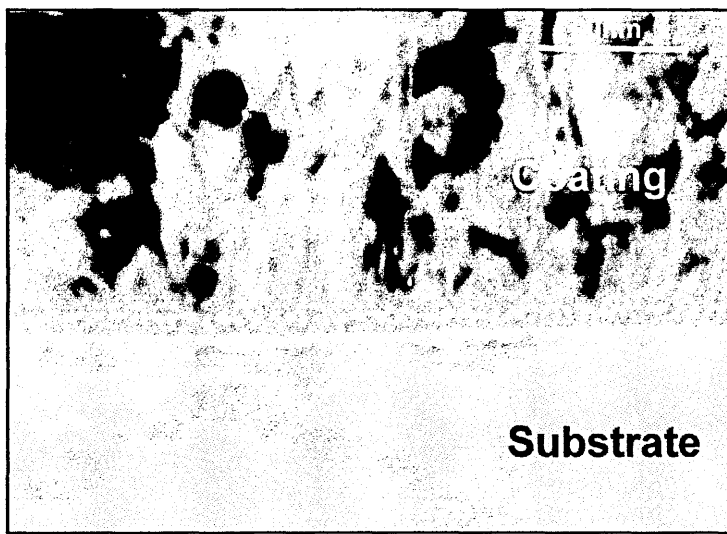
(a)  $U_{\text{bias}} = -1200\text{V}$



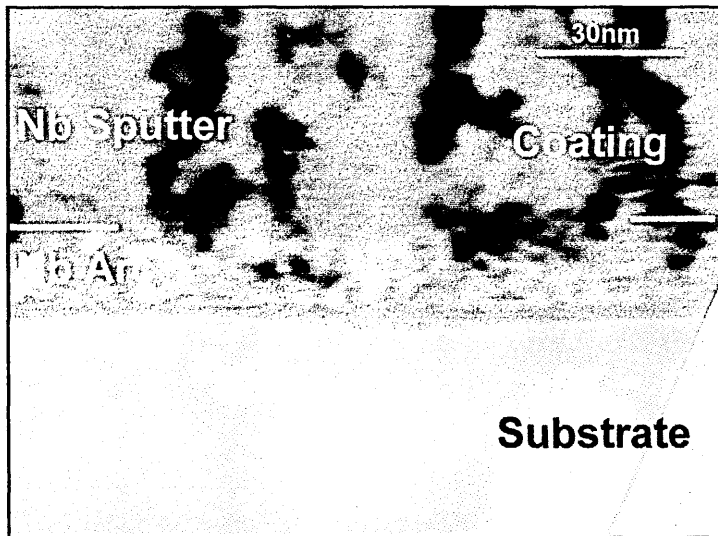
(b)  $U_{\text{bias}} = -1000\text{V}$



(c)  $U_{\text{bias}} = -800\text{V}$

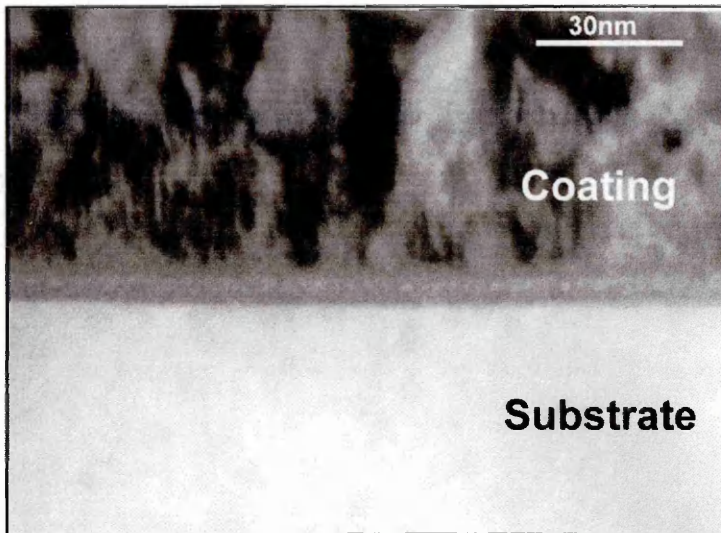


(d)  $U_{\text{bias}} = -600\text{V}$

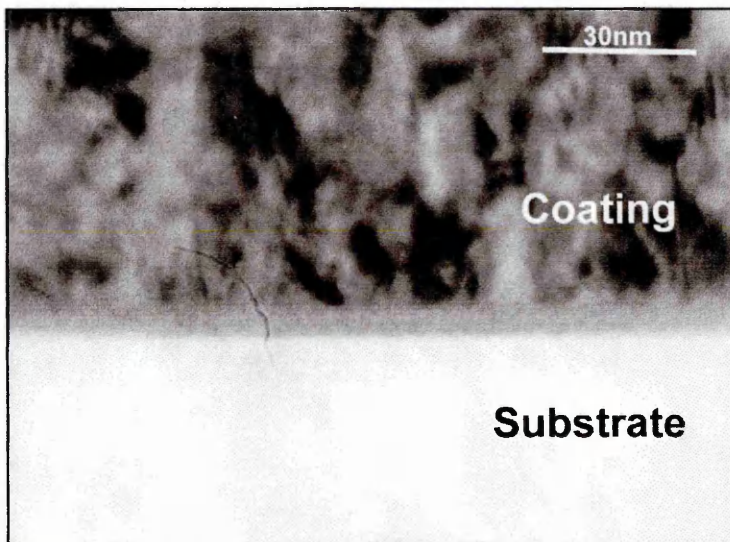


(f)  $U_{\text{bias}} = -400\text{V}$

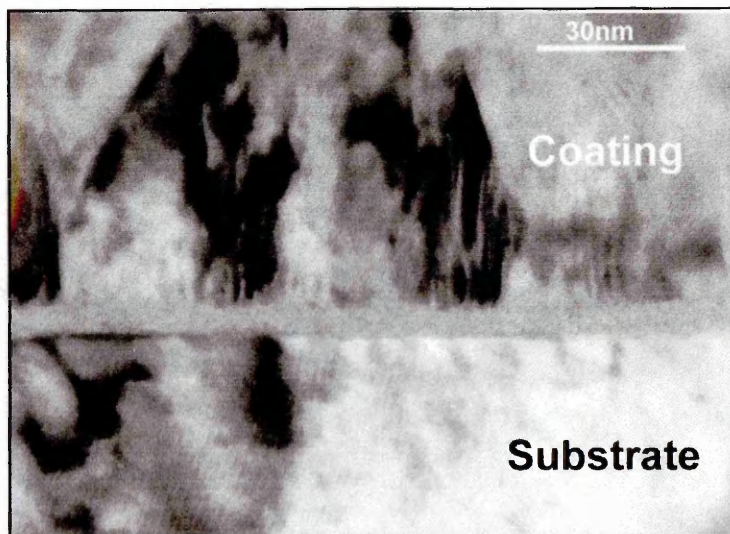
Fig. 4.20. X-TEM images of interfacial region ( $P=2.3 \cdot 10^{-3}$  mbar)



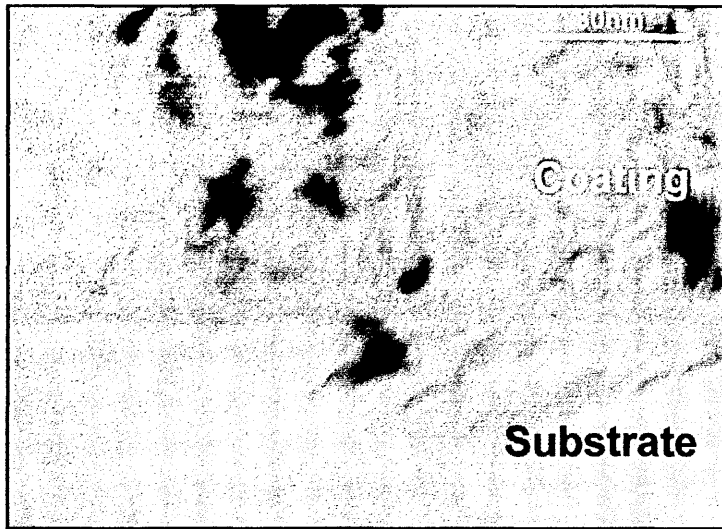
(a)  $U_{\text{bias}} = -1200\text{V}$



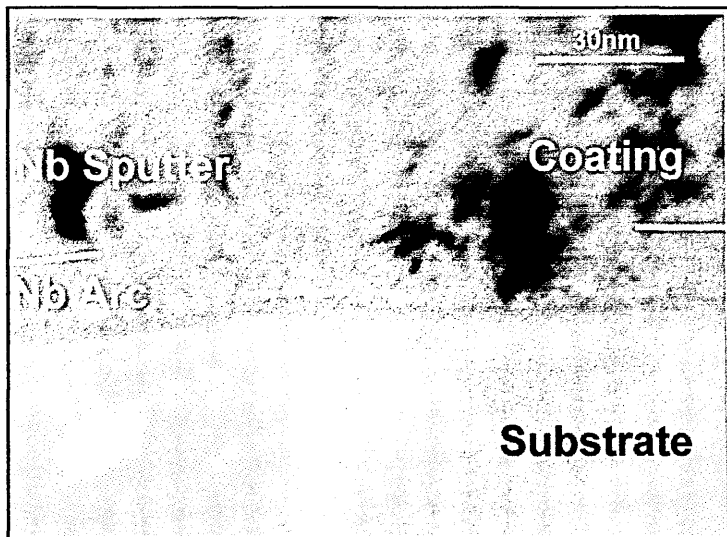
(b)  $U_{\text{bias}} = -1000\text{V}$



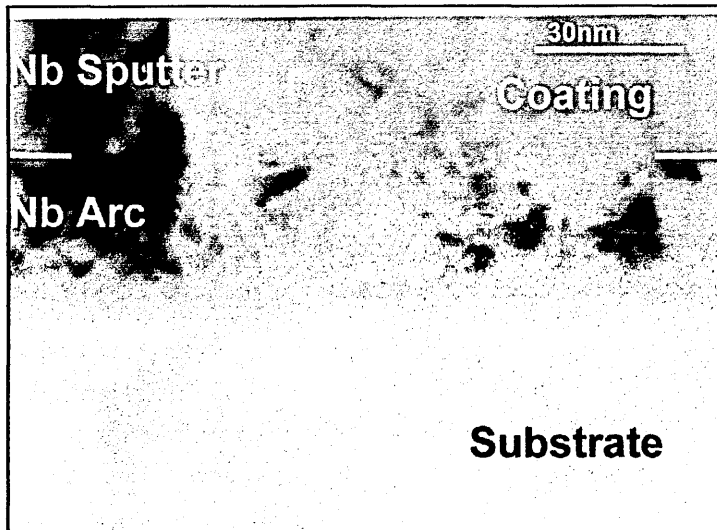
(c)  $U_{\text{bias}} = -800\text{V}$



(d)  $U_{\text{bias}} = -600\text{V}$



(e)  $U_{\text{bias}} = -400\text{V}$

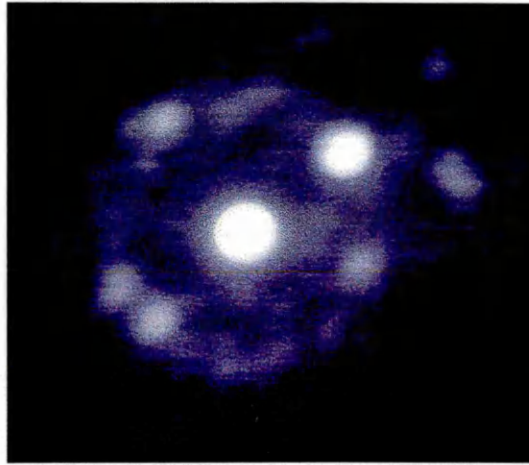


(f)  $U_{\text{bias}} = -200\text{V}$

Fig. 4.21. X-TEM images of interfacial region ( $P=8.3 \cdot 10^{-4}$  mbar)



(a) thicker area



(b) thinner area

Fig. 4.22. Convergent-beam/ selected area diffraction pattern of interface region ( $U_{\text{bias}}=800\text{V}$ ,  $P=8.3 \cdot 10^{-4}$  mbar)

As mentioned previously, the samples produced with bias voltages of -600V to -1200V all show the amorphised layer, grown under the impact of the heavy, energetic Nb ions. However, it can be seen from fig.4.23. that the apparent thickness of this modified region is dependent on the ion energies and the working gas pressure. The layer thickness generally decreases with decreasing ion energy; only in the higher pressure series no change was observed between substrate bias voltages of -800V and -1200V. The thickness appears to be greater overall when the lower etching pressure was used, especially at higher ion energies.

The amorphised layer is still present with a thickness of 3nm when using a bias voltage of -400V as can be seen from the dark ribbon in figures 4.20.(e) and 4.21.(e). However, there is also evidence of an additional layer of deposited Nb top of the dark ribbon,

identified as “Nb arc” on the micrographs. This layer is approximately 15nm thick and is characterised by a disrupted, fine-grained structure, grown during the etching stage under lower energetic ion bombardment, i.e. 1.2keV. This deposition layer increases in thickness when the ion energies are further decreased to 0.6keV i.e. using a substrate bias voltage of -200V (fig. 4.21.f). The Nb deposition layer now extends approximately 30nm into the coating and is again of a fine-grained nature. The interface is less sharp and there is no evidence of the typical sharp ribbon characterising the amorphised layer at the substrate/ coating interface.

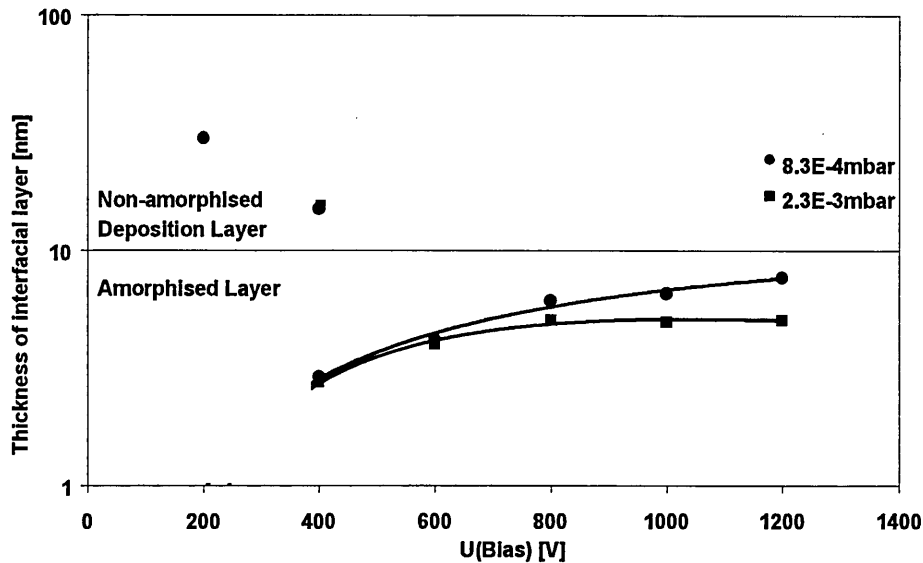
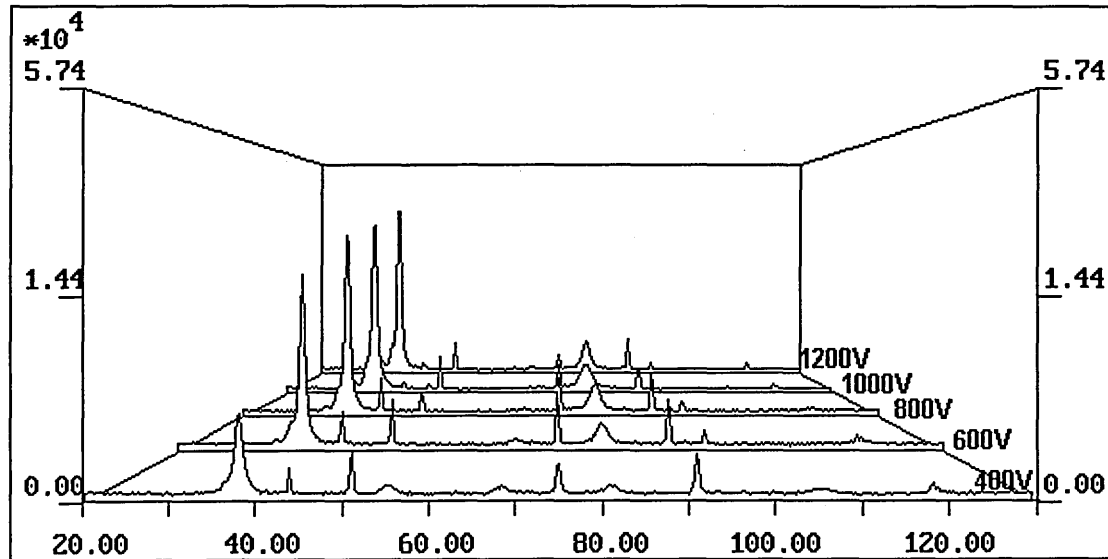


Fig. 4.23. Apparent thickness of interface layer

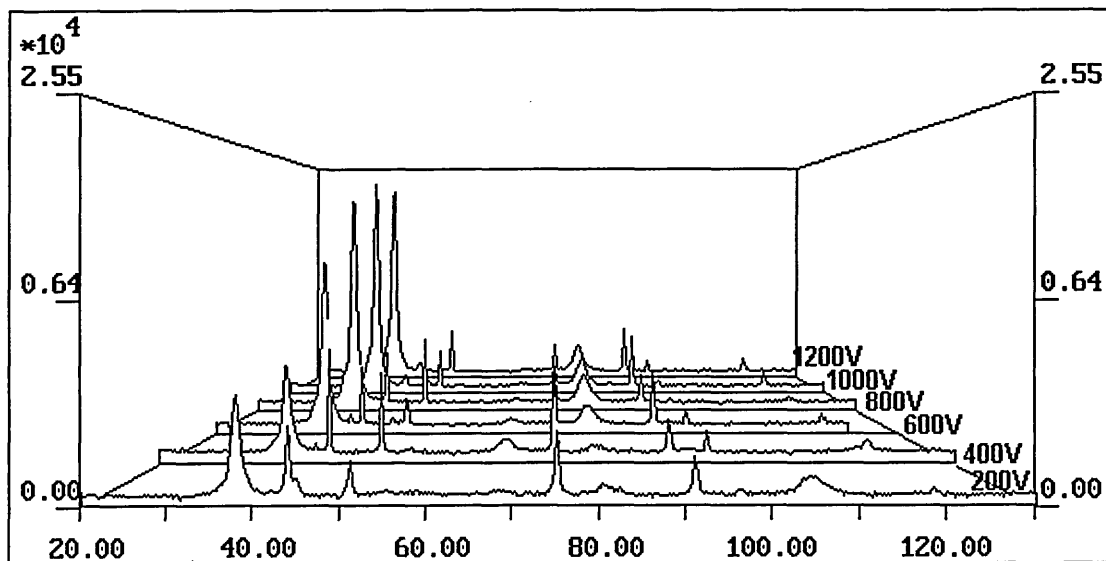
#### 4.1.4.2. Texture

High angle XRD traces of the coatings are shown in fig.4.24. The corresponding texture values are given in figure 4.25. All coatings deposited after ion etches using bias voltages in the range of -600V to -1200V show a very pronounced {110} preferred orientation with texture values ranging from  $P = 5.9$  ( $U_{\text{bias}} = -600\text{V}$ ) to  $P = 6.0$  ( $U_{\text{bias}} = -1200\text{V}$ ). This strong texture can be observed in both series, i.e. at low- and high etching pressures. Lower substrate bias voltages during the etching stage lead to a significant change in the preferred orientation of the coatings. In the case of  $U_{\text{bias}} = -400\text{V}$ ,  $P = 2.3 \times 10^{-3}$  the crystallographic orientation is defined by a major {110} ( $P = 2.9$ ) and a minor {111} ( $P = 2.1$ ) texture component. When the substrate bias voltage is further reduced to -200V ( $P = 8.3 \times 10^{-4}$  mbar) the {111} texture component becomes

dominant with a texture parameter of  $P = 4.4$ . The coating deposited after ion etching at  $U_{\text{bias}} = -400\text{V}$ ,  $P = 8.3 \times 10^{-4}$  does not follow this trend but rather shows a more mixed distribution of crystallographic planes. However, despite that exception, it seems that the UBM coatings deposited onto a deposition layer, which was generated during low-energy Nb ion etching (i.e. substrate bias voltages of  $-200\text{V}$  and  $-400\text{V}$ ), tend to shift from a  $\{110\}$  to a  $\{111\}$  preferred orientation.

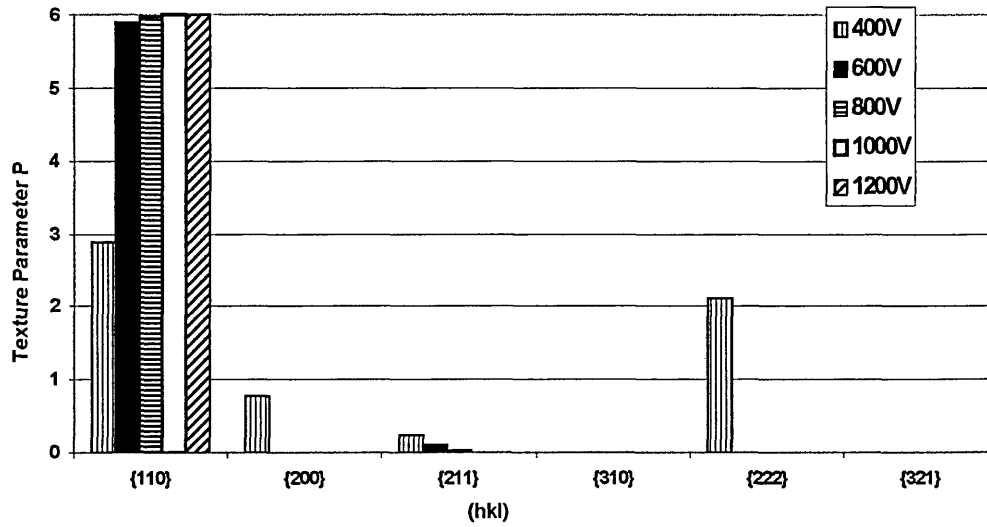


(a)  $P = 2.3 \times 10^{-3}$  mbar

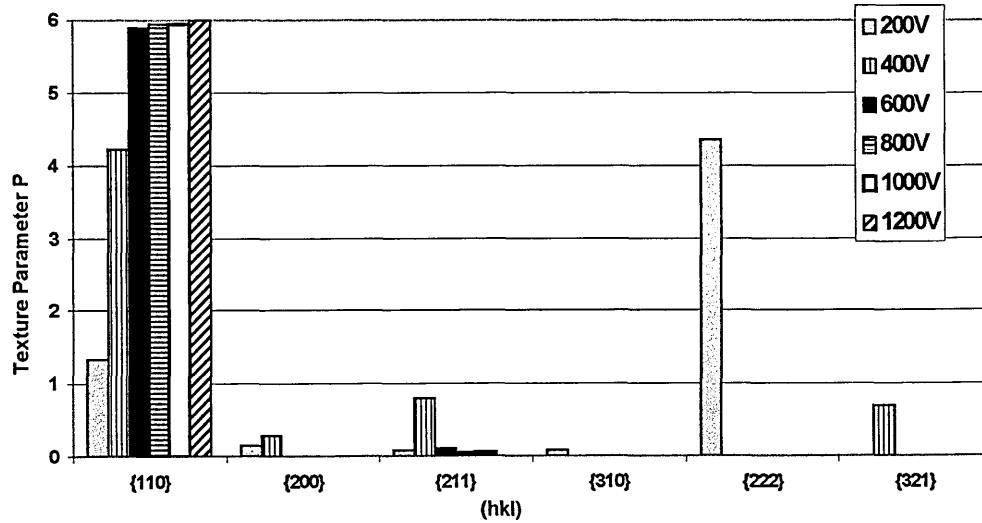


(b)  $P = 8.3 \times 10^{-4}$  mbar

Fig. 4.24. High angle XRD traces



(a)  $P=2.3 \times 10^{-3}$  mbar



(b)  $P=8.3 \times 10^{-4}$  mbar

Fig. 4.25. Texture values

#### 4.1.4.3. Corrosion Resistance

A potentiodynamic polarisation scan of one coated sample ( $U_{\text{bias}} = -800\text{V}$ ,  $P=8.3 \times 10^{-4}$  mbar), is shown representatively in fig.4.26. It can be seen from the polarisation curve that, despite a coating thickness of only 300nm, the corrosion or pitting resistance is greatly improved compared with uncoated stainless steel (section 4.1.1.4.). The sample

passivates and the pitting potential is raised to around +1000mV (+200mV for uncoated stainless steel) The anodic current density is similar to that of bulk Nb with a value of  $\approx 3 \cdot 10^{-6} \text{ Acm}^{-2}$ , as opposed to the maximum recordable current density of  $10^{-1} \text{ Acm}^{-2}$  for stainless steel. The corrosion results obtained from the remaining samples are summarised by comparing the pitting potentials and the anodic current densities taken at +700mV (fig. 4.27.). It can be seen that generally the corrosion behaviour is improved for all samples compared to uncoated stainless steel.

However, the corrosion resistance strongly differs with pitting potentials ranging from +300mV to +1050mV and anodic current densities ranging from  $10^{-4} \text{ Acm}^{-2}$  to  $10^{-6} \text{ Acm}^{-2}$ . There is a surprisingly strong influence of the ion energy, i.e. substrate bias voltage, during Nb ion etching prior to coating deposition on the corrosion performance of the coating/ substrate system. The best corrosion resistance, i.e. passivation up to more than +1000mV and current densities approaching  $10^{-6} \text{ Acm}^{-2}$ , is achieved with “medium” bias voltages i.e. -600V and -800V. The corrosion or pitting resistance is significantly reduced when using bias voltages at the low and high end of the employed scale, i.e. substrate bias voltages of -200V, -400V and -1000V, -1200V. This tendency, i.e. the influence of the etching bias voltage, can be observed for both sample series, i.e. at high and low etching pressure, while the etching pressure itself does not seem to have any significant influence on the corrosion resistance of the substrate/ coating systems.

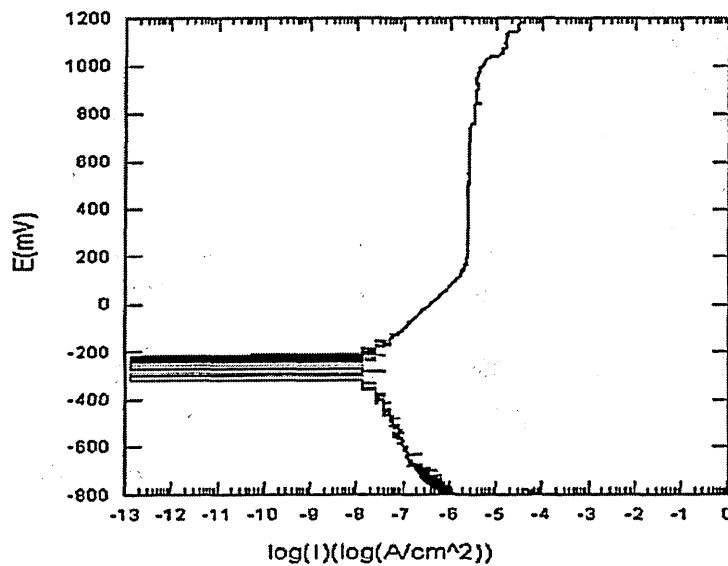
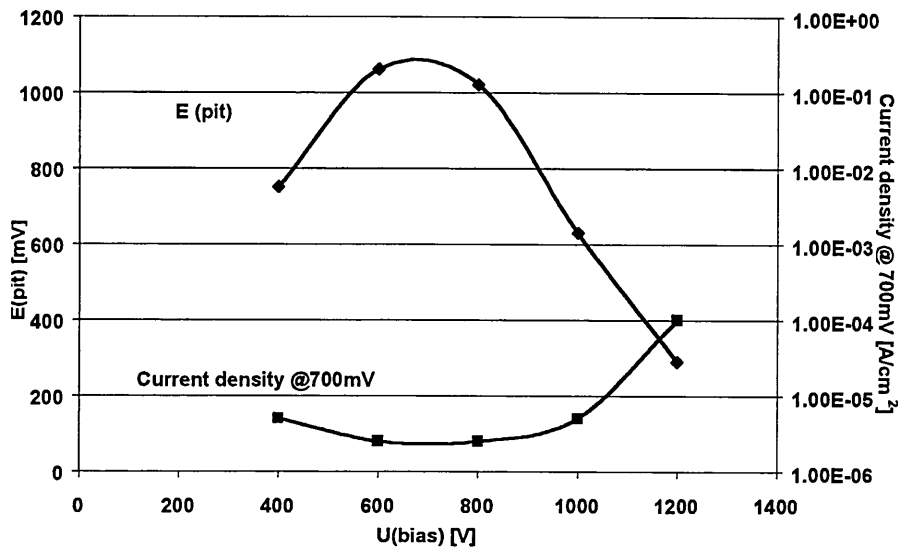
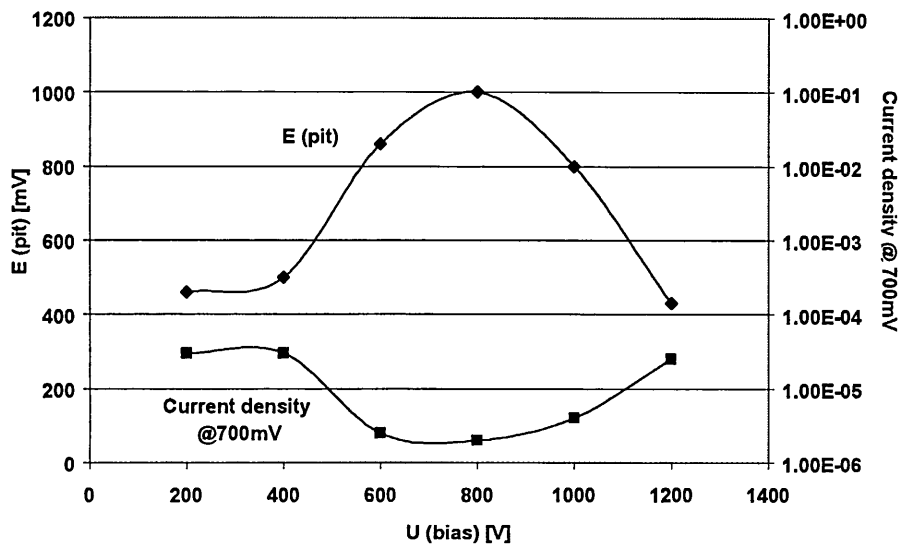


Fig. 4.26. Potentiodynamic polarisation curves in 3% NaCl ( $U_{\text{bias}}=800\text{V}$ ,  $P=8.3 \cdot 10^{-4}$  mbar)



(a)  $P = 2.3 \cdot 10^{-3}$  mbar



(b)  $P = 8.3 \cdot 10^{-4}$  mbar

Fig. 4.27. Pitting potentials and anodic current densities

In the case of substrate material that was etched applying bias voltages in the range of -400V to -1200V, with no additional coating, a surprisingly similar behaviour can be observed. A polarisation scan of one etched sample ( $U_{\text{bias}} = -600\text{V}$ ) is shown representatively in fig.4.28.

The results are again summarised by means of the pitting potentials and the anodic current densities (@+700mV) shown in figure 4.29. The bombardment with Nb ions from the cathodic arc source significantly improves the pitting resistance of the stainless steel. The corrosion behaviour in the polarisation test is very similar to that of the

samples with an additional Nb sputter coating as discussed above. The pitting potentials are raised to values of +600mV to +1100mV compared with +200mV for untreated stainless steel. The current densities in the anodic region are in the range of  $4 \cdot 10^{-4} \text{ Acm}^{-2}$  to  $1.5 \cdot 10^{-6} \text{ Acm}^{-2}$ . Again, there is a significant influence of the ion energy of the Nb ions on the corrosion performance. In a similar manner to the samples with an additional Nb film, the highest corrosion resistance is achieved with “medium” substrate bias voltages i.e. -600V and -800V. The performance deteriorates slightly using a substrate bias voltage of -400V and considerably when using -1200V.

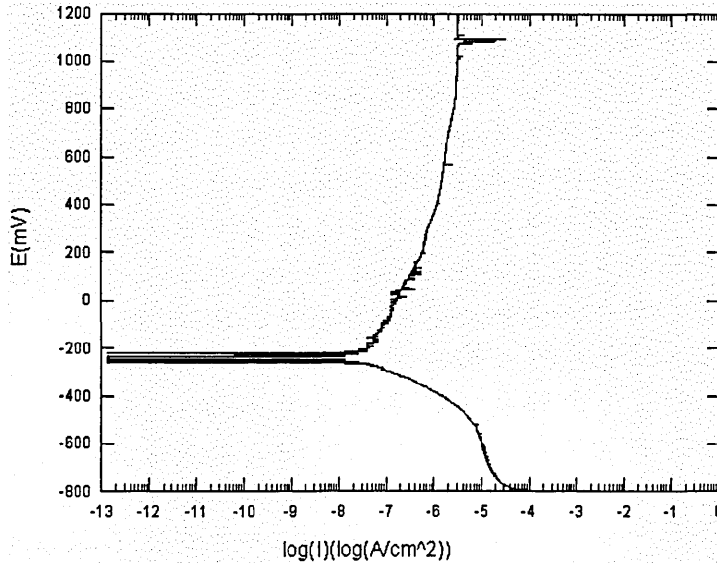


Fig.4.28. Potentiodynamic polarisation curves in 3% NaCl ( $U_{\text{bias}} = -600\text{V}$ )

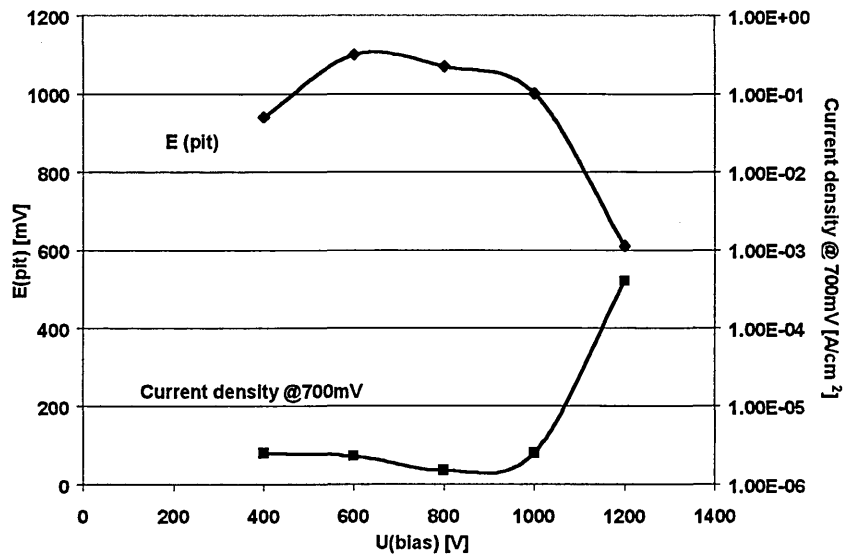


Fig. 4.29. Pitting potentials and anodic current densities

### 4.1.5. Intermediate Nb Ion Etching

The following paragraph summarises results obtained from Nb coatings that were subjected to two “intermediate” Nb ion etches during sputter deposition using substrate bias voltages of -1200V and -600V respectively as described in 3.2.2.(V).

#### 4.1.5.1. Physical Properties

The thickness of both films is approximately 1.3 $\mu\text{m}$  indicating no significant re-sputtering of Nb during the etching steps. The microhardness values are  $\text{HK}_{0.003} = 1010$  ( $U_{\text{bias}} = -1200\text{V}$  during intermediate etching steps) and  $\text{HK}_{0.003} = 980$  ( $U_{\text{bias}} = -600\text{V}$  during intermediate etching steps). These values are nearly double as high as that of the same coating deposited without intermediate etching steps ( $\text{HK}_{0.003} = 600$ , section 4.1.1.1.). Surface roughness values are  $R_a = 0.063\mu\text{m}$  (-1200V) and  $R_a = 0.087\mu\text{m}$  (-600V) respectively.

#### 4.1.5.2. Microstructure

Cross-sectional TEM images are shown in fig.4.30. Both films exhibit competitive growth and a coarse columnar morphology with average column diameters of approximately 80nm (measured at 0.5 $\mu\text{m}$  from the substrate/ coating interface), which is larger than the value of 65nm obtained for the same coating deposited without intermediate etching (fig.4.2.(a)). The bombardment of the Nb film with highly energetic Nb ions creates two discrete zones visible throughout the cross-sections. In the case of ion energies of 3.6keV (i.e.  $U_{\text{bias}} = -1200\text{V}$ ), this zone is characterised by a relatively sharp ribbon with a thickness of approximately 10nm. Using ion energies of 1.8keV (i.e.  $U_{\text{bias}} = -600\text{V}$ ) leads to the formation of a less sharp, diffuse modified area with a thickness of a few tens of nm, visible as a lighter band in the TEM images. In both cases, the nature of the modified areas appears different from the amorphised layers created at the substrate/ coating interface during bombardment with Nb ions from the cathodic arc (fig.4.20. and 4.21.) The columnar structure of the sputtered coatings is not interrupted by the intermediate etching stages but continuous growth of the columns through the modified layers can be observed and even some broadening of the columns appears to take place, especially in the case of  $U_{\text{bias}} = -600\text{V}$ .

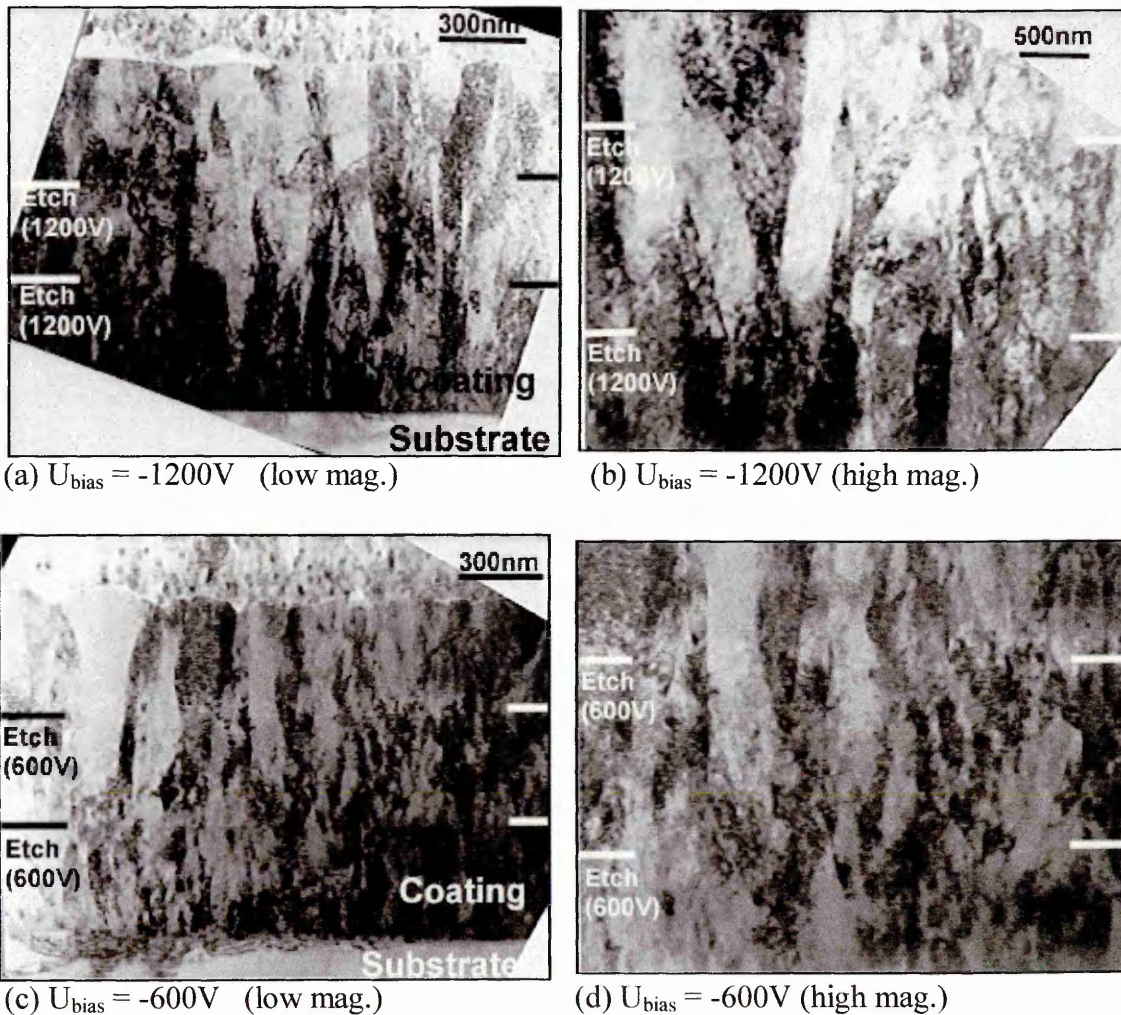


Fig. 4.30 Cross-sectional TEM images

#### 4.1.5.3. Crystallographic Structure

High angle XRD traces of the two coatings are shown in fig.4.31. For reasons of comparison, the diffraction pattern of the same coating deposited without intermediate etching steps is also presented (section 4.1.1.3.). The reflections of the two coatings with intermediate etches (fig.4.31. (a) and (b)) appear broad and asymmetric compared to that without intermediate etches. The FWHM (Full Width/ Half Maximum) values of the  $\{110\}$  reflections were measured as 0.672 (intermediate etch,  $U_{\text{bias}} = -600\text{V}$ ), 0.970 (intermediate etch,  $U_{\text{bias}} = -1200\text{V}$ ) and 0.454 (no intermediate etch).

Fig.4.32. shows a glancing angle diffraction pattern of the  $\{200\}$  reflection of two different coatings, i.e. intermediate etch at  $U_{\text{bias}} = -1200\text{V}$  and no intermediate etch. The asymmetric peak of the intermediately etched coating can be deconvoluted into two

components, with the lattice parameter of the 'a' axis almost identical to that of the Nb bcc plane without intermediate etching. This may suggest the presence of a second, tetragonal phase in the Nb films, which causes the asymmetry of the reflection peaks. As a consequence of this, accurate determination of texture and residual stresses was not possible.

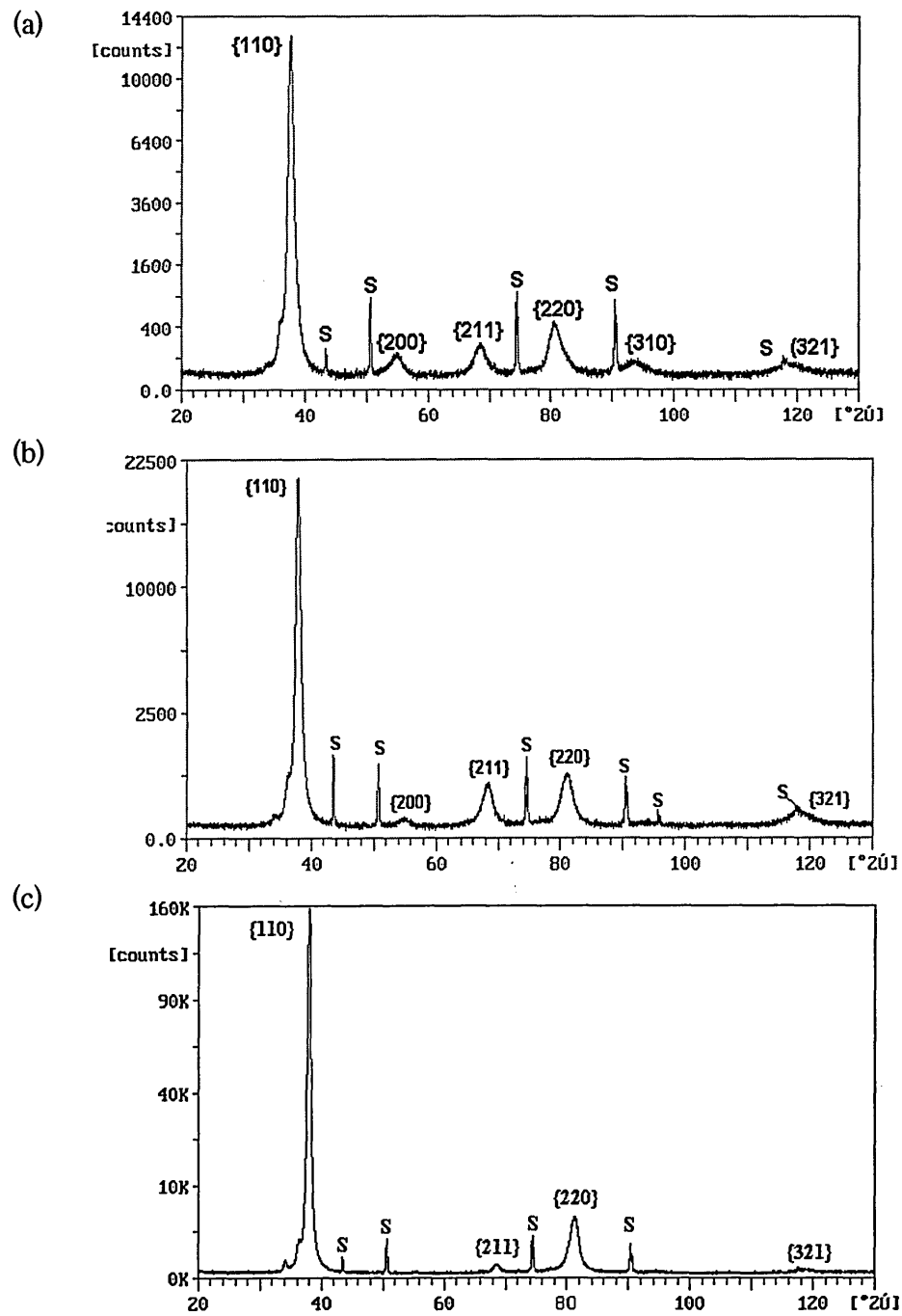


Fig. 4.31. High angle XRD traces: Intermediate etch  $U_{\text{bias}} = -1200\text{V}$  (a); Intermediate etch  $U_{\text{bias}} = -600\text{V}$  (b), No intermediate etch (c)

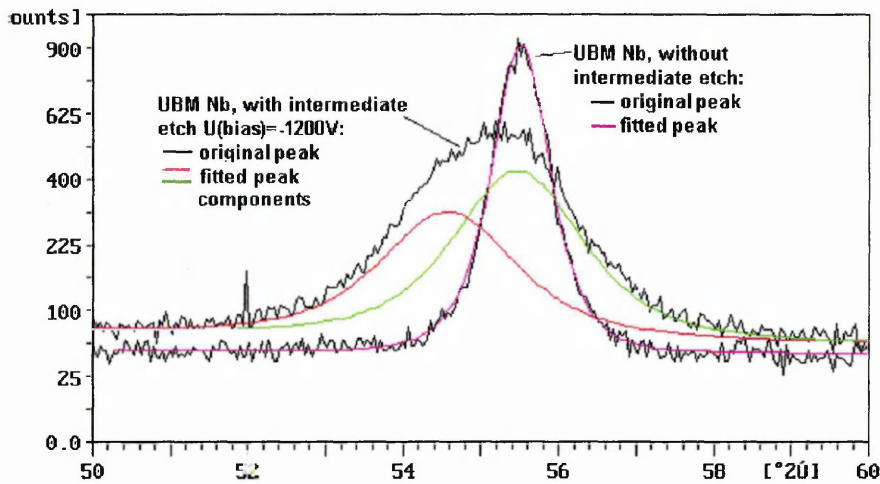


Fig.4.32. Peak fitting of the {200} reflection; GD-XRD with incidence angle = 0.5°

#### 4.1.5.4. Corrosion Resistance

Potentiodynamic polarisation curves of the two coated samples are shown in fig.4.33. Both Nb coatings are characterised by low anodic current densities similar to the Nb coating deposited without any intermediate etching steps (figure 4.6.(b)). The coating, which was subjected to intermediate etches using a bias voltage of -600V, exhibits passivation throughout the range of the scan and fully protects the stainless steel substrate. The sample produced with intermediate etches using a bias voltage of -1200V shows some metastable pitting at around +300mV indicated by the increase in current density. However, the pitting is only minor and does not result in any severe corrosive attack of the substrate. The current density stabilises immediately and tends towards a value of  $10^{-5} \text{ Acm}^{-2}$ .

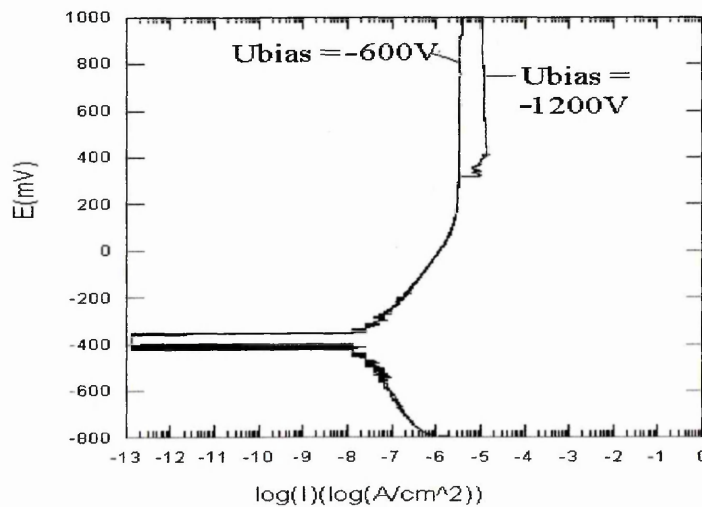
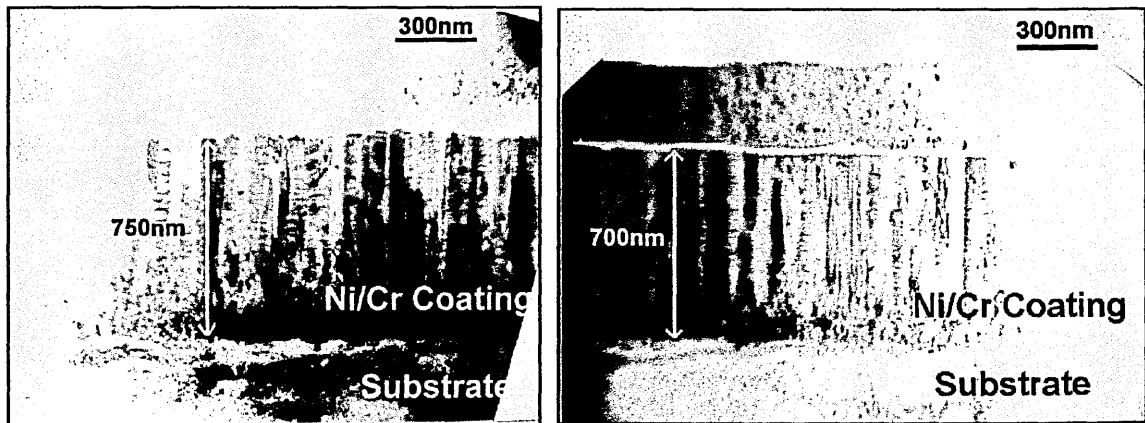


Fig. 4.33 Potentiodynamic polarisation in 3% NaCl

### 4.1.6. Etching Rate

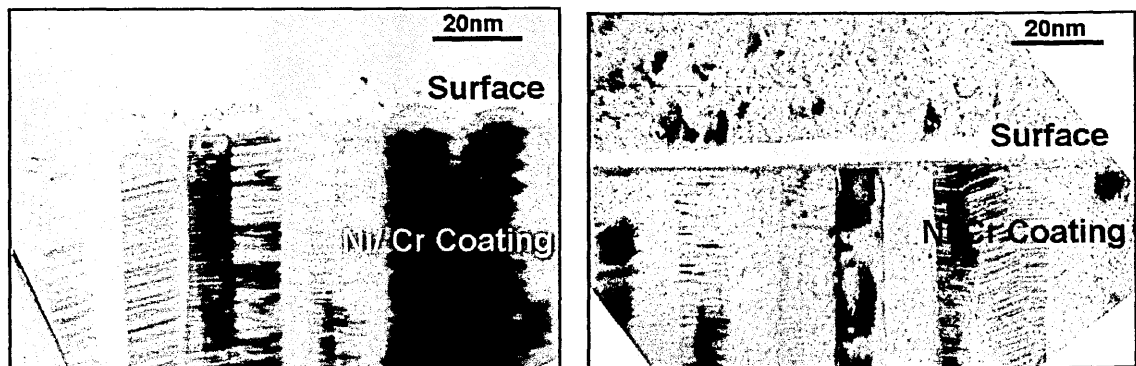
Stainless steel was coated with a UBM NiCr coating. One half of the coating was subsequently masked and the whole sample was subjected to a Nb ion etch using a substrate bias voltage of  $-1200\text{V}$  as described in 3.2.2.(VI).

Fig. 4.34. shows cross-sectional TEM images of the masked, i.e. non-etched coating area, and of the unmasked, i.e. etched coating area.



(a) Non-etched coating

(b) Etched coating



(c) Non-etched coating (Surface)

(d) Etched coating (Surface)

Fig.4.34. X-TEM images

Comparison of the coating thickness of the etched and the non-etched coating area, shown in fig.4.34.(a) and (b), reveals that bombardment of the Ni/Cr layer with Nb ions from the cathodic arc source lead to removal or sputtering of only  $\approx 50\text{nm}$  of coating material. This yields an etching rate of approximately  $4 \text{ nm} \cdot \text{min}^{-1}$  using a substrate bias voltage of  $-1200\text{V}$ . The higher magnification images in fig.4.34. (c) and (d) show, that

the impact of the Nb ions led to preferential sputtering of the faceted column tops resulting in a significant “smoothing” effect of the coating surface.

The high magnification image in fig.4.35. shows the presence of a thin layer on the surface of the Nb ion etched coating, which is not present on the untreated, i.e. non-etched coating surface. The layer is approximately 8nm in thickness and apparently of a highly disrupted or possibly amorphised nature, similar to the interfacial layer generated during Nb ion etching of stainless steel substrate as shown in fig.4.20.(a) and fig.4.21(a). In both cases, the layer is generated under the impact of the heavy, highly energetic Nb ions.

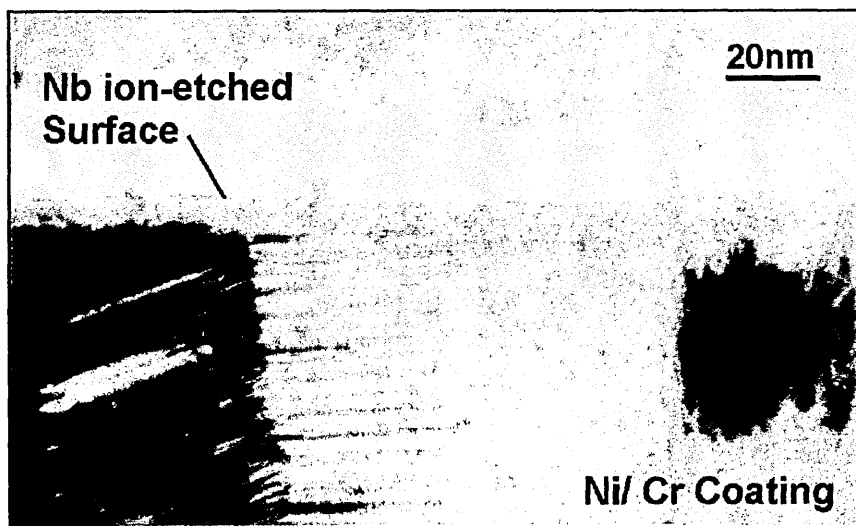


Fig. 4.35. Surface layer generated during Nb ion bombardment

## **4.2. Niobium Coatings on Brass Substrates**

The following section summarises results obtained from Nb-based coating systems on brass materials as described in 3.2.2.(VII) to (IX) with respect to their corrosion resistance.

### **4.2.1. Substrate Ion Etch**

The substrate material, polished brass coupons, was subjected to a Nb ion etch using a bias voltage of -600V with no additional coating. The corrosion performance is compared to untreated brass by potentiodynamic polarisation curves shown in figure 4.36. The corrosion potential of untreated brass is -220mV. The peak in current density at around -50mV is associated with the formation of a protective layer of copper oxide, i.e. Cu<sub>2</sub>O. The passive oxide layer, visible as a red tarnish on the sample, reduces the corrosion rate i.e. the anodic dissolution of Cu and Zn, and the current density tends towards a value  $10^{-2} \text{ Acm}^{-2}$ .

Bombardment of brass with Nb ions from the cathodic arc source did not improve the corrosion performance, as it did for stainless steel (fig.4.28.). The polarisation curve is almost identical with that of untreated brass and the sample as well is characterised by the typical dark surface film after the polarisation measurement associated with the formation of copper oxide.

As the treatment of the brass with Nb ions did not yield any improvement in the corrosion resistance, the subsequent experiments were carried out using Ar ion etching for the substrate sputter cleaning process.

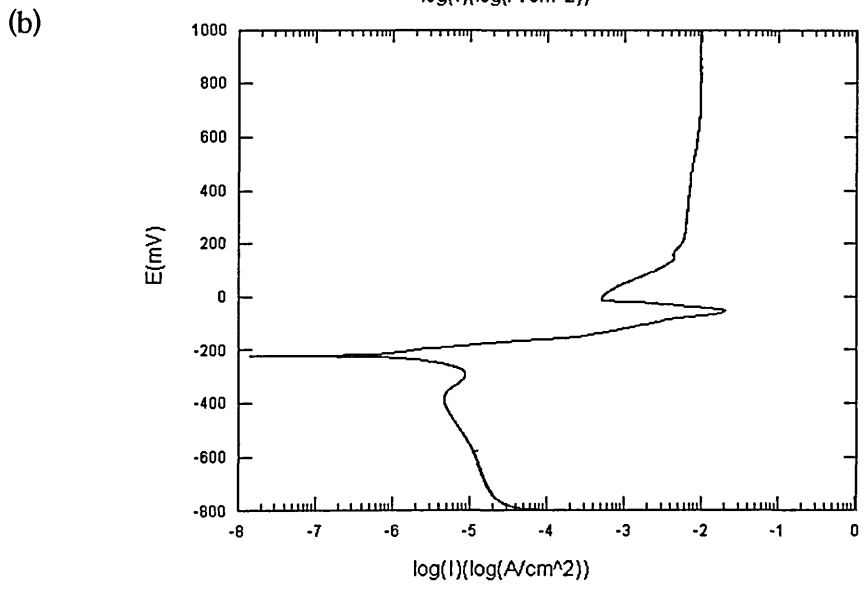
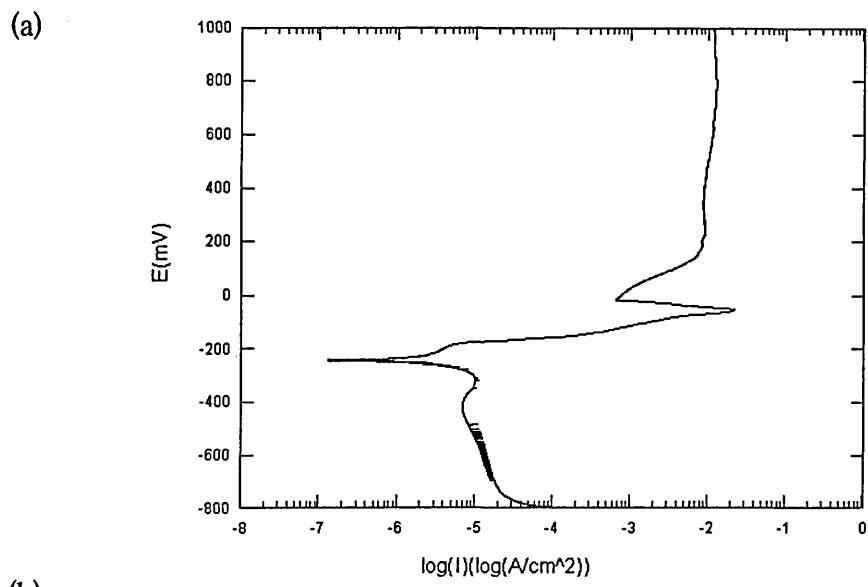


Fig. 4.36. Polarisation in 3% NaCl: Untreated brass (a); Nb ion etched brass (-600V) (b)

#### 4.2.2. Zn-Diffusion Barrier

Brass coupons were coated with three different Zn diffusion-barrier layers, i.e. CuAlFe (a), CuAlFe + NiCr (b) and Cu (c), followed by a Nb top coating as described in 3.2.2.(VIII). The coating thicknesses are approximately 1.0 $\mu\text{m}$  for CuAlFe and Cu, 0.8 $\mu\text{m}$  for NiCr and 1.3 $\mu\text{m}$  for Nb. The corrosion resistance is investigated by potentiodynamic polarisation measurements (fig. 4.37.) SEM cross-sectional images of the samples after the corrosion test are shown in fig. 4.38.

The corrosion resistance is improved for all three coating systems in comparison with uncoated brass. The “shape” of the polarisation curves between  $E_{\text{corr}}$  and  $-50\text{mV}$  is similar to that bulk Nb. At this potential however, there is again a distinctive peak in current density indicating the formation of copper oxide and hence the exposure of the Cu-based diffusion barrier and/or the brass substrate through pores or defects in the Nb coating as well as through the NiCr layer in case of fig.4.37.(b). The corrosion performance, as indicated by the anodic current densities, is strongly influenced by the type of diffusion barrier. In the case of CuAlFe as the intermediate layer, the current density starts to increase at  $+400\text{mV}$  and reaches a value of  $10^{-3} \text{ Acm}^{-2}$  ( $+700\text{mV}$ ). This is related to severe anodic dissolution of the CuAlFe diffusion barrier as well as the brass substrate resulting in “uplifting” of the Nb film as can be seen from the SEM image in fig. 4.38.(a).

The addition of a NiCr layer on top of the CuAlFe layer improves the corrosion resistance as indicated by the reduced current density ( $\approx 8 \cdot 10^{-5} \text{ Acm}^{-2}$   $+700\text{mV}$ ). However, the CuAlFe layer as well as the brass substrate is still attacked as shown in fig. 4.38.(b). The SEM image suggests preferential dissolution of the CuAlFe layer while the NiCr layer remains partially intact.

A substantial improvement in the corrosion resistance is obtained when Cu is used as the diffusion layer. Above  $+100\text{mV}$  the anodic current density remains low and constant with a value of around  $2 \cdot 10^{-5} \text{ Acm}^{-2}$ . The corrosive attack is reduced to some localised pitting with no severe dissolution of the Cu layer or the brass substrate. However, the Nb coating does not fully passivate and protect the substrate as it did on stainless steel substrates.

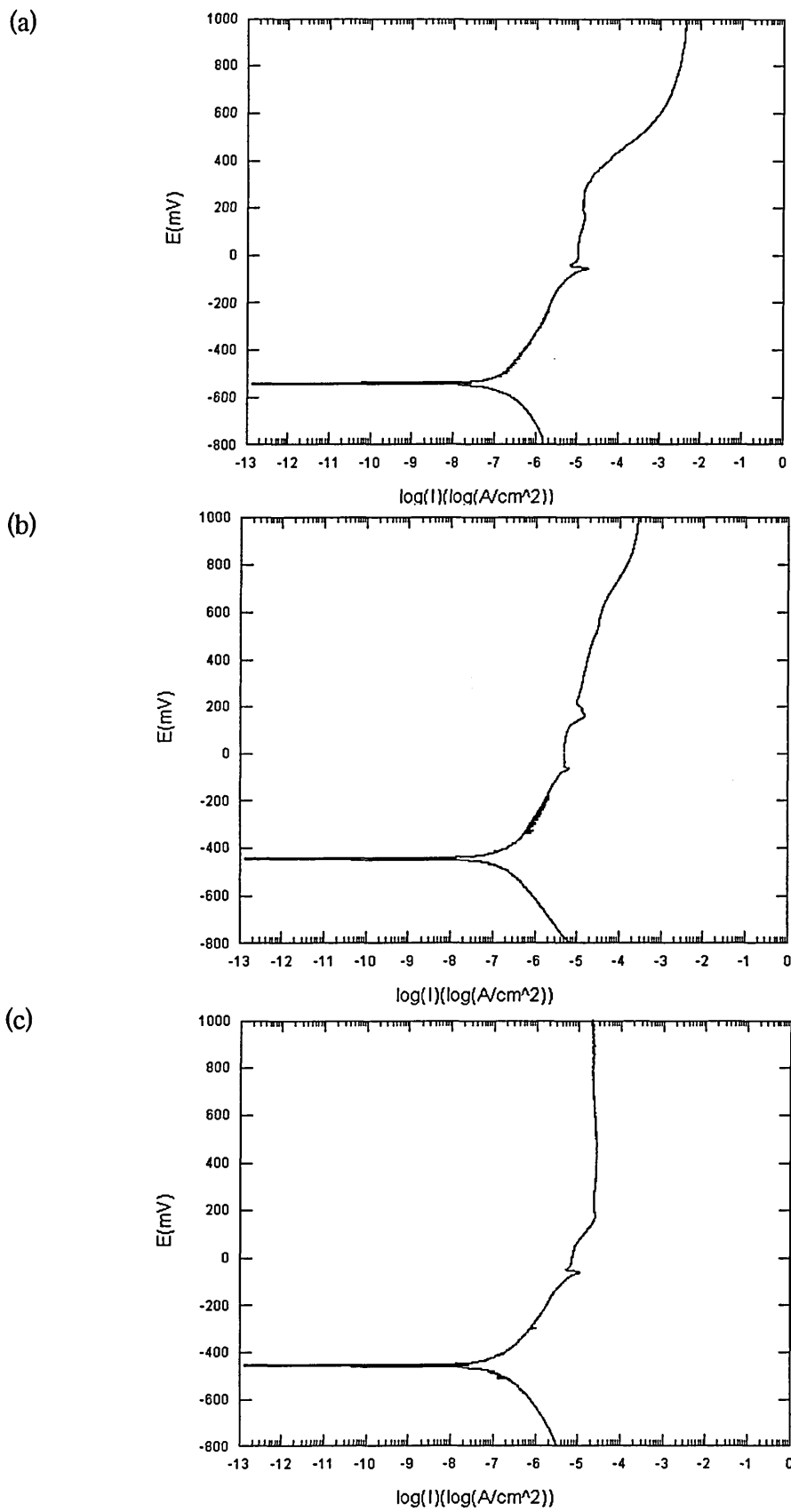
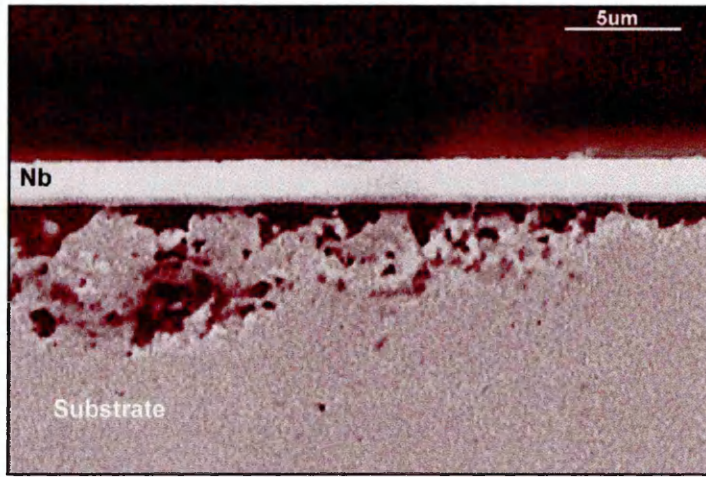
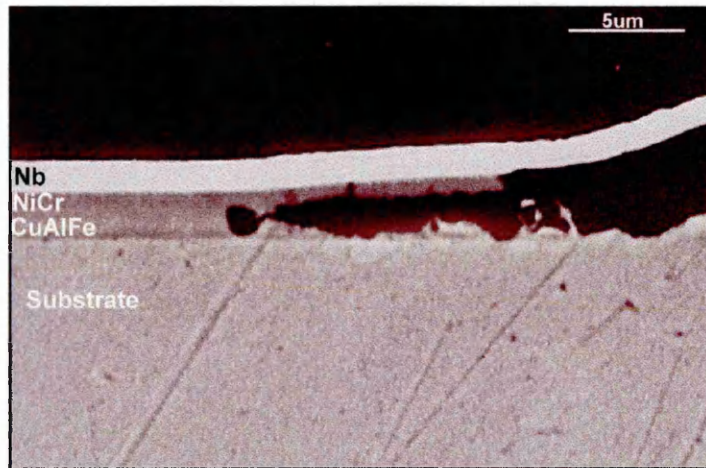


Fig.4.37. Polarisation in 3% NaCl: CuAlFe (a), CuAlFe + NiCr (b), Cu (c)

(a)



(b)



(c)

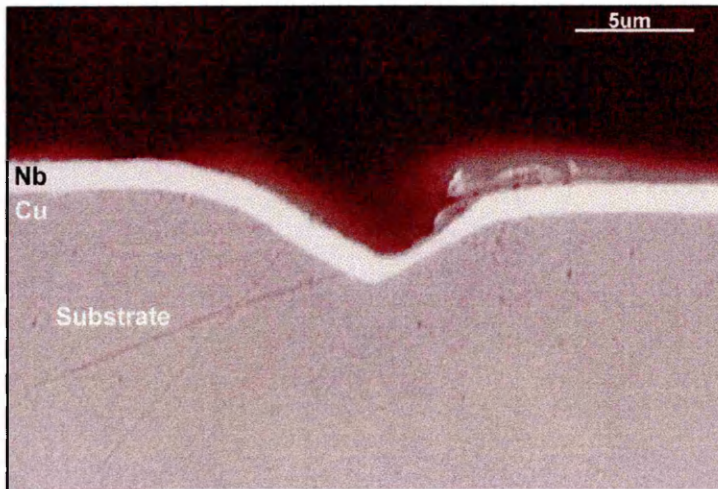


Fig.4.38. Cross-sectional SEM of coated samples after polarisation in 3%NaCl: CuAlFe (a), CuAlFe + NiCr (b), Cu (c)

### 4.2.3. Intermediate Nb Ion Etching

The Cu diffusion barrier was subjected to a Nb ion etch, using a bias voltage of -600V, prior to deposition of the Nb layer as described in 3.2.2.(IX). The polarisation curve is shown in fig.4.39.

The corrosion potential as well as the “shape” of the polarisation curve up to -50mV show similarities to uncoated brass or Cu indicating a higher degree of exposure of the Cu layer in the initial stages of the scan compared to the coating with no intermediate etching step (fig.4.37.(c)), probably caused by an increase in the number of growth defects from droplet generation during the etching stage. However, the current density in the anodic region as well the number and sizes of pits after the corrosion test is very similar to the coating with no intermediate etch. This indicates that there is no significant influence on the corrosion performance of the coating system Cu/ Nb on brass by bombardment of the Cu layer with Nb ions from the cathodic arc source.

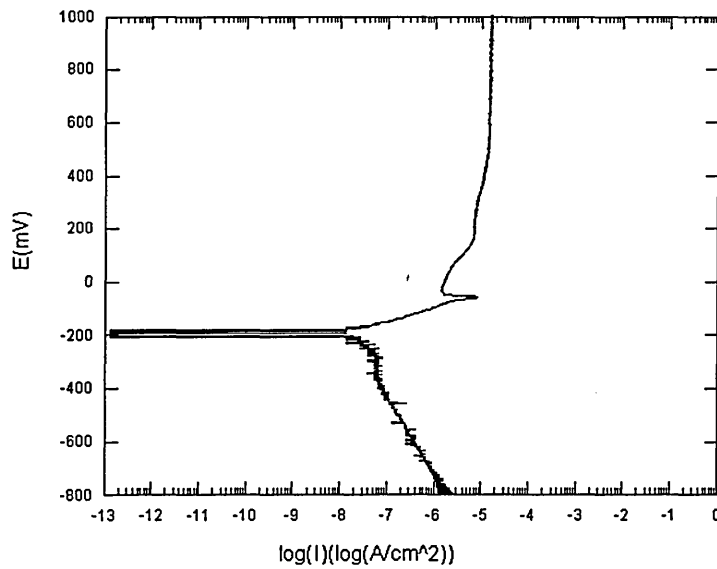


Fig.4.39. Polarisation in 3% NaCl

## 4.3. Industrial Applications

### 4.3.1. Niobium Coatings on Stainless Steel Substrates

The corrosion performance of the “optimised”, 1.3 $\mu\text{m}$  thick, PVD Nb coating (i.e. Nb ion etch/ low temperature UBM deposition) is compared to commercially available, standard hard chrome and electroless nickel coatings with a coating thickness of 25 $\mu\text{m}$ . All three coatings are deposited on polished 304 stainless steel substrates. Potentiodynamic polarisation curves are shown in fig.4.40. The chromium coating behaves similarly to bulk chromium and exhibits passivity over a range of approximately 1100mV with a low anodic current density of  $10^{-5}$  to  $10^{-6}$   $\text{Acm}^{-2}$ . However, at a potential of +750mV the increase in current density indicates the transpassive dissolution of the protective oxide film, i.e. active corrosion of the chromium coating. In the case of the electroless nickel-phosphorus coating, the relatively high anodic current density ( $10^{-2}$   $\text{Acm}^{-2}$  @+700mV) can be attributed to corrosive attack of the nickel coating, probably accompanied by the formation of nickel phosphate; rapid tarnishing of the coating surface was observed. The PVD Nb coating stays passive, i.e. protective throughout the range of the scan as described in 4.1.2.4.

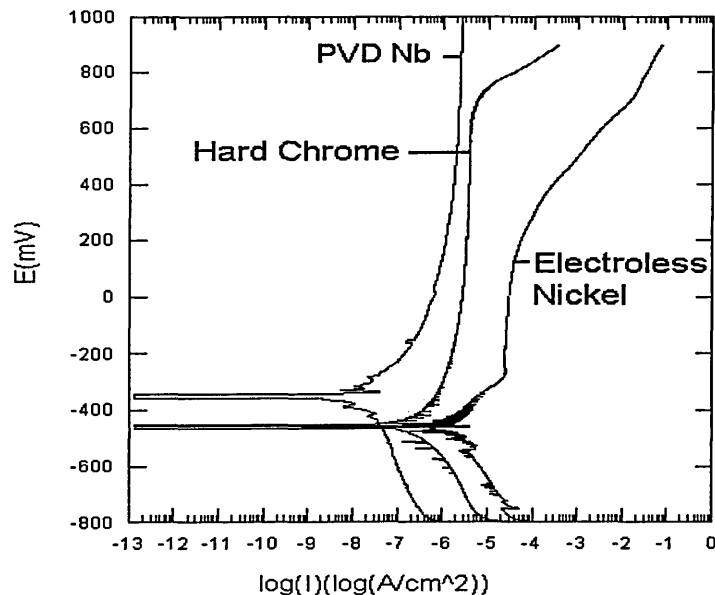


Fig. 4.40. Potentiodynamic polarisation curves in 3% NaCl solution

### 4.3.2. Niobium Coatings on Brass Substrates

The corrosion performance of the “optimised” PVD coating on brass (i.e. Ar ion etch/ UBM Cu layer/ UBM Nb top-coating) is compared to an electroplated Ni/ Cr coating with a coating thickness of approximately 10µm. This coating is used as a standard corrosion barrier coating for brass substrates and was supplied by A.T.Cross Ltd. Both films are deposited on the same polished brass coupons. The plated Ni/ Cr coating exhibits passivation up to +200mV with no apparent signs of copper oxide formation from the brass substrate, as would be indicated by a “peak” in current density at around -50mV. At +200mV however, passivity breaks down followed by a steep increase in anodic current density, which represents severe corrosive attack of the brass substrate and the Ni/ Cr coating itself. The Nb/ Cu sputter coated brass substrate behaves in a superior manner in the polarisation test with a low anodic current density and only minor pitting as described in 4.2.2.

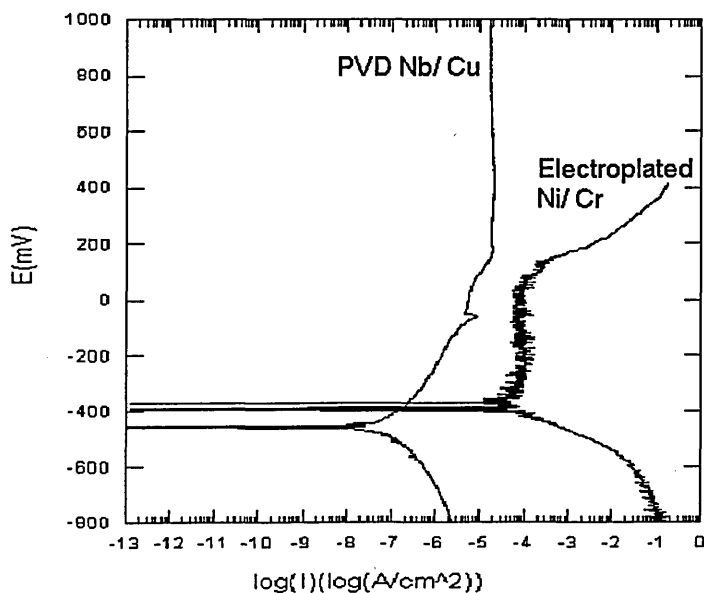


Fig.4.41. Potentiodynamic polarisation in 3% NaCl

The above PVD coating system was successfully deposited in a commercial production process at A.T.Cross Ltd. on brass pen barrels and pen caps, with and without an additional, approximately 0.4µm thick TiAlN top-coating. The coatings were tested in the company’s routine quality control test. The coated parts were reported to generally pass the corrosion tests, e.g. salt spray and artificial sweat tests.

## **5. Discussion**

### **5.1. Niobium Coatings on Steel Substrates**

#### **5.1.1. Corrosion Resistance/ Microstructure**

##### **5.1.1.1. UBM Coatings/ Interface Region**

As discussed previously in chapter 1, the high melting point of Nb is, in principle, regarded as a disadvantage in PVD, as it becomes increasingly difficult to produce dense film morphologies with decreasing homologous temperature. This effect is described by the structure zone models presented in section 2.5. With a homologous temperature  $T/T_M$  of 0.24 (deposition temperature  $T = 673\text{K}$ , melting point  $T_M = 2773\text{K}$ ), the traditional structure zone models, i.e. Thornton and Messier (fig.2.11), predict the development of zone 1 structures. This structure is characterised by an open columnar or porous film morphology arising from insufficient ad-atom surface mobility and dominant shadowing effects, which intrinsically can be detrimental for corrosion protection purposes, as it allows transfer of any corrosive medium to the substrate. As discussed later in this section, a passivated Nb coating will behave cathodically to most substrate materials including steel and brass, hence a small anode (exposed substrate material) to cathode (coating) surface area can result in severe corrosive attack of the substrate material. The corrosion results presented in literature [1]-[4] tend to confirm the predicted difficulties involved in the deposition of dense, corrosion resistant PVD Nb coatings.

The passive and protective corrosion behaviour of the initial UBM Nb coating (section 4.1.1., fig.4.6.) on stainless steel substrate was hence a rather surprising positive result. The polarisation measurements reveal an electrochemical behaviour similar to bulk Nb with no apparent influence, i.e. exposure, of the substrate material. With regards to literature on Nb coatings, such a behaviour has only been achieved by IBAD deposition of  $2.5\mu\text{m}$  thick Nb coatings under concurrent  $250\text{eV}$  Ar ion bombardment (section 2.3.3.1. [5]) and by vacuum plasma spraying of Nb coatings with a thickness of  $250\mu\text{m}$  (section 2.3.3.1. [6]), i.e. involving deposition under relatively high ion bombardment or by deposition of very thick coatings.

From these results it was initially concluded that the high degree of ionisation during UBM deposition was sufficient to produce Nb coatings of a dense, protective structure. This seemed to be confirmed by X-TEM micrographs (fig.4.2.(a), (b)), which show no apparent inter- or intra-columnar porosity in the UBM coating and a morphology which can be described by a zone T or zone 2 structure according to the structure zone models. A similar, fully protective corrosion behaviour could even be achieved when the deposition temperature was decreased to 250°C and the ion bombardment was minimised by reducing the unbalancing effect of the magnetrons i.e. the coil current from 6A to 3A (section 4.1.2.4., fig.4.12.). The columnar morphology of this coating can also be described by a zone 2 or a zone T structure (section 4.1.2.2., fig.4.8.). However, the reduced ion bombardment in combination with the lower deposition temperature led to an increase in column size, enhanced competitive growth and a higher surface roughness. Both parameters, ion bombardment and temperature, basically influence the “heat” input into the surface and near surface region. Thus, the coarser coating morphology is a result of the decreased ad-atom surface mobility as well as fewer re-sputtering and re-deposition events. However, there is no apparent porosity (TEM) and again the initial conclusion was drawn, that a dense film morphology was responsible for the protective corrosion behaviour.

The results presented in section 4.1.3. surprisingly revealed that fully passive polarisation characteristics could only be achieved if Nb ion etching from the cathodic arc source is used as the etching pre-treatment of the steel substrate prior to coating deposition. In contrast, the coatings deposited after bombardment with Cr and Ar ions exhibited pitting followed by localised corrosion of the stainless steel substrate. As there are no significant differences in the overall morphology of the three Nb coatings but significant differences in the interface regions (section 4.1.3.2., fig.4.13.), this result indicates two aspects:

- (i) There must be a considerable influence of the interface region, generated during the substrate ion bombardment prior to deposition, on the corrosion behaviour of the substrate/ coating system
- (ii) If there is a significant influence of the interface on the corrosion behaviour, the coating structure can not be fully dense, i.e. it must be porous

Porosity can be either a macroporosity or a microporosity. The first arises from large growth defects such as detached droplets or macroparticles produced during the cathodic arc ion etching pre-treatment. The latter is determined by the growth

morphology itself, e.g. open columnar structures arising from insufficient adatom mobility as described by the structure zone models. Although there is no apparent porosity in the coatings as indicated by X-TEM micrographs (except fig.4.14.), the presence of underdense regions can not be excluded, as TEM foils sample a very small area. Future experimental work will be necessary to satisfactorily answer the question of porosity.

The different features of the interface regions and their influence on the corrosion resistance may be explained as follows. The dark ribbon generated during etching with Nb ions from the cathodic arc source (section 4.1.3.2., fig.4.13.(b)) is of a very fine crystalline or “amorphised” nature as shown in section 4.1.4.2., fig.4.22. The presence of such an amorphised region has been described earlier for substrate ion etching from a cathodic arc source by Salagean et. al. using a Nb target (section 2.3.3.2. [7]), by Petrov et al using a  $Ti_{0.85}Nb_{0.15}$  target [8] and by Datta et.al. (section 2.3.3.2 [1]). No details about the origin of the layer are given in the latter publication. Bombardment of the steel surface prior to deposition with metal ions can result in the desired removal i.e. sputtering of surface contaminants, the formation of a deposition layer as well as sub-surface ion penetration. The latter can cause a number of events including (i) sputtering of substrate material, (ii) ion implantation, (iii) “radiation damage” i.e. generation of vacancies, interstitial point defects, dislocations and (iv) disruption of surface crystallography and morphology e.g. amorphisation. Which of these events occur on the steel substrate is a function of the properties of the substrate material and of the bombarding ions, i.e. ion energy and ion mass. The impact of the heavy, highly energetic Nb ions on the steel substrate generates a high density of residual defects, which results in the observed amorphisation of the upper few nanometers of the interface region. In order to analyse the composition of the interface region, a stainless steel substrate was Nb ion etched under the same process conditions, but then coated with TiAlN instead of Nb (TiAlN was chosen as it is a standard coating at SHU). The layer was found to be a compositionally intermixed Nb/ steel region, as evident from fig.5.1., which shows a STEM-EDX profile across the interface region. The thickness of the structurally altered layer, observed in the TEM (fig.4.13.(b)), is consistent with that of the compositionally intermixed region, i.e.  $\approx 8\text{nm}$ . The “tail” of the Nb profile on the coating side of the analysed sample should be disregarded as it most likely stems from contamination of the TiAl targets during the etching step. It will be shown later in this

section that the interface region is formed by a combination of ion implantation and Nb layer deposition.

The interface generated during bombardment of the stainless steel substrate with the lighter (atomic mass Cr = 52) and less energetic Cr ions differs significantly (section 4.1.3.2., fig.4.13.(d)). The amount of surface damage is clearly reduced compared with Nb ion bombardment and there is no evidence of an amorphised region. The structurally altered layer extends into the sub-surface region to a depth of approximately 20nm.

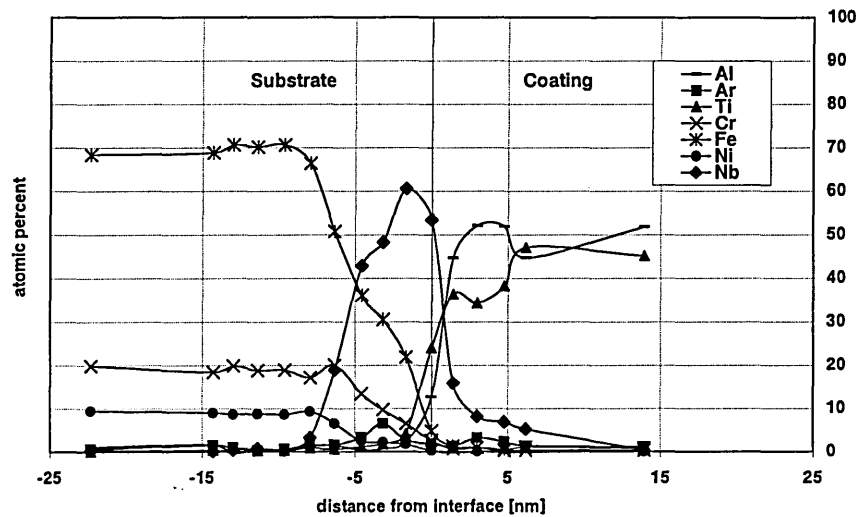


Fig.5.1. EDX profile across Nb etched/ stainless steel interface ( $U_{bias} = -1200V$ )

Bombardment with singly charged Ar ions with a much reduced ion flux, ion energy and ion mass (atomic mass Ar = 40) leads to a diffuse interface with large underdense regions (section 4.1.3.2., fig.4.13.(e)). The presence of these underdense regions must be related to an insufficient cleaning effect during the substrate ion etching stage, leaving behind contaminations such as oxides.

It is believed that the dense, amorphised nature of the interface region formed under bombardment with Nb ions acts as an effective barrier against pitting and corrosive attack of the stainless steel substrate. It is well known that amorphous metal systems are much more resistant to pitting and crevice corrosion compared with their equivalent crystalline alloy [9]. This is due to the lack of grain boundaries, second phases, compositional segregation and large crystalline defects. The pitting and crevice resistance of a glassy Fe-Cr-Ni alloy for example is dramatically increased compared to conventional stainless steel, i.e. the pitting resistance of this alloy is the same at only 7% Cr as compared to 12% minimum Cr required in most stainless steels [9]. This is

believed to be due to an improvement of the strength of the passive layer on the Fe-Cr-Ni alloy caused by the glassy state.

The thin, amorphised interface layer acts as a corrosion barrier and increases the pitting resistance, given the case that the corrosive electrolyte reaches the stainless steel substrate via defects or pores in the niobium coating, and hence supports the coating in its protective properties. In the case of substrate etching with Cr or Ar ions this additional barrier is not given. Two aspects have to be considered with regards to the mechanism in which the amorphised interfacial layer enhances the corrosion resistance. Firstly, a “structural” protection is given by the amorphisation, i.e. the reduction of pit initiation sites such as grain boundaries. Although the modified region is not truly amorphous, it is believed that the degree of homogeneity based on the disordered structure is high enough to provide enhanced corrosion resistance [10]. Secondly, it might be speculated that the layer “chemically” improves the corrosion resistance by forming the compositionally intermixed region. Kim et al. [10] and Li et.al. [11] produced amorphous Cr-Nb and Fe-Cr-Ni-Nb alloys respectively by sputter deposition and found improved corrosion resistance compared to the alloy constituents and to bulk stainless steel. The authors relate this to (i) the uniformity and homogeneity of the amorphous alloy (i.e. structural protection) and (ii) to the formation of a passive film of higher stability and protective quality (i.e. chemical protection). Introduction of Nb in the interface region by ion implantation and/ or the formation of a thin (amorphised) Nb layer during substrate ion etching might result in a similar effect i.e. chemical stabilisation of the passive film.

A second aspect is that Cr ions probably are more effective in sputter cleaning the substrate i.e. in removing the oxide layer on the stainless steel prior to deposition than Nb ions [12], thus possibly decreasing the “natural” corrosion resistance of the substrate and allowing easier pit initiation. The rather poor corrosion resistance of the Ar ion etch sample is additionally related to the presence of large underdense regions at the interface, which allow lateral penetration of the corrosive electrolyte along the interface resulting in the observed adhesive failure during corrosive attack.

The importance of the interface region is further substantiated by the findings presented in section 4.1.4., i.e. by the significant influence of the substrate bias voltage during Nb ion etching on the corrosion resistance of the substrate/ coating system (fig.4.27.).

Additionally, the fact that as-etched substrate material exhibits similar corrosion resistance to those with an additional UBM Nb coating (fig.4.29.) is a clear indicator for the importance of the interface region. The nature of the interface (fig.4.20., 4.21.) as well as the corrosion behaviour (fig.4.27.) is strongly influenced by the energy of the bombarding Nb ions. The best corrosion resistance is observed with medium substrate bias voltages of  $-600$  and  $-800\text{V}$ , whereas bombardment at higher ion energies ( $U_{\text{bias}} = -1200\text{V}$ ,  $(-1000\text{V})$ ) as well as at lower ion energies, ( $U_{\text{bias}} = -200\text{V}$ ,  $(-400\text{V})$ ) leads to a significant decrease in the pitting and corrosion resistance.

The influence of the substrate bias voltage on the interface region and on the corrosion resistance may be explained as follows.

Fig.5.2. (a) again shows the STEM EDX profiles across the interface of a Nb ion etched steel substrate, which was already presented in fig.5.1. It can be seen that the Nb profile can be deconvoluted by a two component fit, which indicates the presence of a Nb deposition layer in addition to the Nb implantation profile. This suggests that the net sputter rate of the bombarding Nb ions is not high enough to compensate for the growth of a deposition layer formed by neutrals from the arc source [12]. As shown in fig.4.34. (section 4.1.6.) the sputter- or removal rate of a NiCr (80/ 20) coating by bombardment of Nb ions from the arc source ( $U_{\text{bias}} = -1200\text{V}$ ) is only 50nm. It can be expected that this rate is even less for “real” substrate ion etching, i.e. etching of bulk material, as the density of bulk material will be higher than that of the NiCr coating and the substrate surface will not be as faceted. The low removal or etching rate can be related to the low sputter yield of Nb ions with a value of 1.4 (for  $\text{Nb}^{3+}$  at  $U_{\text{bias}} = -1200\text{V}$ ) compared with e.g. a value of 2.8 for  $\text{Cr}^{2+}$  ions at the same bias voltage (sputter yields obtained by TRIM simulations [13]). Fig.5.2. (b) and (c) show EDX profiles across the interface regions generated by Cr ion bombardment at two different bias voltages,  $-1200\text{V}$  and  $-400\text{V}$  (from [12]). At a substrate bias voltage of  $-1200\text{V}$  (ion energy:  $2.4\text{keV}$ ) (fig.5.2.(b)) the Cr depth distribution is dominated by ion implantation with no indication of any deposition layer. Only when the substrate bias voltage is reduced to  $-400\text{V}$  (ion energy:  $0.8\text{keV}$ ) a deposition layer forms as can be seen from fig.5.2.(c). Similar to Nb ion etching at  $-1200\text{V}$ , the Cr peak can be deconvoluted into two components indicating a combination of ion implantation and the formation of a deposition layer. This comparison shows how significantly the interface regions differ, depending on the ion species, i.e. Nb or Cr ions.

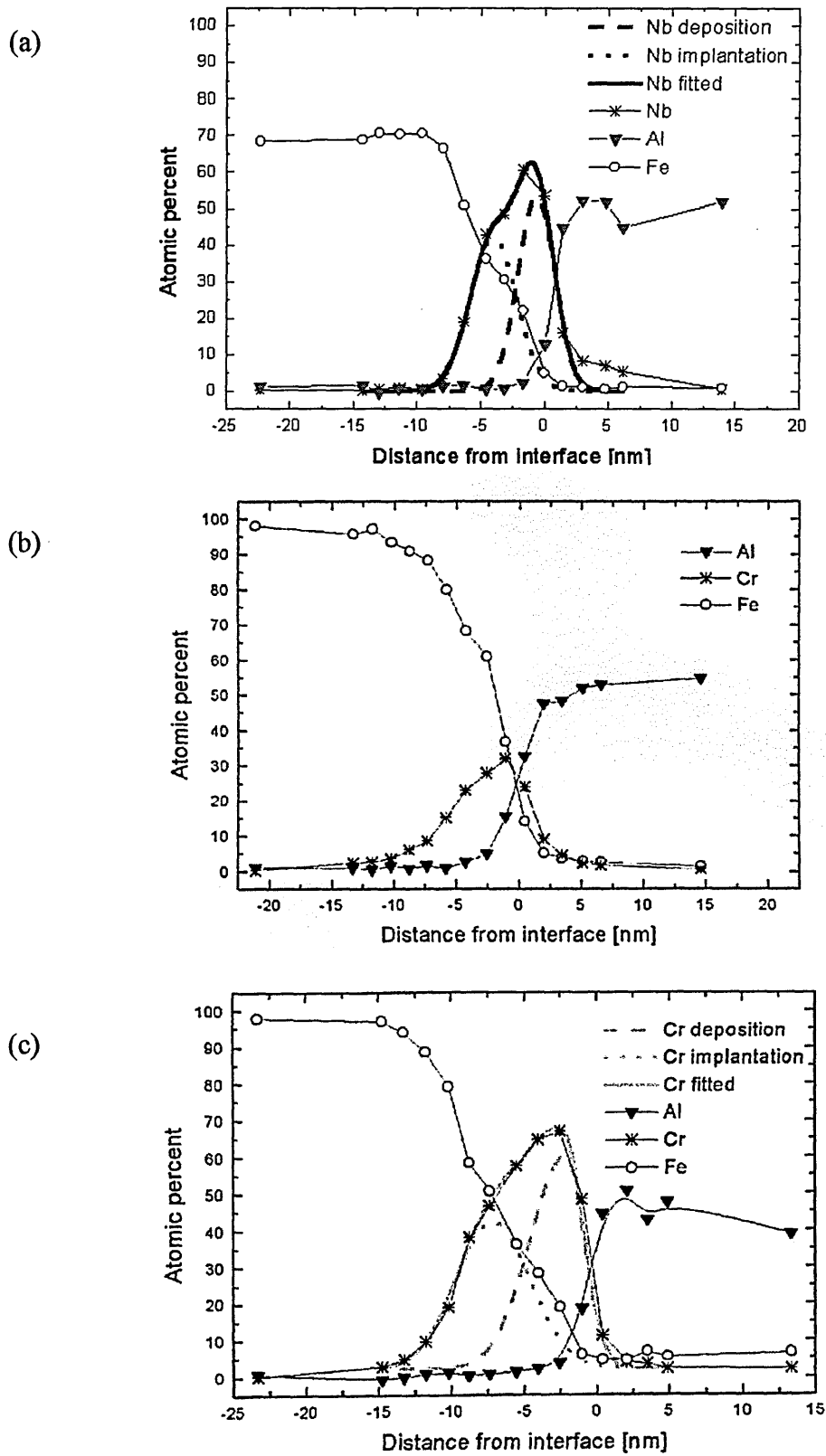


Fig.5.2. STEM-EDX profiles: Nb-etch,  $U_{\text{bias}} = -1200\text{V}$  (a), Cr-etch,  $U_{\text{bias}} = -1200\text{V}$  (b), Cr-etch,  $U_{\text{bias}} = -400\text{V}$  (c) [12]

Despite the formation of a deposition layer at a substrate bias voltage of  $-1200\text{V}$  the impact of the heavy Nb ions still leads to amorphisation and compositional intermixing of Nb and steel. With decreasing substrate bias voltage, i.e. ion energies, a further decrease in sputtering events can be expected in favour of growth of the deposition layer, until amorphisation and intermixing events are fully suppressed at  $U_{\text{bias}} = -200\text{V}$  as can be seen from the X-TEM image in fig.4.21.(f) (section 4.1.4.). It is believed that, in terms of corrosion resistance, Nb ion bombardment at “medium” ion energies i.e. substrate bias voltages of  $-600$  and  $-800\text{V}$ , leads to an optimum combination between the two competing mechanisms. These mechanisms are amorphisation and compositional intermixing of the Nb/ steel region on the one hand and Nb deposition on the other hand. At a substrate bias voltage of  $-1200\text{V}$  and possibly  $-1000\text{V}$ , sputtering and intermixing events are so strong as to allow the presence of steel substrate, i.e. Fe, at the immediate surface of the interface, hence reducing the “chemical protection” component. Li et.al. have shown that preferential dissolution of Fe can decrease the corrosion resistance of an amorphous Fe-Cr-Ni-Nb alloy [11]. In the case of low substrate bias voltages, layer deposition is dominant and the ion energies are not sufficient to cause disruption of the crystalline structure, thus reducing the “structural protection” component.

Figure 5.3. shows depth profiles of steel subjected to Nb ion bombardment at different substrate bias voltages. The profiles were obtained by TRIDYN simulations [14], assuming an ion charge state of  $3+$ , an ion to neutral ratio of  $6:4$  and a particle flux (ion plus neutrals) of  $2 \times 10^{17} \text{ cm}^{-2} \text{ s}^{-1}$ . The remaining input parameters were taken from the default values of the program. The values used for the simulations are based on first assumptions, hence the profiles are only used to show a trend rather than giving quantitative results. However, the above stated mechanisms seem to be confirmed by the simulated profiles. In all three cases the maximum Nb concentration lies outside the steel substrate indicating the formation of a deposition layer, rather than pure ion implantation. At a substrate bias voltage of  $-1200\text{V}$ , Fe is not “buried” by Nb but “drawn” to the surface of the interface region through intermixing and re-sputtering, In contrast, there is no Fe present at the surface using substrate bias voltages of  $-600$  and  $-800\text{V}$ . In the case of  $-200\text{V}$ , the low ion energies cause the formation of a pure deposition layer with no interfacial mixing. Further STEM EDX profiling and computer simulations as well as chemical analyses utilising e.g. XPS will be necessary to substantiate the proposed mechanisms.

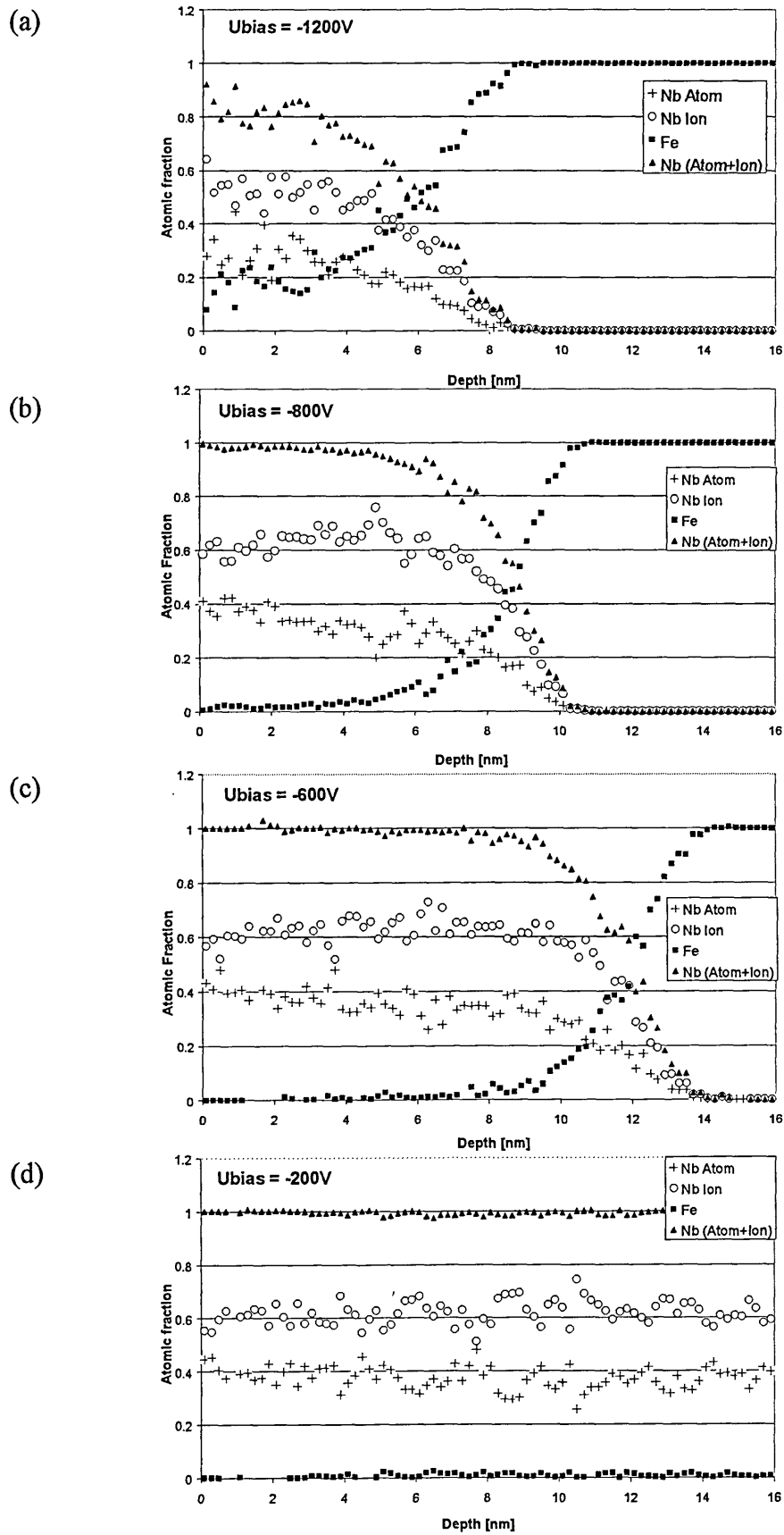


Fig.5.3. TRIDYN Profiles:  $U_{bias} = -1200V$  (a),  $-800V$  (b),  $-600V$  (c),  $-200V$  (d)

The reduction in working gas pressure did not have a significant effect. The interface layer appears slightly thicker compared with that at higher gas pressures, possibly as a result of fewer charge exchange events between Nb ions and the working gas and hence more energetic ion bombardment. However, the corrosion resistance is not improved (fig.4.27.), therefore the higher working gas pressure should be utilised to provide greater stability of the arc discharge on Nb.

### 5.1.1.2. SCAE/ UBM

The refined coating morphology of the coating deposited by steered cathodic arc evaporation compared with the sputtered coating (section 4.1.1.2., fig.4.2.) can be related to the difference in the layer forming species. In UBM these are mostly neutral Nb atoms with energies in the order of 10eV and bombardment of the growing film is mainly by Ar ions with energies of approximately 75eV. In SCAE on the other hand, the layer forming species are multiply ionised Nb ions with average ion energies up to 225eV assuming a maximum average charge state of 3+. This is confirmed by the charge distribution presented in fig.5.4., which compares optical emission spectra of a SCAE and a UBM Nb discharge in the ABS coating unit employed in the present study [15]. The spectra reveal the presence of Nb<sup>+</sup>, Nb<sup>2+</sup> and Nb<sup>3+</sup> in the SCAE discharge, whereas only neutral Nb atoms are detected in the UBM discharge.

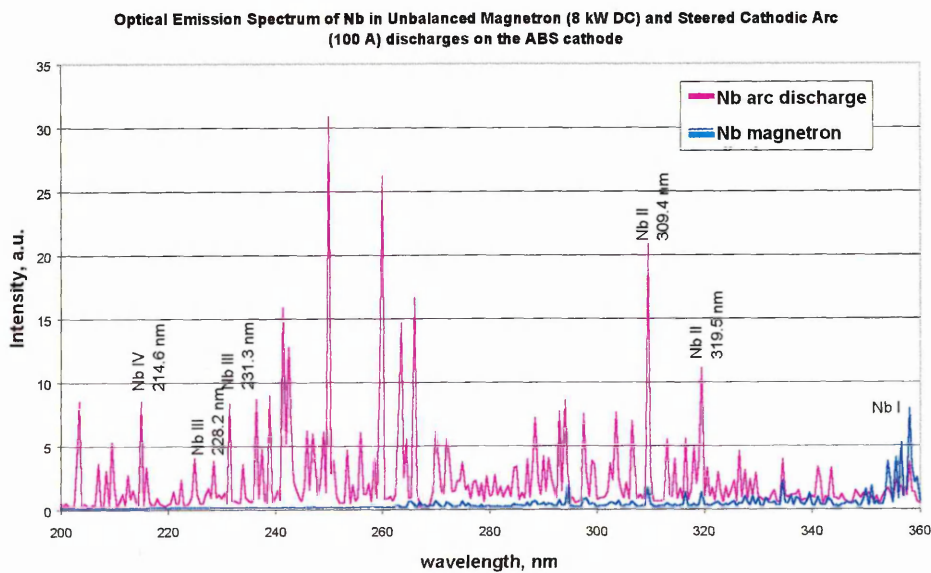


Fig.5.4. Optical emission spectra of SCAE and UBM Nb discharge [15]

The enhanced ion bombardment during SCAE increases the overall energy delivered to the growing film, hence increasing adatom surface mobility and the input of “heat” in the near surface region. Further effects of the enhanced ion bombardment are re-sputtering of loosely bound atoms and possibly the generation of point defects that can act as nucleation sites. The considerably lower deposition rate should also be taken into consideration as a possible influential parameter. In summary, SCAE deposition should produce films of a denser microstructure compared with UBM.

However, in the employed polarisation measurements the arc evaporated coatings do not stay passive but exhibit pitting i.e. localised corrosion of the stainless steel substrate, in contrast to the fully protective behaviour of the UBM coating (section 4.1.1.4., fig.4.6.). With regards to the “denser” or more refined microstructure of the coatings compared with the UBM film and the fact that the substrates were also Nb ion etched prior to coating deposition, this result must be related to the higher number of macroparticles and hence growth defects in the coatings. These growth defects can act as easy pathways for the corrosive electrolyte to reach the substrate resulting in the observed pitting behaviour above a certain potential. Initially, the current density increases rapidly, similar to uncoated stainless steel. With increasing potential, the slope flattens and the current density increases only slightly. This is related to the formation of corrosion products, “blocking” the pathway and restricting the active area for corrosive attack.

#### 5.1.1.3. General Remarks on Corrosion

A freshly prepared Nb surface will behave as the anode when coupled to stainless steel as shown by experimental results and as expected by the less noble corrosion potential. Thus, it is frequently suggested in literature that a newly exposed Nb coating will sacrificially protect a newly exposed stainless steel substrate [5], [16]. Although true, this statement is rather misleading, as the sacrificial protection is only valid for non-oxide covered, bare metal surfaces. In a defective Nb coating a galvanic couple will be formed between Nb and the stainless steel substrate. In a natural environment e.g. a NaCl solution open to air with no application of an external potential, the galvanic potential of the couple will rise due the natural formation of an oxide layer. Nb will act as the anode and “sacrificially” oxidise (passivate) while the steel substrate will remain

un-attacked as expected. However, as this process continues, the now passivated Nb will become the cathode in the galvanic couple. The potential will rise above the breakdown potential of stainless steel, as was “artificially” invoked in the polarisation measurements, and stainless steel will then corrode as the anode in the galvanic couple. This leads to the typical corrosion characteristics observed in the polarisation measurements of e.g. the SCAE coatings on stainless steel, i.e. pit formation and finally spallation of the protective coating as a result of local dissolution of the steel and a small anode to cathode surface area ratio.

The “time until breakdown” of a freshly prepared Nb/ 316 stainless steel couple in Ringer solution (a salt solution isotonic with blood serum) was estimated as only between 11 to 210 day [16]. Although polarisation measurements, as employed in the present study, do not represent real life behaviour, they can be a useful and important tool in determining the qualities of the substrate/ coating system by raising the potential above the critical value and monitoring whether breakdown occurs or not. In the latter case, as observed with the Nb-etch/ UBM coatings, this behaviour is believed to be a good indication for high corrosion resistance.

## 5.1.2. Other Properties and Resume

### 5.1.2.1. Comparison of Nb Coatings deposited by UBM and SCAE (section 4.1.1.)

The power-normalised deposition rate for Nb in a non-reactive atmosphere is approximately three times higher using unbalanced magnetron sputtering (input power = 8kW  $\Rightarrow$  dep.rate = 0.093  $\mu\text{m}\cdot\text{KW}^{-1}\cdot\text{h}^{-1}$ ) compared with steered cathodic arc evaporation (input power = 4-5KW  $\Rightarrow$  dep.rate = 0.030- 0.038  $\mu\text{m}\cdot\text{KW}^{-1}\cdot\text{h}^{-1}$ ), both during three-fold substrate rotation. The discrepancy in efficiency can be related to the extremely high evaporation enthalpy of Nb, which is the third highest of the elements with a value of 690 KJ/ mol [17]. Furthermore, only approximately 3% of the input energy in cathodic arc evaporation are consumed by evaporation of the cathode material as shown below. The approximate energy dissipation fractions in a cathodic arc are [18]:

- (i) Heat conducted to the cathode or “conductive cooling” (34%),
- (ii) Electron emission (21%),

- (iii) Evaporation (3%),
- (iv) Vapour ionisation (7%),
- (v) Kinetic energy of ions (23%) and thermal energy of electrons (10%) leaving the near cathode region.

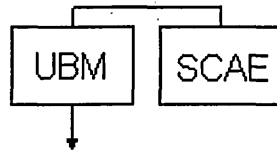
Additionally, the energy needed for vapour ionisation as well as the kinetic energies of the Nb ions leaving the cathode are expected to be considerably higher compared with other metals due to the high average charge state of Nb ions in a cathodic arc source.

The increase in surface roughness (section 4.1.1.1.) by a factor of two of the SCAE coating compared with the UBM coating is related to enhanced formation of macroparticles during arc evaporation, whereas droplets in the sputtered film only stem from the substrate ion etching step.

The strong preferred {110} orientation (section 4.1.1.3.), observed in the UBM coating, is thermodynamically favoured for vapour deposited bcc metals, as the texture development in thin films is driven by the reduction of surface and interface energies. It therefore favours the closest packed {110} planes ( $1.41 \text{ atoms/ a}^2$ ) parallel to the coating/ substrate interface. This principle of texture evolution is frequently accepted in literature (e.g. [19]-[22]). However, on the basis of this mechanism, the shift towards a {111} texture component in the arc evaporated coatings seems contradictory as higher adatom surface mobility and lower deposition rate should make it even easier for the depositing atoms to reach their energetically favourable state. Texture evolution in thin films is highly complex and no attempt shall be made here to explain the observed results. However, a possible interpretation may be found by considering another mechanism. It has been shown that another driving force for texture evolution is preferential re-sputtering of different planes by low energy ion bombardment during film growth [23]-[26]. The increased ion bombardment during SCAE will result in enhanced re-sputtering of condensed atoms compared with UBM deposition. As the ion energy is relatively low, the ions preferentially sputter the atoms in the outer planes by direct knock on [25]. The closest packed planes, i.e. the {110} planes, parallel to the surface will be sputtered preferentially. The considerably lower packing density of the {111} planes ( $0.57 \text{ atoms/ a}^2$ ) will reduce the re-sputtering effect and possibly promoting the observed change in texture evolution.

Residual stresses in the Nb coatings are of compressive nature, which, in principle, is desirable in terms of corrosion protection (section 4.1.1.3.). The thermal stress component is compressive due to the more than two times higher thermal expansion coefficient of the stainless steel substrate compared with Nb (section 3.3.5.2., equ.3.8.). The origin of the compressive intrinsic stress component can be related to incorporation of gas atoms e.g. Ar atoms into the Nb lattice. Additionally, ion bombardment during film growth or “ion peening” can create compressive stresses. The considerably lower stress value of the SCAE might be explained by the greater input of “heat” in the near surface region from enhanced ion bombardment and the considerably lower deposition rate, both of which may allow arrangement of depositing atoms to lower energetic sites and possibly annihilation of stress active defects [27]. The higher lattice parameter of the SCAE coating compared with that of the UBM coating can not be explained at present.

With regards to higher efficiency, i.e. deposition rate, higher controllability of the process temperature and superior corrosion performance, UBM is the preferred deposition technology over SCAE to deposit Nb coatings.

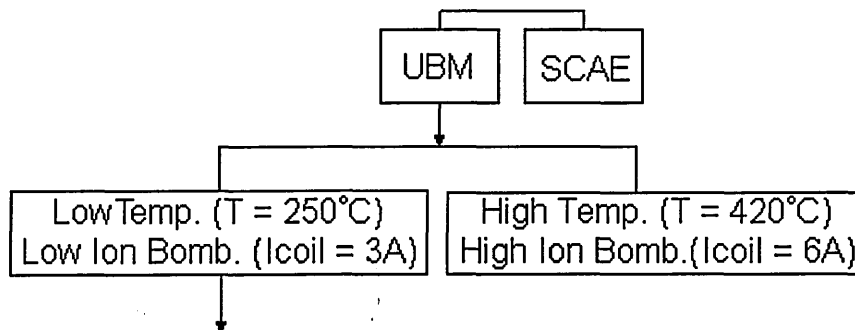


#### 5.1.2.2. Influence of Temperature and Ion Bombardment on UBM Nb Coatings (section 4.1.2.)

As discussed previously (5.1.1.1.) the reduced ion bombardment in combination with a lower deposition temperature leads to a coarsening of the coating structure and enhanced competitive growth in the case of the coating deposited at 250°C with an unbalancing coil current of 3A compared to 420°C and 6A during deposition of the high temperature coating. The difference in coating structure is reflected in the surface roughness values (section 4.1.2.1.). A roughening effect can be observed for the low temperature film, which stems from the lower adatom surface mobility as well as less pronounced preferred resputtering of the column tops.

There is no influence on the texture development, as both films exhibit a strong, thermodynamically favoured, {110} crystallographic orientation (section 4.1.2.3.). However, the ion bombardment and the temperature during film growth have a significant influence on intrinsic stresses in the Nb films. The intrinsic stress in the low temperature coating is still compressive, but the value is nearly halved. The tendency of this result is in agreement with the work carried out by Wu (section 2.3.3.2. [28]) and Cuomo et. al. (section 2.3.3.1. [29]). The reduction in compressive stress can be attributed to the reduced Ar ion bombardment and the lower deposition temperature i.e. (i) reduced “ion-peening” effect and (ii) possibly a less dense coating structure i.e. easier accommodation of Ar or residual gas atoms. Additionally, the reduced Ar ion bombardment may have decreased the incorporation of Ar atoms into the lattice. Determination of the residual gas content would be necessary to substantiate these results. The change in residual stresses is also reflected in the lower hardness value for the low temperature coating, however, the drop in hardness is not as significant as one might expect (section 4.1.2.1.).

As discussed previously (5.1.1.1.), the corrosion behaviour is not affected by the reduced deposition temperature and ion bombardment as evident from the potentiodynamic polarisation measurements (section 4.1.2.4., fig.4.12.). This can again be regarded as an indicator for the importance of the interface layer. Both coatings remain fully protective and behave similarly to bulk Nb. Hence, under the employed process conditions (i.e. Nb ion etching prior to deposition), a deposition temperature of 250°C and an unbalancing coil current of 3A are sufficient to produce corrosion resistant Nb coating on stainless steel substrates.



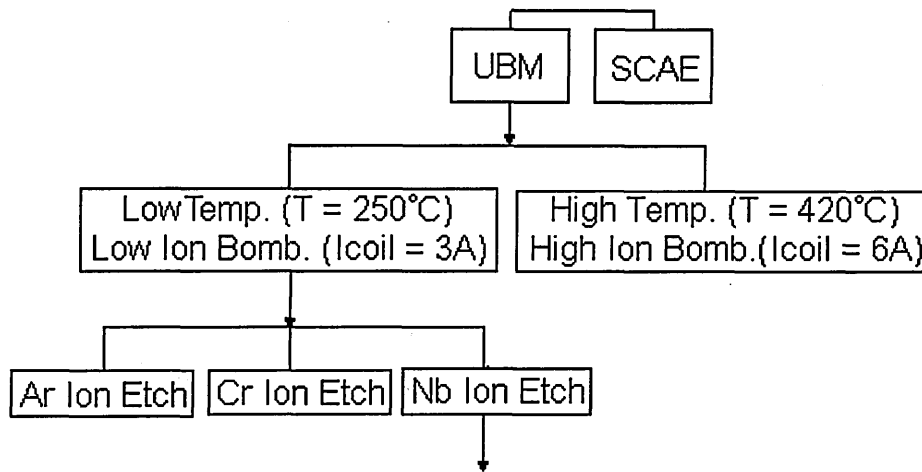
### 5.1.2.3. Influence of the Ion Etching Pre-Treatment prior to UBM Deposition (section 4.1.3.)

The comparatively low surface roughness of the coating deposited after glow discharge Ar ion etching in contrast to that of the Nb and Cr metal ion-etched samples is related to the elimination of droplet formation during the etching stage (section 4.1.3.1.). The similar roughness value of the Cr ion etched sample compared with the Nb ion etched sample can be attributed to the fact that, despite its higher melting point, Cr ion etching generates droplets of a size similar to that of Nb. This is related to the high vapour pressure of Cr, i.e. the possibility of sublimation of the droplets during flight from the cathode to the substrate or after arrival at the substrate as has been shown by [30], [31].

The influence of the ion etching pre-treatment on the crystallographic orientation of the subsequently deposited Nb coatings can not be explained at this point (section 4.1.3.3., fig.4.16.). On the basis of the observed differences in the interface regions it can only be speculated that etching with Nb ions “primes” the substrate surface in such a way as to allow grain growth with minimised interface and surface energies, i.e. {110} planes parallel to the substrate/ coating interface, from the early stages on. In the case of Ar ion etching locally contaminated areas on the substrate surface can restrict the energetically favourable growth, as they reduce the ad-atom mobility [32], resulting in a more random distribution of crystallographic planes. Additionally, it is believed that the substrate surface temperature in the early stages of deposition is highest after the energetic Nb ion etch, as a considerably more rapid increase in temperature was observed compared with etching using Cr and especially Ar ions. In the latter case, auxiliary radiant heating had to be used to maintain the desired temperature during the etching stage. The observed differences in intrinsic stress values (section 4.1.3.3.) are significant considering that all three coatings were grown under identical deposition conditions and can not be explained at present.

The differences in intrinsic stresses are reflected in the hardness values, which increase in the order of Nb etch < Cr etch < Ar etch (section 4.1.3.1).

Due to the significant influence of the ion etching pre-treatment on the corrosion resistance of the Nb coating/ stainless steel system, as discussed previously in section 5.1.1.1., Nb ions from the cathodic arc should be used as the etching species prior to coating deposition.

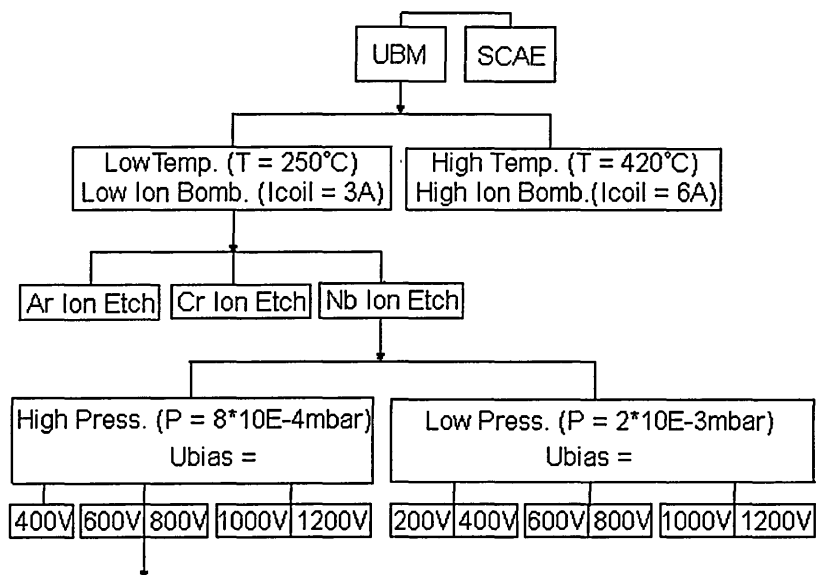


#### 5.1.2.4. Nb Ion Etching prior to Coating Deposition: Influence of Working Gas Pressure and Substrate Bias Voltage during Etching (section 4.1.4.)

It was observed that the UBM Nb coatings deposited after Nb ion etching at low substrate bias voltages, i.e.  $-200V$  and  $-400V$ , show a tendency to shift from the thermodynamically favoured  $\{110\}$  to a  $\{111\}$  major texture component (section 4.1.4.2.). It is interesting to note that the purely arc evaporated Nb coating (section 4.1.1.3.) also exhibits a  $\{111\}$  preferred orientation as discussed previously in 5.1.2.1. As shown by the X-TEM micrographs in fig.4.20 (e) and fig. 4.20.(e),(f), low-energy Nb ion etching ( $U_{bias} = -200V, -400V$ ) from the cathodic arc leads to the formation of a deposition layer with a thickness of up to 30nm. This layer is in principle an arc evaporated thin film, on which the UBM coatings are subsequently deposited. Hence, it may be speculated that this initial arc deposition layer exhibits a strong  $\{111\}$  texture component, similar to the pure SCAE Nb coatings, which subsequently influences the texture evolution in the UBM coating, hence causing the shift towards a  $\{111\}$  preferred orientation.

As shown by the corrosion results discussed previously in 5.1.1.1., Nb ion etching of the stainless steel substrate appears to be most beneficial using “medium” substrate bias

voltages of  $U_{\text{bias}} = -600\text{V}$  and  $U_{\text{bias}} = -800\text{V}$ . As the working gas pressure, in the employed pressure range, does not have a significant effect on the corrosion resistance, the higher working gas pressure should be utilised to provide greater stability of the arc discharge on Nb.



#### 5.1.2.5. Intermediate Nb-ion etching (section 4.1.5.)

Under the employed process conditions, intermediate bombardment of the growing film with Nb ions from the arc source did not lead to the desired disruption of the columnar coating morphology (section 4.1.5.2., fig.4.30.). The high hardness values of  $HK_{0.003} \approx 1000$  (section 4.1.5.1.) and the broad and asymmetric reflections obtained by X-ray diffraction (section 4.1.5.3., fig.4.31.) are indicative for incorporation of residual gas atoms in the Nb lattice, which can lead to embrittlement of the metal or solid solution hardening and hence the marked increase in hardness. The peak deconvolution presented in fig.4.32. indicates the presence of a second, tetragonal phase. The phase can not be identified at present, but a  $\beta$ -phase with tetragonal characteristics has also been observed for sputter deposition of the closely related tantalum [33]. The presence of this phase is very likely to be related to the intermediate etching steps, i.e. bombardment of the growing Nb film by energetic Nb ions from the cathodic arc source. The induced “heat” or energy, i.e. increase in surface temperature, enhances the reactivity of the film forming species with residual gas atoms, which are always present in the coating chamber, e.g. water vapour or nitrogen being adsorbed at the chamber

walls. The solubility of oxygen and nitrogen as interstitials in Nb increases with increasing temperature [34], [35]. Determination of the residual gas content would be necessary to substantiate these results.

There were no significant effects on the corrosion resistance of the coatings.

## 5.2. Niobium Coatings on Brass Substrates (section 4.2.)

The beneficial effect of Nb ion etching of the substrate on the corrosion performance of the substrate/ coating system, found with the stainless steel/ Nb coating system, could not be achieved with brass substrates (section 4.2.1., fig.36). This may be due to the absence of either a structural and/ or chemical protection stemming from a modified interface region. Further TEM analysis is necessary. Based on this result, Ar ion etching is the more convenient sputter cleaning method due to the higher controllability of the substrate temperature compared with metal ion etching. The adhesive failure of the coating related to an insufficient cleaning effect by the Ar ions, which was observed with stainless steel substrates, was not the case for brass substrates. This might be related to the higher sputtering coefficient of Cu compared with steel (sputter yield for 500eV Ar ions: Cu = 2.35, Fe = 1.10 [36]) and its lower affinity to oxygen, and hence a more efficient sputter cleaning of the substrate surface.

The polarisation measurements show that a pure Cu layer, as Zn diffusion barrier, is superior to a CuAlFe bronze and CuAlFe/ NiCr layers (section 4.2.2., fig.4.37.). Interpretation of the corrosion results is difficult as up to five different metals are involved resulting in complex electrochemical interactions. In the case of CuAlFe, preferential dissolution of Fe as well as of Al (Dealuminification) might be responsible for the poor corrosion performance. Both, passivated Nb and Cu, will behave cathodically and enhance preferential dissolution of Fe, Al and possibly Zn (Dezincification) from the substrate, although brasses with less than 15% Zn are generally immune to dezincification [9]. However, de-aluminification and -zincification are enhanced in environments containing chloride anions, such as used in the polarisation measurements, as well as by a deficiency of oxygen, i.e. in a crevice or under a coating. The additional NiCr coating improves the corrosion performance slightly by reducing the corrosive attack of the brass substrate. However, dissolution of the intermediate layers still results in failure of the substrate/ coating system. Corrosive attack of the sample with the Cu layer is only localised i.e. in small pits and the

corrosion rate is limited by the formation of copper compounds such as cuprous and cupric oxides and possibly chlorides. Similar to stainless steel, the relatively noble metal Cu behaves anodically to the, in principle less noble, but passivated Nb. One explanation for the insufficiently protective behaviour of the Nb coating might be the above mentioned absence of a protective interfacial layer.

However, the PVD coating system appears to be superior to the industrially used, electroplated NiCr coating, as evaluated by polarisation measurements (section 4.3.2.).

Similar to Nb ion etching of the brass substrate, no beneficial effects were achieved by bombardment of the intermediate Cu layer with Nb ions prior to deposition of the Nb coating.

### **5.3. Summary and Future Work**

Nb can be successfully deposited by unbalanced magnetron sputtering at low deposition temperatures and under reduced ion bombardment, which will allow development of Nb based coating systems on temperature sensitive substrates for e.g. decorative applications. However, sufficient corrosion protection on stainless steel substrates was only given if the substrate is subjected to bombardment with Nb ions from the cathodic arc source prior to coating deposition. This result demonstrates the influence of the interfacial region with regards to properties of the substrate/ coating system. The author believes that the importance of the interface region is at present not sufficiently recognised in PVD deposition of corrosion resistant coatings. It will be important and necessary in future to investigate fundamentally the mechanisms involved as well as the possibilities, which might arise from optimised interface development. This is emphasised by the fact that the corrosion resistance of the stainless steel/ Nb system is not only influenced by the ion species generating the interface but that it is also very sensitive to the energy of the bombarding ions. The interface generated under bombardment of ions with “medium” ion energies i.e. 1.8KeV to 2.4KeV (substrate bias voltages of -600V, -800V) was found to be most beneficial in complementing the corrosion resistance of the subsequently sputter-deposited Nb coating. This is believed to be due to an optimised combination of structural and chemical protection mechanisms. Future investigations are necessary to substantiate these first results. Optimised interface architecture will allow optimisation of the substrate/ coating systems e.g. minimisation of the coating thickness. One might go as far as to say that

the interface region could be of more importance than the coating itself in cases such as the one investigated in the present study. For the stainless steel/ Nb system however, a Nb coating will always be necessary to mechanically protect the thin interfacial region and to guarantee long term protection

With regards to application of amorphous metals for improved corrosion resistance, D.A. Jones predicted in 1992 [9]: “Applications making use of the improved corrosion resistance of amorphous metals are limited.... However, deposition or insitu formation of [amorphous] corrosion resistant surface coatings may become attractive, when the technology and the cost of the coating process can be reduced.” It is believed that the present results fulfil these requirements and that formation of a chemically stable, amorphised interface layer in combination with a crystalline, corrosion resistant coating might present a possible alternative to amorphous coatings in PVD.

The beneficial effects of Nb ion bombardment of the substrate is however sensitive to the nature of the substrate and could not be transferred to brass. Although no full passivation is achieved, the corrosion behaviour of the brass/ Cu / Nb system, evaluated by electrochemical polarisation measurements, is superior to industrially used electroplated coating systems. The higher quality in combination with environmental aspects makes PVD deposition of Nb the favourable technology. However, the future will have to show whether these positive factors will outweigh economical demands i.e. the higher cost efficiency electroplating of e.g. NiCr has to offer.

Proposed future work based on the presented results can be summarised as following:

- (i) X- TEM, convergent-beam electron diffraction and glancing-angle XRD analyses to further investigate texture evolution mechanisms and crystallographic structures
- (ii) Determination of the residual gas contents in the coatings using SEM-EDX analyses and XPS profiling
- (iii) Long term and “real life” corrosion studies in different corrosive environments, e.g. salt spray testing
- (iv) Investigation of the effect of Nb ion bombardment on substrate materials other than stainless steel and brass.

## References to Chapter 5

- [1] P.K.Datta, K.N.Strafford, L.P.Ward, Proc. 28<sup>th</sup> Conf. Australasian Corr. Assoc., (1988), 7-10.1
- [2] L.P.Ward, K.N.Strafford, T.P.Wilks, C.Subramanian, J.Mater.Proc.Technol., 56, (1996), 364
- [3] L.P.Ward, Proc. AMPT, (1995), Dublin, Ireland, 79
- [4] L.P.Ward, P.K.Datta, Proc. AMPT, (1995), Dublin, Ireland, 1240
- [5] J.H.Hsieh et.al., Surf.Coat.Technol., 49, 1991, 83
- [6] J.D.Reardon, F.N.Longo, C.R.Clayton, K.G.K.Doss, Thin Solid Films, 108, 1983, 459
- [7] E.E.Salagean, D.B.Lewis, J.S.Brooks, W.-D.Münz, I.Petrov, J.E.Greene, Surf.Coat.Technol., 82, (1996), 57
- [8] I.Petrov, P.Losbichler, D.Bergstrom, J.E.Greene, W.-D.Münz, T.Hurkmans, T.Trinh, Thin Solid Films, 302, (1997), 179
- [9] Principles and Prevention of Corrosion, D.A.Jones, Macmillan Publishing Company, 1992, New York, USA
- [10] J.H.Kim et.al., Corr.Sci., 36 (3), (1994), 511
- [11] X.-Y.Li, Corr.Sci., 41, (1999), 1095
- [12] C.Schönjahn, H.Paritong, L.A.Donohue, W.-D.Münz, R D.Twesten, I.Petrov, in Electron Microscopy and Analysis 1999, Proc. I.o.P. EMAG, (1999), Sheffield, UK, 75
- [13] J.Ziegler, J.A.Biersack, The Stopping and Ranges of Ions in Matter, Pergamon Press, 1985, New York, USA
- [14] TRIDYN (version 4.0), W.Moeller, Institute of Ion-Beam Physics and Materials Research, Forschungszentrum Rossendorf, 1989, Dresden, Germany
- [15] A.Ehiasarian, Ph.D. research work, Sheffield Hallam University, 1999, Sheffield, UK
- [16] J.Gluszek, J.Masalski, Brit.Corr.J., 27 (2), (1992), 135
- [17] WebElements Periodic Table, www.webelements.com, Mark Winter, University of Sheffield, Sheffield, UK
- [18] S.Falabella, D.A.Karpov in Handbook of Vacuum Science and Technology, R.L.Boxman, P.J.Martin, D.M.Sanders (Ed.), Noyes Publications, 1995, New Jersey, USA, 399
- [19] C.V.Thompson, Ann.Rev.Mater.Sci., 20, (1990), 245

- [20] L.Hultman, J.-E.Sundgren, J.E.Greene, D.B.Bergstrom, I.Petrov, J.Appl.Phys., 78 (9), (1995), 5395
- [21] J.E.Greene et.al., Appl.Phys.Lett., 67 (20), (1995), 2928
- [22] G.Knuyt, C.Quaeyhaegens, J.D'Haen, L.M.Stals, J.Vac.Sci.Technol., 76-77, (1995), 311
- [23] L.S.Yu, J.M.E.Harper, J.J.Cuomo, D.A.Smith, J.Vac.Sci.Technol., A4 (3), (1986), 443
- [24] R.M.Bradley, J.M.E.Harper, D.A.Smith, J.Appl.Phys., 60 (12), (1986), 4160
- [25] C.Gautier, H.Moussaoui, F.Elstner, J.Machet, Surf.Coat.Technol., 86-87, (1996), 254
- [26] H.Ji, G.S.Was, J.W.Jones, N.E.Moody, J.Appl.Phys., 81 (10), (1997), 6754
- [27] D.B.Lewis, L.A.Donohue, M.Lembke, W.-D.Münz, R.Kuzel, V.Valvoda, C.J.Blomfield, Surf.Coat.Technol., 114, (1999), 187
- [28] C.T.Wu, Thin Solid Films, 64, (1979), 103
- [29] J.J.Cuomo, J.Vac.Sci.Technol., 20 (3), (1982), 349
- [30] S.Creasey, D.B.Lewis, I.J.Smith, W.-D.Münz, Surf.Coat.Technol., 97 (1997), 163
- [31] W.-D.Münz, I.J.Smith, D.B.Lewis, S.Creasey, Vacuum., 48, (1997), 473
- [32] C.Gautier, J.Machet, Thin Solid Films, 289, (1996), 34
- [33] Thin Film Technology, R.W.Berry, P.M.Hall, M.T.Harris, Van Nostrand Reinhold Company, 1968, New York, USA, 342
- [34] The Chemistry of Niobium and Tantalum, F.Fairbrother, Elsevier Publishing Company, 1967, Amsterdam, The Netherlands, 20
- [35] Properties of Refractory Metals, W.D.Wilkinson, AMS, Gordon and Breach Science Publishers Inc., 1969, New York, USA, 4
- [36] Sputter Deposition, S.L.Rhode in ASM Handbook, Vol.5, ASM International, 1994, Ohio, USA, 573

## **6. Conclusions**

- (i) Nb can be successfully deposited by UBM at low deposition temperatures (250°C) and under reduced ion bombardment onto SCAE Nb ion-etched stainless steel substrates. The substrate/ coating system is resistant to pitting and general corrosion in a 3% NaCl solution and exhibits electrochemical characteristics similar to bulk Nb.
- (ii) The mode of ion etching pre-treatment prior to coating deposition has a pronounced effect on the corrosion performance of the stainless steel/ Nb coating system. Fully protective behaviour could only be achieved if the substrate is bombarded with multiply ionised Nb ions from the cathodic arc source.
- (iii) The impact of the Nb ions leads to amorphisation of the upper few nanometers of the interface region. This interface layer is believed to act as an additional barrier against corrosion due to (i) the structural homogeneity achieved by amorphisation (structural protection) as well as by (ii) chemical stabilisation due the introduction of Nb in the near surface region (chemical protection).
- (iv) The substrate bias voltage during etching with Nb ions has to be carefully chosen to optimise the properties of the interfacial region. Best results were achieved by “medium” bias voltages of –600V and –800V, i.e. by bombardment of ions with average ion energies of up to 1.8KeV to 2.4KeV. This is believed to be due to an optimum combination of structural and chemical protection mechanisms.
- (v) The influence of the interface region on the corrosion resistance is emphasised by the fact that “as etched” stainless steel substrate material exhibits similar corrosion resistance to that with an additional Nb top coating. However, a thin Nb coating is necessary to mechanically protect the thin interface and to guarantee long term corrosion protection.
- (vi) The beneficial effect of Nb ion etching on the corrosion resistance of substrate/ coating systems depends on the substrate material and can at present not be transferred to brass.
- (vii) The corrosion behaviour of the investigated PVD coating systems on stainless steel as well as on brass are superior to commercially produced, electroplated Cr, Ni and NiCr coatings on the same substrate materials, as investigated by electrochemical polarisation measurements in 3% NaCl.

## **6. Appendix**

**Appendix I Deposition Parameters**

**Appendix II Publications**

## Appendix I Deposition Parameters

### (I) Comparison of Nb coatings deposited by UBM and SCAE

	<b>UBM 1</b>	<b>SCAE 1</b>	<b>SCAE 2</b>
<b>(i) Heating and pump down</b>	Pressure = $8 \times 10^{-5}$ mbar Temperature = 250°C	Pressure = $8 \times 10^{-5}$ mbar Temperature = 250°C	Pressure = $8 \times 10^{-5}$ mbar Temperature = 250°C
<b>(ii) Target sputter cleaning</b>	Mode = UBM One target = Nb Cathode power = 1kW Coil current = 0A Substr. bias voltage = 0V Time = 2 min Work. pressure = $3 \times 10^{-3}$ mbar Temperature = 250°C	Mode = UBM One target = Nb Cathode power = 1kW Coil current = 0A Substr. bias voltage = 0V Time = 2 min Work. pressure = $3 \times 10^{-3}$ mbar Temperature = 250°C	Mode = UBM One target = Nb Cathode power = 1kW Coil current = 0A Substr. bias voltage = 0V Time = 2 min Work. pressure = $3 \times 10^{-3}$ mbar Temperature = 250°C
<b>(iii) Substrate sputter cleaning</b>	Mode = SCAE One target = Nb Arc current = 100A Coil current = 0A Substr. bias voltage = -1200V Time = 10 min Work. pressure = $2 \times 10^{-3}$ mbar Temperature = 250- 420°C Rotation = 3-fold	Mode = SCAE One target = Nb Arc current = 100A Coil current = 0A Substr. bias voltage = -1200V Time = 10 min Work. pressure = $2 \times 10^{-3}$ mbar Temperature = 250- 420°C Rotation = 3-fold	Mode = SCAE One target = Nb Arc current = 100A Coil current = 0A Substr. bias voltage = -1200V Time = 10 min Work. pressure = $2 \times 10^{-3}$ mbar Temperature = 250- 420°C Rotation = 3-fold
<b>(iv) Coating deposition</b>	Mode = UBM One target = Nb Cathode power = 8kW Coil current = 6A Substr. bias voltage = -75V Time = 105 min Work. pressure = $3 \times 10^{-3}$ mbar Temperature = 420°C Rotation = 3-fold	Mode = SCAE One target = Nb Arc current = 100A Coil current = 0A Substr. bias voltage = -75V Time = 240 min Work. pressure = $3 \times 10^{-3}$ mbar Temperature = 420°C <b>Rotation = 3-fold</b>	Mode = SCAE One target = Nb Arc current = 100A Coil current = 0A Substr. bias voltage = -75V Time = 240 min Work. pressure = $3 \times 10^{-3}$ mbar Temperature = 420°C <b>Rotation = 2-fold</b>
<b>(iv) Cool down and venting</b>	Temperature < 170°C	Temperature < 170°C	Temperature < 170°C

(II) Influence of Temperature and Ion Bombardment on UBM Nb Coatings

	<b>UBM 1</b>	<b>UBM 2</b>
<b>(i) Heating and pump down</b>	Pressure = $8 \times 10^{-3}$ mbar Temperature = 250°C	Pressure = $8 \times 10^{-3}$ mbar Temperature = 250°C
<b>(ii) Target sputter cleaning</b>	Mode = UBM One target = Nb Cathode power = 1kW Coil current = 0A Substr. bias voltage = 0V Time = 2 min Work. pressure = $3 \times 10^{-3}$ mbar Temperature = 250°C	Mode = UBM One target = Nb Cathode power = 1kW Coil current = 0A Substr. bias voltage = 0V Time = 2 min Work. pressure = $3 \times 10^{-3}$ mbar Temperature = 150°C
<b>(iii) Substrate sputter cleaning</b>	Mode = SCAE One target = Nb Arc current = 100A Coil current = 0A Substr. bias voltage = -1200V Time = 10 min Work. pressure = $2 \times 10^{-3}$ mbar Temperature = 250- 420°C Rotation = 3-fold	Mode = SCAE One target = Nb Arc current = 100A Coil current = 0A Substr. bias voltage = -1200V Time = 10 min (3 x 3.3 min) Work. pressure = $2 \times 10^{-3}$ mbar Temperature = 150- 250°C Rotation = 3-fold
<b>(iv) Coating deposition</b>	Mode = UBM One target = Nb Cathode power = 8kW <b>Coil current = 6A</b> Substr. bias voltage = -75V Time = 105 min Work. pressure = $3 \times 10^{-3}$ mbar <b>Temperature = 420°C</b> Rotation = 3-fold	Mode = UBM One target = Nb Cathode power = 8kW <b>Coil current = 3A</b> Substr. bias voltage = -75V Time = 105 min Work. pressure = $3 \times 10^{-3}$ mbar <b>Temperature = 250°C</b> Rotation = 3-fold
<b>(iv) Cool down and venting</b>	Temperature < 170°C	Temperature < 170°C

(III) Influence of the Ion-Etching Pre-Treatment prior to Sputter Deposition

	UBM (Nb)	UBM (Cr)	UBM (Ar)
<b>(i) Heating and pump down</b>	Pressure = $8 \times 10^{-3}$ mbar Temperature = 250°C	Pressure = $8 \times 10^{-3}$ mbar Temperature = 250°C	Pressure = $8 \times 10^{-3}$ mbar Temperature = 250°C
<b>(ii) Target sputter cleaning</b>	Mode = UBM One target = Nb Cathode power = 1kW Coil current = 0A Substr. bias voltage = 0V Time = 2 min Work. pressure = $3 \times 10^{-3}$ mbar Temperature = 150°C	Mode = UBM One target = Nb One target = Cr Cathode power = 1kW Coil current = 0A Substr. bias voltage = 0V Time = 2 min Work. pressure = $3 \times 10^{-3}$ mbar Temperature = 150°C	Mode = UBM One target = Nb Cathode power = 1kW Coil current = 0A Substr. bias voltage = 0V Time = 2 min Work. pressure = $3 \times 10^{-3}$ mbar Temperature = 220°C
<b>(iii) Substrate sputter cleaning</b>	<b>Mode = SCAE</b> <b>One target = Nb</b> Arc current = 100A Coil current = 0A Substr. bias voltage = -1200V Time = 10 min (3 x 3.3 min) Work. pressure = $2 \times 10^{-3}$ mbar Temperature = 150- 250°C Rotation = 3-fold	<b>Mode = SCAE</b> <b>One target = Cr</b> Arc current = 100A Coil current = 0A Substr. bias voltage = -1200V Time = 10 min (2 x 5 min) Work. pressure = $2 \times 10^{-3}$ mbar Temperature = 150- 250°C Rotation = 3-fold	<b>Mode = Ar Glow discharge</b> One target = Nb One target = Cr Cathode voltage = 200V Coil current = 5A Substr. bias voltage = -1200V Time = 10 min Work. pressure = $4 \times 10^{-3}$ mbar Temperature = 220- 250°C Rotation = 3-fold
<b>(iv) Coating deposition</b>	Mode = UBM One target = Nb Cathode power = 8kW Coil current = 3A Substr. bias voltage = -75V Time = 105 min Work. pressure = $3 \times 10^{-3}$ mbar Temperature = 250°C Rotation = 3-fold	Mode = UBM One target = Nb Cathode power = 8kW Coil current = 3A Substr. bias voltage = -75V Time = 105 min Work. pressure = $3 \times 10^{-3}$ mbar Temperature = 250°C Rotation = 3-fold	Mode = UBM One target = Nb Cathode power = 8kW Coil current = 3A Substr. bias voltage = -75V Time = 105 min Work. pressure = $3 \times 10^{-3}$ mbar Temperature = 250°C Rotation = 3-fold
<b>(iv) Cool down and venting</b>	Temperature < 170°C	Temperature < 170°C	Temperature < 170°C

(IV) Nb-Ion Etching prior to Sputter Deposition: Influence of Working Gas Pressure and Substrate Bias Voltage

	<b>Nb-etch + Nb coating (High pressure series)</b>	<b>Nb-etch + Nb coating (Low pressure series)</b>	<b>Nb-etch only</b>
<b>(i) Heating and pump down</b>	Pressure = $8 \times 10^{-5}$ mbar Temperature = 250°C	Pressure = $8 \times 10^{-5}$ mbar Temperature = 250°C	Pressure = $8 \times 10^{-5}$ mbar Temperature = 250°C
<b>(ii) Target sputter cleaning</b>	Mode =UBM One target = Nb Cathode power = 1kW Coil current = 0A Substr. bias voltage = -0V Time = 2 min Work. pressure = $3 \times 10^{-3}$ mbar Temperature = 250°C	Mode =UBM One target = Nb Cathode power = 1kW Coil current = 0A Substr. bias voltage = -0V Time = 2 min Work. pressure = $3 \times 10^{-3}$ mbar Temperature = 250°C	Mode =UBM One target = Nb Cathode power = 1kW Coil current = 0A Substr. bias voltage = -0V Time = 2 min Work. pressure = $3 \times 10^{-3}$ mbar Temperature = 250°C
<b>(iii) Substrate sputter cleaning</b>	Mode = SCAE One target = Nb Arc current = 100A Coil current = 0A Substr. bias voltage = -1200V, -1000V, -800V, - 600V, -400V Time = 12 min Work. pressure = $2 \times 10^{-3}$ mbar Temperature = 250- 420°C Rotation = 3-fold	Mode = SCAE One target = Nb Arc current = 100A Coil current = 0A Substr. bias voltage = -1200V, -1000V, -800V, - 600V, -400V, -200V Time = 12 min Work. pressure = $8 \times 10^{-4}$ mbar Temperature = 250- 420°C Rotation = 3-fold	Mode = SCAE One target = Nb Arc current = 100A Coil current = 0A Substr. bias voltage = -1200V, -1000V, -800V, - 600V, -400V Time = 12 min Work. pressure = $8 \times 10^{-4}$ mbar Temperature = 250- 420°C Rotation = 3-fold
<b>(iv) Coating deposition</b>	Mode = UBM One target = Nb Cathode power = 10kW Coil current = 6A Substr. bias voltage = -75V Time = 20min Work. pressure = $3 \times 10^{-3}$ mbar Temperature = 420°C Rotation = 3-fold	Mode = UBM One target = Nb Cathode power = 10kW Coil current = 6A Substr. bias voltage = -75V Time = 20min Work. pressure = $3 \times 10^{-3}$ mbar Temperature = 420°C Rotation = 3-fold	<b>None</b>
<b>(iv) Cool down and venting</b>	Temperature < 170°C	Temperature < 170°C	Temperature < 170°C

(V) Intermediate Nb Ion Etching

	Intermediate etches at -600V	Intermediate etches at -1200V
<b>(i) Heating and pump down</b>	Pressure = $8 \times 10^{-5}$ mbar Temperature = 250°C	Pressure = $8 \times 10^{-5}$ mbar Temperature = 250°C
<b>(ii) Target sputter cleaning</b>	Mode =UBM One target = Nb Cathode power = 1kW Coil current = 0A Substr. bias voltage = 0V Time = 2 min Work. pressure = $3 \times 10^{-3}$ mbar Temperature = 200°C	Mode =UBM One target = Nb Cathode power = 1kW Coil current = 0A Substr. bias voltage = 0V Time = 2 min Work. pressure = $3 \times 10^{-3}$ mbar Temperature = 200°C
<b>(iii) Substrate sputter cleaning</b>	Mode = SCAE One target = Nb Arc current = 100A Coil current = 0A Substr. bias voltage = Time = 10-12 min Work. pressure = $2 \times 10^{-3}$ mbar Temperature = 200- 300°C Rotation = 3-fold	Mode = SCAE One target = Nb Arc current = 100A Coil current = 0A Substr. bias voltage = Time = 10-12 min Work. pressure = $2 \times 10^{-3}$ mbar Temperature = 200- 300°C Rotation = 3-fold
<b>(iv) Coating deposition</b>	Mode = UBM One target = Nb Cathode power = 8kW Coil current = 6A Substr. bias voltage = -75V Time = 105 min Work. pressure = $3 \times 10^{-3}$ mbar Temperature = 300 - 420°C Rotation = 3-fold  <b>Two intermediate etching stages (Nb arc) at 1/3 and 2/3 of the sputter deposition time.</b> <b>Substr. bias voltage = -600V</b>	Mode = UBM One target = Nb Cathode power = 8kW Coil current = 6A Substr. bias voltage = -75V Time = 105 min Work. pressure = $3 \times 10^{-3}$ mbar Temperature = 300- 420°C Rotation = 3-fold  <b>Two intermediate etching stages (Nb arc) at 1/3 and 2/3 of the sputter deposition time.</b> <b>Substr. bias voltage = -1200V</b>
<b>(iv) Cool down and venting</b>	Temperature < 170°C	Temperature < 170°C

(VI) Etching Rate

	<b>NiCr coated sample</b>
<b>(i) Heating and pump down</b>	Pressure = $8 \times 10^{-3}$ mbar Temperature = 250°C
<b>(ii) Target sputter cleaning</b>	Mode =UBM One target = Nb Cathode power = 1kW Coil current = 0A Substr. bias voltage = 0V Time = 2 min Work. pressure = $3 \times 10^{-3}$ mbar Temperature = 250°C
<b>(iii) Etching</b>	<b>Mode = SCAE</b> <b>One target = Nb</b> Arc current = 100A Coil current = 0A Substr. bias voltage = -1200V Time = 12 min Work. pressure = $2 \times 10^{-3}$ mbar Temperature = 250- 420°C Rotation = 3-fold
<b>(iv) Coating deposition</b>	None
<b>(iv) Cool down and venting</b>	Temperature < 170°C

(VII) Niobium Coatings on Brass Substrates: Substrate Ion Etch (at A.T.Cross Ltd.)

	<b>Brass 1</b>
<b>(i) Heating and pump down</b>	Pressure = $8 \times 10^{-3}$ mbar Temperature = 250°C
<b>(ii) Target sputter cleaning</b>	Mode =UBM One target = Nb One target = Cu Cathode power = 1kW Coil current = 0A Substr. bias voltage = 0V Time = 2 min Work. pressure = $3 \times 10^{-3}$ mbar Temperature = 150°C
<b>(iii) Substrate sputter cleaning</b>	<b>Mode = SCAE</b> <b>One target = Nb</b> Arc current = 100A Coil current = 0A

	Substr. bias voltage = -600V Time = 10 min (3 x 3.3 min) Work. pressure = $4 \times 10^{-3}$ mbar Temperature = 150- 250°C Rotation = 3-fold
<b>(iv) Coating deposition</b>	<b>None</b>
<b>(iv) Cool down and venting</b>	Temperature < 170°C

(VIII) Niobium Coatings on Brass substrates: Zn-Diffusion Barrier

	<b>Cu layer</b>	<b>CuAlFe layer</b>	<b>CuAlFe + NiCr layer</b>
<b>(i) Heating and pump down</b>	Pressure = $8 \times 10^{-5}$ mbar Temperature = 250°C	Pressure = $8 \times 10^{-5}$ mbar Temperature = 250°C	Pressure = $8 \times 10^{-5}$ mbar Temperature = 250°C
<b>(ii) Target sputter cleaning</b>	Mode =UBM One target = Nb One target = Cu Cathode power = 1kW Coil current = 0A Substr. bias voltage = 0V Time = 2 min Work. pressure = $3 \times 10^{-3}$ mbar Temperature = 180°C	Mode =UBM One target = Nb One target = CuAlFe Cathode power = 1kW Coil current = 0A Substr. bias voltage = 0V Time = 2 min Work. pressure = $3 \times 10^{-3}$ mbar Temperature = 180°C	Mode =UBM One target = Nb One target = Cu Cathode power = 1kW Coil current = 0A Substr. bias voltage = 0V Time = 2 min Work. pressure = $3 \times 10^{-3}$ mbar Temperature = 180°C
<b>(iii) Substrate sputter cleaning</b>	Mode = Glow discharge One target = Nb Cathode voltage = 200V Coil current = 5A Substr. bias voltage = -1200V Time = 10-12 min Work. pressure = $4 \times 10^{-3}$ mbar Temperature = 180- 230°C Rotation = 3-fold	Mode = Glow discharge One target = Nb Cathode voltage = 200V Coil current = 5A Substr. bias voltage = -1200V Time = 10-12 min Work. pressure = $4 \times 10^{-3}$ mbar Temperature = 180- 230°C Rotation = 3-fold	Mode = Glow discharge One target = Nb Cathode voltage = 200V Coil current = 5A Substr. bias voltage = -1200V Time = 10-12 min Work. pressure = $4 \times 10^{-3}$ mbar Temperature = 180- 220°C Rotation = 3-fold
<b>(iv) Coating deposition</b>	<u>1) Cu deposition:</u> Mode = UBM <b>One target = Cu</b> Cathode power = 8kW Coil current = 3A Substr. bias voltage = -75V Time = 15 min Work. pressure = $3 \times 10^{-3}$ mbar Temperature = 230°C	<u>1) CuAlFe deposition:</u> Mode = UBM <b>One target = CuAlFe</b> Cathode power = 8kW Coil current = 3A Substr. bias voltage = -75V Time = 15 min Work. pressure = $3 \times 10^{-3}$ mbar Temperature = 230°C	<u>1) CuAlFe deposition:</u> Mode = UBM <b>One target = CuAlFe</b> Cathode power = 8kW Coil current = 3A Substr. bias voltage = -75V Time = 15 min Work. pressure = $3 \times 10^{-3}$ mbar Temperature = 220°C  <u>2) NiCr deposition:</u> Mode = UBM

	<p>2) <u>Nb deposition</u>  Mode = UBM  One target = Nb  Cathode power = 8kW  Coil current = 3A  Substr. bias voltage = -75V  Time = 105 min  Work. pressure = <math>3 \times 10^{-3}</math> mbar  Temperature = 250°C  Rotation = 3-fold</p>	<p>2) <u>Nb deposition</u>  Mode = UBM  One target = Nb  Cathode power = 8kW  Coil current = 3A  Substr. bias voltage = -75V  Time = 105 min  Work. pressure = <math>3 \times 10^{-3}</math> mbar  Temperature = 250°C  Rotation = 3-fold</p>	<p><b>One target = NiCr</b>  Cathode power = 7kW  Coil current = 3A  Substr. bias voltage = -75V  Time = 60 min  Work. pressure = <math>3 \times 10^{-3}</math> mbar  Temperature = 240°C  3) <u>Nb deposition</u>  Mode = UBM  One target = Nb  Cathode power = 8kW  Coil current = 3A  Substr. bias voltage = -75V  Time = 105 min  Work. pressure = <math>3 \times 10^{-3}</math> mbar  Temperature = 250°C  Rotation = 3-fold</p>
<b>(iv) Cool down and venting</b>	Temperature < 170°C	Temperature < 170°C	Temperature < 170°C

(IX) Intermediate Nb Ion Etching of Cu Baselayer (at A.T.Cross Ltd.)

	<b>Cu layer + intermediate etch</b>
<b>(i) Heating and pump down</b>	Pressure = $8 \times 10^{-3}$ mbar Temperature = 250°C
<b>(ii) Target sputter cleaning</b>	Mode = UBM One target = Nb One target = Cu Cathode power = 1kW Coil current = 0A Substr. bias voltage = 0V Time = 2 min Work. pressure = $3 \times 10^{-3}$ mbar Temperature = 150°C
<b>(iii) Substrate sputter cleaning</b>	Mode = Glow discharge One target = Nb Cathode voltage = 200V Coil current = 5A Substr. bias voltage = -1200V Time = 20 Work. pressure = $5 \times 10^{-3}$ mbar Temperature = 150- 170°C Rotation = 3-fold

<p><b>(iv) Coating deposition</b></p>	<p><u>1) Cu deposition:</u>  Mode = UBM  <b>One target = Cu</b>  Cathode power = 10kW  Coil current = 4A  Substr. bias voltage = -75V  Time = 25 min  Work. pressure = <math>3 \times 10^{-3}</math> mbar  Temperature = 170°C</p> <p><u>2) Intermediate etch:</u>  <b>Mode = SCAE</b>  One target = Nb  Arc current = 100A  Coil current = 0A  Substr. bias voltage = -600V  Time = 10min (3 x 3.3)  Work. pressure = <math>2 \times 10^{-3}</math> mbar  Temperature = 170- 250°C  Rotation = 3-fold</p> <p><u>3) Nb deposition</u>  Mode = UBM  One target = Nb  Cathode power = 10kW  Coil current = 4A  Substr. bias voltage = -75V  Time = 105 min  Work. pressure = <math>3 \times 10^{-3}</math> mbar  Temperature = 250°C  Rotation = 3-fold</p>
	<p><b>(iv) Cool down and venting</b></p>

# Coatings Grown by Combined Steered Arc/Unbalanced Magnetron Deposition

I. Paritong, I. Wadsworth,  
L.A. Donohue,  
W.-D. Münz

Materials Research Institute,  
Sheffield Hallam University, City Campus,  
Pond Street, Sheffield S1 1WB, UK

**SUMMARY** – Niobium is well known for its chemical stability and excellent corrosion resistance which is based on the formation of a stable oxide layer of  $Nb_2O_5$  in aqueous media. It therefore finds wide application in areas where chemical stability is important, such as in chemical engineering equipment. Disadvantages of Nb are its high material costs and the fact that it is not possible to deposit Nb by the rather economic technique of aqueous electrodeposition. However, other deposition techniques such as physical vapour deposition may be used to produce niobium coatings. Due to its high melting point, sputtering is the preferred PVD deposition technology.

Improved corrosion resistance approaching that of bulk Nb was found for  $1\mu\text{m}$  thick Nb coatings on 304 stainless steel substrates. The corrosion performance very much depends on the method of ion etching prior to deposition. Microstructure, texture and microhardness as well are strongly influenced by the type of ion etching pre-treatment and by the temperature during deposition. Nb-ion etching of the 304 stainless steel substrate and consequent Nb deposition with unbalanced magnetron sputtering at a temperature as low as  $250^\circ\text{C}$ , utilising an ion to neutral ratio of 4, leads to dense films. These films exhibit passivation over the whole range of the applied polarisation measurements in a 3% NaCl solution.

## INTRODUCTION

Niobium and tantalum are well known for their chemical stability and corrosion resistance which is due to the formation of a passivating oxide layer<sup>1,2</sup>. Niobium is regarded as 'moderately to highly resistant to corrosion in most aqueous media' and are usually considered highly corrosive such as mineral acids, organic acids and organic liquids<sup>3</sup>. Although tantalum performs better than niobium in its chemical resistance, niobium is an attractive candidate for industrial applications due to its lower density (Nb:  $8.6\text{ g/cm}^3$ ; Ta:  $16.6\text{ g/cm}^3$ ) and its lower material costs. Like aluminium and tantalum, deposition of Nb by electroplating is not possible due to the formation of the electrical insulating layer  $Nb_2O_5$  in aqueous electrolytes.

Sputtering is the preferred PVD technique to deposit refractory metals because sputter yield is virtually independent of the melting point of the material<sup>4</sup> (Nb:  $2552^\circ\text{C}$ , Ta:  $2956^\circ\text{C}$ ). In the case of low deposition temperatures though, a high melting point of the coating material influences the morphology of the coating, as it greatly depends on the ratio  $T_S/T_M$ , where  $T_S$  is the temperature of the substrate and  $T_M$  is the melting point of the material<sup>5,6</sup>. However, it has been

shown that a dendritic, open structured film growth can be avoided by applying sufficient ion bombardment during film growth<sup>7,8</sup>.

A variety of papers have been published which describe the influence of the deposition parameters on the microstructure and physical properties of niobium coatings<sup>9-13</sup>. Relatively little information is available on the corrosion behaviour of niobium coated steel substrates<sup>9,13</sup>. As pointed out by Hsieh et al.<sup>9</sup> Nb-PVD coatings with a corrosion behaviour similar to that of bulk niobium can be produced when optimised deposition parameters are applied using the IBAD technique.

In this study  $1\mu\text{m}$  thick Nb coatings were deposited at  $250^\circ\text{C}$  and at  $420^\circ\text{C}$  on 304 stainless steel substrates in an industrial-sized PVD coating equipment utilising the ABS<sup>TM</sup> technology (combined steered arc/unbalanced magnetron)<sup>14</sup>. This technique allows thin film deposition in highly ionised gas atmospheres and cosputtering of various target materials. Special attention was paid to the ion etching pre-treatment prior to coating. Inert  $\text{Ar}^+$  etching is compared with cathodic arc metal ion etching using Nb-ions ( $\text{Nb}^{1+} - \text{Nb}^{5+}$ ) and Cr-ions ( $\text{Cr}^{1+} - \text{Cr}^{4+}$ ) respectively<sup>15</sup>. Cr was chosen as etching material due to its characteristics to form the smallest sized droplets, in relatively small concentration, of refractory metals used in the ion etching step<sup>16,17</sup>.

## EXPERIMENTAL

### Coating deposition

A schematic cross-section of the HTC

1000-4 ABS<sup>TM</sup> coating chamber (Hauzer Techno Coating, Europe BV, Venlo, The Netherlands) is shown in Figure 1. The vacuum chamber is 1 m in diameter and is equipped with four rectangular dual purpose targets which can be used in either the steered-arc mode or in the magnetron mode by adjustment of the permanent magnetic field located behind the targets<sup>14</sup>. Unbalancing of the magnetrons is accomplished by using electromagnetic coils which are concentrically mounted to the targets. The magnetic pole arrangement of the cathodes leads to a closed field configuration in the vacuum chamber. In this technique average bias current densities between 0.2 and  $5\text{ mA/cm}^2$  can be achieved.

During deposition the substrates

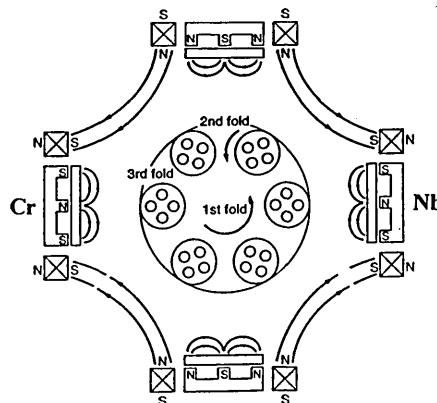


Figure 1. Schematic cross-section of the Hauzer HTC 1000-4 coating chamber.

I. Paritong, I. Wadsworth, L.A. Donohue,  
W.-D. Münz, *Trans IMF*, 1998, 76(4), 144

the interplanar space and  $\lambda$  is the camera constant, which in this particular case was 2.0 nm. From this, major poles were indexed, two first order reflexions  $[0\bar{1}10]$  and  $[0\bar{1}11]$  and two second order reflexions  $[0220]$  and  $[0222]$ .

The sample E, Plate 7(a) and (b), was prepared as a powder and analysed in the TEM. Bright field images were obtained. The image was tilted along from the  $[1\bar{2}10]$  plane, and further tilt led to the  $[2\bar{1}\bar{1}0]$  plane from which the C/A ratio was calculated. The C/A value calculated was 1.065 is consistent with the theoretical 1.09. Edington<sup>19</sup>.

## CONCLUSIONS

### System Evaluation:

The evaluation of the zinc-cobalt alloy system showed that cobalt content in the deposit is directly dependent on electrolyte composition and plating temperature. The current density affects cathodic current efficiency but has no significant effect on cobalt percentage in the alloy.

This investigation showed that hardness increases with increasing cobalt content in the deposit for either as-deposited or heat-treated samples.

Zinc cobalt alloy electrodeposition from alkaline electrolyte manifested anomalous behaviour in the range of current densities and electrolyte composition studied.

### Characterization of the Deposit Structure

In this investigation it was demonstrated that zinc-cobalt alloys deposited from either alkaline or acid, are single phase systems. The  $\eta$  phase found was a substitutional solid solution of cobalt dissolved in the zinc lattice.

After heat-treatment the X-ray diffraction results for samples obtained from electrolytes E and Acid presented extra peaks suggesting the formation of other phases.

The deposit morphology and grain size changed with temperature and cobalt percentage in the electrolyte, however no changes were observed in relation to current density. The more cobalt in the deposit the smaller the grain size. The grain sizes were measured, and typical val-

ues are given in Table 1.

The system was identified as (hcp) hexagonal close-packed according to X-ray and TEM diffraction studies. The unit cell volumes for zinc-cobalt and pure zinc were calculated based on lattice parameters obtained from the X-ray and the former was found similar to pure zinc.

## ACKNOWLEDGMENT

The authors would like to thank the Brazilian Government for the financial support.

## REFERENCES

- 1 W. M. J. C. Verbene, "Zinc-Cobalt alloy electrodeposition". *Transactions of the Institute of Metal Finishing*, (1986) **64**, 30-33.
- 2 A. Brenner (1963) "Electrodeposition of Alloys". Academic Press, New York, vol.1 and 2.
- 3 K. R. Baldwin, et al "A study into the electrodeposition mechanism of zinc-nickel alloys from an acid-sulphate bath". *Transaction Institute of Metal Finishing* (1994) **72** (2), 79-88.
- 4 H. Fukushima, et al "Mechanism of the Electrodeposition of Zinc with Iron-Group metals from Sulfate Baths". *Transactions of the Japan Institute of Metals*, (1983) **24**, (3) 125-131.
- 5 J. W. Dini and H. R. Johnson, Sandia National Laboratory, Technical report No 77-8511 (1977). In: K. R. Baldwin and C. J. E. Smith, "A Study into the Electrodeposition Mechanisms of Zinc-Nickel Alloys from an Acid-Sulphate Bath". *Transactions of the Institute of Metal Finishing*, (1994) **72** (2), 79-88.
- 6 Tu. Zhen-mi, et al "The Electrodeposition of Zn-Co Alloy from a Zincate Bath". *Transactions of the Institute of Metal Finishing*, (1995) **73** (2), 48-49.
- 7 F. A. Lowenheim, "Modern Electroplating". John Wiley & Sons, Inc. London, (1963).  
F. A. Lowenheim, "Deposition of Inorganic Films from Solution". In: J.L. Vossen and W. Kern "Thin Film Processes", Academic Press Inc.

Agitation for Electrodeposition Processes. II. Experimental". *Tractions of the Institute of Finishing*, (1994) **72** (2), 66-71.

- 9 R. Weil and K. Sheppard, "Structure of Electrodeposits: Characterization and the Properties They Affect". *Materials Characterization*, (1992) **28**, 103-112.
- 10 J. P. Celis, M. De. Bonte and J. Roos "Electroplating Technology". *Transactions of the Institute of Finishing*, (1994) **72** (2), 89-93.
- 11 B. D. Cullity, "Elements of X-ray fraction" Addison - Wesley Publishing Reading, Massachusetts (1959)
- 12 C. Hammond, "Introduction Crystallography". Oxford Sci Publications, (1994).
- 13 C. A. Drewien, J. I. Goldstein and R. Marder, " $\eta$  to G P Transformation in Electrodeposited Iron-Zinc Alloy Coating". *Metallurgical and Materials Transactions A*, (1994) **25A**, 1119-1125.
- 14 A. J. Morton, "The  $\gamma$ -Phase Region of Cu-Zn, Ni-Zn and Pd-Zn Bi Systems". *Acta Metallurgica*, (1977) **27**, 863-867.
- 15 R. Sandip and T. Banerjee, "Phase Transformations in Electrolytic Silver-Zinc Alloys". *Electrodeposition Surface Treatment*, (1975) **3**, 289-3
- 16 C. A. Drewien, J. I. Goldstein and R. Marder, "Structure of as-Deposited Iron-Zinc Coatings from Chloride Bath". *Metallurgical and Materials Transactions A*, (1994) **25A**, 249-2
- 17 E. A. Owen and I. G. Edmi (1935). In: R. Sandip and T. Banerjee "Phase Transformations in Electrodeposited Silver-Zinc Alloys". *Electrodeposition and Surface Treatment*, (1975) 289-305.
- 18 E. Raub and B. Wullhorst, (1947) R. Sandip and T. Banerjee, "Phase Transformations in Electrodeposited Silver-Zinc Alloys". *Electrodeposition and Surface Treatment*, (1975) 289-305.
- 19 J. W. Edington, "Electron diffraction in electron microscope". Macmillan Philips Technical Library, (1975).

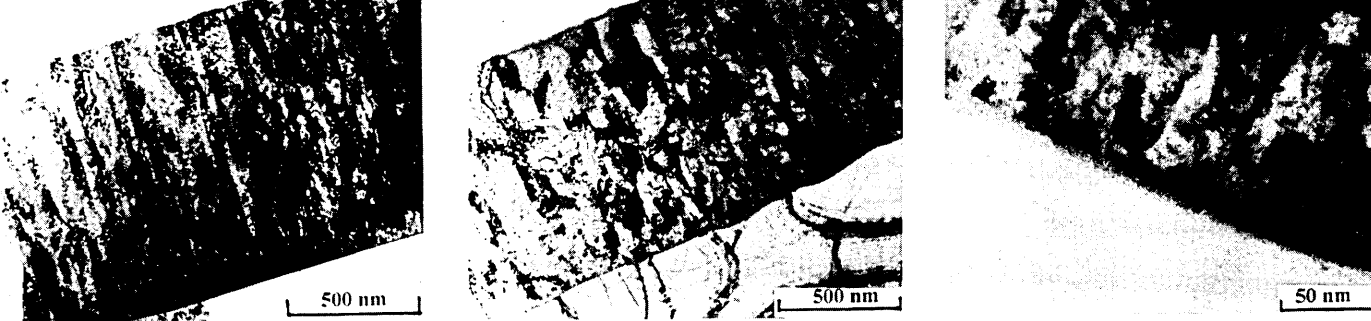


Figure 2. TEM images showing cross-sections of Nb-etch/Nb coatings deposited at 420°C (2a) and 250°C (2b), including the interfacial region (2c)

dergo 3-axis planetary motion. This was ne to allow correlation of the results to e coating of three-dimensional parts ed in industrial applications. Pure Nb atings were deposited from one target. is target was also used for the ion etch- g state, when Nb was the chosen etching aterial. Ion etching with Cr was done om an additional Cr-target opposing the -target as shown in Figure 1. The films ere deposited on stainless steel sub- ates, polished to a 1 μm finish. The depo- sition parameters are given in Table 1.

### st methods for structural and physical operties

The microstructure of the coatings was vestigated using cross-sectional trans- mission electron microscopy.

The phases present, the crystallographic entation and macrostrains were deter- mined by X-ray diffraction using a Philips wder diffractometer in Bragg-Brentano ometry. The crystallographic texture P the coatings was calculated using the verse pole figure technique:

$$P = \frac{I_{hkl}}{R_{hk}} \quad (1)$$

$$\frac{1}{n} \sum_0^n \frac{I_{hkl}}{R_{hkl}}$$

here  $I_{hkl}$  are the intensities from the hkl ections in the specimen and  $R_{hkl}$  are e intensities of the hkl reflections from a dom powder respectively.

The macrostrain  $\epsilon$ , parallel to the coat- substrate interface, was calculated for ch family of planes from the following:

$$\epsilon = \frac{d_{n(hkl)} - d_{0(hkl)}}{d_{0(hkl)}} \quad (2)$$

here  $d_{n(hkl)}$  are the interplanar spacings the specimen and  $d_{0(hkl)}$  are the inter- nar spacings in the unstressed metal pectively.

A Mitutoyo MVK-G1 Knoop indenter h an applied load of 3 g was used to termine the microhardness of the coat- s.

### rosion measurements

tentiodynamic polarisation measure- nts were chosen to evaluate the corro- n performance of the coated specimen. e equipment used was a EG&G tentiostat/Galvanostat 263A. The sam- s were polarised from -800 mV to

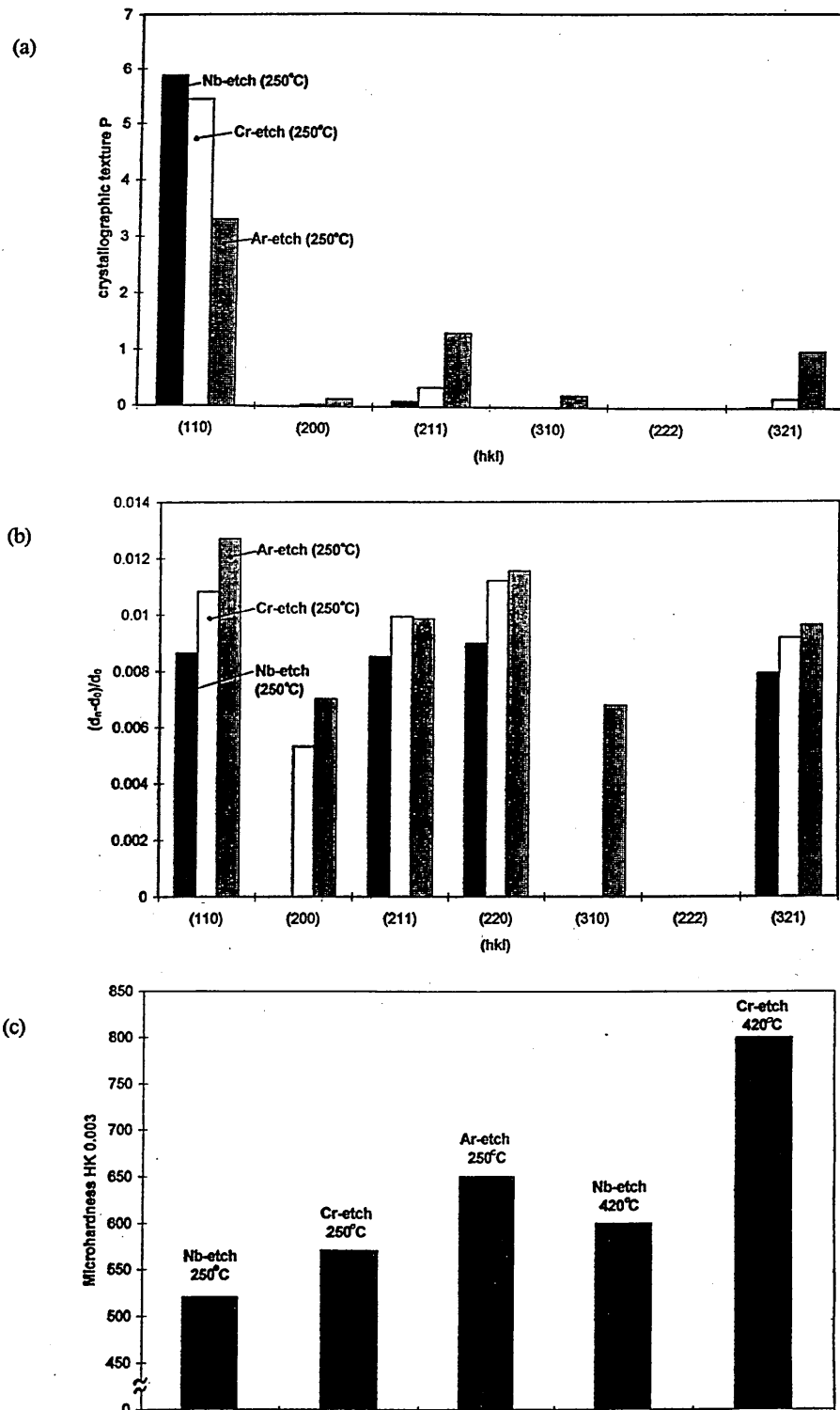


Figure 3. Comparison of the texture of low temperature Nb coatings (a), the macrostrain of low temperature Nb coatings (b) and the microhardness of low and high temperature Nb coatings (c).

Ion etching (10 min)		Nb-deposition (105 min)						
Etching species	Bias Voltage [V]	Temperature [°C]	Nb-Target Power [kw]	Bias Voltage [V]	Bias Current Density [mA/cm <sup>2</sup> ]	Coil Current [A]	Pressure [mbar]	Coating Thickness [μm]
Nb	-1200	250	8	-7S	1	4 × 3	2.7*10 <sup>-3</sup>	1
Cr	-1200	250	8	-75	1	4 × 3	2.7*10 <sup>-3</sup>	1
Ar	-1200	250	8	-75	1	4 × 3	2.8*10 <sup>-3</sup>	1
Nb	-1200	420	8	-75	2	4 × 6	2.8*10 <sup>-3</sup>	1
Cr	-1200	420	8	-75	2	4 × 6	2.7*10 <sup>-3</sup>	1

+900 mV (vs. SCE) in a 3% NaCl solution open to air with a scan rate of 0.5 mV/sec. Prior to the polarisation measurement the testing solution was aerated for 55 min and the samples were cathodically cleaned for 100 sec.

## RESULTS

### Structural and physical properties

Important features of the microstructure of Nb coatings, produced with a Nb-ion etch, are shown in Figure 2a, 2b and 2c. Both films, deposited at 420°C (Figure 2a) and at 250°C (Figure 2b) exhibit a clear columnar structure. However, the high

temperature coating shows a more regular film growth with smaller column diameters and a smoother surface. No inter- or intracolumnar porosity can be observed for both coatings, it can therefore be concluded that dense coatings are grown at a high deposition temperature as well as at a low deposition temperature. As already shown<sup>13</sup>, a thin oxide layer forms on the surface of the Nb-coatings which is commonly known as "natural oxide"<sup>18</sup>. Figure 2c. shows the interfacial region. It is characterised by an amorphised approximately 10 nm thick Nb layer grown under the influence of radiation damage of the

followed by a region of competitive growth. These features are characteristic when Nb-ions are chosen as the etching material, as has been shown earlier for Nb-coatings (Nb-ion etch)<sup>13</sup> and for TiAlNbN-coatings (TiNb-ion etch)<sup>19</sup>.

The ion etching pre-treatment clearly influences the crystallinity of the deposited coatings. Figure 3a shows the crystallographic texture of the three low temperature Nb-coatings produced with Nb-, Cr- and Ar-ion etch. All coatings exhibit a <110> texture. However, the degree of orientation is influenced by the etching material. The strongest <110> orientation can be observed for the Nb-ion etch film followed by the Cr- and Ar-ion etch coatings. A comparison between the macrostrains in the planes parallel to the coating/substrate interface of the three films is given in Figure 3b. Due to Poisson's effect these macrostrains indicate inplane compressive stresses, which are highest for the coating deposited after the Ar-ion etch and lowest for the Nb-ion etch film. According to these results the microhardness-values increase in the order of Nb-, Cr- and Ar-ion etch shown in Figure 3c.

Additional influence of the deposition parameters was found with respect to the deposition temperature as shown in Figures 4a, 4b and 3c. Although the texture and microhardness of the low- and high temperature Nb-films produced with a Nb-ion etch are very similar, significant differences were found when using Cr-ion etching. A shift from a <110> to a <22> preferred orientation can be observed when increasing the deposition temperature from 250°C to 420°C accompanied by a high inplane stress in the high temperature coating. The microhardness changes significantly as well as shown in Figure 3. The Cr-ion etch/high temperature coating exhibits a hardness value of HK 820 compared to HK 570 for the Cr-ion etch/low temperature film.

The increase in macrostrain with increased deposition temperature observed in both cases, Nb-ion etch coatings and Cr-ion etch coatings, is due partly to higher compressive thermal stresses, which are induced by the differences in the thermal expansion coefficients between the niobium film and the stainless steel substrate (Nb: 7.1 MK<sup>-1</sup> 304 SS: 10.1 MK<sup>-1</sup>).

### Corrosion resistance

Polarisation curves of bulk niobium and uncoated 304 stainless steel are given in references in Figure 5a. Passivation can be observed in both cases due to the formation of protective oxide films. However, while Nb stays passive throughout the range of the polarisation scan, breakdown of the passive layer can be seen in the case of stainless steel. The breakdown is initiated by the restricted stability of the oxidised Cr-film due to the presence of chloride ions in the solution<sup>20</sup> and followed by localised corrosion on the samples. This onset of pitting, characterised by the steep increase in current density

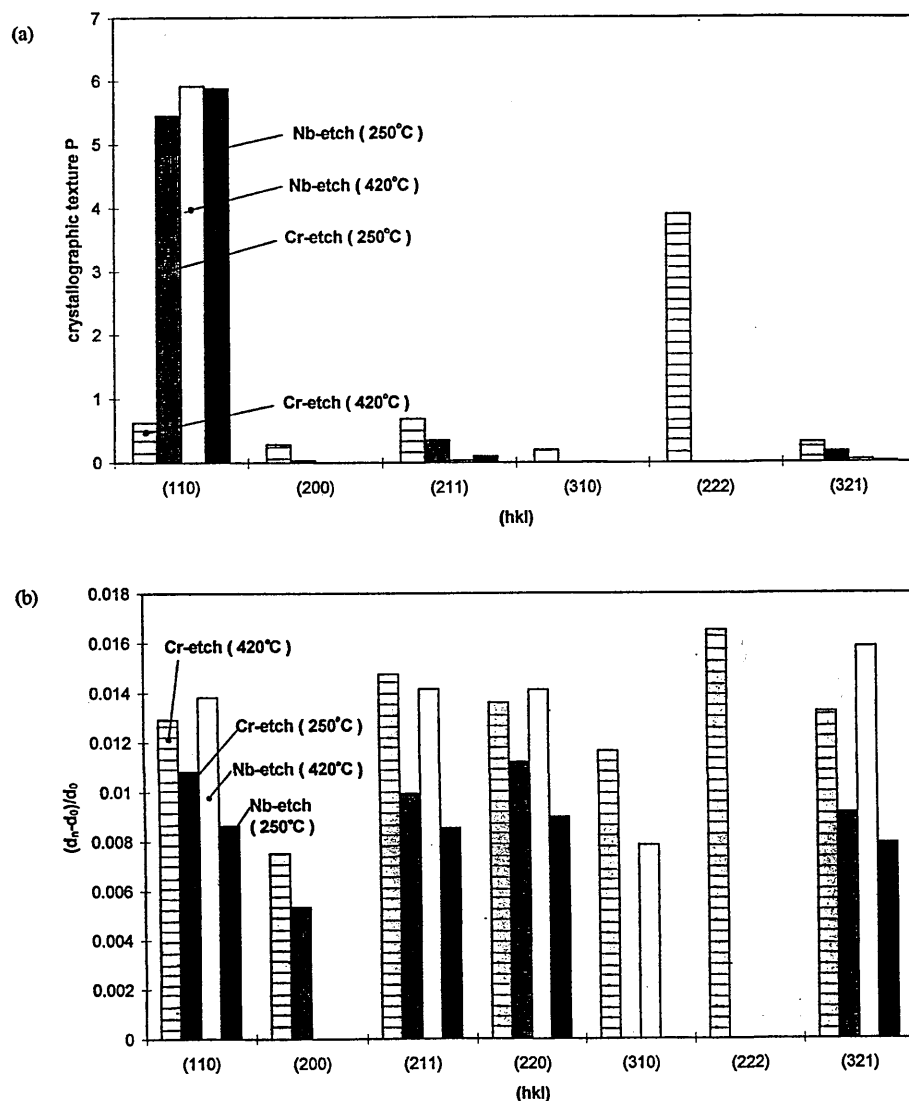
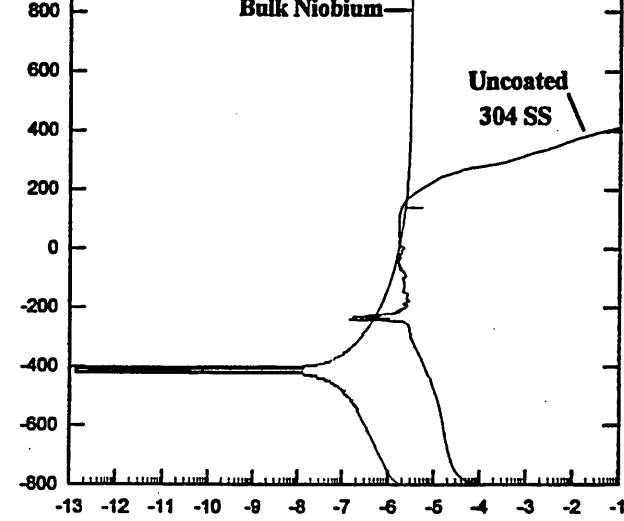


Figure 4. Texture (a) and macrostrain (b) of low and high temperature Nb coatings.



curves of the three low temperature Nb-coatings on 304 stainless steel substrates are shown in Figure 5b. The influence of the etching material on the corrosion performance of the films is evident. The current density in the anodic region is highest for the Ar-ion etch film and lowest for the Nb-ion etch coating. Between +200 and +300 mV the onset of pitting can be observed for both the Cr- and the Ar-ion etch samples. The degree of exposure i.e. of active corrosion of

which is higher for the Ar-ion etch sample compared to the Cr-ion etch coating. However, the current densities in the transpassive region of these two coated samples are smaller than the current density of uncoated steel substrate. The Nb-ion etch coating exhibits excellent corrosion resistance. The sample passivates over the whole range of the scan and its behaviour is very similar to that of bulk niobium, indicating a dense and non-porous coating structure.

Figure 6 shows a cross-section of the corroded Cr-ion etch/Nb-coating on stainless steel. While the steel substrate corrodes locally in form of pits the Nb coating remains unattacked, confirming the noble behaviour of Nb, due to passivation, compared to the more active steel substrate.

The influence of the deposition temperature on the corrosion performance of Nb

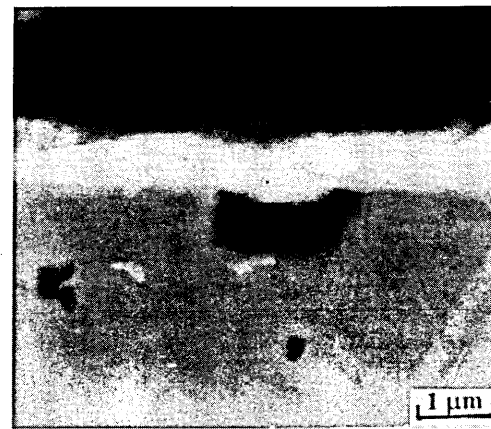
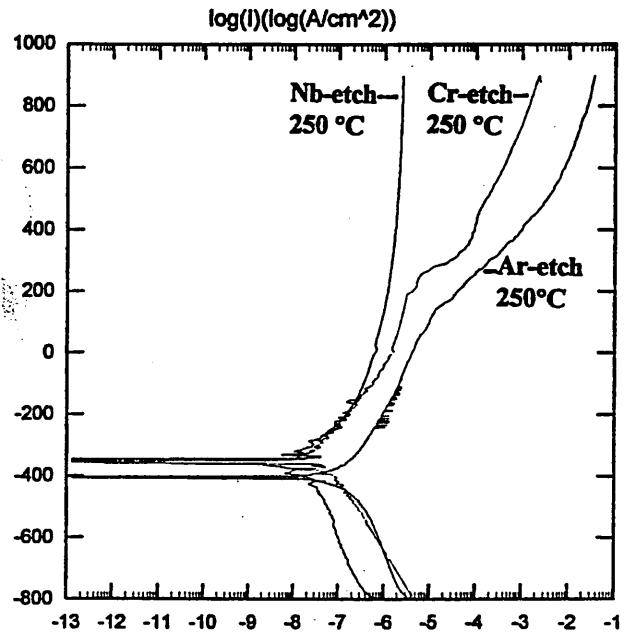


Figure 6. Cross-section of corroded Cr-ion etch/Nb coating (250°C).

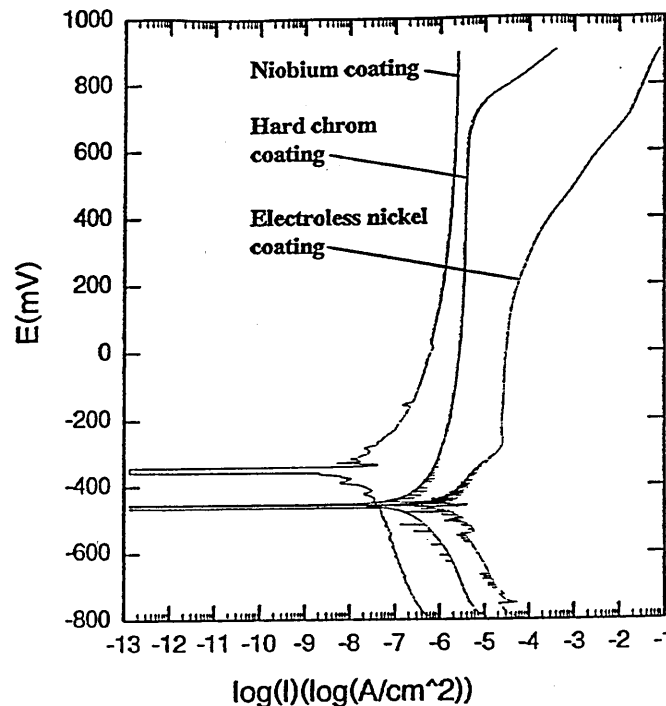
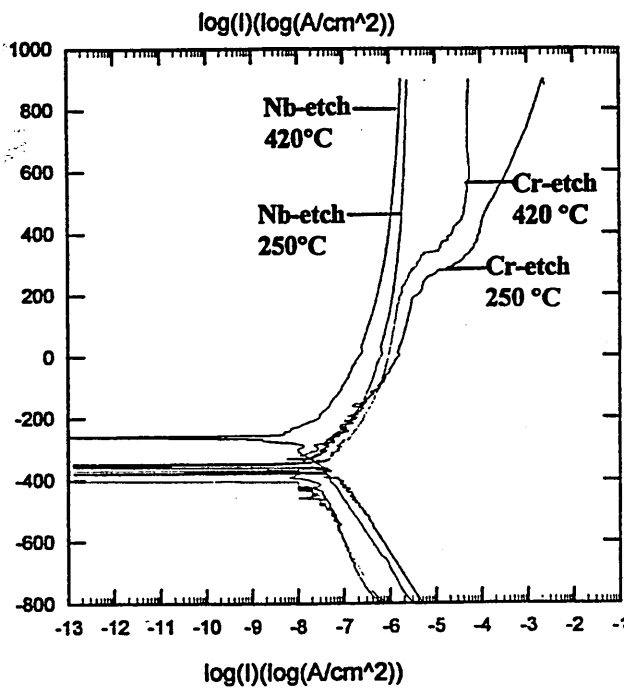


Figure 5. Polarisation curves of bulk niobium and uncoated 304 stainless (a), low temperature Nb coatings (b) and low and high temperature coatings (c).

Figure 7. Polarisation curves of Nb-ion etch/Nb coating (250°C), hard chrome coating and electroless nickel coating on 304 stainless steel.

the case of Nb-ion etching no significant differences in the range of the scan could be seen in the corrosion behaviour of the low and the high temperature coating. This could be expected from the already excellent performance of the film produced at 250°C. In the case of Cr-ion etching the high temperature film exhibits a slightly improved corrosion behaviour compared to the low temperature coating, represented by the extended passive region and the lower current density in the anodic region. The performance of the film though is still not as good as the two coatings produced with a Nb-ion etch.

## DISCUSSION

Both the analyses of the microstructure by TEM and the corrosion results from potentiodynamic polarisation measurements indicate that 1 µm thick dense Nb coatings can be produced if appropriate deposition parameters are chosen. A pore- and void-free microstructure as well as passivation characteristics approaching bulk niobium have been found. The relatively high ion to neutral ratios of 8 (bias current density = 2 mA/cm<sup>2</sup> for the deposition at 420°C) and of 4 (bias current density = 1 mA/cm<sup>2</sup> for the deposition at 250°C), which are attributed to the special design of the coating equipment, clearly influence these positive results. However, the ion etching conditions prior to coating seem to have great, maybe dominating influence on some of the film properties. It may be speculated that the amorphised Nb interlayer is more efficient in covering irregularities in the substrate surface and hence reducing the formation of "weak points" or pores in the coating. As can be seen from Figure 6 corrosion takes place only through defects in the coating, while the coating itself remains unattacked. The fact that the coating produced after the Ar-ion etching pre-treatment exhibits the least protective corrosion performance can lead to the assumption that electrically insulating oxidic inclusions in the steel surface may cause the development of such localised defects, as they cannot be removed by inert Ar-ion etching. The initial stage of the coating growth will then be disturbed as no bias current can be passed via these defects and therefore suppressing any ion bombardment of the growing film. In the case of Cr-ion etching it may be speculated that the generated interlayer is too thin to fully cover these

In addition to corrosive attack via pores or defects in the film adhesive failure has to be encountered for the Ar-ion etch coating, as spallation of the film around the pits has been observed in the SEM after the corrosion test.

The experiments carried out in this study have further shown a clear influence of the etching conditions and the deposition temperature on the texture, macrostrain and resulting microhardness of the films. It is interesting to observe that the corrosion performance deteriorates in the same way as stress and hardness of the coatings increase.

In addition to these results Figure 7 compares the corrosion performance of the 1 µm thick Nb-ion etch/Nb coating (250°C) to commercially available standard hard chrome and electroless nickel coatings (film thickness: 25 µm) in a 3% NaCl solution. All three coatings were deposited on 304 stainless steel substrates. The chromium coating shows a very similar behaviour to that of bulk chromium and exhibits passivity over a range of about 1100 mV. However, at a potential of +750 mV an increase in anodic current density indicates the transpassive dissolution of the passive oxide film. In the case of the electroless nickel-phosphorus coating the relatively high current density can be attributed to the corrosive attack of the nickel coating and the formation of nickel phosphate; rapid tarnishing of the coating surface was observed.

The excellent corrosion performance of the Nb coating is emphasised by this comparison, especially when the differences in coating thickness are taken into consideration.

## CONCLUSIONS

- Corrosion resistant PVD-overcoats with passivation characteristics approaching bulk niobium can be achieved at a temperature as low as 250°C with combined steered arc/unbalanced magnetron sputtering (ABST<sup>TM</sup>) using Nb-metal ion etching as the in vacuo pre-treatment.
- A coating thickness of 1 µm is sufficient to protect polished stainless steel substrates in a 3% NaCl solution.
- The hardness of the coatings reaches approximately half of the value of hard chromium, indicating the potential of interesting wear properties.

gratitude to K. Wilson & Co. (Plate Ltd., Chesterfield, UK. Additionally special thanks to Mr. C. Klaiss.

## REFERENCES

1. G. L. Miller, *Tantalum and Niobium* Butterworths Scientific, London, 1958
2. R. W. Balliet, M. Coscia, F. Hunkeler, *J. Metals.*, **38** (9) (1986)
3. *Metals Handbook*, Vol 2, AS Metals Park, OH, 1990, 10th ed 1144
4. R. W. Berry, P. M. Hall, M. F. Ha *Thin Film Technology*, Van Nostr (1968)
5. B. A. Movchan, A. V. Demchis *Phys. Met. Metallogr.*, **28** (1969) 83
6. J. A. Thornton, *Ann. Rev. Mater.* **7** (1977) 239
7. D. M. Mattox, G. J. Kominiak, *J. Sci. Technol.*, **9** (1972) 528
8. R. Messier, A. P. Giri, R. A. Roy *Vac. Sci Technol. A*, **2** (1984) 500
9. J. H. Hsieh, R. Lee, R. A. Erck, G. Fenske, Y. Y. Su, M. Marek, R. Hochmann, *Surf. Coat. Technol.*, (1991) 83
10. L. P. Ward, P. K. Datta, *Thin S Films*, **271** (1995) 101
11. L. P. Ward, P. K. Datta, *Thin S Films*, **272** (1995) 52
12. L. P. Ward, P. K. Datta, *Proc. AM '95*, Dublin, Ireland, 8-12 Aug 1995
13. E. E. Salagean, D. B. Lewis, J. Brooks, W.-D. Münz, I. Petrov, J. Greene, *Surf. Coat. Technol.*, **82** (19 57
14. W.-D. Münz, F. J. M. Hauzer, Schulze, *Surf. Coat. Technol.*, **50** (19 169
15. I. G. Brown, J. E. Galvin, present at the *XIIIth Int. Symp. on Discha and Electrical Insulation*, P France, June 27-30, 1988
16. W.-D. Münz, I. J. Smith, D. B. Le S. Creasey, *Vacuum*, **48** (5) (1997)
17. S. Creasey, W.-D. Münz, D. B. Le *Surf. Coat. Technol.* (in press)
18. L. Young, *Anodic Oxide Fil* Academic Press, 1962
19. I. Petrov, P. L. Losbichler, Bergstrom, J. E. Greene, W.-D. M T. Hurkmans, T. Trinh, *Thin S Films*, **302** (1997) 179-192
20. M. Pourbaix, *Atlas of Electrochem Equilibria in Aqueous Soluti* NACE, Houston, 1974



# Influence of ion bombardment on structure and properties of unbalanced magnetron grown $\text{CrN}_x$ coatings $\star$

T. Hurkmans <sup>a,\*</sup>, D.B. Lewis <sup>b</sup>, H. Paritong <sup>b</sup>, J.S. Brooks <sup>b</sup>, W.D. Münz <sup>b</sup>

<sup>a</sup> *Hauzer Techno Coating Europe B.V., PO Box 226, 5900 AE Venlo, The Netherlands*

<sup>b</sup> *Materials Research Institute, Sheffield Hallam University, Pond Street, City Campus, Sheffield, South Yorkshire S1 1WB, UK*

Received 1 May 1998; received in revised form 15 January 1999; accepted 19 January 1999

## Abstract

The structures and properties of reactive unbalanced magnetron sputtered  $\text{CrN}_x$  can be influenced by variation of the substrate as voltage and substrate bias current density. At floating potential ( $U_f = -25$  V) the lattice parameter coincides with that of the bulk value for CrN and the compressive stress approaches almost 0 GPa. Increasing the negative bias voltage to  $-200$  V results in a steep increase of the lattice parameter together with an observed increase in the intrinsic stress to  $1 \text{ GPa } \mu\text{m}^{-1}$  at  $U_b = -200$  V. In parallel a change in the texture was observed. At bias voltages below  $U_b = -50$  V the (111) orientation is dominating, whereas at higher bias voltages (220) becomes the major texture.

Increasing the bias current density leads also to an increase in the lattice parameter and internal stress from zero at a bias current density of  $0.9 \text{ mA cm}^{-2}$  to  $1.1 \text{ GPa } \mu\text{m}^{-1}$  at a bias current density of  $4.4 \text{ mA cm}^{-2}$ . Increasing ion bombardment densifies the coatings as can be observed from the hardness increase of HV2120 at  $0.9 \text{ mA cm}^{-2}$  to HV2440 at  $4.4 \text{ mA cm}^{-2}$  at a bias voltage level of  $U_b = -100$  V. The ion energy (bias voltage) obviously influences the hardness more than does the ion flux (bias current density): At  $U_b = 0$  V a hardness value of HV1300 was observed in contrast to HV2200 at  $U_b = -200$  V. In parallel the composition declines to lower nitrogen contents with increasing bias voltage levels, but is more or less independent of the bias current density. © 1999 Elsevier Science S.A. All rights reserved.

**Keywords:**  $\text{CrN}_x$  films; Ion bombardment; Magnetron sputtering; PVD

## 1. Introduction

Under well-controlled reactive unbalanced magnetron sputtering conditions  $\text{CrN}_x$  coatings can be reproducibly deposited as Cr, Cr+N,  $\text{Cr}_2\text{N}$ , and CrN phases and mixtures of Cr+N and  $\text{Cr}_2\text{N}$  as a function of the nitrogen content [1]. Experiments and results outlined in this paper are to be seen as a direct continuation of work reported in Ref. [1]. There the influence of the nitrogen gas flow during reactive unbalanced magnetron sputtering on the nitrogen content of  $\text{CrN}_x$ , texture, hardness, adhesion (critical load and HR-c indentation), and morphology has been described. It has been shown that depending on the nitrogen flow Cr, Cr+N, Cr+N+ $\text{Cr}_2\text{N}$ ,  $\text{Cr}_2\text{N}$ +CrN, and CrN phases can be

identified, whilst using a constant ion bombardment energy of 100 eV and a typical bias ion current density of approx.  $2 \text{ mA cm}^{-2}$  during the growth process at a substrate temperature of  $250^\circ\text{C}$ .

In the present paper the influence of the bias voltage and the bias current density on the growth of nearly stoichiometric  $\text{CrN}_x$  at  $250^\circ\text{C}$  substrate temperature is investigated. The morphology is related to the Messiers structure zone model [2]. Mechanical properties and the microstructure are compared with results published by other researchers in the field of CrN coatings [3,4].

## 2. Experimental details

All coatings have been deposited again in a ABS<sup>®</sup> coating machine HTC-625-Multilab, fabricated by Hauzer Techno Coating Europe B.V., Venlo, The Netherlands [5]. The most important deposition parameters are summarised in Table 1. The magnetic field of the two magnetrons was enhanced by using two

$\star$  Paper presented at the 25th International Conference on Metallurgical Coatings, April 26–May 1, 1998, San Diego, CA, USA.

\* Corresponding author. Tel.: +31 77355 9222;

fax: +31 77354 5854.

E-mail address: thurkmans@hauzer.nl (T. Hurkmans)

Table 1.  
Overview of PVD process settings for CrN<sub>x</sub>

CrN <sub>x</sub> deposition parameters (UBM); 2-fold planetary rotation	
1) Pump down and radiation heating: Time = 60 min	
Controlled temperature = 200 °C	
Base pressure <math> < 1 \times 10^{-3}</math> Pa	
2) Argon ion etch: Time = 20 min	
Controlled temperature = 240 °C	
D.c. bias voltage = -800 V	
D.c. target voltage = -150 V	
Argon pressure = 1 Pa	
3) Closed field unbalanced magnetron sputtering: Time = set to deposit 3 μm	
Controlled temperature = 250 °C	
Cr target d.c. power = 5 kW	
Argon flow rate = 160 sccm	
Nitrogen flow rate = 100 sccm	
D.c. bias voltage = varied between 0 and -200 V	
Coil current = varied between 0 and 40 A	
4) Cooling down and venting	

concentric electromagnetic coils (closed field [5]). This arrangement allows an exactly continuous control of the bias current density in the range of approx. 1–5 mA cm<sup>-2</sup>. Test samples were fabricated from austenitic stainless steel (AISI 304) and high speed steel (HSS : M2). The substrate surface was polished to a surface roughness  $R_a \approx 0.01 \mu\text{m}$ . Thin circular substrates (annealed stainless steel, %30 × 0.5 mm) were used to measure residual stresses in accordance with the deflection method [6].

The microstructure of the coatings was analysed by SEM, XRD (monochromatic Cu K $\alpha$ , Bragg Bretano geometry), and the composition determined by SNMS (secondary neutral mass spectroscopy). Further experimental details are given in Ref. [1]. Corrosion tests were carried out by dynamic polarisation measurement from -800 mV (versus SCE) to +900 mV (versus SCE) in 3% NaCl solution open to air (scan rate: 0.5 mV s<sup>-1</sup>) [7].

### 3. Results and discussion

Figs. 1 and 2 outline the behaviour of process and machine specific parameters which are influenced by the bias voltage and the coil current, respectively. The coils are used in order to change the degree of unbalancing of the magnetrons and thereby the degree of ionisation [5,8–10]. It is clearly shown that the deposition rate decreases while increasing the bias voltage. This is a well known effect [11], also for CrN<sub>x</sub> [4], and may be correlated with an increase of resputtering of the deposited film due to an increase of the dissipated bias power on the surface of the substrate. It is also shown that the total bias current is considerably increased. Interesting to note is that the nitrogen content of the as-deposited films is reduced by increasing the bias voltage. Obviously

it is a result of preferred resputtering of N as the lightest element in the condensed material. The results of Fig. 2 suggest that this must be an impact-controlled effect as the nitrogen content does not change with the coil current when the dependent bias current is increased from 0.35 to 1.7 A and the number of bombarding ions is therefore dramatically increased.

The marginal influence of the increased number of bombarding ions (coil current) on the composition of the coating might be explained by the fact that N<sub>2</sub> and N are preferably ionised having a ionisation potential lower than that of Ar (15.58, 14.53, and 15.76 eV, respectively). Therefore, the increase in the number of bombarding ions may be mainly correlated to a preferred increase in the number of N<sub>2</sub><sup>+</sup> ions. As N<sub>2</sub><sup>+</sup> ions are subjected to the reaction N<sub>2</sub><sup>+</sup> → N<sup>+</sup> + N<sup>0</sup> when they hit the substrate surface, the effective 'resputter rate' will be lower than with the heavier Ar<sup>+</sup> owing to the considerably lower sputter yield of the much lighter N<sup>+</sup> ion. In addition, the preferred 'resputter effect' of condensed N will be compensated for by the high reactivity of the impinging N<sup>+</sup> ions. The oxygen content stayed below 1 at.% within the experiments.

Finally fig. 2 shows the calibration of the coil current scale in units of bias current density. This calibration has been achieved by Langmuir probe measurements and reflects the wide range of ionisation which can be produced in the HTC-625-Multilab ABS<sup>®</sup> PVD system. In the following results only the bias current density will be used as second coating process parameter besides the bias voltage.

SEM fracture cross-section images show the influence of bias voltage and bias current density on the morphology, the densification, and the surface roughness of 3 μm CrN<sub>x</sub> films. Fig. 3a–d confirms Messier's structure zone model [2], exhibiting open dendritic film growth at low bias voltages and dense structures at higher ones. It also shows a smoothing effect on the surface caused by the increased ion bombardment and 'resputter effects'. Finally, Fig. 3d shows an almost structureless fracture cross-section and a very smooth coating surface for CrN<sub>x</sub> at a bias voltage of  $U_b = -200 \text{ V}$ . Fig. 3e and f indicates that high ion current densities also contribute to a smoothing of the film surface at a moderate bias voltage level of  $U_b = -100 \text{ V}$  as has been demonstrated elsewhere for TiN [12].

Fig. 4 outlines that the crystallographic structure of the CrN<sub>x</sub> coatings is strongly affected by the bias voltage. The only phase present was CrN with the well-known B1 NaCl-type fcc structure. Films grown at  $U_b = 0 \text{ V}$  exhibit a preferred (111) orientation [3], characterised by a sharp diffraction peak. The negative deviation from the lattice parameter and the interplanar spacings as compared to the JCPDS reference values for CrN would indicate a residual tensile stress (Table 2), which is typical for dendritic film growth [13] and shown by SEM

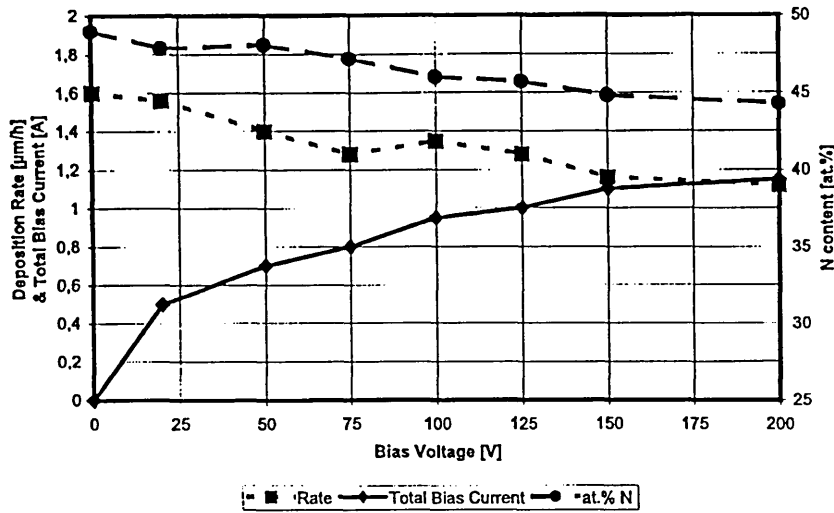


Fig. 1. Influence of bias voltage on deposition rate, nitrogen content, and bias current at a coil current of 12 A.

image Fig. 3a. Increasing the bias voltage leads to a change to positive deviation values of interplanar spacing and lattice parameter indicating the change from residual tensile to compressive stresses. In parallel, a general increase of the peak broadening is observed, indicating increased stress and decrease of grain size [3]. The texture parameter  $T^*$  listed in Table 2 confirms the change from (111) to (220) preferred orientation [3]. The results stemming from the variation of the coil current and herewith the bias current density (Table 3) complete the view which one might infer from the SEM images and the influence of the bias voltage. Enhancing the ion bombardment at a constant bias voltage of  $U_b = -100$  V leads to an increase in the interplanar spacings and the lattice parameter. Accordingly the

texture parameters indicate a transformation from (111) to (220) orientation when the bias current density is increased from  $0.9$  to  $3 \text{ mA cm}^{-2}$ . However, at a bias current density of  $4.4 \text{ mA cm}^{-2}$  an almost randomly oriented structure is observed.

Figs. 5 and 6 outline the influence of bias voltage and bias current density on the mechanical properties of the  $\text{CrN}_x$  coatings. As can be expected from the SEM and XRD data both hardness and residual stress in the coatings increase with increasing bias voltage. Similar tendencies are published for CrN [3], TiN [13–16], NbN [17], TiAlN [15], and HfN [16]. The open structure at  $U_b = 0$  V leads to low hardness values ( $\text{HV}_{0.025} 1300$ ) and to stress values that are so low that they were very difficult to evaluate exactly enough by the deflection

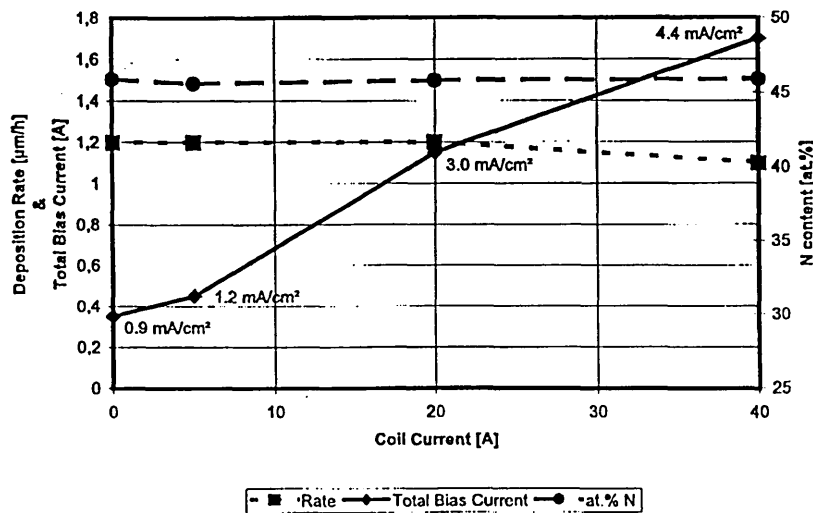


Fig. 2. Influence of coil current on deposition rate, nitrogen content, and bias current (density) at a bias voltage of  $-100$  V.

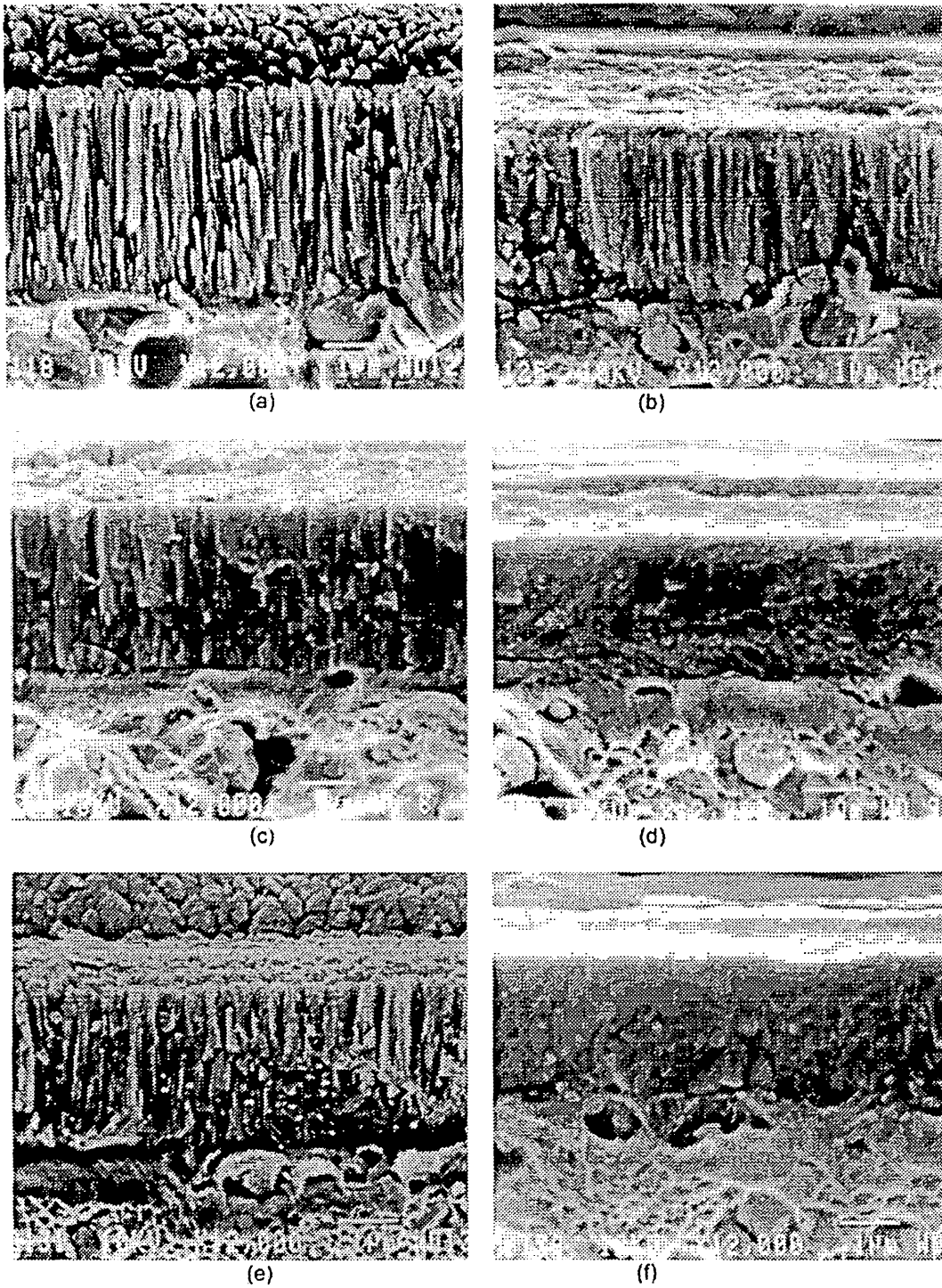


Fig. 3. Scanning electron micrographs showing fracture cross-sections from  $\text{CrN}_x$  coatings deposited at (a)  $U_b = 0 \text{ V}/I_{\text{coil}} = 12 \text{ A}$ , (b)  $U_b = -50 \text{ V}/I_{\text{coil}} = 12 \text{ A}$ , (c)  $U_b = -100 \text{ V}/I_{\text{coil}} = 12 \text{ A}$ , (d)  $U_b = -200 \text{ V}/I_{\text{coil}} = 12 \text{ A}$ , (e)  $U_b = -100 \text{ V}/I_{\text{coil}} = 0 \text{ A}$  and (f)  $U_b = -100 \text{ V}/I_{\text{coil}} = 40 \text{ A}$ .

method in the tensile regime (Table 2,  $U_b = 0 \text{ V}$  and  $U_b = -20 \text{ V}$ ). The stress values in Fig. 5 were normalised to  $1 \mu\text{m}$  film thickness and plotted as 'growing stress'. However, total compressive stresses in this level

(3.5 GPa) may still be considered as moderate. The critical load values  $L_c$  lie in the entire bias voltage range at a fairly high level, namely beyond  $L_c = 60 \text{ N}$ . However, in the range of  $U_b$  from  $-50$  to  $-75 \text{ V}$ , where

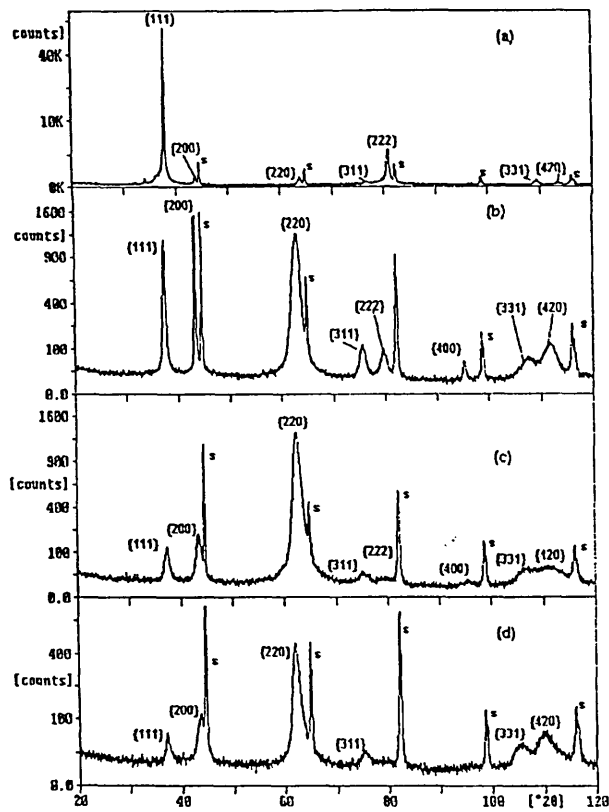


Fig. 4. X-ray diffraction diagrams from CrN<sub>x</sub> coatings deposited at (a)  $U_b=0$  V, (b)  $U_b=-50$  V, (c)  $U_b=-100$  V and (d)  $U_b=-200$  V with a coil current of 12 A.

dense coatings may already be expected, the  $L_c$  value reached a maximum with 100 N. Further increasing the bias voltage led to an increase of the stress values and

to a decrease of the critical load value to  $L_c=65$  N. The Rockwell indentation tests (DB-judgement) showed class '1' results almost over the whole bias voltage range. Only in the range of  $U_b$  from  $-100$  to  $-150$  V, where the decay of  $L_c$  was observed a marginal degradation of the DB-judgement from '1' to '1' to '1.5' was assumed. Increase of the bias voltage from  $U_b$  from  $-100$  to  $-200$  V leads to a marginal increase of hardness from  $HV_{0.025}$  2100 to  $HV_{0.025}$  2200. The results summarised in Fig. 6 are consistent with the results achieved so far; increasing the ion bombardment initiates an increase in the intrinsic compressive stress. The hardness increases from  $HV_{0.025}$  2120 to  $HV_{0.025}$  2440 as a result of the increase of bias current density from 0.9 to 4.4 mA cm<sup>-2</sup>. The adhesion results ( $L_c$  and DB-judgement) show high quality levels over the complete bias current density range.

Fig. 7 reflects the results of the colour measurements using the  $L^*$ ,  $a^*$ ,  $b^*$  colour coordinates (CIELAB units). Only in the regime of open film structure, is a low reflectivity observed. There the surface appears dark and dull ( $L^*=30$ ) owing to light scattering, originated by the rough surface which results from the pyramidal surface morphology of (111) oriented columnar grains and is related to the change in the optical constants due to the dendritic film growth. This result compares well to the observations made on TiN [13]. Both  $a^*$  (1 CIELAB units) and  $b^*$  (3 CIELAB units) are colour neutral (close to zero) at high reflectivity and high film density.

In Fig. 8 the corrosion performance of approx. 3  $\mu$ m CrN<sub>x</sub> produced at  $U_b=0$ ,  $-100$  and  $-200$  V is compared with that of a commercially available standard hard chromium coating (thickness approx. 25  $\mu$ m). CrN

Table 2  
Influence of bias voltage on X-ray data at coil current of 12 A

Bias voltage (V)	Interplanar spacing (Å)			Lattice parameter (Å)	Peak broadening $2\theta$ (FWHM)			Texture parameter $T^*$ (%)								
	$d_{(111)}$	$\Delta d$	$d_{(200)}$		$\Delta d$	$d_{(220)}$	$\Delta d$	$\beta_{(111)}$	$\beta_{(200)}$	$\beta_{(220)}$	{111}	{200}	{220}	{311}	{331}	{420}
Ref JCPDS	2.394		2.068		1.463		4.1465									
0	2.377	-0.72%	2.064	-0.22%	1.463	-0.44%	4.117	0.13	0.27	0.34	96.3	0.8	1.5	0.3	1.5	0.5
20	2.393	-0.03%	2.076	0.38%	1.465	0.12%	4.142	0.1	0.13	0.26	78.5	2.4	8.0	3.5	5.9	1.8
50	2.41	0.65%	2.088	0.90%	1.478	1.0%	4.165	0.49	0.17	1.64	13.0	8.0	54.5	4.5	7.6	12.5
75	2.406	0.51%	2.083	0.72%	1.482	1.29%	4.176	0.79	0.93	1.83	3.1	3.0	80.0	0.7	5.9	7.5
100	2.428	1.41%	2.068	0.90%	1.492	1.95%	4.185	1.07	1.06	1.91	3.0	4.4	80.0	1.0	6.6	5.0
125	2.430	1.49%	2.088	0.99%	1.496	2.23%	4.210	0.97	1.03	1.36	5.5	15.0	42.1	5.4	11.3	20.8
150	2.424	1.25%	2.085	0.8%	1.497	2.28%	4.221	0.81	0.96	1.11	5.6	12.4	29.0	8.2	13.1	31.8
200	2.421	1.12%	2.075	0.35%	1.499	2.44%	4.225	0.82	1.26	1.77	3.1	3.0	80.0	0.7	5.9	7.5

Table 3  
Influence of coil current on X-ray data at bias voltage of -100 V

Coil current (A)	Interplanar spacing (Å)			Lattice parameter (Å)	Peak broadening 2θ (FWHM)			Texture parameter T* (%)					
	$d_{(111)}$ Δ d	$d_{(200)}$ Δ d	$d_{(220)}$ Δ d		$\beta_{(111)}$	$\beta_{(200)}$	$\beta_{(220)}$	{111}	{200}	{220}	{311}	{331}	{420}
Ref. JCPDS	2.394	2.068	1.463	4.1465									
0	2.407	2.089	1.473	4.157	0.54	0.65	0.92	47.7	6.1	26.8	7.3	5.5	6.6
	0.53%	0.99%	0.655										
5	2.406	2.083	1.475	4.159	0.64	0.75	1.42	5.2	16.2	45.5	12.6	6.8	13.8
	0.52%	0.72%	0.81%										
20	2.428	2.068	1.492	4.185	1.07	1.06	1.91	3.0	4.4	80.0	1.0	6.6	5.0
	1.41%	0.90%	1.95%										
40	2.435	2.091	1.495	4.202	0.86	0.98	1.18	13.8	20.3	21.0	13.5	9.3	22.1
	1.73%	1.10%	2.19%										

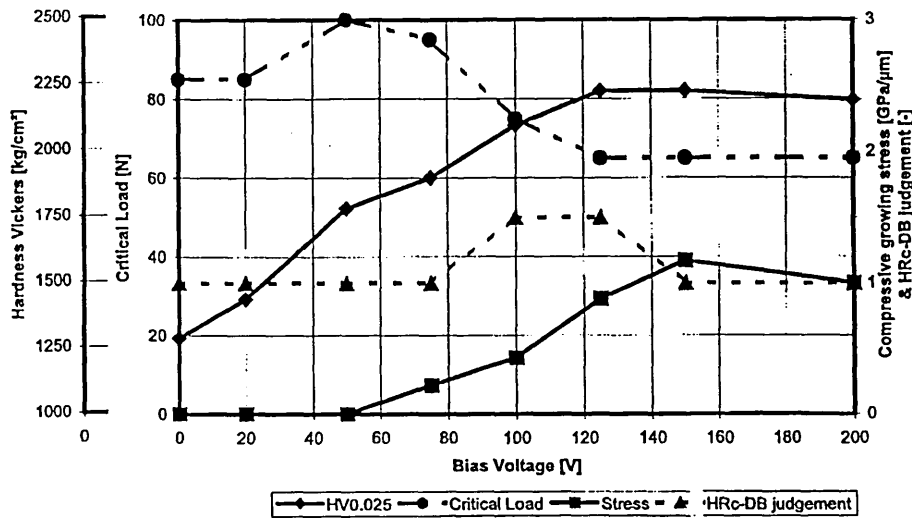


Fig. 5. Influence of bias voltage on the Vickers hardness (25 gf load), internal stress, critical load, and HRc-DB judgement at coil current of 12 A.

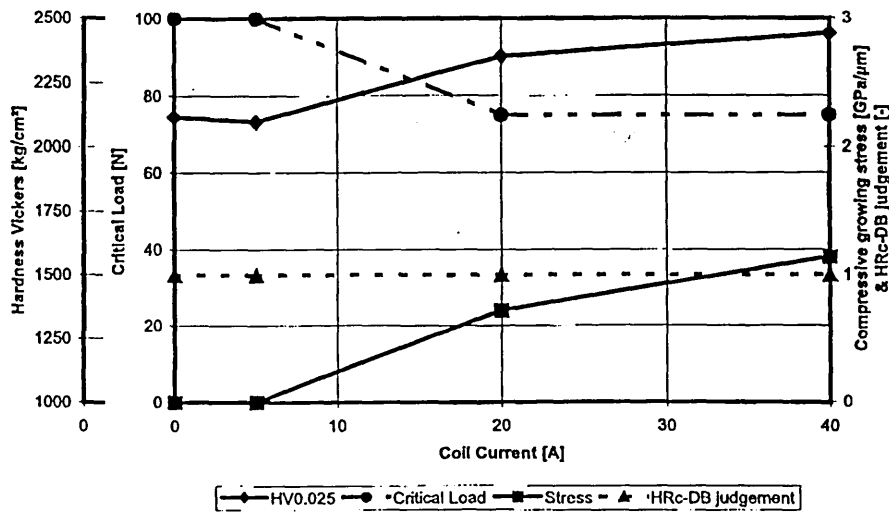


Fig. 6. Influence of coil current on the Vickers hardness (25 gf load), internal stress, critical load, and HRc-DB judgement at a Bias voltage of -100 V.

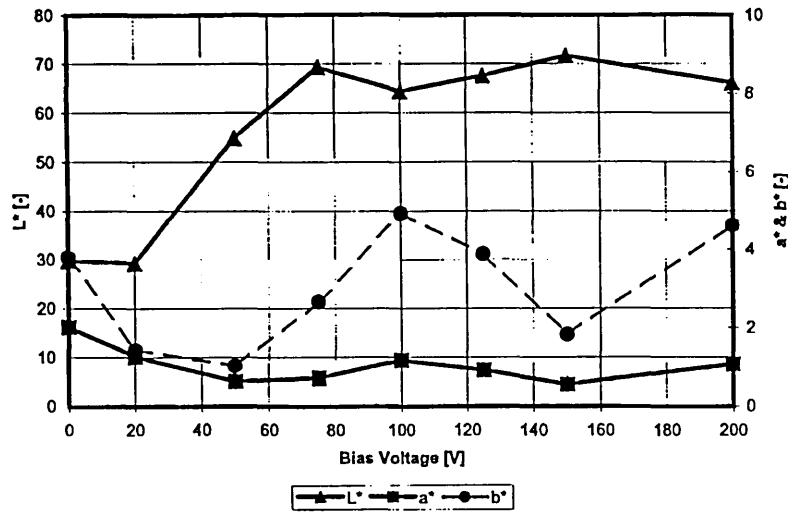


Fig. 7. Influence of bias voltage on colour values  $L^*$ ,  $a^*$ , and  $b^*$  at a coil current of 12 A.

by PVD is a possible candidate to replace hard chromium in many applications, but 25  $\mu\text{m}$  of CrN is still not economically feasible in most cases.

All coatings were tested on 304 stainless steel substrates. The corrosion resistance of the hard chromium coating is clearly superior to that of the CrN<sub>x</sub> films. The hard chromium film shows a very similar behaviour to that of bulk chromium and exhibits passivation over a range of about 1100 mV. At a potential of +750 mV an increase in anodic current density indicates the transpassive dissolution of the passive oxide film. Passivation can also be observed for the two CrN coatings produced

with  $U_b=0$  and  $-100$  V. In both cases the onset of pitting, i.e. localised breakdown of the passive oxide layer occurs at +50 mV, which is indicated by the increase in anodic current. However, the corrosion performance of the coating at  $U_b=-100$  V is clearly better than that for  $U_b=0$  V, which is evident from the lower current densities in the passive region as well as in the transpassive region. This performance may be attributed to the porous structure of the coating in the unbiased condition (Fig. 3). With regard to the poor corrosion behaviour of the highly biased sample we can only speculate at this time: Because of the enhanced compressive stress microcracks will obviously exist within the coating. These cracks, however, are not visible in the SEM micrographs.

#### 4. Conclusions

CrN<sub>x</sub> ( $0.88 < x < 0.98$ ) coating properties are strongly affected by the state of ion bombardment during film growth. Both ion energy (by bias voltage) and number of ions (by ion current density, via coil current) are playing a role with respect to the coating composition and the microstructure. At relatively low energy levels of ion bombardment the NaCl-type coating tends to be (111) oriented, having low residual stresses, low hardness, and open columnar structure. High levels of ion bombardment show a strong (220) preferred orientation, higher residual compressive stresses, higher hardness values, and dense, smooth coatings. Adhesion results were satisfactory over the complete parameter range.

Finally, it has to be acknowledged that the corrosion performance of 3  $\mu\text{m}$  CrN<sub>x</sub> films, under de conditions described in this paper, are still inferior to that of 25  $\mu\text{m}$  hard chromium.

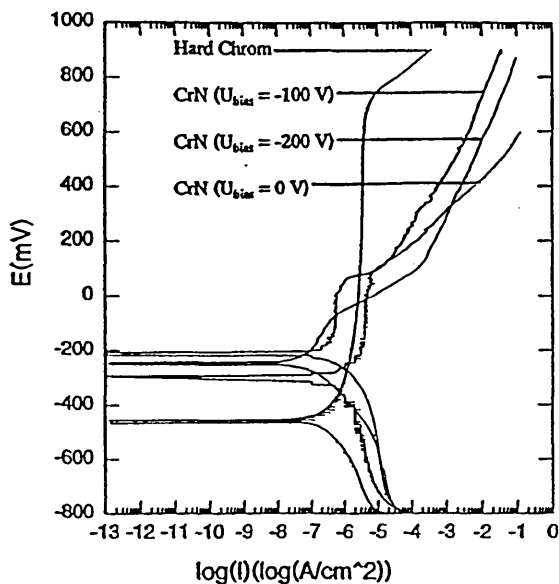


Fig. 8. Corrosion performance of approx. 3  $\mu\text{m}$  CrN<sub>x</sub> produced at  $U_b=0$ ,  $-100$  and  $-200$  V compared with that of approx. 25  $\mu\text{m}$  hard chromium.

## Acknowledgements

Particular thanks are due to Dr. H. Kheyrandish of Mats UK, Liverpool for the SNMS results and Mr. T. Trinh and Mr. W. van Ijzendoorn of Hauzer Techno Coating Europe B.V. Venlo for their assistance in preparing samples and mechanical coating evaluations.

## References

- [1] T. Hurkmans, D.B. Lewis, J.S. Brooks, W.D. Münz, Surf. Coat. Technol. 86 (87) (1996) 192–199.
- [2] R. Messier, A.P. Giri, R.A. Roy, J. Vac. Sci. Technol. A 2 (2) (1984) 500–503.
- [3] C. Gautier, H. Moussaoui, F. Elstner, J. Machet, Surf. Coat. Technol. 86–87 (1996) 254–262.
- [4] G. Berg, C. Friedrich, E. Broszeit, C. Berger, Surf. Coat. Technol. 86–87 (1996) 184–191.
- [5] W.-D. Münz, K. Vannisselroy, R. Tietema, T. Hurkmans, G. Keiren, Surf. Coat. Technol. 58 (1993) 205–212.
- [6] ASM Handbook, Surface Engineering Vol. 5 (1994).
- [7] D.A. Jones, Principles and Prevention of Corrosion, MacMillan, New York, 1992.
- [8] S. Kadlec, J. Musil, W.-D. Münz, G. Håkansson, J.-E. Sundgren, Surf. Coat. Technol. 39–40 (1989) 487–497.
- [9] B. Window, Surf. Coat. Technol. 71 (1995) 93–97.
- [10] M. Zlatanovic, R. Belosevac, A. Kunosic, Surf. Coat. Technol. 90 (1997) 143–149.
- [11] R.F. Bunshah, Deposition Technologies for Films and Coatings, Noyes Publications, Park Ridge, NJ, 1982.
- [12] L. Hultman, W.-D. Münz, J. Musil, S. Kadlec, I. Petrov, J.E. Greene, J. Vac. Sci. Technol. A 9 (3) (1991) 434–438.
- [13] J. Musil, S. Kadlec, V. Valvoda, R. Kuzel Jr., R. Cerney, Surf. Coat. Technol. 43–44 (1990) 259–269.
- [14] D.S. Rickerby, S.J. Bull, Surf. Coat. Technol. 39–40 (1989) 315–328.
- [15] H. Oettel, R. Wiedemann, S. Preissler, Surf. Coat. Technol. 74–75 (1995) 273–278.
- [16] C. Friedrich, G. Berg, E. Broszeit, K.-H. Kloos, Surf. Coat. Technol. 74–75 (1995) 279–285.
- [17] M.S. Wong, W.D. Sproul, X. Chu, S.A. Barnett, J. Vac. Sci. Technol. A 11 (4) (1993) 1528–1533.

Reprinted from

# ***SURFACE & COATINGS TECHNOLOGY***

---

Surface and Coatings Technology 116-119 (1999) 1145-1151

Characterisation of co-sputtered Nb:Cr coatings grown by the combined cathodic arc/unbalanced magnetron sputtering technique

H. Paritong \*, M. Lembke, D.B. Lewis, W.-D. Münz

*Materials Research Institute, Sheffield Hallam University, City Campus, Pond Street, Sheffield S1 1WB, UK*



# SURFACE AND COATINGS TECHNOLOGY

## Editors

B. D. Sartwell (*Washington, DC, USA*)  
A. Matthews (*Hull, UK*)

## Editorial Board

S. Bull (*Newcastle upon Tyne, UK*)  
R. F. Bunshah (*Los Angeles, CA, USA*)  
G. Dearnaley (*San Antonio, TX, USA*)  
H. Herman (*Stony Brook, NY, USA*)  
H. Hintermann (*Ins, Switzerland*)  
A. Inspektor (*Latrobe, PA, USA*)  
H. Jehn (*Schwabisch Gmund, Germany*)  
A. Kinbara (*Ishikawa, Japan*)

A. S. Korhonen (*Espoo, Finland*)  
G.W. Marshall (*Yorkshire, UK*)  
P. Martin (*Sydney, Australia*)  
W.-D. Munz (*Sheffield, UK*)  
A. R. Nicoll (*Wohlen, Switzerland*)  
Y. Pauleau (*Saint Martin d'Herès, France*)  
L. Pranevicius (*Kaunas, Lithuania*)  
D. S. Rickerby (*Derby, UK*)  
S. Schiller (*Dresden, Germany*)  
W. D. Sproul (*Evanston, IL, USA*)  
K. N. Strafford (*London, UK*)  
J.-E. Sundgren (*Linköping, Sweden*)  
R. C. Tucker (*Indianapolis, IN, USA*)  
J. von Stebut (*Nancy, France*)  
R. P. Walters (*Albany, OR, USA*)

## Scope

The increasing requirement for high technology materials with specific performance characteristics in various types of environments has dictated that these materials possess near-surface properties different from their bulk properties. This journal is a principal forum for the interchange of information on the science, technology and applications of thin and thick coatings and modified surfaces which alter the properties of materials. The scope includes all types of coatings and surface modification techniques (including physical vapour deposition, chemical vapour deposition, electroplating and surface modification by directed energy techniques). Of particular emphasis are the emerging advanced processes such as thermal spraying, sputter deposition, activated reactive evaporation, ion plating, molecular beam epitaxy, ion implantation and pulsed laser surface deposition.

Contributions range from original scientific articles concerned with applied research or direct applications of coatings to reviews of current technology in specific areas. Papers are solicited on topics which include one or more of the following areas: (1) characterization of coatings and modified surfaces, which includes the determination of composition, structure, adhesion, and internal stresses; (2) the application of coatings and modified surfaces to alter the mechanical, chemical or optical properties of materials. Mechanical properties include friction, wear, erosion, hardness and load bearing capacity. Chemical properties include corrosion and oxidation. Optical and electro-optical properties include reflectivity, selective absorption and electroluminescence. Particular emphasis is also placed on the emerging surface engineering technologies and coatings with a diversity of applications such as diamond, diamond-like carbon, and cubic boron nitride. Other interdisciplinary areas include thermal barrier coatings and coatings for biomedical applications and materials conservation.

## Abstracting/Indexing Services

This journal is cited by the following services:  
Engineering Index, FIZ Karlsruhe, Metal Finishing Abstracts, Current Contents — Engineering, Technology and Applied Sciences, Physikalische Berichte, Cambridge Scientific Abstracts, Chemical Abstracts, Fluid Abstracts, Metals Abstracts, Physics Abstracts, PASCAL/Centre National de Recherche Scientifique, Solid State Abstracts.

Pre-publication abstracts of articles in *Surface and Coatings Technology* and other related journals are now available weekly in electronic form via CoDAS, a new direct alerting service in condensed matter and materials science run jointly by Elsevier Science and Institute of Physics Publishing. For details on a free one-month subscription contact Paul Bancroft on fax +44 1179 294318 or e-mail bancroft@iopublishing.co.uk.

**Publication Information:** *Surface and Coatings Technology* (ISSN 0257-8972). For 1999 volumes 109–121 are scheduled

for publication. Subscription prices are available upon request from the Publisher or from the Regional Sales Office nearest you or from this journal's website (<http://www.elsevier.nl/locate/surfcoat>). Further information is available on this journal and other Elsevier Science products through Elsevier's website: (<http://www.elsevier.nl>). Subscriptions are accepted on a prepaid basis only and are entered on a calendar year basis. Issues are sent by surface standard mail (surface within Europe, air delivery outside Europe). Priority rates are available upon request. Claims for missing issues should be made within six months of the date of dispatch.

**Orders, claims and product enquiries:** please contact the Customer Support Department at the Regional Sales Office nearest you:

**New York:** Elsevier Science, PO Box 945, New York, NY 10159-0945, USA;  
phone: (+1) (212) 633 3730 [toll free number for North American customers: 1-888-4ES-INFO (437-4636)];  
fax: (+1) (212) 633 3680;  
e-mail: [usinfo-f@elsevier.com](mailto:usinfo-f@elsevier.com)

**Amsterdam:** Elsevier Science, PO Box 211, 1000 AE Amsterdam, The Netherlands;  
phone: (+31) 20 4853757; fax: (+31) 20 4853432;  
e-mail: [nlinfo-f@elsevier.nl](mailto:nlinfo-f@elsevier.nl)

**Tokyo:** Elsevier Science, 9-15 Higashi-Azabu 1-chome, Minato-ku, Tokyo 106-0044, Japan;  
phone: (+81) (3) 5561 5033; fax: (+81) (3) 5561 5047;  
e-mail: [info@elsevier.co.jp](mailto:info@elsevier.co.jp)

**Singapore:** Elsevier Science, No. 1 Temasek Avenue, #17-01 Millenia Tower, Singapore 039192;  
phone: (+65) 434 3727; fax: (+65) 337 2230;  
e-mail: [asiainfo@elsevier.com.sg](mailto:asiainfo@elsevier.com.sg)

**Rio de Janeiro:** Elsevier Science, Rua Sete de Setembro 111/16 Andar, 20050-002 Centro, Rio de Janeiro - RJ, Brazil;  
phone: (+55) (21) 509 5340; fax: (+55) (21) 507 1991;  
e-mail: [elsevier@campus.com.br](mailto:elsevier@campus.com.br) [Note (Latin America): for orders, claims and help desk information, please contact the Regional Sales Office in New York as listed above]

**US mailing notice:** *Surface and Coatings Technology* (ISSN 0257-8972) is published semimonthly by Elsevier Science S.A. (PO Box 211, 1000 AE Amsterdam, The Netherlands). Annual subscription price in the USA US\$ 4622.00 (valid in North, Central and South America), including air speed delivery. Periodical postage rate paid at Jamaica, NY 11431.

**USA POSTMASTER:** Send address changes to *Surface and Coatings Technology*, Publications Expediting, Inc., 200 Meacham Avenue, Elmont, NY 11003.  
**AIRFREIGHT AND MAILING** in the USA by Publications Expediting Inc., 200 Meacham Avenue, Elmont, NY 11003.



# Characterisation of co-sputtered Nb:Cr coatings grown by the combined cathodic arc/unbalanced magnetron sputtering technique

H. Paritong \*, M. Lembke, D.B. Lewis, W.-D. Münz

*Materials Research Institute, Sheffield Hallam University, City Campus, Pond Street, Sheffield S1 1WB, UK*

## Abstract

Niobium and chromium are both well known for their corrosion resistance due to the formation of protective oxide films. Sputtering is the preferred physical vapour deposition technique to deposit refractory metals such as Nb, but owing to its high melting point high ion bombardment and/or high deposition temperatures are necessary to grow dense Nb films. Further disadvantages of Nb are its relatively low hardness values and the low oxidation resistance of Nb. The present paper discusses experiments of co-sputtering Cr and Nb using the combined cathodic arc/unbalanced magnetron technique. The corrosion resistance of the 1  $\mu\text{m}$  thick coatings deposited on 304 stainless steel substrates at 250 and 420°C is investigated by potentiodynamic polarisation measurements in a 3% NaCl solution. The formation of solid solutions of Cr in Nb and of the intermetallic phase of  $\text{Cr}_2\text{Nb}$  were found to increase the microhardness, as well as the oxidation resistance, of the sputtered coatings substantially in comparison with pure Nb films. © 1999 Elsevier Science S.A. All rights reserved.

*Keywords:* Cr; Co-sputtering; Magnetron sputtering; Nb; Thin films

## 1. Introduction

The corrosion resistance of Nb and Cr is based on the formation of stable oxide films of  $\text{Nb}_2\text{O}_5$  and  $\text{Cr}_2\text{O}_3$  respectively in aqueous media. However, the corrosion resistance of chromium in solutions containing chloride ions is restricted by the transpassive dissolution of the protective oxide layer. Niobium, on the other hand, exhibits excellent corrosion behaviour and the stable oxide film remains intact in most highly corrosive environments [1,2]. Sputtering is the preferred physical vapour deposition (PVD) technology to deposit refractory metals like niobium, as the sputter yield is virtually independent of the melting point of the material [3]. However, owing to its high melting point ( $T_M = 2468^\circ\text{C}$ ) intensive ion bombardment [4,5] and/or deposition temperatures as high as 400°C are necessary to produce protective, non-porous Nb films [6,7]. Another way to improve and densify the niobium coating structure can be by co-deposition of alloying elements such

as Cr [8–10] or Zr [7]. Turley [8] suggested that depositing Nb and Cr at a composition of mutual insolubility (50:50) would lead to a disruption of the open columnar-type growth structure and hence densification of the coating morphology. Hsieh et al. [10] report about dense and column-free Nb–30%Cr alloy coatings with improved corrosion resistance deposited by IBAD. Other aspects of alloying additions of Cr to Nb considered in this study are the influence on the oxidation resistance and the microhardness by solid solution hardening and by the formation of intermetallic phases respectively. In the present study approximately 1  $\mu\text{m}$  thick Nb–Cr coatings of different composition were deposited by co-sputtering in an industrial-sized arc bond sputtering (ABS) coating chamber. The ABS technology combines the two PVD techniques of steered cathodic arc evaporation and unbalanced magnetron sputtering and allows deposition in highly ionised gas atmospheres as well as co-sputtering of various target materials [11]. The influence of the deposition parameters — i.e. substrate temperature, substrate bias voltage and the unbalancing effect of the magnetrons — as well as of the Cr content of the films was investigated with regard to their crystallographic structure and microstructure, hardness, corrosion- and oxidation-resistance.

\* Corresponding author. Tel.: +44-114-225-3500; fax: +44-114-225-3501.

*E-mail address:* h.paritong@shu.ac.uk (H. Paritong)

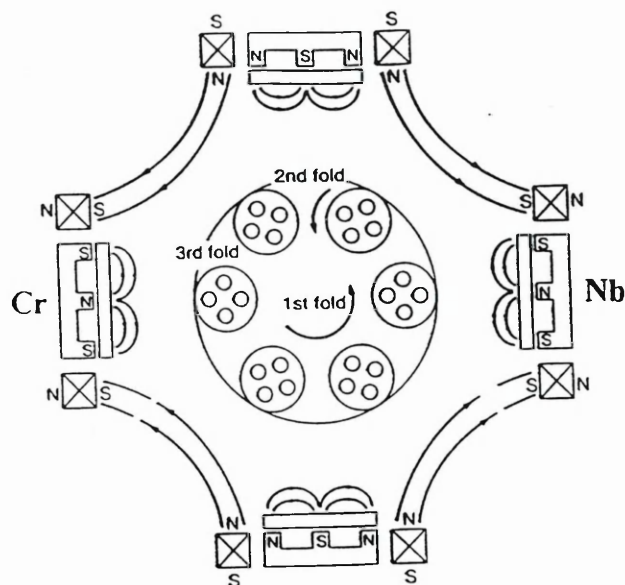


Fig. 1. Schematic cross-section of the Hauzer HTC 1000-4 coating chamber.

## 2. Experimental

### 2.1. Coating deposition

Fig. 1 shows a schematic cross-section of the HTC 1000-4 ABS coating chamber. The chamber is equipped with four dual purpose cathodes, which can be used in either the cathodic arc or the unbalanced magnetron mode. The magnetic pole arrangement of the cathodes leads to a closed magnetic field configuration in the coating chamber. Unbalancing of the magnetrons is accomplished by electromagnetic coils that are concentrically mounted to the cathodes [11]. During deposition only one Cr and one Nb target were used; these were opposite each other, as shown in Fig. 1. In situ substrate cleaning prior to coating deposition was performed in the steered cathodic arc mode using Cr ions as the etching species. Cr was chosen as the etching material owing to its characteristic of forming the smallest-sized

droplets, in relatively low concentration, of refractory metals [12]. The etching time was 10 min and the substrate bias voltage was set to  $-1200$  V. The substrates were coated in the unbalanced magnetron mode, undergoing three-axis planetary motion, at process temperatures of  $420$  and  $250^{\circ}\text{C}$ . The deposition parameters are given in Table 1. Coatings 1 and 7 are pure Nb coatings. Coatings 2–5 were deposited with an applied power of  $0.5$  kW to the Cr target. During deposition of coatings 2–5 the power on the Cr target was kept constant while the degree of ion bombardment of the growing film was increased for each process by increasing either the coil current or the substrate bias voltage. Higher Cr concentrations were achieved for coatings 6 and 8 by applying  $1.0$  kW and  $1.5$  kW respectively to the Cr target. The films were deposited on 304 stainless steel and on M2 high speed steel substrates, polished to a  $1\ \mu\text{m}$  finish.

### 2.2. Characterisation of the coatings

The chemical composition of the coatings was determined by glow discharge optical emission spectroscopy (Leco 750 GDS). A Philips powder diffractometer in Bragg–Brentano geometry was used to determine the phases present, the crystallographic texture and the lattice parameter. The texture was calculated using the inverse pole figure technique [13]; determination of the lattice parameter was performed by Cohen–Wagner plots. The hardness of the thin films was assessed with a Mitutoyo Knoop indenter using a load of  $3$  gf. Thermogravimetric measurements in a linear ramp mode ( $1^{\circ}\text{C}/\text{min}$  in air) were used to investigate the oxidation behaviour of the coated stainless steel coupons with an effective surface area of  $16\ \text{cm}^2$  (Cahn TG131). Additionally, two selected samples were treated isothermally at  $700^{\circ}\text{C}$  for  $8$  h in air. The microstructure of two selected coatings was investigated with cross-sectional transmission electron microscopy (TEM) (Philips CM20). The corrosion resistance of the coated specimen

Table 1  
Deposition parameters; Cr-content, lattice parameter, hardness and texture values of the deposited coatings

Coating number	Coating deposition						Cr-content (at.%)	Lattice parameter ( $\text{\AA}$ )	Hardness ( $\text{HK}_{0.003}$ )	Texture	
	Temperature ( $^{\circ}\text{C}$ )	Nb-target power (kW)	Cr-target power (kW)	Bias voltage (V)	Coil current (A)	Deposition rate ( $\mu\text{m h}^{-1}$ )				{110}	{111}
1	420	8	0	$-75$	$4 \times 8$	0.72	0	3.3529	820	0.62	3.90
2	420	8	0.5	$-75$	$4 \times 6$	0.76	14	3.3526	1270	0.62	3.90
3	420	8	0.5	$-75$	$4 \times 8$	0.74	12	3.3531	1250	1.40	3.00
4	420	8	0.5	$-100$	$4 \times 8$	0.69	8	3.3608	1270	5.38	0.33
5	420	8	0.5	$-125$	$4 \times 8$	0.63	5	3.3632	1200	5.00	0.76
6	420	7	0	$-75$	$4 \times 8$	0.82	53	–	1320	–	–
7	250	8	0	$-75$	$4 \times 3$	0.77	0	3.3341	560	5.447	0
8	250	8	1	$-75$	$4 \times 3$	0.85	36	–	1230	–	–

was investigated by means of potentiodynamic polarisation scans from  $-800$  to  $+900$  mV in a 3% NaCl solution open to air. All potential are recorded versus a saturated calomel electrode. The equipment used was an EG&G Potentiostat/Galvanostat 263A.

### 3. Results and discussion

The Cr-contents and deposition rates are given in Table 1. A decrease in deposition rate and Cr content can be observed for coatings 2–5 with increasing unbalancing coil current (i.e. ion density) as well with increasing substrate bias voltage (i.e. ion energy). Increasing either parameter leads to enhanced ion bombardment of the growing film and hence causing an increase in the overall re-sputter rate of the condensed atoms. The observed change in relative Cr concentration is due to the differences in sputter yield between Nb and Cr (0.6 for Nb and 1.18 for Cr for 500 eV  $\text{Ar}^+$  ions [14]), which leads to enhanced preferential re-sputtering of the condensed Cr atoms with increasing ion bombardment. X-ray diffraction (XRD) patterns of the coatings show the formation of solid solutions of Cr in Nb for coatings 2–5 (Fig. 2). The presence of the intermetallic phase of  $\text{Cr}_2\text{Nb}$  is evident for coating 6 with a Cr content of 53% (Fig. 3). The intermetallic phase is also present in coating 8 (36% Cr), but to a lesser extent than in coating 6. The calculated lattice parameters, as well as the values of the  $\{110\}$  and  $\{111\}$  major textural components, are given in Table 1. The lattice parameter increases with decreasing Cr content and increasing ion bombardment during deposition, as can be seen from coatings 2–5. The influence of the Cr content on the lattice parameter can be attributed to contraction of the Nb lattice by dissolving the smaller Cr atoms (atomic radii: Nb, 1.45 Å; Cr, 1.27 Å). Higher ion bombardment causes increased intrinsic compressive stresses induced during film growth. These stresses act in the planes perpendicular to the coating–substrate interface, hence increasing the lattice spacing in the planes parallel to the interface. A third parameter causing the lattice expansion described above is the thermal stress component, as indicated by the considerable difference in lattice parameters between the low and high temperature pure Nb coatings (coatings 1 and 7 respectively). Most films exhibit a pronounced  $\{110\}$  texture, except coatings 1 and 3 where a shift towards a  $\{111\}$  preferred orientation can be observed. The  $\{110\}$  texture is thermodynamically favoured for bcc metals such as Nb and Cr, as the texture development is driven by the reduction of surface and interface energies and, therefore, favours the closest packed  $\{110\}$  planes [15,16]. The shift in preferred orientation for coatings 1 and 3 cannot be explained at present.

A substantial increase in hardness was achieved by

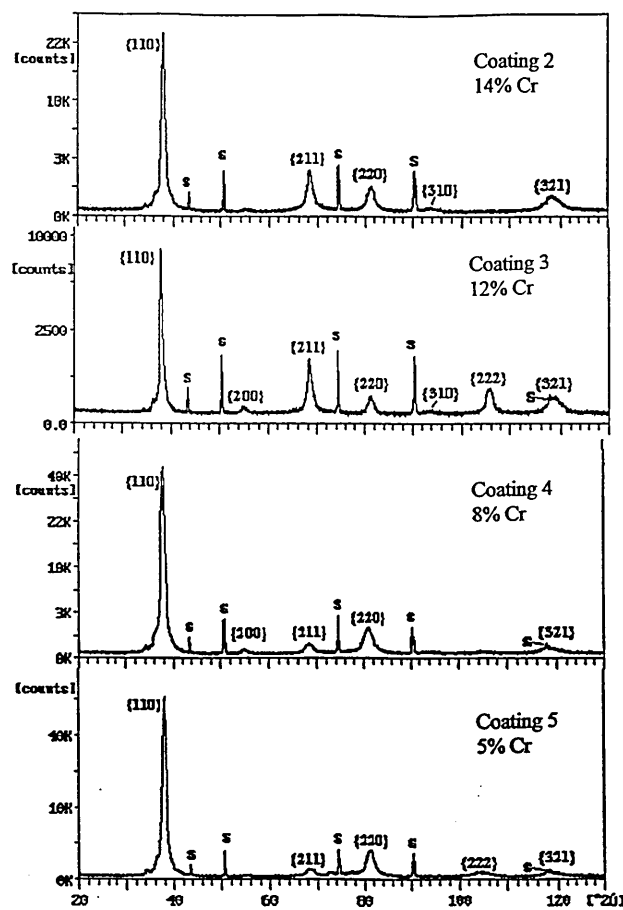


Fig. 2. XRD pattern of as-deposited coatings 2–5.

alloying additions of Cr, as shown in Table 1. Whereas the pure Nb films exhibit hardness values of  $\text{HK}_{0.003} = 580$  for the low temperature coating and  $\text{HK}_{0.003} = 820$  for the high temperature coating, hardness values of up to  $\text{HK}_{0.003} = 1320$  were observed for the co-sputtered Nb–Cr coatings. Coating 6, with a Cr concentration of 53%, exhibits the highest hardness value, but Cr contents as low as 5–14% (coatings 2–5) already increase the hardness considerably to values between 1200 and 1270  $\text{HK}_{0.003}$ . The hardness appears to be determined by two effects: i.e. solid solution hardening (Cr concentration) on the one hand and residual stresses, intrinsic or thermal, on the other hand. The effects become clear when comparing the microhardness values of the following coating pairs: (a) coating 1, coating 3 (increase in hardness by solid solution hardening); (b) coating 1, coating 7 (increase in hardness by increased residual stresses); (c) coating 2, coating 4 (same hardness by superimposing both effects). Despite overall higher hardness values due to residual stresses in the thin films, the results obtained are in good agreement with literature microhardness values of bulk Nb–Cr alloys [17]. The highest value is reported for

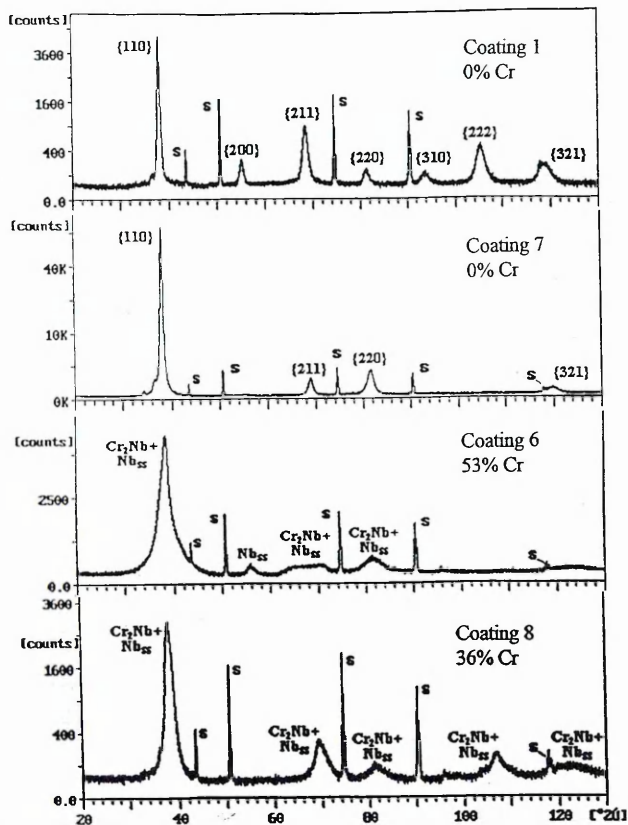


Fig. 3. XRD pattern of as-deposited coatings 1 and 7 and of coatings 6 and 8.

alloys containing 55–57% Cr, measured on a mixture of the phases Nb+Cr<sub>2</sub>Nb.

TEM cross-sectional micrographs of the two films with the highest Cr contents (coatings 6 and 8) are shown in Fig. 4. Both films exhibit a clear columnar structure. The low temperature coating with a Cr content of 36% (coating 8) is characterised by a region of pronounced competitive growth followed by a broad columnar morphology and rounded column tops. Coating 6, with 52% Cr, grown under higher ion bombardment at a higher deposition temperature, shows a considerable refined film morphology with smaller column diameters and a smoother top surface. Smoothing of the surface is due to increased preferential re-sputtering of the column tops with increased ion bombardment. Selected-area diffraction patterns taken over the whole coating area showed weak reflection spots with a lattice spacing of 4.01 Å in both films, associated with the {111} reflection of the phase Cr<sub>2</sub>Nb, thus confirming the XRD findings. However, the observed columnar morphology is not in agreement with the work by Turley [8] and Hsieh et al. [10], who suggested a disruption of the columnar structure by alloying additions of Cr of 30% and 50% respectively. It should be noted that the microstructural observations made by the authors, as well as in Refs. [9,18], were based on scanning electron microscopy and XRD analyses.

Polarisation curves of the coated specimens and of the uncoated 304 stainless steel substrate are given in Fig. 5. A substantial increase in corrosion resistance

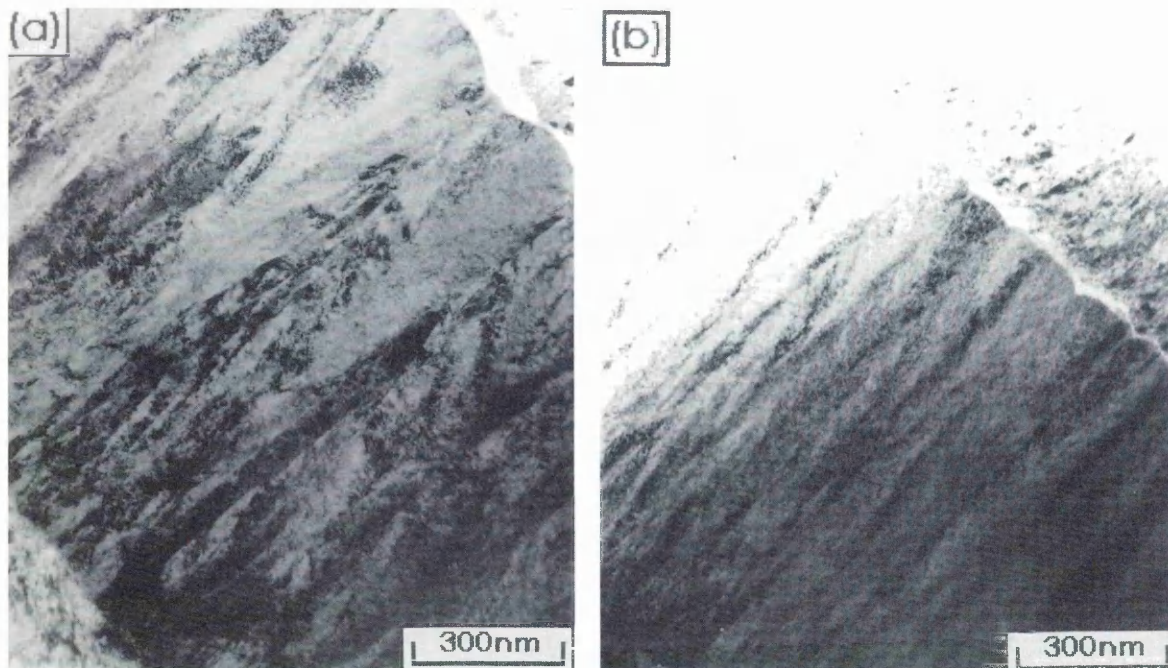


Fig. 4. TEM cross-sections of coating 8 (a) and coating 6 (b).

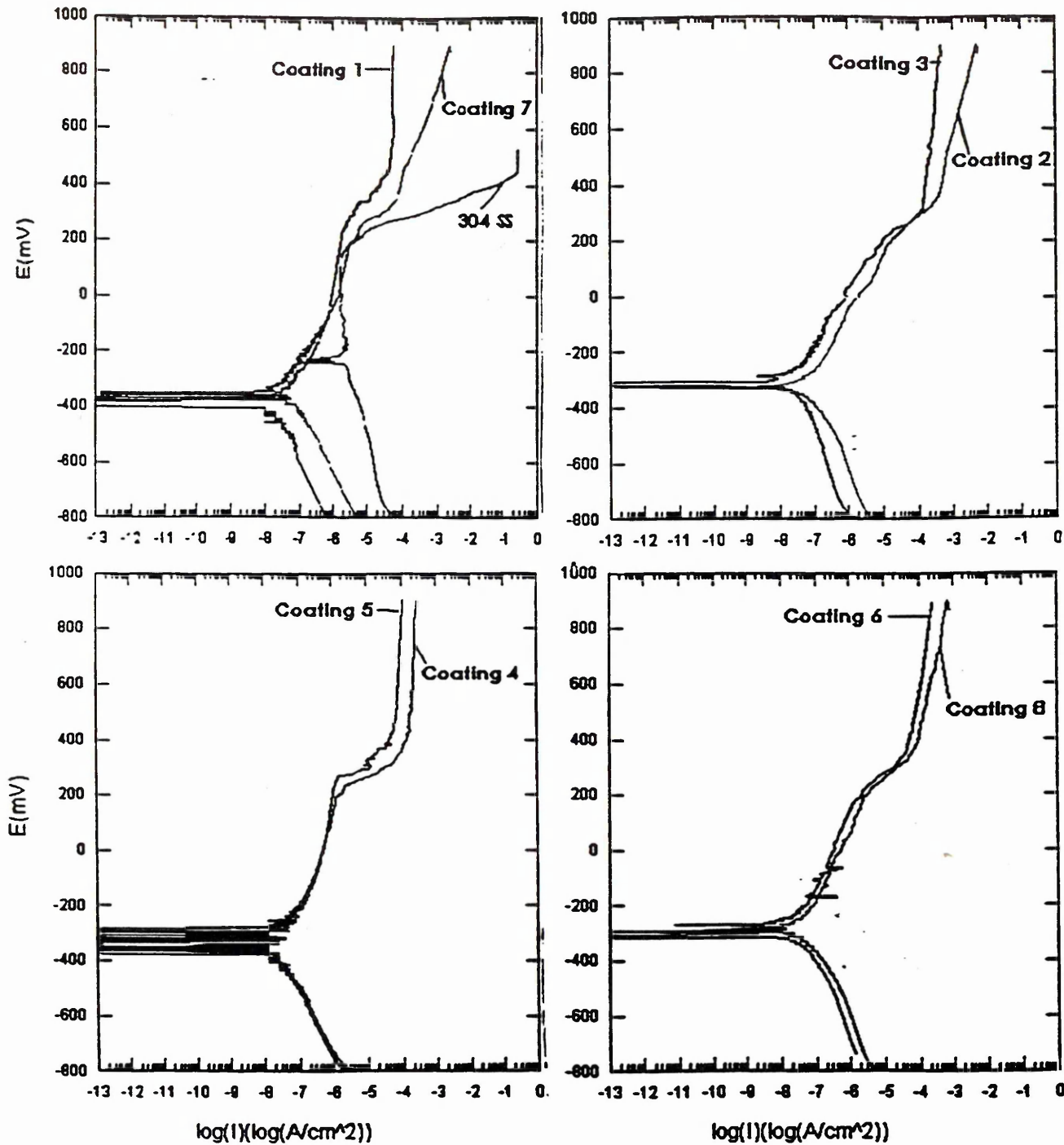


Fig. 5. Polarisation curves of uncoated 304 stainless steel and of coatings 1–8 on 304 stainless steel substrates in a 3% NaCl solution open to air.

compared with the uncoated steel substrate was observed for all coated specimens, as indicated by extended passive regions and lower current densities in the anodic region. However, none of the coatings shows a fully protective, i.e. passive behaviour; between +250 and +400 mV the onset of localised pitting can be observed for all coated samples. Comparison of the two pure Nb films (coatings 1 and 7) shows an improved corrosion

resistance for coating 1, which most likely can be attributed to densification of the microstructure due to increased deposition temperature and ion bombardment during film growth. The influence of the ion bombardment on the corrosion behaviour is also evident when comparing coatings 2–5. Both increased coil current and substrate bias voltage clearly improved the corrosion performance of the coatings, as indicated by the decrease

in current densities in the passive as well as in the transpassive regions. Again, this can be attributed to densification of coating morphology with increasing ion bombardment. The difference in the corrosion resistance between the two coatings with the high Cr contents (coatings 6 and 8) is not as significant as might be expected from the microstructural observations made by TEM (Fig. 4). Further investigations are necessary to clarify the results. However, alloying additions of Cr do not seem to influence significantly the corrosion performance of the deposited films, which appears to be determined predominantly by the degree of ion bombardment, i.e. unbalancing coil current and substrate bias voltage. This is evident from the fact that coating 5 exhibits the best corrosion protection, i.e. the lowest current density, of all the co-sputtered Nb–Cr films. Furthermore, it is important to notice that the range of passivity, or the pitting potential, is highest for the pure Nb coatings, which indicates an electrochemical rather than a microstructural influence of the Cr concentration on the corrosion behaviour.

Fig. 6 shows the results of the thermogravimetric measurements of the coated specimens, as well as of the uncoated stainless steel substrate. No significant improvement in the oxidation behaviour was achieved with low alloying additions of Cr (coatings 2–5) compared with pure Nb; for reasons of simplification, only the curves of the pure Nb film (coating 1) and of coatings 6 and 8 are therefore shown in Fig. 6. Below 400°C the first stages of oxidation of the coated specimen are determined by the solution of oxygen in either the Nb lattice or the Nb–Cr lattice [19]. The formation of suboxides during this pre-transition period has also been reported for Nb [19,20]. The onset of accelerated oxidation (breakaway oxidation [19]) of the pure Nb film occurs between 450 and 500°C, which is associated with the formation of a cracked and porous scale of Nb<sub>2</sub>O<sub>5</sub> that offers little or no protection against further oxidation. Calculations have shown that the increase in weight

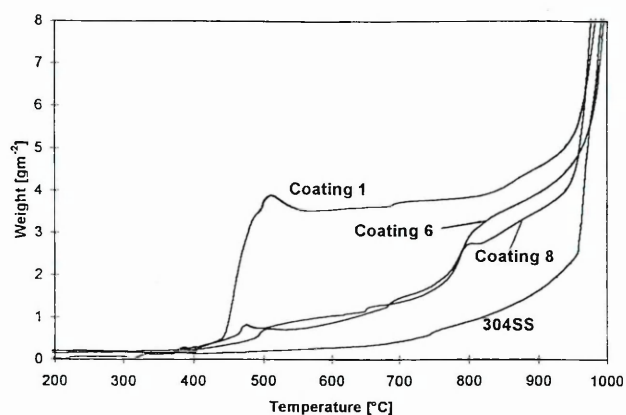


Fig. 6. Thermogravimetric oxidation rates in air of coatings 1, 6 and 8 on stainless steel substrates as well as of uncoated 304 stainless steel.

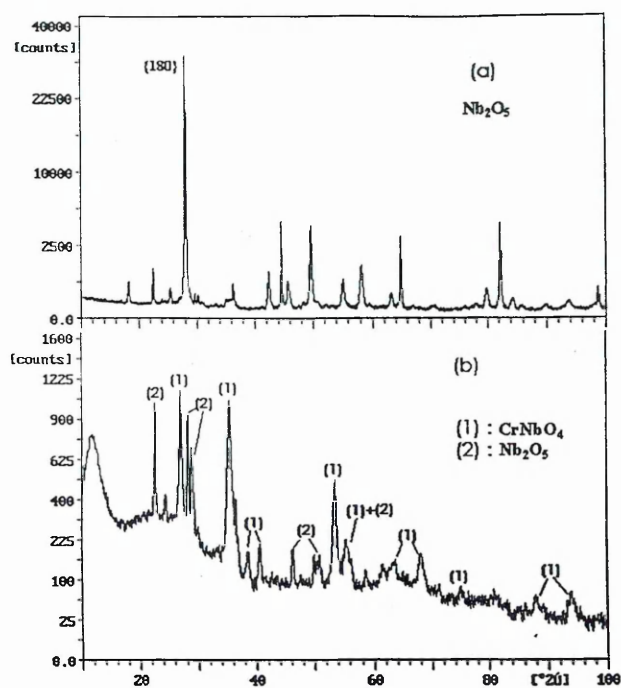


Fig. 7. XRD pattern of coating 1 (pure Nb coating) (a) and coating 6 (53% Cr) (b) after oxidation in air at 700°C for 8 h. Pattern (a) was obtained from the oxidation product on the coated substrate; pattern (b) was obtained from the oxidation product as a powder mounted on a glass slide.

in that temperature range reflects oxidation of the entire coating to stoichiometric Nb<sub>2</sub>O<sub>5</sub>. The XRD pattern of coating 1 after oxidation at 700°C for 8 h [Fig. 7(a)] confirms the formation of Nb<sub>2</sub>O<sub>5</sub>. The rate and formation of the porous, non-protective scale of Nb<sub>2</sub>O<sub>5</sub> is often regarded as a result of cracking of an initially adherent and protective scale. This is associated with the high oxide-to-metal volume ratio for Nb (Nb<sub>2</sub>O<sub>5</sub>/Nb=2.69 [21]), inducing high compressive biaxial stresses leading to breakdown of the protective scale [21–23]. A considerable improvement in the oxidation resistance was achieved with the high alloying additions of Cr in coatings 6 and 8. Between 450 and 800°C the weight gain is significantly reduced compared with the pure Nb film. The weight increases slowly and nearly linear in that temperature range, and only at temperatures above 800°C can a more rapid increase in oxidation be observed, which most probably can be attributed to cracking of a protective Cr-rich oxide scale. XRD analysis of coating 6 after oxidation at 700°C [Fig. 7(b)] identified the scale as NbCrO<sub>4</sub>, which is in agreement with the Nb<sub>2</sub>O<sub>5</sub>–Cr<sub>2</sub>O<sub>3</sub> phase diagram investigated by Goldschmidt [24]. The XRD pattern also showed the presence of Nb<sub>2</sub>O<sub>5</sub>. The improvement in oxidation resistance can hence most likely be attributed to the formation of a scale of greater stability that is less prone to cracking than Nb<sub>2</sub>O<sub>5</sub>. This can be explained by a decrease in oxide-to-metal volume ratio

( $\text{Cr}_2\text{O}_3/\text{Cr}=2.07$  [21]) increasing the stability of the adherent, protective oxide scale and hence offering greater protection against oxidation [21,22]. Other factors influencing the oxidation behaviour of Nb, not considered here, are a strong dependency of the onset and rate of the breakaway oxidation on the crystallographic orientation of the metal [19] and the valency effects of the alloying metal [19,21].

#### 4. Conclusions

A considerable increase in hardness of sputtered Nb coatings can be observed with low alloying additions of Cr; hardness values of  $\text{HK}=1320$  can be achieved with a Cr content of 53%, leading to the formation of the intermetallic phase of  $\text{Cr}_2\text{Nb}$ .

All coatings deposited in the experiments described here show significantly improved corrosion behaviour in a 3% NaCl solution compared with 304 stainless steel, independent of their Cr content.

Ion bombardment during deposition clearly improves the corrosion performance of the coatings. However, fully protective behaviour was not achieved. This may be related to the Cr ion etching step chosen in the present experiments. Prior investigation [7] has shown that corrosion-resistant Nb coatings with passivation characteristics approaching bulk Nb can be achieved using Nb ion etching as the in vacuo pre-treatment.

High alloying additions of Cr considerably improve the oxidation resistance of PVD Nb coatings. Cr concentrations beyond 30% protect the films against severe oxidation up to  $750^\circ\text{C}$ .

#### Acknowledgement

The authors would like to thank Dr I. Wadsworth for his support in regard to the TEM analyses.

#### References

- [1] G.L. Miller, Tantalum and Niobium, Butterworths Scientific, London, 1958.
- [2] R.W. Balliet, M. Coscia, F.J. Hunkeler, *J. Met.* 38 (9) (1986) 25.
- [3] R.W. Berry, P.M. Hall, F.M. Harris, *Thin Film Technology*, Van Nostrand, 1968.
- [4] J.A. Thornton, *Annu. Rev. Mater. Sci.* 7 (1977) 239.
- [5] R. Messier, A.P. Giri, R.A. Roy, *J. Vac. Sci. Technol. A*: 2 (2) (1984) 500.
- [6] E.E. Salagean, D.B. Lewis, J.S. Brooks, W.-D. Münz, I. Petrov, J.E. Greene, *Surf. Coat. Technol.* 82 (1996) 57.
- [7] H. Paritong, I. Wadsworth, W.-D. Münz, *Trans. IMF* 76 (4) (1998) 144.
- [8] M. Turley, *Surf. Coat. Technol.* 39–40 (1989) 135.
- [9] K.J.A. Mawella, J.A. Sheward, *Thin Solid Films* 193 (1990) 27.
- [10] J.H. Hsieh, W. Wu, R.A. Erck, G.R. Fenske, Y.Y. Su, M. Marek, *Surf. Coat. Technol.* 51 (1992) 212.
- [11] W.-D. Münz, F.J.M. Hauzer, D. Schulze, *Surf. Coat. Technol.* 50 (1992) 169.
- [12] W.-D. Münz, I.J. Smith, D.B. Lewis, S. Creasey, *Vacuum* 48 (5) (1997) 473.
- [13] D. Rickerby, A.M. Jones, B.A. Bellamy, *Surf. Coat. Technol.* 37 (1989) 111.
- [14] J.L. Vossen, J.J. Cuomo, Glow discharge sputter deposition, in: J.L. Vossen, W. Kern (Eds.), *Thin Film Processes*, Academic Press, 1978, p. 12.
- [15] H. Ji, *J. Appl. Phys.* 81 (10) (1997) 6754.
- [16] C.V. Thompson, R. Carel, *Mater. Sci. Forum* 204–206 (1996) 83.
- [17] D.A. Prokoshkin, E.V. Vasileva, *Alloys of Niobium*, S. Monson, Israel, 1965.
- [18] L. Fedrizzi, Y. Massiani, J.P. Crousier, M. Dapor, P.L. Bonora, *Corrosion* 46 (1990) 499.
- [19] P. Kofstad, *High Temperature Oxidation of Metals*, Wiley, New York, 1966.
- [20] N. Norman, P. Kofstad, O.J. Krudtaa, *J. Less-Common Met.* 4 (1962) 124.
- [21] W.D. Klopp, C.T. Sims, R.I. Jaffee, in: *Proceedings of the 2nd U.N. International Conference on the Peaceful Uses of Atomic Energy*, Geneva (1958) 502.
- [22] O. Kubaschewski, B.E. Hopkins, *Oxidation of Metals and Alloys*, Butterworths, London, 1962.
- [23] D.W. Aylmore, S.J. Gregg, W.B. Jepsen, *J. Electrochem. Soc.* 107 (1960) 495.
- [24] H.J. Goldschmidt, *Metallurgica* 373 (1960) 211.

# Instructions for Authors

## Submission of Papers

Manuscripts (original and two clear copies) should be submitted to one of the Editors:

for authors in the Americas

**Dr. B. D. Sartwell**, Surface Chemistry Branch,  
Naval Research Laboratory, Code 6170, Washington,  
DC 20375, USA;

and for authors elsewhere

**Professor A. Matthews**, Director, The Research Centre in  
Surface Engineering, The University of Hull, Cottingham  
Road, North Humberside, HU6 7RX, UK.

Contributions are accepted on the understanding that the authors have obtained the necessary authority for publication. Submission of a manuscript implies that it is not under consideration for publication elsewhere.

## Types of contributions

- original papers
- invited or contributed reviews on specific topics
- brief communications on topics of immediate interest
- notices of meetings, symposia and short courses
- technical notes for "Current Industrial Practices" section

## Languages

Papers will be published in English. Both English and US spelling are permitted, provided that spelling is consistent within an article.

Authors in Japan please note that information about how to have the English of your paper checked, corrected and improved (*before submission*) is available from: Elsevier Science K.K., Editorial Service, 1-9-15 Higashi Azabu, Minato-ku, Tokyo 106-0044, Japan; Tel.: +81 3 5561 5032; Fax: +81 3 5561 5045.

## Manuscript preparation

Three copies of the manuscript should be submitted, in double-spaced typing on pages of uniform size with a wide margin on the left. The title page should be a separate sheet, bearing title, author(s)' name(s) and their full addresses, and a footnote with the corresponding author's Telephone, Fax numbers and E-mail Address.

Some flexibility of presentation will be allowed but authors are urged to arrange the subject matter clearly under such headings as Introduction, Experimental details, Results, Discussion etc. Each paper should have an abstract of 100–200 words.

References should be numbered consecutively (numerals in square brackets) throughout the text and collected together in a reference list at the end of the paper. Journal titles should be abbreviated according to the Chemical Abstracts Service Source Index, 1970 edition, and supplements. The abbreviated title should be followed by volume number, year (in parentheses) and page number.

## Submission of electronic text

The final text should be submitted on a 3.5 in or 5.25 in diskette (in addition to a hard copy with original figures).

Double density (DD) or high density (HD) diskettes formatted for MS-DOS or Apple Macintosh compatibility are acceptable, but must be formatted to their capacity before the files are copied on to them. The files should be saved in the native format of the wordprocessing program used. Most popular wordprocessor file formats are acceptable. It is essential that the name and version of the wordprocessing program, type of computer on which the text was prepared, and format of the text files are clearly indicated.

## Illustrations

Line drawings and cyclic or aromatic formulae should be in a form suitable for reproduction. They may be drawn in black ink on drawing paper (letter height, 3–5 mm), but the use of good quality computer-generated figures is encouraged. They should preferably all require the same degree of reduction, and should be submitted on paper of the same size as, or smaller than, the main text to prevent damage in transit. Photographs should be submitted as clear black-and-white prints on glossy paper. Each illustration must be clearly numbered.

Illustrations can be printed in colour when they are judged by the Editor to be essential to the presentation. The publisher and the author will each bear part of the extra costs involved. Further information concerning colour illustrations and the costs to the author can be obtained from the publisher.

Legends to the illustrations must be submitted in a separate list.

All tables and illustrations should be numbered consecutively and separately throughout the paper.

## Proofs

Authors will receive proofs, which they are requested to correct and return as soon as possible. No new material may be inserted in the text at the time of proofreading. All joint communications must indicate the name and full postal address of the author to whom proofs should be sent.

## Further information

All questions arising after the acceptance of manuscripts, especially those relating to proofs, should be directed to: Elsevier Science Ireland Ltd. Elsevier House, Brookvale Plaza, East Park, Shannon, Co. Clare, Ireland. Tel.: +353 61 709609; fax: +353 61 709107.

The full and complete instructions to authors can be found on the World Wide Web: please visit our website which is accessible via the Elsevier Surfaces and Interfaces HomePage at <http://www.elsevier.nl/locate/surfaces>

## Offprints

Twenty-five offprints will be supplied free of charge to the author(s). Additional offprints can be ordered at prices shown on the offprint order form which accompanies the proofs.

# IMPROVEMENT OF CORROSION RESISTANCE OF UNBALANCED MAGNETRON DEPOSITED Nb COATINGS BY HIGH ENERGY METAL ION PRETREATMENT

H. Paritong

*The quality of corrosion resistant thin films depends on a number of factors, in particular the microstructure and degree of porosity of the coating. The microstructure of thin films deposited by the physical vapour deposition technique of unbalanced magnetron sputtering is strongly influenced by the deposition temperature and by the melting point of the condensed material. It becomes increasingly difficult to produce dense coatings at low deposition temperatures for metals such as Nb with a melting point  $T_M = 2500^\circ\text{C}$ . The present study investigates the influence of ion etching pretreatment and of deposition temperature on the corrosion resistance of Nb thin films deposited by the combined cathodic arc-magnetron sputter deposition technique.*

*Metal ion etching using Cr ions and Nb ions is compared to inert Ar ion etching. The coatings, deposited on 304 stainless steel substrates, are tested by potentiodynamic and potentiostatic polarisation measurements in a 3%NaCl solution and compared to electroplated chromium and electroless nickel films.*

*The author is in the Materials Research Institute, Sheffield Hallam University, Pond Street, Sheffield S1 1WB, UK. Contribution to the 1998 Bodycote International Prize Paper Competition.*

© 1999 IoM Communicaitons Ltd.

## INTRODUCTION

Niobium is well known for its excellent corrosion resistance which is based on the formation of a stable oxide layer of  $\text{Nb}_2\text{O}_5$ . This natural oxide protects Nb against corrosion in most organic and inorganic acids up to  $100^\circ\text{C}$  except HF.<sup>1,2</sup> Although Ta exhibits an even better corrosion behaviour, Nb is the favoured candidate for thin film applications because of greater availability, lower density, and a lower melting point (Ta  $2956^\circ\text{C}$ , Nb  $2468^\circ\text{C}$ ). Electrochemical deposition of Nb is not possible owing to the insulating surface oxide layer. Sputtering is the preferred physical vapour deposition (PVD) technique to deposit refractory metals such as Nb, since the sputter yield is virtually independent of the melting point of the material.<sup>3</sup> In the present study  $1\ \mu\text{m}$  thick Nb coatings were deposited using the combined steered cathodic arc-unbalanced magnetron sputtering technique.<sup>4</sup> The influence of the ion etching pretreatment of the substrate before deposition and of the deposition temperature on the film properties, especially corrosion resistance, is discussed. Inert Ar ion etching is compared with cathodic arc metal ion etching using Nb ions and Cr ions. The corrosion resistance of the PVD Nb coatings is further compared to that of commercially available standard hard chromium and electroless nickel films with coating thickness of  $25\ \mu\text{m}$ .

## STRUCTURAL MODELS FOR SPUTTERED THIN FILMS

The high melting point of Nb makes it extremely difficult to deposit dense films at low deposition temperatures. However, broad industrial application of a corrosion resistant coating requires the possibility of low temperature deposition, e.g. at  $250^\circ\text{C}$ , to be able to coat temperature sensitive materials such as

case hardened steel, brass, or aluminium. The influence of the deposition temperature and melting point of the coating material as well as of the working gas pressure on the microstructure of sputter deposited films has been investigated by Thornton.<sup>5</sup> According to Thornton's structure zone model a minimum deposition temperature of  $800^\circ\text{C}$  would be necessary to obtain dense Nb coatings. However, the use of plasma assisted deposition processes, such as the unbalanced magnetron sputtering technique employed in the present study, reveals new opportunities to reduce the minimum temperature necessary to produce dense films. Messier *et al.*<sup>6</sup> have shown that increasing the energy of ionised particles, which bombard the growing films, leads to densification of the coating morphology even at low temperatures. However, ion energies beyond  $80\ \text{eV}$  can lead to defect and stress formation<sup>7</sup> thus limiting the use of high ion energies. Freller<sup>8</sup> and Hultman *et al.*<sup>9</sup> have investigated the influence of the number of bombarding ions during deposition. It has been shown that increasing the ion current density and the ion/neutral ratio can lead to further densification of the condensing film.

The unbalanced magnetron sputtering technique employed in the present study along with the closed field configuration in the coating chamber allows intense ion bombardment of the growing film in highly ionised gas atmospheres and hence the deposition of dense coatings even at low deposition temperatures.

## EXPERIMENTAL

### Coating deposition

The Hauzer 1000-4 ABS coating chamber used in the present study has four rectangular cathodes which can be used either in the cathodic arc or

# 1998 Bodycote International Prize Paper Competition

Following the success of the first Bodycote International Prize Paper Competition, held in 1997, the 1998 competition drew 17 entries from the UK, continental Europe, and the USA. Eight shortlisted authors were invited to submit full length papers, from which three finalists were chosen to present their papers to an invited audience at Bodycote's Annual Dinner held at UMIST, Manchester, UK on 1 December 1998. The competition was judged by a panel chaired by Professor H. C. A. Hankins of Bodycote. The three prizewinning papers together with three of the shortlisted contributions are reproduced on the following pages:

- 144 *First Prize (\$3000)* H. Paritong  
Improvement of corrosion resistance of unbalanced magnetron deposited Nb coatings by high energy metal ion pretreatment
- 149 *Second Prize (\$1500)* C.-X. Li  
Consideration of fretting fatigue properties of plasma nitrided En19 steel
- 154 *Third Prize (\$1000)* C. Blawert  
Plasma immersion ion implantation: innovative technology for surface treatment of stainless steels
- 159 *Shortlisted* S. Hanson  
Surface engineering by powder coinjection moulding
- 163 *Shortlisted* K. Reichert  
Thermal stability of Al-O-N PVD films and comparison with Al<sub>2</sub>O<sub>3</sub> films as diffusion barriers
- 168 *Shortlisted* V. Subramanian  
Silane based metal pretreatments as alternatives to chromating

The 1999 competition has already been announced and is open to any full time or part time student and also to anyone who has graduated in the last 18 months, in which case the paper must describe work completed while the author was still a student. Full details may be found on the Bodycote website at [www.bodycote.com/html/edu\\_ppc.html](http://www.bodycote.com/html/edu_ppc.html) or alternatively may be obtained from: Professor H. C. A. Hankins, Bodycote International plc, Hulley Road, Hurdsfield, Macclesfield, Ches. SK10 2SG, UK, tel. +44 (0) 1625 505300, fax +44 (0) 1625 505313.

the unbalanced magnetron mode. Controlled unbalancing of the magnetrons, i.e. control of the degree of ionisation in the coating chamber, is accomplished by electromagnetic coils which are concentrically mounted to the cathodes.<sup>10</sup> The magnetic pole arrangement of the cathodes, together with the electromagnetic coils, leads to a closed magnetic field configuration in the chamber. The coatings were deposited on M2 high speed steel and 304 stainless steel substrates polished to a 1  $\mu\text{m}$  finish. Before deposition the substrates were subjected to an ion etch using Nb, Cr, and Ar ions as the etching species. During etching a negative bias voltage of  $-1200\text{ V}$  was applied to the substrates. Film deposition was performed in the unbalanced magnetron sputtering mode at substrate temperatures of 250 and 420°C. The negatively biased substrates ( $-75\text{ V}$ ) were coated from one Nb target, undergoing three axis planetary motion to allow correlation of the results to the deposition on three-dimensional parts for industrial applications. The deposition parameters are given in Table 1.

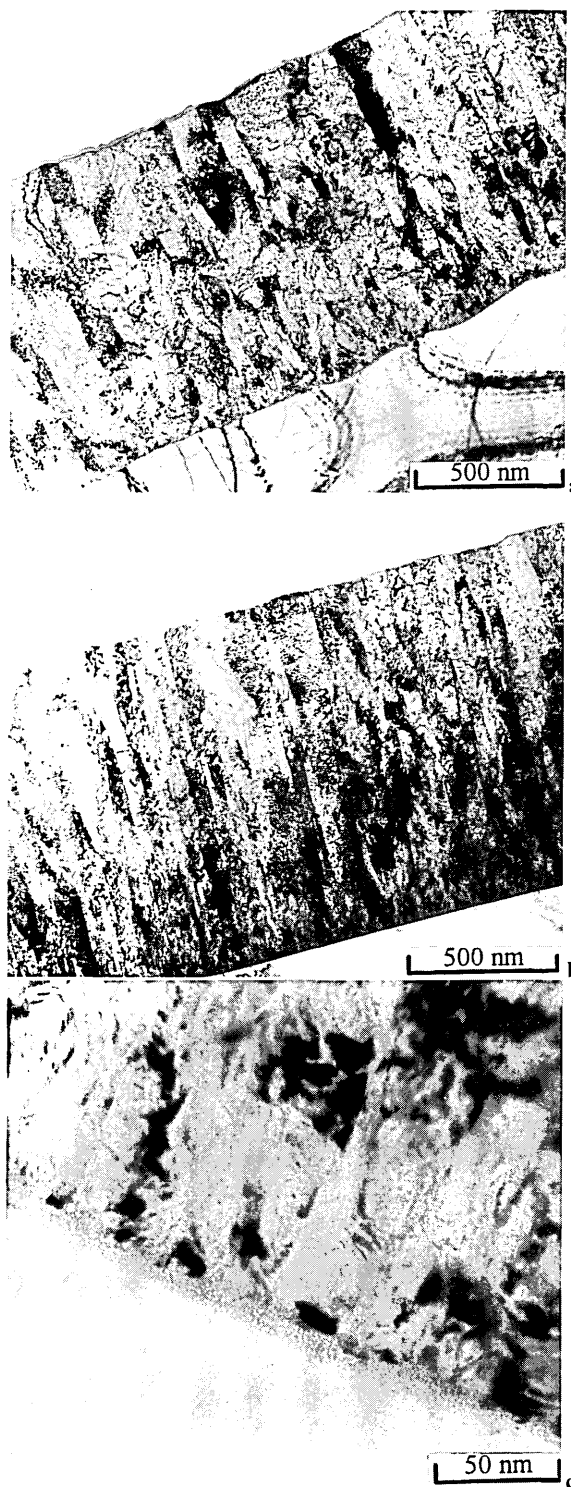
### Characterisation

The microstructure of the coatings was investigated with cross-sectional transmission electron microscopy (Philips CM20). A Philips powder diffractometer in Bragg-Brentano geometry was used to determine the lattice parameter and the residual stresses present in the thin films. The lattice parameters were calculated from Cohen-Wagner plots<sup>11</sup> and the residual stresses were determined by the  $\sin^2 \psi$  method.<sup>12</sup> The hardness of the films was assessed with a Mitutoyo Knoop indenter using a load of 3 g. The corrosion resistance of the coated specimens was investigated by potentiodynamic polarisation scans from  $-800$  to  $+900\text{ mV(SCE)}$ . Additionally, the specimens were tested by means of potentiostatic polarisation measurements at a potential of  $+400\text{ mV(SCE)}$  for 90 min. Both experiments were carried out in 3% NaCl solution in air. The equipment used was an EG&G potentiostat 263A.

## RESULTS AND DISCUSSION

### Microstructural and physical properties

Cross-sectional TEM micrographs of the two Nb etched, Nb coated specimens are shown in Fig. 1. Both films exhibit a clear columnar structure, with no apparent inter- or intracolumnar porosity. The low temperature coating (Fig. 1a) is characterised by a region of pronounced competitive growth near the interface, followed by a broad columnar morphology and rounded column tops. The high temperature coating (Fig. 1b) shows a more regular, refined film growth with smaller column diameters and a

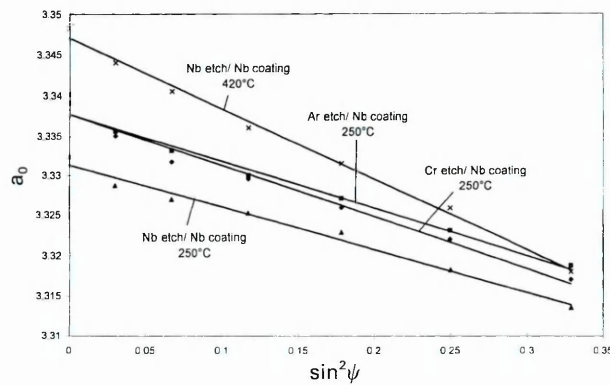


a low temperature deposition (250°C); b high temperature deposition (420°C); c interfacial region

1 Cross-sectional TEM images of Nb ion etched, Nb coated specimens

Table 1 Ion etching and Nb coating deposition parameters

Ion etching (10 min)		Nb coating deposition (105 min)			
Etching species	Bias voltage, V	Temperature, °C	Bias voltage, V	Bias current density, $\text{mA cm}^{-2}$	Unbalancing coil current, A
Nb	1200	420	$-75$	2	6
Nb	1200	250	$-75$	1	3
Cr	1200	250	$-75$	1	3
Ar	1200	250	$-75$	1	3



2 Stress determination using  $\sin^2 \psi$  plots

smoother top surface. These improved morphological coating features are caused by the higher deposition temperature as well as by the increase in applied unbalancing coil current during deposition, i.e. by the increased ion bombardment of the growing film. Figure 1c shows the interfacial region, which is characterised by a very sharp, approximately 10 nm thick amorphised Nb layer. This layer is grown under the impact of the heavy, high energetic Nb ions during the Nb metal ion etch. The interfacial region is then followed by a region of pronounced competitive growth. These observations are in agreement with earlier work reporting similar characteristic features for Nb coatings (Nb ion etch)<sup>13</sup> and for TiAlNbN coatings (TiAlNb ion etch).<sup>14</sup>

The calculated lattice parameters, stress values, and hardness results are summarised in Table 2. Stress values were determined from the slope of the linear functions using the  $\sin^2 \psi$  method as shown in Fig. 2. The stresses are compressive, as indicated by the negative sign of the slope. Residual stresses in thin films are a combination of two components, that is intrinsic, i.e. growth induced, stresses on the one hand and thermal stresses on the other.<sup>12</sup>

In the case of the low temperature Nb films the coating deposited after the Nb ion etch is the least stressed. It is assumed that this may be, among other factors, owing to a reduction in lattice mismatch between the steel substrate and the Nb coating, caused by the Nb interlayer which is formed during the Nb metal ion etch. This leads to a reduction in the intrinsic stress component and hence to a decrease in the overall residual stress in the coating. The observed low residual stress of this film is reflected in the lattice parameter of 0.3295 nm compared to 0.3294 nm of bulk Nb. Using Cr ions and Ar ions as the etching species before coating deposition leads to a considerable increase in the measured residual stresses and lattice parameter, which can be attributed

Table 2 Lattice parameters, stress values, and hardness values of experimental specimens

Etching species	Coating temperature, °C	Lattice parameter, nm	Stress values, GPa	Hardness, HK0-003
Nb	420	0.3476	1.97	600
Nb	250	0.3295	1.19	520
Cr	250	0.3341	1.45	560
Ar	250	0.3346	1.33	650

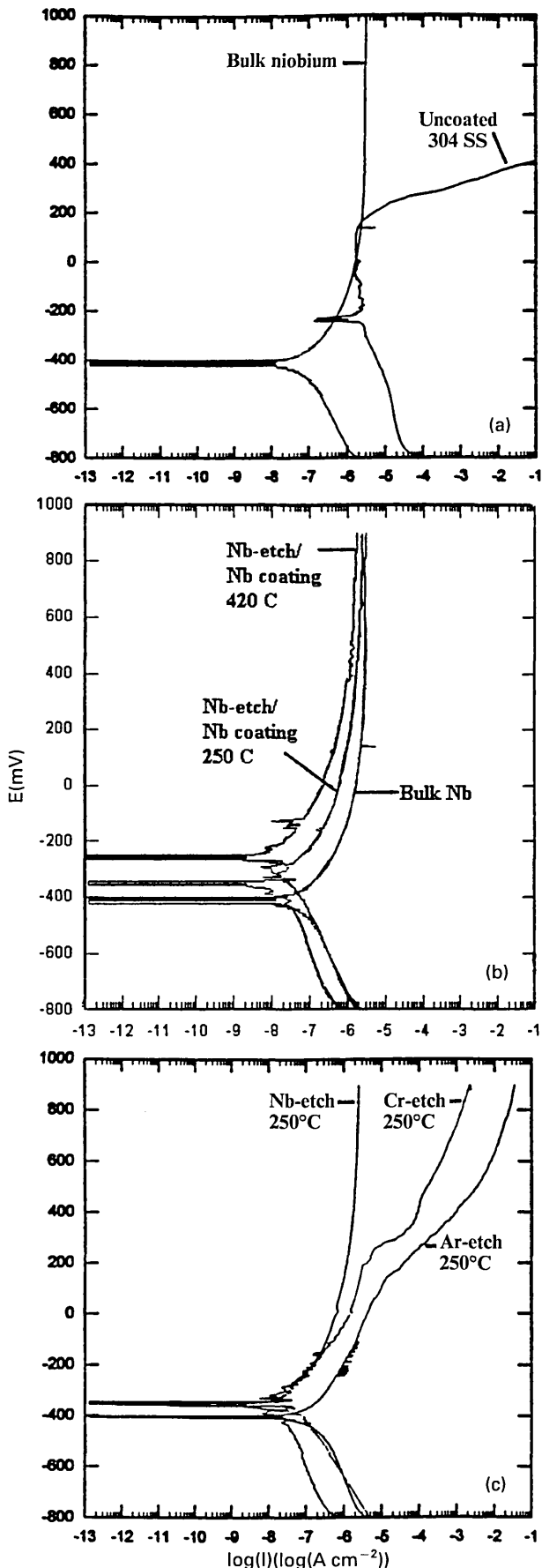
to a higher intrinsic stress component in these films. The influence of the deposition temperature and of the unbalancing coil current, i.e. ion density, on the residual stress is evident when comparing the low and the high temperature Nb ion etch coatings. It is assumed that the intrinsic component of the high temperature coating is increased by enhanced ion bombardment of the growing film owing to a higher unbalancing coil current ( $I_{\text{coil}} = 3$  A for the low temperature coating,  $I_{\text{coil}} = 6$  A for the high temperature coating). A second aspect to be considered is the thermal stress component. A higher deposition temperature leads to increased compressive thermal stresses, which are induced by the differences in the thermal expansion coefficients between the stainless steel substrate and the Nb coating. The measured stress values are reflected in the hardness results, with the exception of the Ar ion etch coating. The considerable high hardness value may be attributed to a reduction in the grain size in this film compared to metal ion etch-Nb coatings, as has been reported in earlier work.<sup>13</sup>

### Corrosion resistance

The results of potentiodynamic polarisation measurements are shown in Fig. 3. Curves of bulk Nb and of the uncoated 304 stainless steel substrate are given as references in Fig. 3a. The polarisation curve of bulk Nb is characterised by a very low and constant current density in the anodic region which indicates passivation, i.e. the formation of a stable oxide layer of Nb<sub>2</sub>O<sub>5</sub>. This oxide film protects the metal against corrosion over the whole range of the scan. Passivation is also evident in the case of the stainless steel substrate between -200 and +200 mV. At +200 mV however, breakdown of the passive layer occurs, as indicated by the rapid increase in anodic current density. This breakdown of the Cr rich oxide film is initiated by the presence of chloride ions in the electrolyte, followed by localised pitting and finally severe corrosion, i.e. dissolution, of the metal.

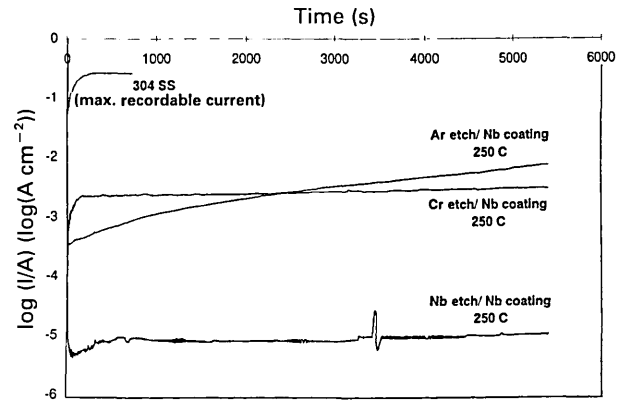
Polarisation curves of the two Nb ion etched, Nb coated specimens are given in Fig. 3b and compared to bulk Nb. Both coated specimens, deposited at 250 and at 420°C, exhibit excellent corrosion resistance. The coatings passivate and fully protect the stainless steel substrate over the whole range of the scan, as indicated by the low and constant current densities in the anodic region. No pitting was observed at all. The passivation characteristics of the two thin Nb films are very similar to that of bulk Nb, indicating dense coating structures with a low defect density. It is important to notice that these results were achieved with a coating thickness of only 1 μm at a deposition temperature as low as 250°C.

Figure 3c compares the corrosion performance of the three low temperature Nb coatings. The influence of the etching material on the corrosion resistance is evident. The performance of the film deposited after Nb ion etching is excellent and fully protective, as described above. Using Cr and Ar ions as the etching species slightly decreases the protective behaviour of the Nb films. Between +200 and +300 mV the onset of pitting can be observed for both of the coated specimens. The degree of exposure, i.e. of active corrosion of the steel substrate through defects in the coating or pits, is represented by the anodic



a bulk Nb and uncoated 304 SS; b bulk Nb and Nb ion etched, Nb coated specimens (250 and 420°C); c Nb coatings (250°C), shows influence of ion etching pretreatment

3 Polarisation curves of given specimens in 3%NaCl solution



4 Potentiostatic polarisation measurements of Nb coatings (250°C) in 3%NaCl at +400 mV, showing influence of ion etching pretreatment

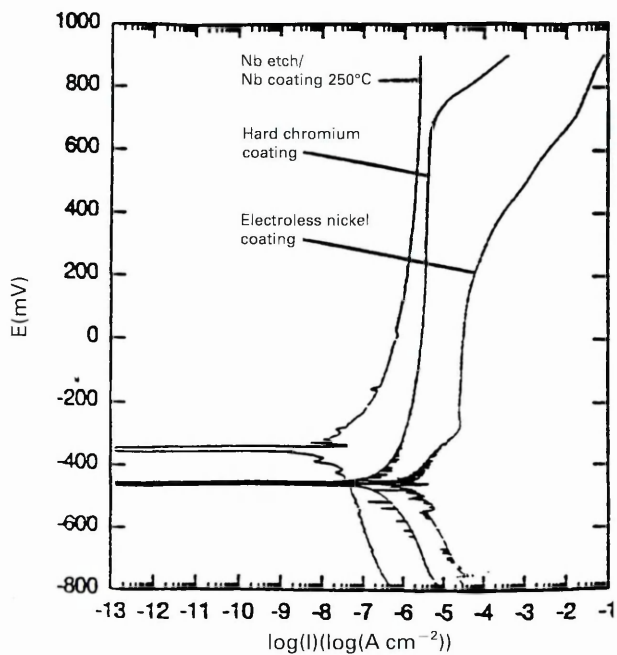
current density, which is higher for the Ar ion etch specimen than for the Cr ion etch coating. The results of potentiodynamic polarisation scans are reflected in the potentiostatic measurements, as shown in Fig. 4. The current densities recorded at a constant potential of +400 mV are lowest for the Nb ion etch coating and highest for the Ar ion etch film. It is important to note that the Nb ion etch film remains protective even after 90 min, polarised at a potential which would lead to severe corrosion and dissolution of the stainless steel substrate, as can be seen from the curve obtained for the uncoated steel substrate.

It is assumed that the influence of the ion etching pretreatment on the corrosion resistance of the Nb films originates from different effects. It may be speculated that the amorphised Nb interlayer, generated during the Nb ion etch, can cover irregularities in the substrate surface and hence reduce the number of 'weak points' or defects in the coating. In addition to corrosive attack via defects in the film, adhesive failure must be encountered for the Ar ion etch coating, as small areas of spallation of the film around the pits were observed after the corrosion test. Finally, the differences in residual stresses have to be considered in the case of the low temperature coatings, as high stresses in thin films may enhance spallation or cracking of the protective coating during corrosion testing and hence increase the exposed substrate surface area.

Figure 5 compares the corrosion performance of the PVD Nb coating (Nb ion etch, 250°C) with that of commercially available standard hard chromium and electroless nickel films deposited on the same substrate material, by means of potentiodynamic polarisation scans. The chromium coating is passive over a range of about 1100 mV. However, at a potential of +750 mV the transpassive dissolution of the passive oxide film occurs, as indicated by the increase in anodic current density. In the case of the electroless nickel-phosphorus coating the high current density in the anodic region can be attributed to corrosive attack of the nickel coating, accompanied by tarnishing of the coating surface.

**CONCLUSIONS**

1. It is possible to deposit corrosion resistant Nb coatings at substrate temperatures as low as 250°C if appropriate plasma conditions (ion bombardment)



5 Polarisation curves of Nb ion etched-Nb coated (250°C) specimen, hard chromium coating, and electroless nickel coating in 3%NaCl solution

and an appropriate etching pretreatment (Nb ion etch) are chosen.

2. Potentiodynamic polarisation measurements reveal a high potential for the PVD Nb coatings to compete with electroplated chromium and electroless nickel. However, these preliminary results have to be

supplemented by standardised corrosion tests such as salt spray tests.

## ACKNOWLEDGEMENTS

The author would like to thank Professor W.-D. Münz and Dr B. Lewis for their valuable help and advice.

## REFERENCES

1. G. L. MILLER: 'Tantalum and niobium'; 1958, London, Butterworths Scientific.
2. R. W. BALLIET, M. COSCIA, and F. J. HUNKELER: *JOM*, 1986, **38**, 25.
3. R. W. BERRY, P. M. HALL, and M. F. HARRIS: 'Thin film technology'; 1968, Princeton, NJ, Van Nostrand.
4. W.-D. MÜNZ, F. J. M. HAUZER, and D. SCHULZE: *Surf. Coat. Technol.*, 1992, **50**, 169.
5. J. A. THORNTON: *Ann. Rev. Mater. Sci.*, 1977, **7**, 239.
6. R. MESSIER, A. P. GIRI, and R. A. ROY: *J. Vac. Sci. Technol. A*, 1984, **2**, 500.
7. I. PETROV, L. HULTMANN, U. HELMETSON, J.-E. SUNDGREN, and J. E. GREENE: *Thin Solid Films*, 1989, **169**, 299.
8. H. FRELLER: in 'Proceedings of SURTEC 89', (ed. H. Czichos and L. G. E. Vollrath), 133; 1989, Berlin, Carl Hansa Verlag.
9. L. HULTMANN, W.-D. MÜNZ, J. MUSIL, S. KADLEC, I. PETROV, and J. E. GREENE: *J. Vac. Sci. Technol. A*, 1991, **9**, 434.
10. W.-D. MÜNZ, F. J. M. HAUZER, D. SCHULZE, and B. BUIL: *Surf. Coat. Technol.*, 1991, **49**, 161.
11. D. RICKERBY, A. M. JONES, and B. A. BELLAMY: *Surf. Coat. Technol.*, 1989, **37**, 111.
12. J. A. SUE and G. S. SCHAJER: 'ASM handbook', Vol. 5, 'Stress determination for coatings', 645; 1994, Materials Park, OH, ASM International.
13. E. E. SALAGEAN, D. B. LEWIS, J. S. BROOKS, W.-D. MÜNZ, I. PETROV, and J. E. GREENE: *Surf. Coat. Technol.*, 1996, **82**, 57.
14. I. PETROV, P. L. LOSBICHLER, D. BERGSTROM, J. E. GREENE, W.-D. MÜNZ, T. HURKMANS, and T. TRINH: *Thin Solid Films*, 1997, **302**, 179-192.

Proc. Euroamat '99, September 1999, Munich

## **PVD Interface design of niobium coatings on steel substrates by cathodic arc generated high energy ion bombardment**

H. Paritong/ C. Schoenjahn/ L.A. Donohue/ W.-D. Münz  
Material Research Institute, Sheffield Hallam University, Sheffield UK

### **1. Introduction**

The quality and nature of the interface between substrate and coating plays a key role in the performance of PVD coatings. The use of multiply charged metal ions from a steered cathodic arc source as opposed to inert Ar ions as the etching species prior to deposition results generally in improved adhesion and hence coating performance [1], [2]. To minimise the number and size of macroparticles or droplets during arc evaporation, high melting point materials such as Nb or Cr should be used as the etching material [3], [4]. However, the interfacial region generated during ion bombardment can show substantially different features depending on the ion species used and can influence a series of properties such as the corrosion performance in the case of Nb films [5], [6]. It has been shown that passivation characteristics similar to bulk Nb can be obtained from a Nb coating deposited on a stainless steel substrate that was subjected to bombardment with multiply charged Nb ions from the steered cathodic arc [6]. However, the same coating deposited onto a substrate material pre-treated with Cr ions or Ar ions prior to deposition did not show the same excellent behaviour but exhibited pitting and local corrosion of the stainless steel substrate. Hence, substantial influence from the interfacial region on the corrosion resistance of the coating/ substrate system was assumed. The impact of the heavy, highly energetic Nb ions on stainless steel generates a sharp interface characterised by an amorphised Nb rich interlayer with no evidence of radiation enhanced diffusion of the Nb ions [5], [6], [7]. The present study further investigates the nature of the interfacial region created by Nb ions from the steered cathodic arc source and the influence on the corrosion performance with regard to the average ion energies as well as to the working gas (argon) pressure during etching. The latter parameter is of interest as sufficient high working gas pressures can be beneficial for the stability of the cathodic arc operated at low arc currents when using high melting point materials such as Nb ( $T_m=2500^\circ\text{C}$ ).

### **2. Experimental**

#### **2.1. Substrate ion etching and coating deposition**

The PVD equipment used was a Hauzer 1000-4 ABS coating machine [8]. The coating chamber has four rectangular cathodes, which can be used either in the steered cathodic

arc or the unbalanced magnetron sputtering mode. Etching with the steered cathodic arc and sputter deposition was carried out from one identical Nb target. A series of different experimental conditions was carried out as summarised in table 1. The substrates, rolled 304 austenitic stainless steel, were etched for 12min from the Nb steered arc under two different working gas pressures with variation of the substrate bias voltage i.e. ion energy. The substrates were then coated with a 300nm thick Nb film in the unbalanced magnetron sputtering. Mode. One set of samples was etched only without any additional sputter coating.

**Table 1.** Etching and Deposition parameters

	Series 1	Series 2	Series 3
<i>Nb-ion etching (CA)</i>			
Arc Current [A]	100	100	100
Neg. Substrate Bias Voltage [V]	200, 400, 600, 800,	400, 600, 800,	400, 600, 800,
Pressure [mbar]	1000, 1200	1000, 1200	1000, 1200
Temperature [°C]	$8.3 \cdot 10^{-4}$	$2.3 \cdot 10^{-3}$	$8.3 \cdot 10^{-4}$
	~400	~400	~400
<i>Nb-coating (UBM)</i>			
Neg. Substrate Bias Voltage [V]			-
Bias current density [ $\text{mAcm}^{-2}$ ]	75	75	-
Temperature [°C]	~3	~3	-
	~420	~420	

## 2.2. Characterisation

The interfacial region of the coated samples was characterised with cross-sectional transmission electron microscopy using a Philips CM20 microscope. The corrosion resistance of the different samples was investigated by potentiodynamic polarisation measurements in a 3% NaCl solution open to air. Prior to the scan the samples were cathodically cleaned. The equipment used was an EG&G potentiostat 263A.

## 3. Results and Discussion

No significant difference in overall coating morphology could be observed by TEM with regard to the etching pressure and the ion energy. All coatings show competitive growth and a relatively broad columnar structure. X-TEM bright field images of the different interface regions of coating series 1 ( $P=8.3 \cdot 10^{-4}$  mbar) are shown in figure 1. The substrates etched with Nb ions with ion energies of 3.6keV to 1.8keV (i.e.  $U_{\text{bias}}=-1200\text{V}$  to  $-600\text{V}$ ;  $E_{\text{ion}} = z \cdot e \cdot U_{\text{bias}}$ , where  $z = \text{charge state} = 3$  [9]) show the typical amorphised Nb-rich interlayer grown under the impact of the heavy, high energetic Nb ions [5].

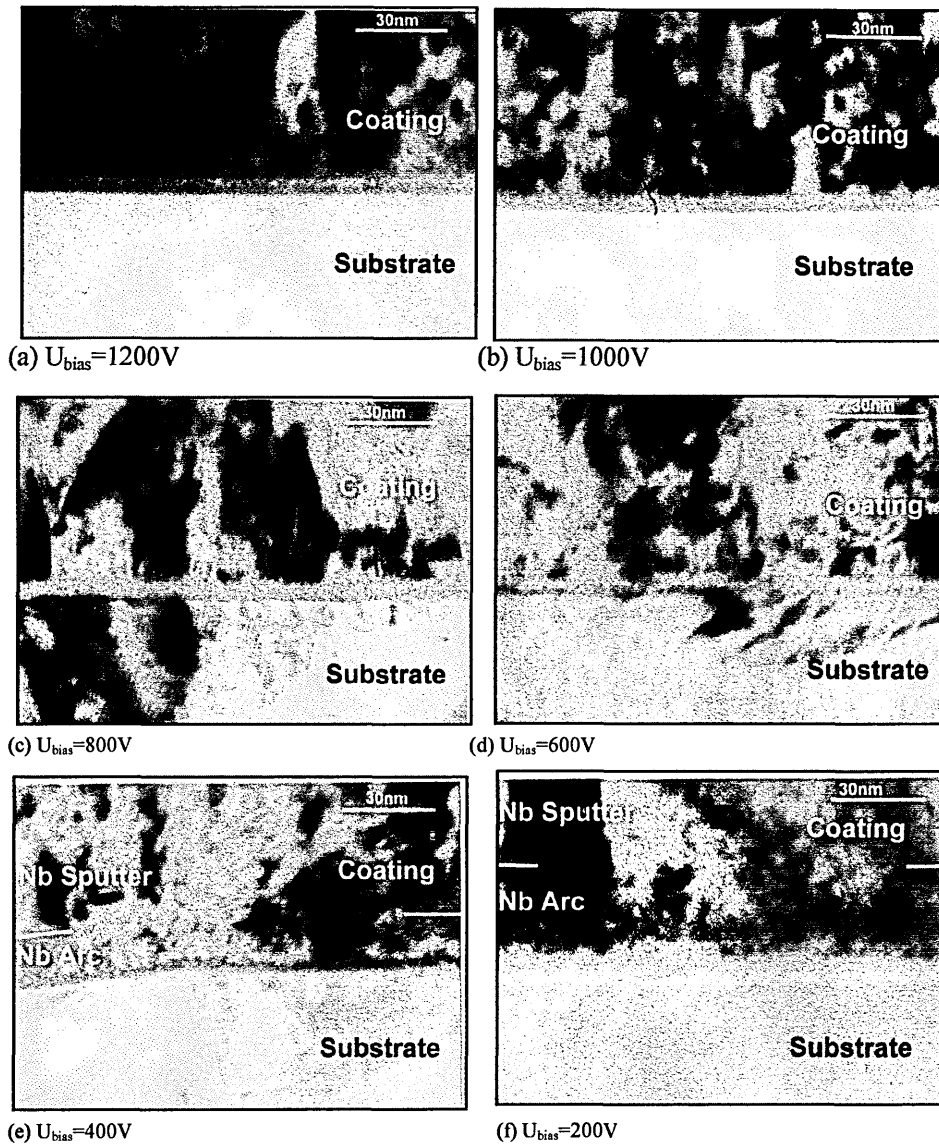


**Figure 1.** X-TEM images of interfacial regions ( $P=8.3 \cdot 10^{-4}$  mbar)

The thicknesses of the interlayers are in the range of  $\sim 8$ nm ( $U_{\text{bias}}=-1200$ V) to  $\sim 4$ nm ( $U_{\text{bias}}=-600$ V). The layer is still present in the case of  $U_{\text{bias}}=-400$ V as can be seen from the relatively dark ribbon in fig.1e with a thickness of 3 nm, however, there is also evidence of a Nb deposition layer on top of the dark ribbon. The latter is approximately 15 nm thick and is characterised by a disrupted, fine-grained structure, grown during the etching stage under the lower energetic ion bombardment. This deposition layer grows in thickness when the ion energies are further decreased to 0.6keV i.e. using a substrate bias

voltage of -200V (fig.1f). The Nb deposition layer reaches approximately 30nm into the coating and is again of a fine-grained nature. In this case, the interface is rather diffuse and there is no evidence of the typical sharply contoured dark ribbon characterising the amorphised intermixed layer at the substrate. The samples etched at  $2.3 \times 10^{-3}$  mbar, not shown here, had similar features.

Potentiodynamic polarisation scans of untreated stainless steel and of one coated sample ( $U_{\text{bias}} = -800\text{V}$ ,  $P = 8.3 \times 10^{-3}$  mbar) are shown in fig.2. The untreated stainless steel passivates between -200mV and +200mV due to the formation of a Cr rich oxide layer. However, the stability of this protective layer is restricted by the presence of chloride anions which leads to breakdown of the passive film i.e. pitting at +200mV followed by severe localised anodic dissolution of the steel which is indicated by the steep increase in current density. The introduction of Nb leads to much improved corrosion behaviour as can be seen from fig.2. The pitting potential is raised to approximately 1000mV compared to 200mV for untreated stainless steel. Accordingly, the anodic current density is reduced to  $< 10^{-5} \text{Acm}^{-2}$  opposed to the maximum recordable current density of  $10^{-1} \text{Acm}^{-2}$  for stainless steel. Further results on the corrosion resistance are summarised in fig.3. Fig.3a,b outline the influence of the Ar background pressure during the metal ion etch prior to deposition as a function of the bias voltage during the etching step. Fig.3c shows the results of the etched-only substrates with no additional Nb coating. In all three cases the pitting potentials ( $E_{\text{pit}}$ ) and the anodic current densities (taken at +700mV) are plotted against the bias voltage. Surprisingly, all three conditions show a very similar behaviour. Neither the Ar background pressure nor the presence of a 300nm Nb sputter top coating show a distinct influence on the corrosion resistance. In all three cases the highest corrosion resistance is achieved with “medium” bias voltages that is -600V and -800V (i.e. ion energies of 1.8keV and 2.4keV), while it is reduced when using bias voltages of the low and the high end of the employed scale.

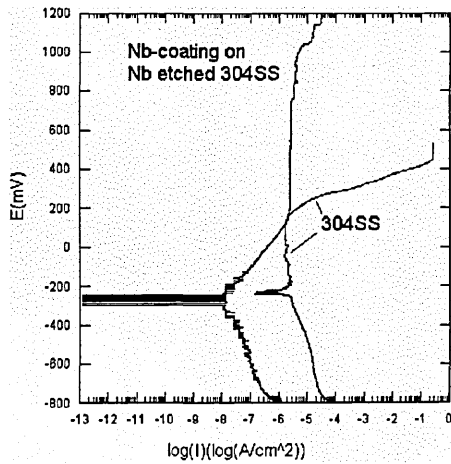
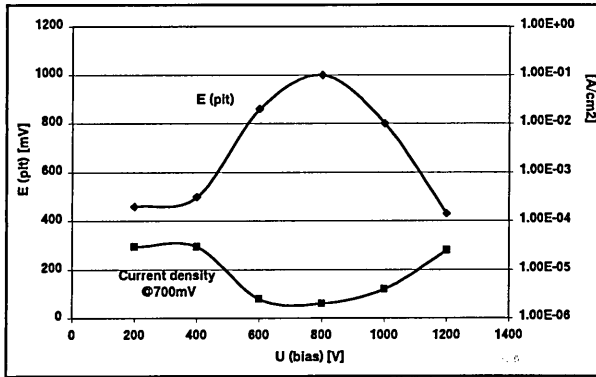
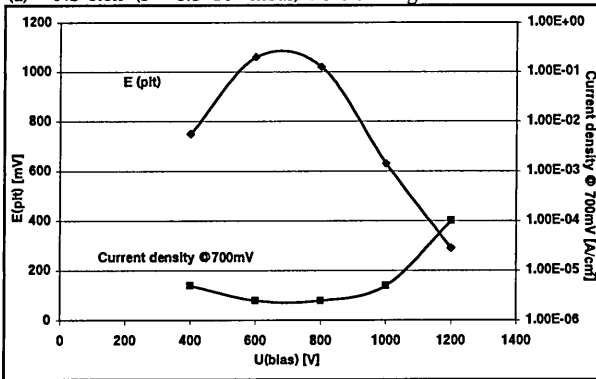


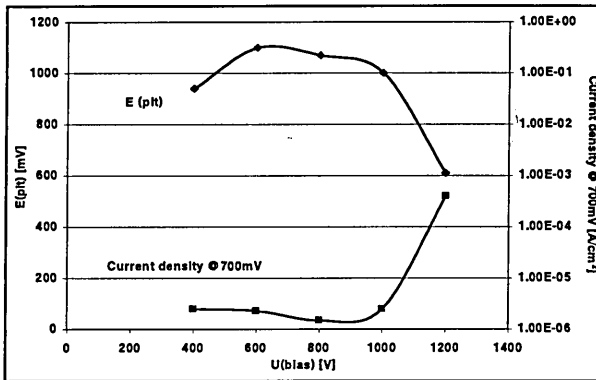
Figure 2. Potentiodynamic polarisation in a 3% NaCl solution



(a) Nb-etch ( $P = 8.3 \cdot 10^{-4}$  mbar) + Nb coating



(b) Nb-etch  $P = 2.3 \cdot 10^{-3}$  mbar + Nb coating



(c) Nb-etch only ( $P = 8.3 \cdot 10^{-4}$  mbar)

Figure 3. Pitting potentials and current densities (@+700mV)

In the case of low bias voltages (-200V, -400V i.e.  $E_{ion} = 0.6\text{keV}$ ,  $1.2\text{keV}$ ) this behaviour is believed to be due to the reduced formation (-400V) or non presence (-200V) of the amorphised layer and the formation of a less dense, columnar deposit during the etching stage. In the case of high bias voltages such as -1200V ( $E_{ion} = 3.6\text{keV}$ ) the behaviour can not fully be explained yet but is believed to be influenced by a reduced Nb concentration at the intermediate interface due to enhanced re-sputtering of Nb during the metal ion

etch. It is important that the improved corrosion resistance accounts not only for the samples with an additional Nb sputter coating but also for the ones that were Nb ion etched only, indicating the importance of the amorphised interfacial layer. However, for practical applications, a mechanically protective Nb sputter layer will probably always be necessary. In summary, the bombardment of the steel by highly energetic Nb ions is believed to influence the corrosion performance in two ways: a) Chemically, that is by introducing a metal with a high chemical stability and the formation of a stable oxide and b) Structurally, that is by the formation of an amorphised layer which leads to reduction of the pit initiation sites hence increasing the pitting resistance.

#### 4. Conclusions

- Treatment of stainless steel with Nb ions from the steered cathodic arc with or without an additional Nb sputter layer significantly improves the corrosion behaviour compared to untreated stainless steel.
- The presence of an amorphised Nb-rich interlayer grown under the impact of the Nb ions is believed to be essential for the improved corrosion performance by influencing it in two ways, that is chemically as well as structurally.
- The nature of the interfacial layer and hence the corrosion resistance is strongly influenced by the energy of the bombarding ions.
- The ion energy or substrate bias voltage during etching has to be carefully chosen to optimise the protection by the interfacial layer.

#### 5. References

- [1] W.-D.Münz, J.Schroeder, H.Pechstein, G.Håkansson, L.Hultman, J-E.Sundgren, Proc. SURTEC Berlin, (Ed.: A.Czichos, L.G.Vollrath), Hanser, Muenchen, 1989, 61
- [2] G.Håkansson, L.Hultman, J-E.Sundgren, J.E.Greene, W.-D.Münz, Surf.Coat.Technol. 1991, 48, 51
- [3] S.Creasey, D.B.Lewis, I.J.Smith, W.-D.Münz, Surf.Coat.Technol. 1997, 97, 163-175
- [4] W.-D.Münz, I.J.Smith, D.B.Lewis, S.Creasey, Vacuum. 1997, 48, 473-481
- [5] E.E.Salagean, D.B.Lewis, J.S.Brooks, W.-D.Münz, I.Petrov, J.E.Greene, Surf.Coat.Technol. 1996, 82, 57-64
- [6] H.Paritong, I.Wadsworth, L.A.Donohue, W.-D.Münz, Trans.IMF. 1998, 76(4), 144
- [7] I.Petrov, P.Losbichler, D.Bergstrom, J.E.Greene, W.-D.Münz, T.Hurkmans, T.Trinh, Thin Solid Films. 1997, 302, 179-192
- [8] W.-D.Münz, D.Schulze, F.J.M.Hauzer, Surf.Coat.Technol. 1992, 50, 169
- [9] A.Anders, Phys.Rev. 1997, E55, 969-981

## **Influence of Cr<sup>+</sup> and Nb<sup>+</sup> substrate sputter cleaning on the formation of Ti<sub>1-x</sub>Al<sub>x</sub>N/steel interfaces generated in a combined cathodic arc/unbalanced magnetron deposition system**

**C Schönjahn<sup>a</sup>, H Paritong<sup>a</sup>, L A Donohue<sup>a</sup>, W-D Münz<sup>a</sup>, R D Twesten<sup>b</sup>, and I Petrov<sup>b</sup>**

<sup>a</sup>Materials Research Institute, Sheffield Hallam University, Howard Street, Sheffield S11WB UK,

<sup>b</sup>Fredrick Seitz Materials Research Laboratory University of Illinois, 104 South Goodwin Avenue, Urbana, Illinois 61801 USA

**ABSTRACT:** The choice of arc cathode material (Cr or Nb) and the negative bias potential ( $U_b = 400-1200$  V) during metal ion etching of steel substrates prior to unbalanced magnetron sputter deposition of Ti<sub>1-x</sub>Al<sub>x</sub>N ( $x=0.54$ ) influences the microstructure and chemistry of the interface region as revealed by XTEM and STEM-EDX analysis. Cr ion bombardment at  $U_b=1200$ V results in Cr implantation profile with a net etching. Subsequent Ti<sub>1-x</sub>Al<sub>x</sub>N growth exhibits local epitaxy with underlying substrate grains. Cr ion bombardment at  $U_b=400$ V and Nb at  $U_b =1200$ V results in metal implantation and deposition. On such surfaces Ti<sub>1-x</sub>Al<sub>x</sub>N shows a competitive growth with small column size and open boundaries.

### **1. INTRODUCTION**

Substrate sputter cleaning is a key step in Physical Vapour Deposition controlling coatings adhesion, which is essential for any coating applications. Generally Ar ion bombardment in an Ar glow discharge plasma is carried out prior to sputter deposition by negatively biasing the substrates. Münz et al (1989) and Håkansson et al (1991) show that Ti metal ion etch in a cathodic arc discharge results in a structurally and compositionally modified layer within the substrates, which was correlated with the improved adhesion. Arc evaporation, however, produces rougher coatings compared to sputtering, due to macro particles, emitted from the cathode. To combine the advantages of metal ion etching with sputter-deposition, a coating system (HTC-1000-4) was developed, which incorporates four cathodes, each of which can be operated in both modes (Münz et al 1992). With four targets, the choice of the target material for ion etching is so no longer limited to the target material required for subsequent sputter deposition. High melting point and high vapour pressure materials can be used as target material in order to minimise number and size of macro particles deposited on the substrate surface during metal ion etching (Münz et al 1997 and Creasey et al 1997). Cr and Nb were found to be well suited in this respect, however, ion etching with the two elements may results in different interface architecture and coating adhesion because of differences in atomic mass, charge distribution and solubility in iron. Here we compare the microstructure and microchemistry of Ti<sub>1-x</sub>Al<sub>x</sub>N/steel interfaces formed by Cr and Nb ion bombardment at different bias voltages ( $U_b = 400 -1200$  V) analysed by XTEM and STEM-EDX. The efficiency of substrate material removal is also investigated by measuring the step generated during ion irradiation.

## 2. EXPERIMENT

The HTC 1000-4 system (Münz et al 1992) was equipped with Cr, Nb, and two  $Ti_{0.5}Al_{0.5}$  targets. The process consists of pump down, heating and degassing at 400°C, followed by Cr or Nb ion etching at an arc current of 100A. To stabilise arc operation an Ar partial pressure of  $6 \times 10^{-4}$  mbar (Cr) and  $8 \times 10^{-4}$  mbar (Nb) was used. The substrate negative bias voltage  $U_b$  during metal ion bombardment was varied in the range of 400 to 1200 V. A 100-nm-thick  $Ti_{1-x}Al_xN$  ( $x=0.54$  from RBS) was then deposited at 450°C with 8 kW DC power on each of the two  $Ti_{50}Al_{50}$  targets at a rate of 10 nm/min. The Ar flow during deposition was 200 sccm, while  $N_2$  flow was regulated using an integrating proportional differential controller to maintain a total pressure of  $3.5 \times 10^{-3}$  mbar. The microchemistry of the interface region in XTEM samples was investigated performing energy dispersive x-ray (EDX analysis) in a VG501 Scanning TEM using ~1nm-diameter electron beam. XTEM imaging was carried out in Philips CM20 equipped with LaB<sub>6</sub> filament, operated at 200kV. Substrates were partially covered with a mask during metal ion etching only and the resulting step was measured with a Laserform Talysurf stylus instrument.

## 3. RESULTS AND DISCUSSION

### Cr ion bombardment

Cr ion bombardment with  $U_b=1200$  V for 20 min removes 90 nm of substrate material. STEM-EDX results, Fig. 1, shows that the Cr profile, with a FWHM of 5 nm, initially parallels the Fe signal at the interface then falls to background levels within a distance of 8 nm. The Cr depth distribution can be interpreted as dominated by ion implantation. Indeed, the projected range,  $R_p$ , for

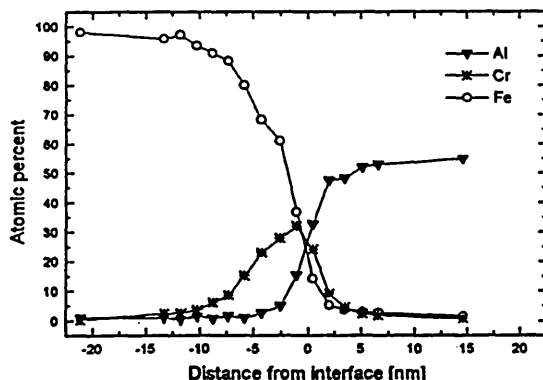


Figure 1 Interface composition after Cr etch at  $U_b=1200V$

implantation and straggling,  $S$ , obtained from TRIM (Ziegler and Biersack 1985), calculations for the maximum charge of  $Cr^{3+}$  (Anders 1997) are 2.7 nm and 1.8 nm, respectively. With the thickness of the etched layer approximately two orders of magnitude larger than the ion range, implantation profiles can be approximated by error functions centred at a depth of  $R+S$ , i.e. -4.5nm in this case. The lateral resolution of the EDX analysis, which is factor determining apparent depth profiles, was estimated to be  $\pm 2.7$  nm from the Al film signal. The Cr signal is, thus, consistent with an implantation profile convoluted with the depth resolution of the technique and, therefore, does not indicate the presence of substantial radiation enhanced diffusion.

At  $U_b=400$  V no evidence of substrate removal was found by step measurements. The Cr-

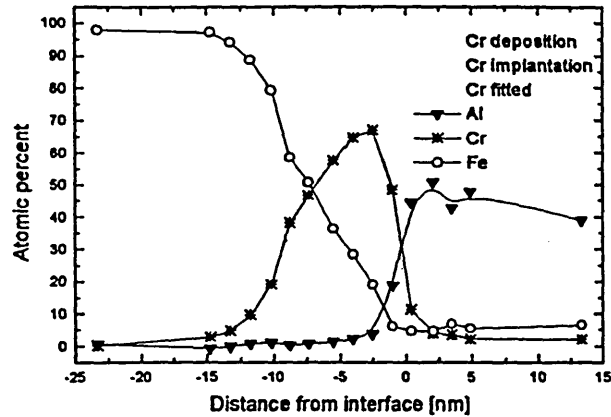


Figure 2 Interface composition after Cr ion bombardment at  $U_b=400V$

profile in Fig 2 can be fitted to two components, indicating Cr enrichment in the substrate due to implantation and the presence of a Cr deposition layer. The presence of an overlayer suggests that the net sputtering rate is not high enough to compensate for film growth deposition from Cr atoms emitted by the cathodic arc. Note that the sputtering yields, obtained from TRIM simulations, with  $U_b = 400 V$  for  $Cr^{2+}$  (1.4) and  $Ar^+$  (1.1) are a factor of two lower than the corresponding values with  $U_b = 1200V$ : 2.8 and 2.4, respectively. Here we have taken the average charge of 2, measured for Cr arcs (Anders 1997).

The different surfaces obtained by Cr bombardment at various  $U_b$  values result in different nucleation and coalescence behaviour in subsequent film growth carried out at identical conditions. The bright field XTEM image (Fig. 3(a)) of a sample pre-etched with  $U_b = 1200 V$ , shows uniform contrast over large areas, consistent with local epitaxial growth of  $Ti_{1-x}Al_xN$  on the clean steel surface as shown in more detail in Schönjahn et al. This growth mode is expected to be beneficial for adhesion as it maximises the bonding energy across the interface. In contrast, a competitive growth with small column size and open boundaries is observed at  $U_b = 400V$  as shown in Figure 3(b).

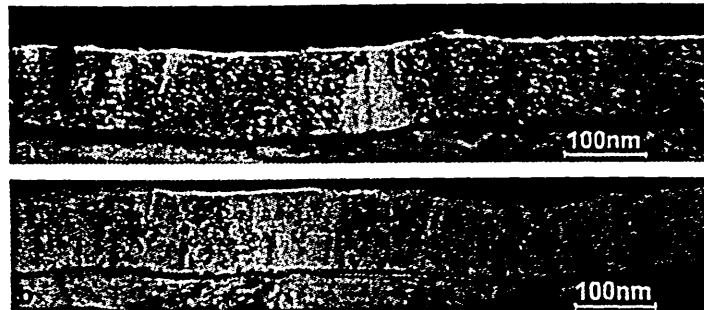


Figure 3 XTEM BF images of  $Ti_{1-x}Al_xN$  grown after Cr ion bombardment at  $U_b=1200V$  (a) and  $U_b=400V$  (b)

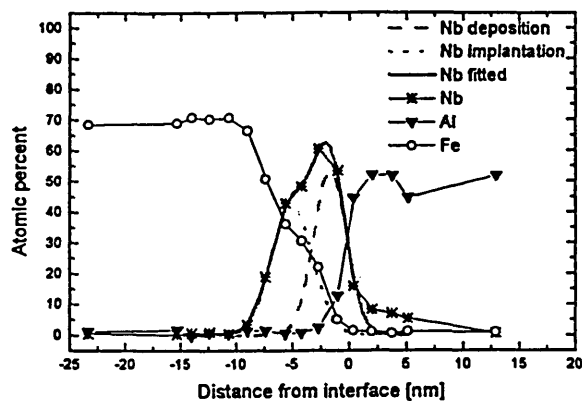


Figure 4 Interface composition after Nb ion bombardment at  $U_b=1200V$

#### *Nb ion bombardment*

The employed step measurement technique was not sensitive enough to show measurable evidence of substrate material removal after Nb ion bombardment independent of the bias voltage. The shape of the Nb profile at  $U_b=1200 V$  is similar to the one obtained for Cr bombardment at  $U_b=400V$ , as shown in Figure 4. Again a two component fit was performed to account for a Nb deposition layer and an ion implanted region. The similarity of the Nb profile to the Cr etch at  $U_b=400V$  can be explained by similar low sputtering yield values (1.4) obtained from TRIM simulation assuming an average charge of  $Nb^{3+}$ . Interfaces generated after Nb bombardment at lower bias voltage show the same features. The  $Ti_{1-x}Al_xN$  coating grown on the Nb layers exhibits competitive growth in analogy to the competitive growth observed on Cr deposition layers.

#### 4. CONCLUSION

It is shown by XTEM and STEM-EDX that: substrate sputter cleaning can be achieved by Cr ion bombardment at  $U_b=1200V$  leading to local epitaxial growth of subsequently deposited  $Ti_{1-x}Al_xN$ . The formation of a metal deposition layer was observed in case of Cr ion bombardment at  $U_b=400V$  or for Nb ion bombardment for  $U_b=600V$  to  $U_b=1200$ . Metal ion implantation was observed for all cases. The formation of a metal layer hinders local epitaxial growth and leads to competitive growth of  $Ti_{1-x}Al_xN$ . The best adhesion should be expected for  $Ti_{1-x}Al_xN$  coatings deposited after Cr ion bombardment at  $U_b=1200V$  as local epitaxy maximises the interface bonding energy.

#### REFERENCES

- Anders A 1997 Phys. Rev. E 55 969-981  
 Creasey S, Lewis D B, Smith I J and Münz W-D 1997 Surf. Coat. Techn 97 163-175  
 Håkansson G, Hultman L, Sundgren J-E, Greene J E, Münz W-D 1991 Surf. Coat. Techn. 48, 51  
 Münz W D, Schroeder J, Pechstein H, Håkansson G, Hultman L and Sundgren J-E 1989  
 Proc. SURTEC Berlin, A. Czichos and L G Vollrath (eds) (München:Hanser) p. 61  
 Münz W-D, Schulze D and Hauzer F J M 1992 Surf. Coat. Techn. 50 169-178  
 Münz W-D, Smith I J, Lewis D B and Creasey S Vacuum 48 473-481.  
 Schönjahn C, Donohue L A, Lewis D B, Münz W-D, Twesten R D and Petrov I unpublished  
 Ziegler J and Biersack J A 1985, The Stopping and Ranges of Ions in Matter (New York: Pergamon)

Deutsche Patentanmeldung:

DPA 19933930.9

**Einfluß der Teilchenenergie von Nb-Ionen beim Ätzen von  
Substraten auf das Korrosionsverhalten nach der  
Beschichtung**

Autoren: Hilke Paritong  
Cornelia Schönjahn  
Wolf-Dieter Münz

Sheffield Hallam University

PVD Niob Schichten haben sich in Korrosionstests als extrem stabil erwiesen. So kann z.B. die Korrosion von rostfreiem Stahl gegen Chlor-Ionen erheblich reduziert werden, wenn z.B. Stahl 304 mit 1  $\mu\text{m}$  Nb beschichtet wird /1/.

Es hat sich ferner gezeigt, daß für das optimale Verhalten von mit unbalancierten Magnetrons abgeschiedenen Niob-Schichten die Vorbehandlung des Stahlsubstrates von eminenter Bedeutung ist. So hat sich im Detail herausgestellt, daß der Korrosionsstrom deutlich reduziert und das Lochfrase-Potential angehoben werden kann, wenn die in-vacuo Ätz-Reinigungsstufe anstatt mit inerten Ar-Ionen oder metallischen Cr-Ionen mit ebenfalls metallischen Nb-Ionen durchgeführt wird (Abb.1). Die beiden metallischen Ionenarten werden dabei aus dem Plasma einer kathodischer Bogenentladung extrahiert /1/.

Es wurde in diesen ersten Untersuchungen ein Potentialunterschied von 1,2 kV zur Beschleunigung der Ionen benutzt. Dies ist zugleich die höchste einstellbare Beschleunigungsspannung unter den gegebenen apparativen Bedingungen. Dabei wurde davon ausgegangen, daß die Beschleunigungsspannung so hoch als möglich sein soll, um entsprechende Ätzraten und damit effektive Reinigungseffekte zu erzielen. Nunmehr wurden Experimente mit Nb-Ionen durchgeführt unter Verwendung von Beschleunigungsspannungen im Bereich von 0,2 bis 1,2 keV. Dabei ergab sich das überraschend neue Ergebnis, daß ein optimaler Beschleunigungsspannungsbereich zwischen 0,6 and 0,9 kV existiert, insbesondere bei 0,8 kV, indem ein besonders hohes Lochfrase-Potential bei minimalem Korrosionsstrom erzielt werden kann (Abb.2). Dieser bevorzugte Beschleunigungsspannungsbereich kommt zur Geltung, wenn man das Substrat alleine mit einer Ätzbehandlung versieht oder in Kombination mit einer nachfolgenden niederenergetischen Beschichtung mit dem unbalancierten Magnetron (0,075kV). Abb. 3 gibt Aufschluß über das Erscheinungsbild einer unbeschichteten und einer "nur" geätzten Probe nach einem Korrosionstest.

Es soll jedoch herausgestellt werden, daß für die industrielle Anwendung "nur" geätzte Oberflächen wahrscheinlich weniger relevant sind. Geringfügige mechanische Beschädigungen reichen aus, um unbeschichtetes Substratmaterial freizulegen. In diesem Falle erweist sich eine 0,5 bis 1  $\mu\text{m}$  dicke Nb-Schicht nicht nur als weiter verstärkter Korrosions- sondern auch als mechanischer Schutz, und unabhängig ob die Nb-Schicht vollkommen dicht ist oder eine gewisse Restporosität aufweist (Thornton-Mochvan-Demishin-Struktur-Modell).

Die Experimente haben auch gezeigt, daß die flächenhafte Ausbreitung von Lochfraseeffekten kleiner sind, wenn die "Nb<sup>+</sup> geätzte" Probe auch mit Nb 0,5  $\mu\text{m}$  dick beschichtet wurde. Abb. 4 gibt ein Element-Profil wieder, das mittels Mikrosonde (STEM-EDX) an dem Querschnitt einer Stahlprobe erzielt wurde, nachdem diese bei einer Beschleunigungsspannung von 0,6 kV mit Nb-ionen 12 Minuten lang vorbehandelt und mit 300nm TiAlN beschichtet wurde. Der Einfluß der Behandlungsdauer wurde bisher noch nicht systematisch untersucht.

Die Probe zeigt eine deutliche Nb-Anreicherung an der Oberfläche während das Maximum des Implantationsprofils bei 2,5nm deutlich innerhalb des Substratbereiches zu finden ist.

Es ist des weiteren hervorzuheben, daß es in Praxis vorteilhaft ist, zunächst mit effektiver Ätzvorbehandlung zu beginnen (-1.2kV), oder diese bei noch

höherer Beschleunigungsspannung , z.B. bei 1,5 kV durchzuführen, um dann die Ätzspannung auf den optimierten Bereich von 0,6 bis 0,9 kV zu reduzieren.

In diesem Fall wird sichergestellt, daß besonders stark verunreinigte Substrate zunächst effektiv geätzt werden und z.B. von Oberflächenoxiden befreit werden, bevor der Beschuß mit weniger energiereichen und daher weniger reinigungsaktiven Nb-Ionen stattfindet.

Es wurde auch festgestellt, daß die vorhandene Restporosität von Nb-Schichten reduziert werden kann, wenn man das Schichtwachstum während der Beschichtung mit dem unbalancierten Magnetron ein oder mehrmals unterbricht und den optimalen Nb-Ionenbeschuß mit 0,6kV stattfinden läßt , um besonders dichte dünne Zwischenschichten (10nm Abb.4) in die Gesamtschicht einzubauen.

Es hat sich auch als überaus positiv erwiesen, die optimierte Nb-Ionen Ätzbehandlung in anderen PVD Hartstoffschichten einzufügen, sei es entweder als reine Nb-Ionenätzbehandlung oder als Zwischenschicht oder sowohl als auch. Besonders positive Ergebnisse wurden erzielt bei CrN/NbN-Superlattice Schichten. Darüber hinaus können auch monolytisch abgeschiedene schichten wie TiN, CrN, TiAlN, TiCN, ZrN, ZrCN, HfN, Al<sub>2</sub>O<sub>3</sub> entschieden verbessert werden.

/1/ H. Paritong, I.Wadsworth, I.A. Donohue, W.-D. Münz, Trans. IMF, 1998, 76(4), 144

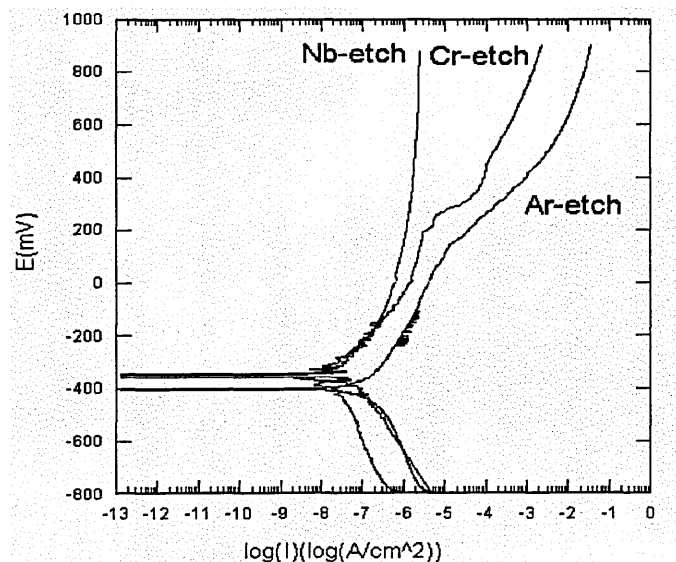


Fig.1. Einfluss der Substratvorbehandlung auf das Korrosionsverhalten von Nb Schichten

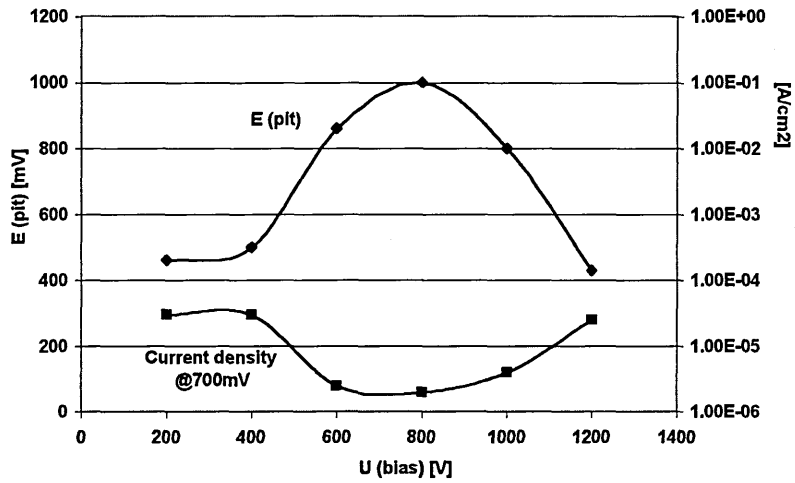
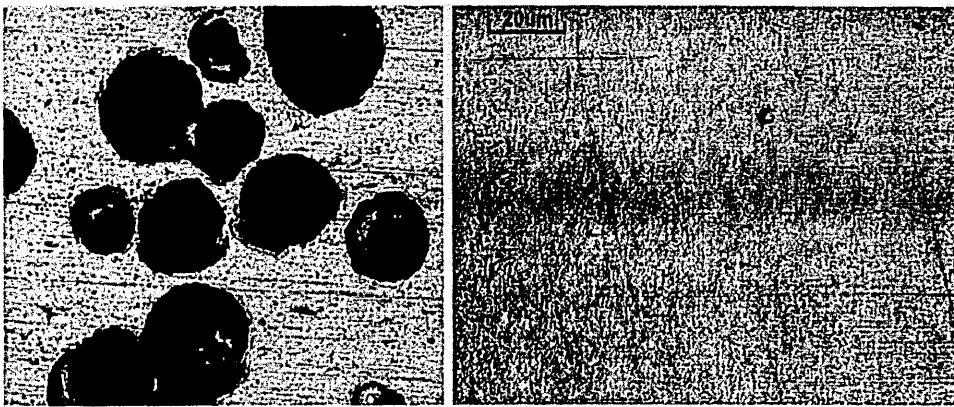


Fig.2 Einfluss der Beschleunigungsspannung während des Ätzens auf den Korrosionswiderstand von Nb Schichten



(a) Unbehandelter Edelstahl (b) Nb-Ionen geätzter Edelstahl

Fig.3. Oberfläche nach Korrosionstest

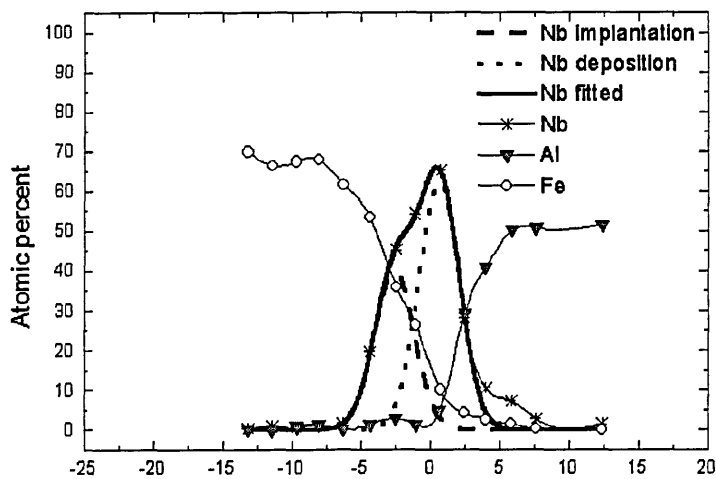


Fig.4. STEM-EDX